Lecture Notes in Electrical Engineering 608

Axaykumar Mehta
Abhishek Rawat
Priyesh Chauhan *Editors*

Advances in Electric Power and Energy Infrastructure

Proceedings of ICPCCI 2019

Springer

Lecture Notes in Electrical Engineering

Volume 608

The book series *Lecture Notes in Electrical Engineering* (LNEE) publishes the latest developments in Electrical Engineering - quickly, informally and in high quality. While original research reported in proceedings and monographs has traditionally formed the core of LNEE, we also encourage authors to submit books devoted to supporting student education and professional training in the various fields and applications areas of electrical engineering. The series cover classical and emerging topics concerning:

- Communication Engineering, Information Theory and Networks
- Electronics Engineering and Microelectronics
- Signal, Image and Speech Processing
- Wireless and Mobile Communication
- Circuits and Systems
- Energy Systems, Power Electronics and Electrical Machines
- Electro-optical Engineering
- Instrumentation Engineering
- Avionics Engineering
- Control Systems
- Internet-of-Things and Cybersecurity
- Biomedical Devices, MEMS and NEMS

For general information about this book series, comments or suggestions, please contact leontina.dicecco@springer.com.

To submit a proposal or request further information, please contact the Publishing Editor in your country:

China

Jasmine Dou, Associate Editor (jasmine.dou@springer.com)

India, Japan, Rest of Asia

Swati Meherishi, Executive Editor (Swati.Meherishi@springer.com)

Southeast Asia, Australia, New Zealand

Ramesh Nath Premnath, Editor (ramesh.premnath@springernature.com)

USA, Canada:

Michael Luby, Senior Editor (michael.luby@springer.com)

All other Countries:

Leontina Di Cecco, Senior Editor (leontina.dicecco@springer.com)

**** Indexing: The books of this series are submitted to ISI Proceedings, EI-Compendex, SCOPUS, MetaPress, Web of Science and Springerlink ****

More information about this series at http://www.springer.com/series/7818

Axaykumar Mehta · Abhishek Rawat ·
Priyesh Chauhan
Editors

Advances in Electric Power and Energy Infrastructure

Proceedings of ICPCCI 2019

Springer

Editors
Axaykumar Mehta
Department of Electrical Engineering
IITRAM
Ahmedabad, Gujarat, India

Abhishek Rawat
Department of Electrical Engineering
IITRAM
Ahmedabad, Gujarat, India

Priyesh Chauhan
Department of Electrical Engineering
IITRAM
Ahmedabad, Gujarat, India

ISSN 1876-1100 ISSN 1876-1119 (electronic)
Lecture Notes in Electrical Engineering
ISBN 978-981-15-0205-7 ISBN 978-981-15-0206-4 (eBook)
https://doi.org/10.1007/978-981-15-0206-4

This Springer imprint is published by the registered company Springer Nature Singapore Pte Ltd.
The registered company address is: 152 Beach Road, #21-01/04 Gateway East, Singapore 189721, Singapore

Preface

This book presents a part of the proceedings of International Conference on Power, Control and Communication Infrastructure (ICPCCI2019) held on 4–5 July 2019 at Institute of Infrastructure Technology, Research and Management (IITRAM), Ahmedabad. The conference was technically and financially supported by Space Application Centre (SAC)—Indian Space Research Organization (ISRO), Institution of Engineers India (IEI), Gujarat Council on Science and Technology (GUJCOST), Govt. of Gujarat, and Science and Engineering Research Board (SERB), Govt. of India. The conference aimed to be a melting pot of researchers from academia and R&D organizations, and practicing engineers from the utilities, industries and service providers to discuss, share and promote ideas related to state-of-the-art innovations in technologies for the Power-Control-Communication sectors. The conference included four keynote speeches: 1. C–band SAR Payload based on active antenna concept by Dr. Tapan Mishra, Distinguished Scientist, Senior Advisor to Secretary, DOS/Chairman, ISRO, 2. Intelligent hand-held robotics for surgery by Dr. Kalyana Veluvolu, Associate professor, Kyungpook National University, South Korea, 3. Transformers for Modern Power Grids by Dr. Parag Upadhyay, Principal R&D Scientist, US Corporate Research Center of ABB, Raleigh, NC, USA, and 4. Importance of Ethics in Research Publishing by Mr. Aninda Bose, Senior Editor, Springer. There was also an industry talk on Role of Energy Storage in Indian Power System by Mr. J. D. Trivedi, Engineer, State Load Dispatch Centre, Gujarat Energy Transmission Corporation Limited, Vadodara. The papers were presented in eight technical sessions, viz. 1. Power System Protection & Planning, 2. Communication Systems—I, 3. Control & Microgrids, 4. Computational Intelligence in Electrical System, 5. Integration of Renewable Energy Sources and Electric Vehicles, 6. Communication Systems—II, 7. Power Converters & Control, 8. Condition Monitoring & Energy Economics.

This book covers the papers presented on latest research trends showcasing the state-of-art innovations with related challenges and potential solutions in the area of electrical power generation-integration-transmission-distribution-conversion-storage-control, electrical machines, power quality, energy management, electrical infrastructure of future grids-buildings-cities-transportation, energy conversion, plasma

technology, renewable energy & grid integration, energy storage systems, power electronic converters, power system protection & security, FACTS and HVDC, power quality, power system operation & control, computer applications in power systems, energy management, energy policies & regulation, power & energy education, restructured power system, microgrids, electrical machines & drives, transportation electrification, optimal operation, electricity-gas-water coordination, condition monitoring & predictive maintenance of electric equipment, and asset management. This book will be useful to the researchers, academicians, students and professionals working in the field as well R&D organizations in the domain of electrical power and energy infrastructure.

We, the editors of this book are thankful to all the contributors who have submitted their research papers to ICPCCI2019 to keep the standard high. The editors would also like to acknowledge the reviewers from the various domains for their prompt and constructive assessments. We would also like to thank the International Advisory Committee and the chairpersons of different committees. Our special thanks to Series Editors, Lecture Notes in Electrical Engineering, Springer for giving us the opportunity to publish this edited volume in the series. We are indeed grateful to Mr. Aninda Bose, Senior Editor, Hard Sciences, Springer Nature India, for the cooperation and support to bring out this volume.

Ahmedabad, India

Axaykumar Mehta
Abhishek Rawat
Priyesh Chauhan

Contents

About the Editors

Axaykumar Mehta received his Bachelor of Engineering in Electrical Engineering (1996), M.Tech (2002) and Ph.D. (2009) degrees from Gujarat University, Ahmedabad, Indian Institute of Technology Kharagpur, and Indian Institute of Technology Bombay, respectively. He is currently an Associate Professor at the Institute of Infrastructure Technology, Research and Management (IITRAM), Ahmedabad, Gujarat, India. He has more than 20 years of teaching experience at the undergraduate and graduate levels at various premier institutions. He has published more than 75 research papers, book chapters in national/international conference proceedings, books and journals. He has authored three books with Springer Nature Singapore and also published five patents at the Indian Patent Office, Mumbai. His research interests include sliding mode controls, networked control systems, multi-agent systems, and control of smart grids/microgrids. Dr. Mehta received the Pedagogical Innovation Award from Gujarat Technological University (GTU) in 2014, Dewang Mehta National Education award (Regional) for best professor in Electrical Engineering in 2018. He is a senior member of the IEEE, member of the IEEE Industrial Electronics Society (IES) and Control System Society (CSS), and life member of the Indian Society for Technical Education (ISTE), Institute of Engineers India (IEI), Systems Society of India (SSI), and Society of Power Engineers (SPE).

Abhishek Rawat received his Bachelor of Engineering in Electronics and Communication Engineering (2001), from Rajiv Gandhi Technological University, Bhopal. He received his Master of Technology (2006) and Ph.D. (2012) from Maulana Azad National Institute of Technology Bhopal, India. He is currently an Assistant Professor at the Institute of Infrastructure Technology, Research and Management (IITRAM), Ahmedabad, Gujarat, India. He has 16 years of research, academic and professional experience in the different premier institutions. Dr. Rawat is senior member IEEE and has published more than 50 articles in international journals, book chapters, national and international conference proceedings. He received the Young Scientist Award from MPCOST Bhopal in 2007,

involved in the field trails of the IRNSS receiver and published four Indian patents. His research interests includes Navigation systems, Satellite Communication and Peripheral security etc.

Priyesh Chauhan is an Assistant Professor at the Department of Electrical Engineering, Institute of Infrastructure Technology, Research and Management (IITRAM), Ahmedabad, India. He received his Ph.D. in Electrical Engineering (Power Electronics & Electric Drives) from the IIT Delhi, New Delhi, in 2014. He has 17 years of research, academic and professional experience. Dr. Chauhan has published four papers in refereed international journals and 18 papers in international conference proceedings. His main research interests are in renewable energy-based off-grid and microgrid-interactive distributed generation, ship power systems architecture and optimization, energy storage integration, and power management systems.

A New Objective Function for Optimal Coordination of Directional Over-current Relays

Jay Shah, Nirmal Khristi, Vipul N. Rajput and Kartik S. Pandya

Abstract This paper presents a novel objective function to obtain the optimum relay settings of directional over-current relays (DOCRs). The proposed improved objective function (IOF) is developed to solve the problems of previously proposed OFs. The proposed research work modifies the previous OFs by introducing a new weighting factor and adding a new term, for fixing mis-coordination problem and minimizing the operating times of both primary and backup relays. The performance of the proposed IOF is evaluated by using 3- and 8-bus test systems. The simulation results reflect the superiority of IOF, compared to other variety of OFs presented in the literature.

Keywords Genetic algorithm · Objective function · Over-current relay · Power system protection · Relay setting · Relay coordination

1 Introduction

Because of cost-effectiveness, the DOCRs are generally applied for primary protection in distribution systems and as a backup protection of transmission systems [1]. In the coordination procedure of relays, the primary relays should be operating within specified time to signal circuit breaker to remove faulty part. On the other hand, backup relays should come in action only after the certain time interval for

J. Shah (✉) · V. N. Rajput
Dr. Jivraj Mehta Institute of Technology, Anand, India
e-mail: jayshah9512@gmail.com

V. N. Rajput
e-mail: vipulrajput16986@gmail.com

N. Khristi
Amul Dairy, Anand, India
e-mail: nirmalkhristi@gmail.com

K. S. Pandya
Charotar University of Science and Technology, Changa, India
e-mail: kartikpandya.ee@charusat.ac.in

A. Mehta et al. (eds.), *Advances in Electric Power and Energy Infrastructure*, Lecture Notes in Electrical Engineering 608,
https://doi.org/10.1007/978-981-15-0206-4_1

avoiding the mis-coordination. It is because the backup relays disconnect fettle part along with faulty part of power systems, affecting the bigger share of network from unwanted power interruption [2]. Furthermore, the operation of DOCRs is depended on the relay settings, named plug setting (PS) and time multiplier settings (TMS). The optimal values of these settings must be required to obtain for the accurate relay coordination [3]. For this task, optimization- and mathematical improvement-based various approaches are presented in the literature.

At the first era of the optimization-based approaches, the linear programming (LP) [4, 5] and nonlinear programming (NLP) [6] methods became popular to solve the coordination problem of DOCRs. After that, heuristic and hybrid methods gain good recognition for obtaining the optimal relay settings for solving the problem of relay coordination. These approaches comprise genetic algorithm (GA) [7–9], particle swarm optimization [10], seeker algorithm harmony search algorithm [3], invasive weed optimization [11], water cycle algorithm [12], GA-LP [1], GA-NLP [13], fuzzy-GA [14], ant colony optimization-LP [15], etc.

In the last few years, various approaches based on the improvement of problem formulation are also presented for minimizing the operational time of relays in addition with minimizing the numbers of coordination constraints [7–9]. The commonly used OF [1, 13] is developed for reduction of weighted sum of operating time of primary relays. In this OF, only time of operation of primary relays (T_{pr}) is minimized. This method may lead the larger functional time for relay operating in backup and hence higher discrimination time among primary and backup (*P*/*B*) relays. Various modified OF-based methods are compared in the previous study in [16]. From this analysis, the OF presented in [7] is found to be efficient than other OFs presented in [17–19]. Regardless of the benefits of the OF presented in [7], the problem of large T_{pr} and T_{br} with large discrimination time can be existed for larger interconnected systems. The main contribution of the paper is that the problem associated with previous OFs has been resolved by proposing improved objective function. In other way, the projected method can decrease the discrimination time between *P*/*B* relay pairs along with minimizing of T_{pr} and T_{br}.

2 Coordination Problem Statement

Equation (1) shows the commonly used OF [1, 13] in which weighted summation of functioning times of primary relays are reduced.

$$\text{OF1} = \min\left(\alpha_1 \sum_{i=1}^{n} T_{\text{pr},i}\right) \tag{1}$$

where n is the number of primary relays in the system and $T_{\text{pr},i}$ is the functioning time of primary relay R_i. The α_1 is the weight allocated for the time of operation of the relay R_i and is generally fix to unity [13].

The over-current relays appointed in this paper are appraised as IEC-based standard inverse definite minimum time (IDMT) characteristic shown as follows [20].

$$T_{\text{op}} = \frac{0.14}{\left(I_{R_i}/\text{PS}_i\right)^{0.02} - 1} \times \text{TMS}_i \tag{2}$$

where T_{op} is functional time of relay R_i. I_{R_i} is fault current detected by relay R_i. TMS_i and PS_i symbolize the time multiplier setting and plug setting of relay R_i, respectively.

In relay coordination problem, different limits and coordination constraints are required to be satisfied, which are described in upcoming sub-section.

(i) Protection coordination criteria: The successive operations of *P*/*B* relays should fulfil the coordination measures to prevent the mis-coordination. The FCTI is the minimum fixed coordination time interval for function of *P*/*B* relays for a same fault. It is generally designated between 0.2 and 0.5 s [1]. The coordination limitation for a primary relay R_i and backup relay R_j can be specified as

$$T_{\text{br},j} - T_{\text{pr},i} \geq \text{FCTI} \tag{3}$$

where $T_{\text{pr},i}$ and $T_{\text{br},j}$ are the operational period of primary and backup relays in respective manner.

(ii) Boundaries of relay settings: The boundary constraints on TMS and PS are expressed as

$$\text{TMS}_{\text{min},i} \leq \text{TMS}_i \leq \text{TMS}_{\text{max},i} \tag{4}$$

$$\text{PS}_{\text{min},i} \leq \text{PS}_i \leq \text{PS}_{\text{max},i} \tag{5}$$

where $\text{TMS}_{\text{min},i}$ and $\text{TMS}_{\text{max},i}$ are the lowest and highest values of TMS for relay R_i, respectively. $\text{PS}_{\text{min},i}$ and $\text{PS}_{\text{max},i}$ are, respectively, the minimal and maximal PS values of relay R_i. Practically, the PS of the relay should be selected greater than the maximum load current and smaller than lowest fault current [13, 19].

(iii) Boundaries for operating time of relay: A relay needs minimal duration to operate, and also it should not consume enormous amount of time to react. Mathematically, this can be represented as

$$T_{\text{min},i} \leq T_{\text{op},i} \leq T_{\text{max},i} \tag{6}$$

where $T_{\text{min},i}$ and $T_{\text{max},i}$ are minimum and maximum operating time of relay R_i, respectively. In the case of violation in any coordination constraints, mis-coordination exist and OF cannot result in an optimal solution.

3 Problem Statement

The most well-known OF expressed by Eq. (1) reduces the operating time of just primary relays. In the extensive interconnected power system, the number of coordination constraints for *P*/*B* relay pairs is higher. In this situation, chances of larger discrimination time and responding duration of backup relay are higher.

To reduce the functioning time of relays alongside discrimination time and backup relays, a range of OFs are presented in the literature [17–19]. However, these OFs have problem of mis-coordination. Authors in [7] have presented the modified OF for eliminating the mis-coordination cases which are expressed by Eq. (7).

$$\text{OF2} = \min\left(\alpha_1 \sum_{i=1}^{n} T_{\text{pr},i}^2 + \alpha_2 \sum_{k=1}^{N} (\Delta T_k - |\Delta T_k|)^2\right) \tag{7}$$

$$\Delta T_k = T_{\text{br},j} - T_{\text{pr},i} - \text{FCTI} \tag{8}$$

where ΔT_k is discrimination time between *P*/*B* relay pair.

The negative value of ΔT_k explains the mis-coordination case. It means that the coordination constraint has been not satisfied. Further, the higher positive value of ΔT_k shows the greater values of discrimination time and accordingly longer operation time of backup relay. The value of ΔT_k under or near to zero on positive scale represents the accurate coordination.

This OF can eliminate the mis-coordination cases, but it functions same as OF1 in case of positive value of ΔT_k. Therefore, the problem of larger discrimination time as well as larger responding time of backup relays is still befallen.

This problem is clarified by taking weighting factors $\alpha_1 = 1$ and $\alpha_2 = 20{,}000$ in following two cases:

Case 1: $\Delta T_k = 0.2$, $T_{\text{pr},i} = 0.23$, $T_{\text{br},j} = 0.63$, FCTI = 0.2, OF2 = 0.0529
Case 2: $\Delta T_k = 0.4$, $T_{\text{pr},i} = 0.23$, $T_{\text{br},j} = 0.83$, FCTI = 0.2, OF2 = 0.0529

When the OF2 is analysed for above two cases, it has same answers as value of OF2 is 0.0529 s. Because of same value of the OF, there is the chances of selection of Case 2 by optimization algorithm. However, Case 1 has less value of backup as well as discrimination time. This analysis shows that the OF2 is not sensitive to positive value of ΔT.

4 Proposed Method

To overcome the difficulties of the OF2, it is improvised by adding new terms and weight factor. It is illustrated by following equation.

$$\text{IOF} = \alpha_1 \sum_{i=1}^{n} T_{\text{pr},i}^2 + \sum_{k=1}^{N} \left(\alpha_2 (\Delta T_k - |\Delta T_k|)^2 + \alpha_3 (\Delta T_k + |\Delta T_k|)^2\right) \quad (9)$$

where α_1, α_2 and α_3 are weighting factors having values in order of 1, 200 and 1. When ΔT_k is positive ($\Delta T_k > 0$), the term ($\Delta T_k - |\Delta T_k|$) will become zero and second term of IOF will be $4 \times \alpha_3 \times (\Delta T_k)^2$. Similarly, this term becomes as $4 \times \alpha_2 \times (\Delta T_k)^2$ for negative value of ΔT_k ($\Delta T_k > 0$). It is also noted that the suitable value of weight factors is also needed to select. Moreover, the IOF is tested for the same cases as considered for OF2. The values for α_1, α_2 and α_3 are considered in order of 1, 200 and 1.

Case 1: $\Delta T_k = 0.2$, $T_{\text{pr},i} = 0.23$, $T_{\text{br},j} = 0.63$, FCTI = 0.2, IOF = 0.2129
Case 2: $\Delta T_k = 0.4$, $T_{\text{pr},i} = 0.23$, $T_{\text{br},j} = 0.83$, FCTI = 0.2, IOF = 0.6929

It is clearly shown from the above analysis that algorithm selects Case 1 as optimum solution than Case 2. This way, the IOF eliminates the problem associated with OF2. The flow diagram of the proposed method using GA is illustrated in Fig. 1.

5 Result and Discussion

In this section, OF1, OF2 and IOF with different weight factors are implemented on 3-bus and 8-bus standard test systems. For both the systems, the range PS is 0.5–2.5, whereas TMS is selected between 0.1 and 1.1. Also, the CT ratio for each relay is 500:1, and FCTI is expected to be 0.2 s for each *P*/*B* relay pair. Table 1 gives the details of control parameters of GA for both test systems.

5.1 3-Bus System

The single-line diagram of 3-bus system with 6 DOCRs is illustrated in Fig. 2. The remaining detail of the system can be found [21]. As explained in above section, IOF is capable to solve the problem of longer discrimination time and functioning time of backup relays associated with OF2. However, for obtaining the best optimum solution, an appropriate selection of weighting factors value is also required. For this purpose, several logical trial-and-error-based different values of α_1, α_2 and α_3 are tested in this section. Different cases with variety of weighting factors are presented in Table 2. In Table 2, the Case 1 and Case 2 signify the OF1 and OF2, whereas Case 3 and Case 4 symbolize the IOF with different values of weight factors.

By implementing the OF1, OF2 and IOF using GA, the acquired results of relay settings are presented in Table 3. Table 4 shows the obtained operational time of *P*/*B* relays, whereas discrimination time is given in Table 5. It is apparently observed from Table 4 that the total operating duration of primary relays is same for Case 1

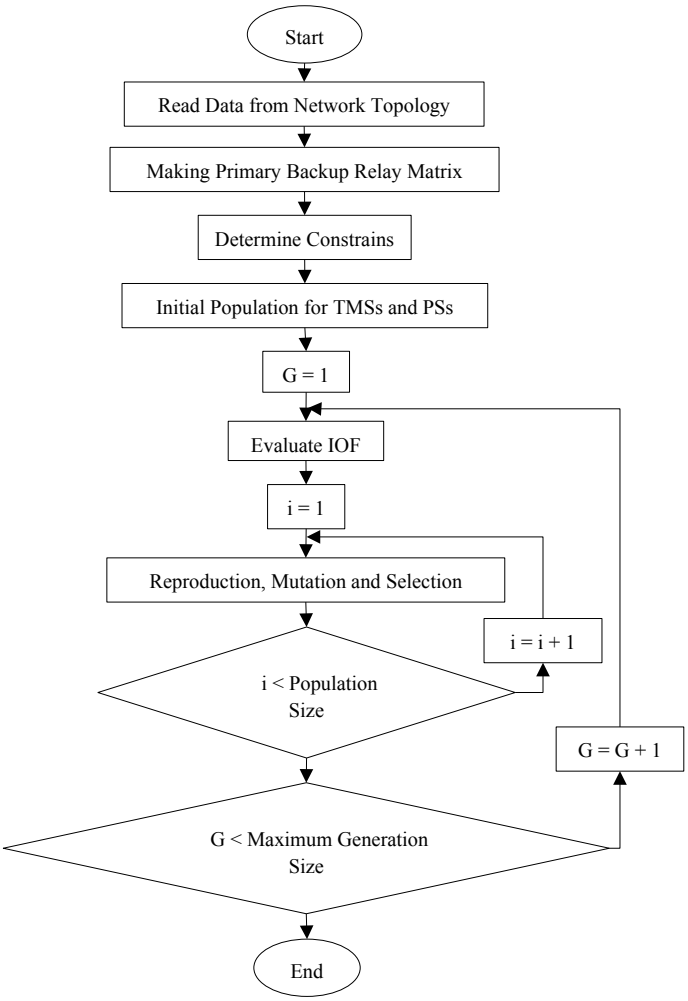

Fig. 1 Flow chart of proposed method

Table 1 GA parameters

GA parameters	Value	GA parameters	Value
Number of generations	4000	Crossover rate	0.95
Size of population	100	Mutation	0.01

and Case, and lower than the Case 3 and Case 4. On the other hand, total functioning time of backup relays is minimum in Case 3 and Case 4 compared to remaining cases. It is noted from Table 5 that no infeasible solution is observed in any cases. Further, the discrimination time obtained for Case 3 and Case 4 is almost zero, which is better than Case 1 and Case 2.

Fig. 2 3-bus test system

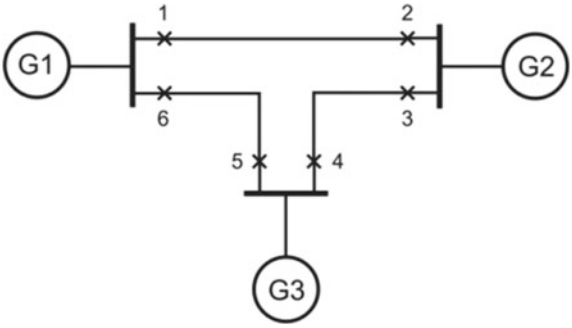

Table 2 Different cases with variety of weighting factors

Case number	α_1	α_2	α_3
Case 1	1	–	–
Case 2	1	20,000	–
Case 3	1	20,000	1
Case 4	1	200	1

Table 3 Relay settings obtained for 3-bus system

Relay no	Case 1		Case 2		Case 3		Case 4	
	PS	TMS	PS	TMS	PS	TMS	PS	TMS
1	1.9345	0.1000	1.9345	0.1000	1.9345	0.1000	1.9345	0.1000
2	1.2921	0.1001	0.6494	0.1212	0.5000	0.1294	0.5000	0.1294
3	1.7189	0.1000	1.7189	0.1000	1.7189	0.1000	1.7189	0.1000
4	1.6264	0.1000	1.6264	0.1000	1.6264	0.1000	1.6264	0.1000
5	1.1416	0.1033	1.1514	0.1031	0.6781	0.1194	0.6781	0.1194
6	1.1850	0.1000	1.1850	0.1000	0.9245	0.1159	0.9245	0.1159

Table 4 T_{pr} and T_{br} obtained for 3-bus system

Relay no	Case 1		Case 2		Case 3		Case 4	
	T_{pr} (s)	T_{br} (s)	T_{pr} (s)	T_{br} (s)	T_{pr} (s)	T_{br} (s)	T_{pr} (s)	T_{br} (s)
1	0.2399	0.4119	0.2399	0.4119	0.2399	0.4119	0.2399	0.4119
2	0.2000	0.5349	0.2000	0.4844	0.2000	0.4476	0.2000	0.4476
3	0.2119	0.4000	0.2119	0.4000	0.2119	0.4000	0.2119	0.4000
4	0.2325	0.4000	0.2325	0.4000	0.2325	0.4000	0.2325	0.4000
5	0.2000	0.5058	0.2000	0.5333	0.2000	0.4399	0.2000	0.4399
6	0.2324	0.4325	0.2324	0.4325	0.2476	0.4325	0.2476	0.4325
SUM (s)	1.3167	2.6852	1.3167	2.6622	1.3319	2.5319	1.3319	2.5319

Table 5 Discrimination time (ΔT) obtained for 3-bus system

Sr. no.	*P*/*B* relays pair		Cases			
	PR	BR	Case 1 (s)	Case 2 (s)	Case 3 (s)	Case 4 (s)
1	1	5	0.0660	0.0934	0.0000	0.0000
2	2	4	0.0000	0.0000	0.0000	0.0000
3	3	1	0.0000	0.0000	0.0000	0.0000
4	4	6	0.0000	0.0000	0.0000	0.0000
5	5	3	0.0000	0.0000	0.0000	0.0000
6	6	2	0.1025	0.0521	0.0000	0.0000
$\sum \Delta T$ (s)			0.1684	0.1454	0.0000	0.0000

From above analysis, it is concluded that the OF1 and OF2 represented by Case 1 and Case 2 give lowest operating duration of primary relays, whereas IOF represented by two cases with different weight factors gives less discrimination time and backup operating time.

5.2 8-Bus System

To check the performance of all the OFs, it is further test for 8-bus system with 14 DOCRs and 20 *P*/*B* relays pairs as shown in Fig. 3. The detail of the systems can be obtained from [21].

The relay settings of relays obtained by implementing the OFs are presented in Table 6. The summary of results for total functioning time of primary relays, backup relays and discrimination time is given in Table 7. As obvious from the

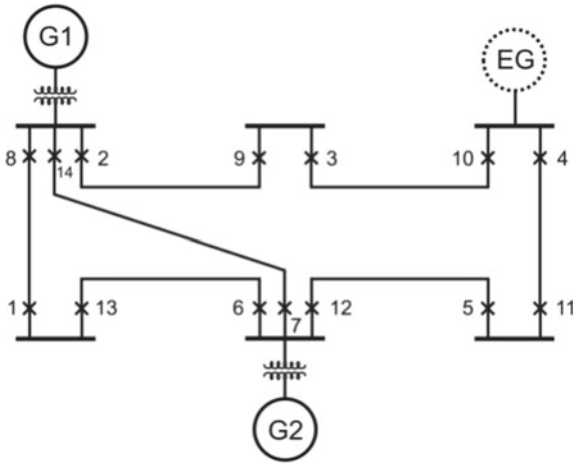

Fig. 3 8-bus test system

Table 6 Relay settings for 8-bus system

Relay no	Case 1		Case 2		Case 3		Case 4	
	PS	TMS	PS	TMS	PS	TMS	PS	TMS
1	1.6342	0.1000	0.5750	0.3495	0.9926	0.2364	1.6342	0.1000
2	2.5000	0.1821	0.5357	0.5506	0.5510	0.5306	2.5000	0.1821
3	2.5000	0.1607	0.5129	0.5081	0.7761	0.4402	2.5000	0.1607
4	2.5000	0.1182	0.7835	0.3711	0.5000	0.4245	2.5000	0.1182
5	1.7050	0.1000	0.5000	0.3503	0.5120	0.3335	1.7050	0.1000
6	2.5000	0.1284	0.5000	0.4879	0.6586	0.3837	0.5522	0.2474
7	2.5000	0.1677	0.7761	0.4669	0.9686	0.4178	2.5000	0.1677
8	2.5000	0.1245	0.5188	0.3981	0.5774	0.4001	0.5000	0.2540
9	2.4544	0.1000	0.5407	0.4091	0.7318	0.3067	2.4544	0.1000
10	2.5000	0.1179	0.6765	0.4104	0.5000	0.3938	2.5000	0.1179
11	2.5000	0.1250	0.5570	0.4540	2.2467	0.2057	2.5000	0.1250
12	2.5000	0.1780	0.9377	0.4632	0.5000	0.4731	2.5000	0.1780
13	1.5963	0.1000	0.9723	0.2427	0.5562	0.2967	1.5963	0.1000
14	2.5000	0.1642	0.6188	0.5032	1.0083	0.3653	2.5000	0.1642

Table 7 Total operating time and discrimination time for 8-bus system

Particular	Case 1	Case 2	Case 3	Case 4
$\sum T_{pr}$ (s)	5.9743	11.7177	10.6187	6.098
$\sum T_{br}$ (s)	9.1060	15.0574	13.8467	9.1076
$\sum \Delta T$ (s)	0.6635	1.0118	0.7674	0.4161

results, Case 3 gives better performance compared to Case 2. On the other hand, Case 1 which represents the OF1 gives better results than Case 3 in terms of all the particulars. Therefore, IOF is needed further improvement in terms of weight factors. By performing the improvement in weight factors of the IOF as presented by Case 4, the best results are obtained which is clearly shown in Table 7.

Figure 4 illustrates the mean value of operational time of *P*/*B* relays as well as discrimination time of *P*/*B* relay pairs. It is clearly seen that the Case 4 gives improved results in the form of average value of functioning duration of primary relays (T_{pr}), backup relays (T_{br}) as well as discrimination time (ΔT).

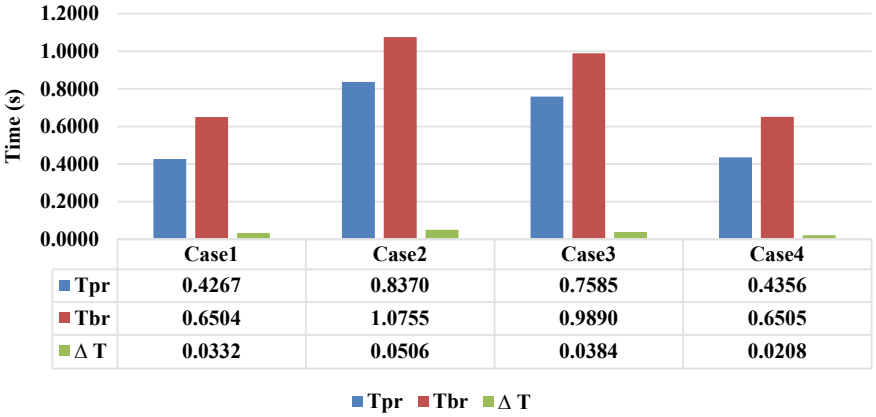

Fig. 4 Average value of operational time of primary and backup relays with discrimination time of *P*/*B* relay pair for 8-bus system

6 Conclusion

This paper presents the new formulation of relay coordination problem and solved using the GA. The proposed improved OF is successfully implemented on two different test systems. The IOF is also tested with considering different value of weight factors. From the results, it is concluded that the IOF with suitable weight factors can solve the issue of higher functioning time of relays. It is also capable to lessen the discrimination time among the operation of *P*/*B* relays pairs.

References

1. Noghabi AS, Sadeh J, Mashhadi HR (2009) Considering different network topologies in optimal overcurrent relay coordination using a hybrid GA. IEEE Trans Power Deliv 24(4):1857–1863
2. Alam MN, Das B, Pant V (2015) A comparative study of metaheuristic optimization approaches for directional overcurrent relays coordination. Electr Power Syst Res 128:39–52
3. Rajput VN, Pandya KS (2017) Coordination of directional overcurrent relays in the interconnected power systems using effective tuning of harmony search algorithm. Sustainable Comput Inf Syst 15:1–15
4. Chattopadhyay B, Sachdev M, Sidhu T (1996) An on-line relay coordination algorithm for adaptive protection using linear programming technique. IEEE Trans Power Deliv 11(1):165–173
5. Urdaneta AJ, Nadira R, Jimenez LP (1988) Optimal coordination of directional overcurrent relays in interconnected power systems. IEEE Trans Power Deliv 3(3):903–911
6. Birla D, Maheshwari RP, Gupta H (2007) An approach to tackle the threat of sympathy trips in directional overcurrent relay coordination. IEEE Trans Power Deliv 22(2):851–858
7. Mohammadi R et al (2010) Optimal relays coordination efficient method in interconnected power systems. J Electr Eng 61(2):75–83
8. Rajput VN, Adelnia F, Pandya KS (2018) Optimal coordination of directional overcurrent relays using improved mathematical formulation. IET Gener Transm Distrib 12(9):2086–2094

9. Razavi F et al (2008) A new comprehensive genetic algorithm method for optimal overcurrent relays coordination. Electr Power Syst Res 78(4):713–720
10. Zeineldin H, El-Saadany E, Salama M (2006) Optimal coordination of overcurrent relays using a modified particle swarm optimization. Electr Power Syst Res 76(11):988–995
11. Castillo C, Conde A, Shih M (2018) Improvement of non-standardized directional overcurrent relay coordination by invasive weed optimization. Electr Power Syst Res 157:48–58
12. Korashy A et al (2019) Modified water cycle algorithm for optimal direction overcurrent relays coordination. Appl Soft Comput 74:10–25
13. Bedekar PP, Bhide SR (2011) Optimum coordination of directional overcurrent relays using the hybrid GA-NLP approach. IEEE Trans Power Deliv 26(1):109–119
14. Alkaran DS et al (2018) Optimal overcurrent relay coordination in interconnected networks by using fuzzy-based GA method. IEEE Trans Smart Grid 9(4):3091–3101
15. Rivas AEL, Pareja LAG, Abrão T (2019) Coordination of distance and directional overcurrent relays using an extended continuous domain ACO algorithm and an hybrid ACO algorithm. Electr Power Syst Res 170:259–272
16. Shah J et al (2017) A comparative study based on objective functions for optimum coordination of overcurrent relays. In: 2017 7th International Conference on Power Systems (ICPS). IEEE
17. Kalage AA, Ghawghawe ND (2016) Optimum coordination of directional overcurrent relays using modified adaptive teaching learning based optimization algorithm. Intell Ind Syst 2(1):55–71
18. So C, Li K (2000) Overcurrent relay coordination by evolutionary programming. Electr Power Syst Res 53(2):83–90
19. Alam MN, Das B, Pant V (2016) An interior point method based protection coordination scheme for directional overcurrent relays in meshed networks. Int J Electr Power Energy Syst 81:153–164
20. Adelnia F, Moravej Z, Farzinfar M (2015) A new formulation for coordination of directional overcurrent relays in interconnected networks. Int Trans Electr Energy Syst 25(1):120–137
21. Amraee T (2012) Coordination of directional overcurrent relays using seeker algorithm. IEEE Trans Power Deliv 27(3):1415–1422

Symmetrical Fault—Swing Discrimination Using RMS Index-Based Superimposed Current Signals

K. R. Andanapalli and M. Biswal

Abstract To maintain reliable and secured power system operation, relays are designed to operate at a faster rate so as to provide an appropriate tripping signal to circuit breakers under any abnormal transient condition. During swing phenomenon, operation of a relay is required to block with the help of PSB function so that any nuisance operation can be avoided. Unblocking operation can easily be issued by the relay in case of an unsymmetrical fault, but detection of symmetrical fault is a difficult task. A novel approach to discriminate three-phase fault from power swing using the root mean square (RMS) value of superimposed current signal is proposed in this paper. Superimposed current signal is estimated by taking the difference between two consecutive cycles considering the recursive window approach. The index is then computed by estimating the RMS value from the one-cycle superimposed current components. The generated index helps the relay to discriminate symmetrical fault from power swing. To verify the response of proposed method, a 400 kV, 50 Hz WSCC 9-bus test system is considered and simulated with different fault cases. The power system model is simulated using PSCAD/EMTDC software, and results indicate the robustness of the proposed algorithm.

Keywords Transmission lines · Superimposed current components · RMS index · Power swing · Symmetrical faults

1 Introduction

Power swing condition may arise in power system due to the occurrence of fault, line outages, generator outages and abrupt change in the load [1]. Distance relay is designed to generate trip command whenever quantified apparent impedance enter into its operating characteristics and remains in it. But for non-fault cases like power

K. R. Andanapalli (✉) · M. Biswal
Department of Electrical Engineering, NIT Raipur, Raipur, Chhattisgarh, India
e-mail: akumarraja.a@gmail.com

M. Biswal
e-mail: mbiswal.ele@nitrr.ac.in

A. Mehta et al. (eds.), *Advances in Electric Power and Energy Infrastructure*, Lecture Notes in Electrical Engineering 608,
https://doi.org/10.1007/978-981-15-0206-4_2

swing, switching event, etc., the apparent impedance may likewise go into the operating zone causing undesirable tripping of the relay. Specially to handle relay operation during power swing phenomenon, PSB (power swing blocking) function is provided [2]. Unblocking of PSB function is crucial if any fault occurs during swing so that an immediate clearance of the fault is possible. Availability of sequence components for any unsymmetrical fault during power swing can easily be detected, but these components are absent in stable conditions. Detection of symmetrical fault during the power swing is an arduous task to perform by the relay. Different schemes have been suggested by the researchers to mitigate the symmetrical fault-swing discrimination issue [3–17]. These techniques can be categorized as signal processing-based, analytical-based, intelligence-based methods and decomposition techniques.

Other techniques such as wavelet transforms [3, 4], Prony analysis [5], DFT [6] and LES-based approaches [7] are also utilized to discriminate three-phase (symmetrical) fault from power swing contingent upon the extraction of high-frequency content presents in transient signal. The methods were capable of detecting the fault accurately within a power cycle. But it requires more sampling rate, and computational burden is also very high. Further, few analytical approaches were additionally developed to discriminate symmetrical fault from power swing. Some of them are autoregression analysis [8], moving average technique [9], transient monitor index-based method [10], phase space method [11] and Teager–Kaiser energy operator-based method [12]. In these methods, the threshold requires to discriminate the required events is system dependent and may fail during different critical situations like high-resistance fault, with presence of noise in input signal and under varying fault location. A wide area measurement-based technique is proposed in [13]. Furthermore, Teager–Kaiser energy operator combined with HHT in [14] and zero filtering technique using Hilbert transform [15] can detect symmetrical fault from swing. However, they are suitable and have high computational complexity. The review of all the techniques and the merits and demerits is described clearly in [16].

The paper presents a novel approach by which symmetrical fault can be easily and accurately discriminated from power swing that is proposed. The method uses superimposed current signal to estimate the RMS value. For study, the WSCC 9-bus test system is considered and simulated using EMTDC/PSCAD software. For result analysis, the influence of high fault resistance and the effect of variation of fault distance on the response of proposed method are considered. Results show that the proposed method provides accurate results of different fault cases, and the speed of operation is high irrespective of the severity of the event.

The paper is organized as follows: Sect. 2 briefly discusses the proposed methodology and Sect. 3 provides the result analysis part followed by conclusions in Sect. 4.

2 Proposed Methodology

A novel technique is implemented to detect symmetrical fault during power swing which is proposed using superimposed current components of three-phase signals. This technique utilizes three-phase current signals at relay end, and then the superimposed components are estimated. One-cycle superimposed current components are utilized to estimate the RMS index which helps to distinguish the fault from swing phenomenon.

2.1 Superimposed Current Component (SCC)

One-cycle superimposed current signal can be estimated using two consecutive cycles as (1)

$$I_{\mathrm{scc}_n}(k+1-N:k) = I_n(k+1-N:k) - I_n(k+1-2N:k-N) \tag{1}$$

where I_{scc_n} and I_n denote the set of superimposed current components and measured current signal for nth phase, suffix n represents the phases A, B and C, respectively, k represents the $(2N)$th sampling instant, and N specifies the number of samples over one cycle.

One-cycle superimposed current signal is then used to estimate the RMS index.

2.2 Root Mean Square (RMS) Index

For generating the RMS index using one-cycle superimposed current component, the index term of superimposed current components of nth phase (I_{scc_n} index') is calculated by considering three successive samples from superimposed current component samples of nth phase as given in Eq. (2).

$$I_{\mathrm{scc}_n}\mathrm{index}(k) = I_{\mathrm{scc}_n}(k) - \left(\frac{I_{\mathrm{scc}_n}(k+1) + I_{\mathrm{scc}_n}(k-1)}{2}\right) \tag{2}$$

Each index value is iteratively updated until the termination criteria of end of each cycle. By considering the obtained index from Eq. (3), the RMS index can be calculated as

$$I_{\mathrm{scc}_n}\mathrm{rms\ index}(k) = \sqrt{\frac{\sum_{k=2}^{N}\left(I_{\mathrm{scc}_n}\mathrm{index}(k)\right)^2}{N}} \tag{3}$$

where I_{scc_n} rms index represents superimposed current components of nth phase signal. Using the RMS index as mentioned in Eq. (3), fault-swing discrimination task can be performed. The RMS index values of the superimposed current signal of each phase will be significantly higher during symmetrical fault and approximately zero during the swing phenomenon. But to avoid relay maloperation, a threshold (h) is selected to accomplish the detection and discrimination task correctly. As per the rule,

$$\begin{aligned} &\text{if} \quad I_{\mathrm{scc}_n}\text{rms index}(k) > h \Rightarrow \text{Trip signal is generated} \\ &\text{Otherwie} \Rightarrow \text{blocking operation} \end{aligned} \tag{4}$$

In order to validate the merit of the proposed method, response for different fault and swing cases is tested considering standard power system model.

3 Simulation Results

The efficacy of proposed method, three-phase fault detection during swing phenomenon, is tested for different fault situation by varying fault location and fault resistance. In this work, WSCC 9-bus system [17] shown in Fig. 1 is considered and simulated using EMTDC/PSCAD software. A distributed transmission line model with 50 Hz nominal frequency is considered for the study. The sampling rate of current signal is maintained at 1 kHz.

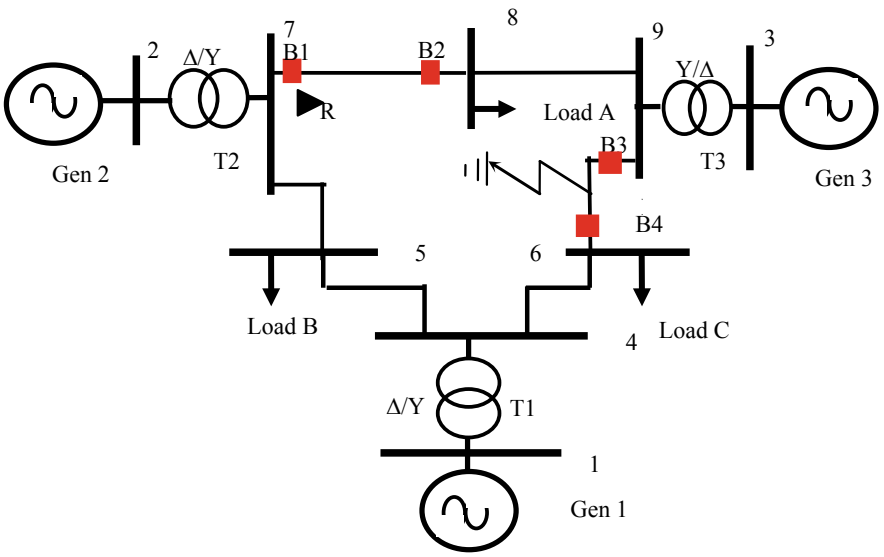

Fig. 1 A 400 kV, 50 Hz WSCC 3-machine, 9-bus system

The performance of the proposed method is verified under swing phenomenon, symmetrical fault is initiated on line 9–6 at 1.0 s, and breakers 'B3' and 'B4' are opened (at 1.3 and 1.45 s) to clear the fault. As a consequence, the relay observes stable and unstable swing. During such phenomena, the distance relay '*R*' located at bus 7 needs to be blocked. When a symmetrical fault occurs during either stable or unstable power swing, then the relay *R* should be unblocked to detect the fault.

3.1 Result for Symmetrical Fault During Stable and Unstable Power Swing

To validate the performance of the proposed method under fault during stable and unstable power swing, a three-phase fault is initiated on the line 7–8 at 4.85 s. The response of this method is illustrated in Figs. 2 and 3. From Figs. 2a and 3a, it is observed that the relay *R* experiences stable and unstable power swings in the current signals. Also observed that the maximum swing frequencies are 0.7 Hz for stable and 6.6 Hz for unstable. Conversely, the proposed RMS index is computed and compared with the fixed threshold '*h*'. During stable and unstable power swings, the index is well below the threshold '*h*' and exceeds the threshold during three-phase fault as observed from Figs. 2b and 3b. Symmetrical fault is detected at 4.854 s during stable swing and at 4.856 s during unstable swing. Thereafter, the relay *R* generates a TRIP command as shown in Figs. 2c and 3c to the corresponding circuit breaker, respectively. This clearly demonstrates the effectiveness of the proposed method.

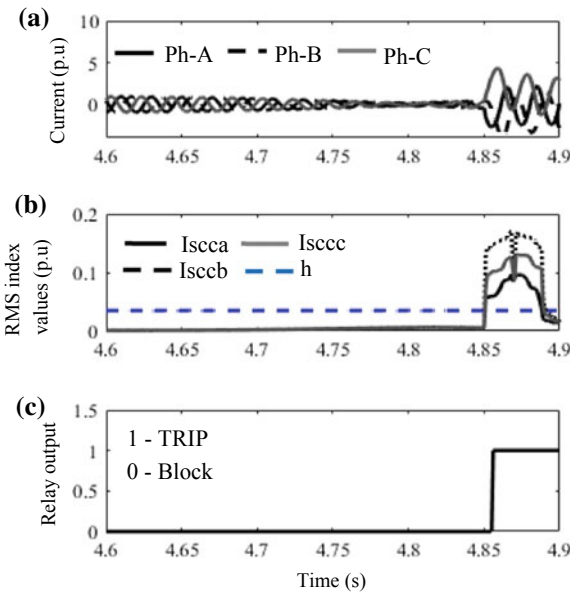

Fig. 2 Result of three-phase fault detection during the stable power swing (0.7 Hz), **a** three-phase current signal, **b** RMS index values and **c** relay output

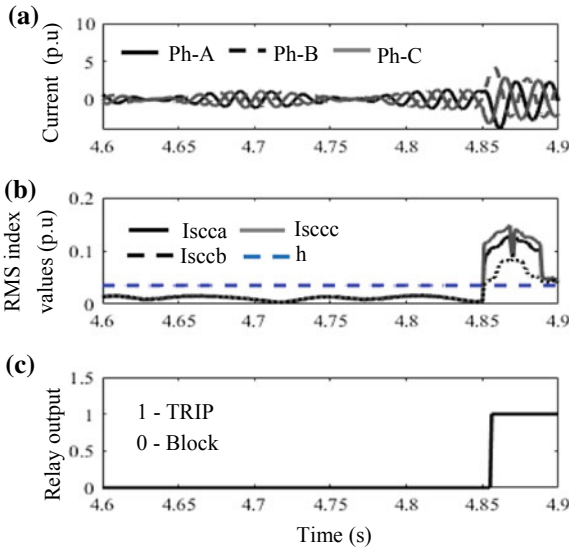

Fig. 3 Result of three-phase fault detection during the unstable power swing (6.6 Hz), a three-phase current signals, **b** RMS index values and **c** relay output

3.2 Result for Close-in Symmetrical Fault During Power Swing

To elucidate the performance of the proposed method under close-in symmetrical fault during the power swing, a three-phase fault is simulated at 10 km from relay R with fault inception time of 4.68 s. The results are shown in Figs. 4 and 5.

The magnitudes of the three-phase fault currents that measured at the relay location significantly differ from swing condition as shown in Figs. 4a and 5a. During symmetrical fault, the proposed index value is large enough as compared with the swing scenario. This identifies and discriminates the symmetrical fault and swing condition. From Figs. 4b and 5b, it is disclosed that the fault is accurately detected during both stable and unstable swing at 4.684 and 4.686 s, respectively. Accordingly, the corresponding TRIP signals are initiated to clear the fault as shown in Figs. 4c and 5c. From the result, it is concluded that the fault detection is achieved within a half cycle.

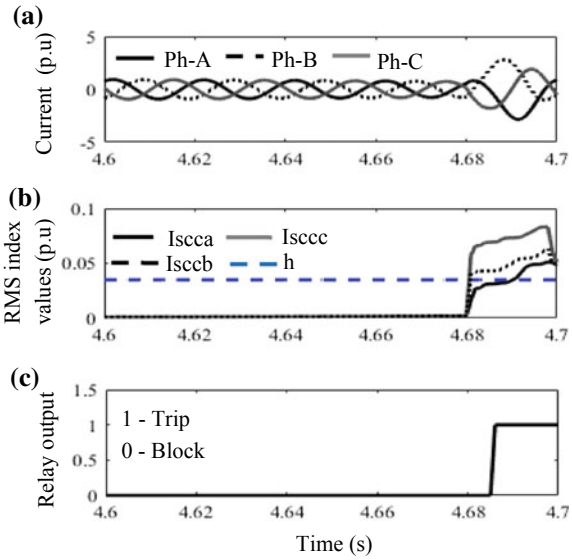

Fig. 4 Result of close-in symmetrical fault under stable swing, **a** three-phase current signals, **b** RMS index values and **c** relay output

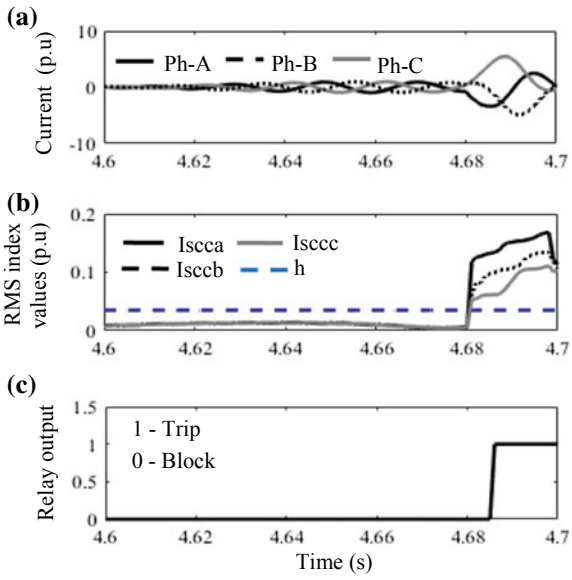

Fig. 5 Result of close-in symmetrical fault under unstable swing, **a** three-phase current signals, **b** RMS index values and **c** relay output

3.3 *Result for Far-End Symmetrical Fault During Power Swings*

To assess the presentation of proposed technique at far-end symmetrical fault case during power swing, a three-phase fault is created at 85% of the line between the buses 7–8 at 3.35 s. The output for this case is depicted in Figs. 6 and 7.

From Figs. 6a and 7a, it is observed that the relay *R* measures the three-phase current signals under far-end three-phase fault during stable and unstable power swing. Figures 6b and 7b represent the proposed RMS index computation and compared with the threshold '*h*'. Also, it is noticed that the index value lies below the specified value during stable and unstable power swing, whereas it exceeds the specified value during a three-phase fault. Therefore, symmetrical fault is detected at 3.356 s during stable swing and at 3.357 s during unstable swing. Later, the relay R generates a TRIP command as shown in Figs. 6c and 7c. Thus, the proposed method gives an accurate fault detection within a half cycle after fault initiation.

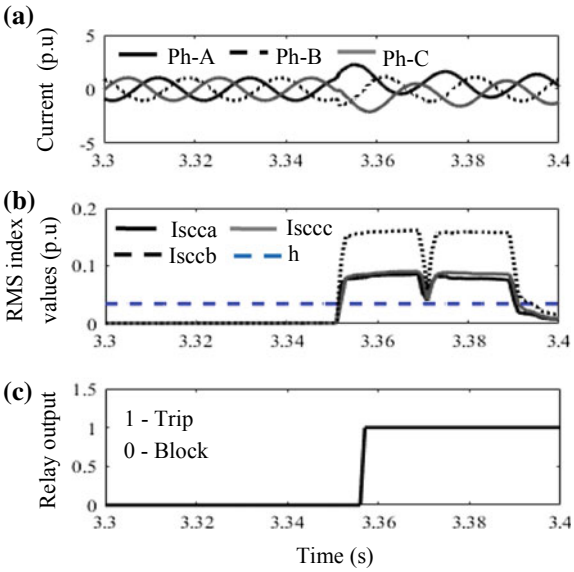

Fig. 6 Result of far-end symmetrical fault under stable swing, **a** three-phase current signals, **b** RMS index values and **c** relay output

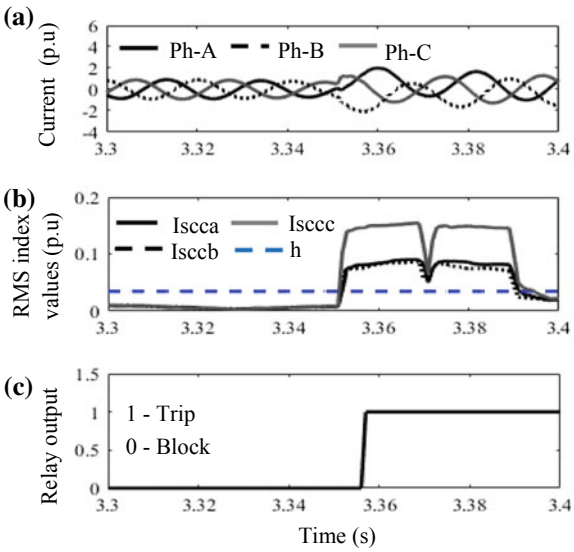

Fig. 7 Result of far-end symmetrical fault under unstable swing, **a** three-phase current signals, **b** RMS index values and **c** relay output

3.4 Impact of High-Resistance Symmetrical Faults During Power Swing

To check the validity of the proposed method for this case, a symmetrical fault with 500 ohms high fault resistance is considered during a power swing condition.

The fault is incepted at 5.5 s during swing with a distance of 50 km from relay end. The assessment results of the presented method are shown in Figs. 8 and 9, respectively. From Figs. 8a and 9a, it is shown that the relay *R* measures the current signals at high-resistance fault during power swing with stable and unstable condition. Conversely, the proposed RMS index is computed and compared with the fixed threshold '*h*'. During stable and unstable power swing, the index lies below the threshold '*h*' and exceeds the threshold '*h*' during three-phase fault as observed from Figs. 8b and 9b. The symmetrical fault is detected at 5.505 s during stable swing and at 5.506 s during unstable swing. Thereafter, the relay *R* generates a TRIP command to the corresponding circuit breaker as shown in Figs. 8c and 9c. In this regard, proposed method is able to detect the symmetrical fault within a half cycle after fault inception during the power swing.

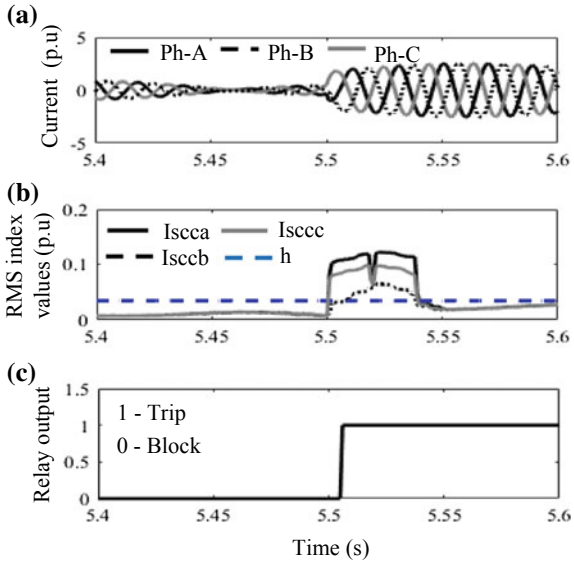

Fig. 8 Result of high-resistance fault during stable swing, **a** three-phase current signals, **b** RMS index values and **c** relay output

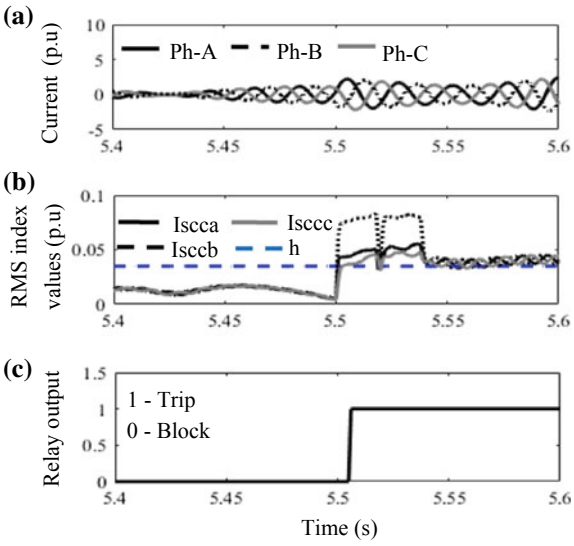

Fig. 9 Result of high-resistance fault during unstable swing, **a** three-phase current signals, **b** RMS index values and **c** relay output

4 Conclusions

In this paper, a novel power swing-symmetrical fault discrimination approach is proposed which computes the superimposed current signal first, and using three consecutive values, an index is developed. Next, based on recursive window, one-cycle calculated indices are used to estimate the RMS index. This RMS index is a reliable index to detect symmetrical fault during power swing. The RMS index is negligible during power swing irrespective of swing frequency and significantly higher during symmetrical fault. The magnitude of this RMS index is influenced by fault location, fault resistance and fault inception time. From the reported results, it can be concluded that the method is fast as detection time is less than half cycle and reliable enough to accomplish the assign task. The method is very simple, reliable and fast, and as it is based on recursive window, the future study will be performed to check the performance of the method is other dependable situations so that it can be tested in a real power networks.

References

1. Power System Relay Committee (2005) Power swing and out-of-step considerations on transmission lines. IEEE PSRC Working Group D6, New York
2. Kundur P (1994) Power system stability and control. Tata McGraw-Hill, New York
3. Brahma SM (2007) Distance relay with out-of-step blocking function using wavelet transform. IEEE Trans Power Deliv 22(3):1360–1366
4. Dubey R, Samantaray SR (2013) Wavelet singular entropy based symmetrical fault-detection and out-of-step protection during power swing. IET Gener Transm Distrib 7(10):1123–1134
5. Lotfifard S, Faiz J, Kezunovic M (2010) Detection of symmetrical faults by distance relays during power swings. IEEE Trans Power Deliv 25(1):81–87
6. Mahamedi B, Zhu J (2012) A novel approach to detect symmetrical faults occurring during power swing using frequency components of instantaneous three-phase active power. IEEE Trans Power Deliv 27(3):1368–1375
7. Rao JG, Pradhan AK (2016) Accurate phasor estimation during power swing. IEEE Trans Power Deliv 31(1):130–137
8. Rao JG, Pradhan AK (2012) Differential power-based symmetrical fault detection during power swing. IEEE Trans Power Deliv 27(3):1557–1564
9. Rao JG, Pradhan AK (2015) Power swing detection using moving averaging of current signals. IEEE Trans Power Deliv 30(1):368–376
10. Khodaparast J, Khederzadeh M (2015) Three-phase fault detection during power swing by transient monitor. IEEE Trans Power Syst 30(5):2558–2565
11. Dubey R, Samantaray SR, Panigrahi BK, Venkoparao VG (2016) Phase-space based symmetrical fault detection during power swing. IET Gener Transm Distrib 10(8):1947–1956
12. Kumar J, Jena P (2017) Solution to fault detection during power swing using Teager–Kaiser energy operator. Arab J Sci Eng 42:1–11
13. Kundu P, Pradhan AK (2014) Wide area measurement based protection support during power swing. Int J Elect Power Energy Syst 63:546–554
14. Biswal S, Biswal M (2018) Fault-swing discrimination using Hilbert-hung transform integrated discrete Teager-Kaiser energy operator. IET Sci Meas Technol 12(7):829–837
15. Prabhu MS, Nayak PK, Pradhan G (2018) Detection of three-phase fault during power swing using zero frequency filtering. Int Trans Electr Energy Syst 1–15

16. Andanapalli K, Nagaraju KV, Biswal M (2018) Symmetrical fault detection during power swing: a comparative study. In: Proceedings of the EECCMC international conference on electrical, electronics, computers, communication, mechanical and computing
17. Nayak PK, Pradhan AK, Bajpai P (2013) A fault detection technique for the series compensated line during power swing. IEEE Trans Power Deliv 28(2):714–722

Realization of Solid-State DC Circuit Breaker for HVDC System

Yogeshwari Prajapati and Mulav P. Rathod

Abstract This paper proposes a solid-state DC circuit breaker (SS DC CB) for high-voltage direct current (HVDC) system. HVDC system is recently in trends for electrical power transmission in the world. In favor of cost, bulk power transmission, efficiency, long-distance losses, it is more effective than HVAC. Every system has some limitations. In HVDC system, converter is the only option for protection against malfunction, dead short circuit, and unwanted conditions. Such overburden on converter can make complicated control of it. DC circuit breaker is more convenient device for such protection than converter. Existing DC circuit breakers require more time to clear the fault. SS DC CB can provide protection against short circuit and line charge. SS DC CB realizes fast opening operation because it does not have moving part and arc discharge. A series of experimental results demonstrates that the time required for SS DC CB is less.

Keywords DC circuit breaker · HVDC transmission · Fault protection

1 Introduction

In recent years, HVDC transmission system is widely used in large capacity and long-distance power transmission. [1]. In high-voltage alternating current (HVAC) transmission system, as line voltage increases, its reactive power losses increase. Ferranti effect limits the distance of transmission of power over AC lines. The cost of conductor increases which in turn increases HVAC transmission cost [2]. In place of HVAC, HVDC transmission system has many advantages. In HVDC transmission, only two conductors are required for single line, so the conductor cost is less. They

Y. Prajapati · M. P. Rathod (✉)
Sardar Vallabhbhai Patel Institute of Technology, Vasad, India
e-mail: mulavrathod.elect@svitvasad.ac.in

Y. Prajapati
e-mail: yogeshwari_prajapati@yahoo.com

A. Mehta et al. (eds.), *Advances in Electric Power and Energy Infrastructure*, Lecture Notes in Electrical Engineering 608,
https://doi.org/10.1007/978-981-15-0206-4_3

need less space compared to AC line for the same voltage rating. There is no need for synchronism between the two AC systems which connected together by the DC link is the main advantage of HVDC system. [3]. Power flow through a DC line can be easily controlled by grid using different control methods of different devices. HVDC does not transmit short-circuit power in case of faults and disturbances. There is no technical limit of the distance to transmit the power in HVDC system. In HVDC there is limitation of Reactive Power, Harmonics & Transmission line length compared to HVAC [4]. HVDC is also advantageous when the control of real power is desirable to manage normal or post-contingency flows on the network which increases the transfer capability [5]. As every system has its limitations, in HVDC the cost of terminal equipment is high. DC link blocks the transmission of reactive KVA load, so the receiving end network must be capable of supplying the total reactive component of power required by the loads and inverters. In HVDC, there is no availability of DC circuit breaker which is the main limitation of HVDC transmission system. The available breakers have slow speed of breaking action, so there is short life span and high maintenance cost due to the destructive effects of the arc [6]. That is why the design of DC circuit breaker with low fault clearing time is necessary. The switching of semiconductor base circuit breaker is fast enough to keep voltage disturbance within acceptable limits [7]. It has high switching speed and low maintenance [8]. There are mechanical and hybrid circuit breakers, but solid-state circuit breakers based on high-power semiconductor offer more advantages than these two with respect to speed and life [9]. Mechanical breaker has fault clearing time of 20–60 ms, and hybrid breaker has fault clearing time of 5–30 ms [10]. DC circuit breaker can cut off the short-circuit current immediately when DC fault occurs. It is the key equipment for HVDC transmission to avoid the whole DC system shutdown conditions and to protect the whole system from fault [11]. This breaker can be placed at transmission, distribution, and generation systems. The basic block diagram of system containing solid-state DC circuit breaker is as shown in Fig. 1.

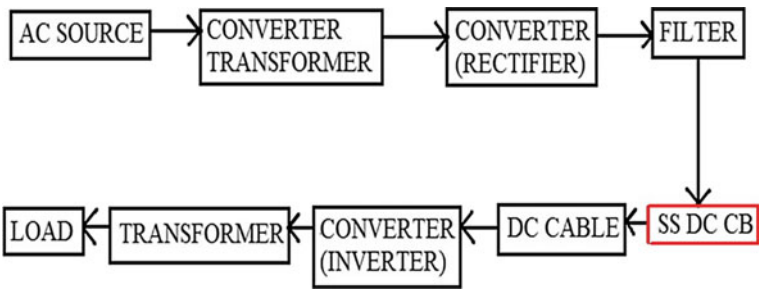

Fig. 1 Block diagram of system containing solid-state DC circuit breaker

2 Solid-State DC Circuit Breaker

High-power semiconductor devices such as thyristor (SCR), insulated gate bipolar transistors (IGBTs), insulated gate commutated thyristor (IGCT) [6], gate turn-off thyristor (GTO) can be used in SS DC circuit breaker. IGBTs are voltage control devices and have high conduction losses which limit its use in SS DC CB. SCR is another semiconductor device. It is current-controlled device. One can control the turn on time of SCR but for make SCR off commutating circuit is require in DC system. So, it is said as semi-control device. In AC system, SCR offs at every zero crossing, so there is no need of commutating circuit to make it off. There are mainly two methods for commutating SCR: natural commutation and forced commutation. In AC system at zero crossing, reverse voltage is applied across SCR and makes SCR off. In DC system, there is no zero crossing, so SCR is forcefully turn off using different commutation methods like self-commutation using L & C components, complimentary commutation, auxiliary (current) commutation and external pulse commutation. Here, simulation of breaker using complimentary commutation and current commutation is carried out using PSCAD software and results are analyzed.

2.1 Complimentary Commutation

Complimentary commutation consists of two SCRs, capacitor and a resistor, used for charging of capacitor. Main SCR (SCRm) is turned on; thus, there are two current paths. One of them is through the load, and the other is through the capacitor. Auxiliary SCR (SCRa) is used to commutate the SCRm. When SCRa is turned on, the energy stored in the capacitor is released through the SCRm which forcefully turns off the SCRm. Thus, the load is disconnected.

In Fig. 2, R_L is the load and R_C is the charging resistor. The simulation of this circuit is at the voltage 230 V, and the turn off time is about 5.5 ms as shown in Fig. 3.

2.2 Current Commutation

This commutation technique consists of three SCRs, a capacitor, inductor, and a diode as shown in Fig. 5. Initially, SCRa is turned on to provide the charging path to the capacitor. After the capacitor is fully charged, SCRa automatically turns off. Now, SCRm is turned on to supply the load. As SCRm is turned on, the capacitor is reversely charged through the inductor and diode path. Now to turn off the SCRm, SCRa is turned on and the energy stored in the capacitor is released through the SCRm which forcefully turns off the SCRm. The simulation of this circuit is done at 230 V, and it gives the turn off time of about 3 ms which is shown in Fig. 4.

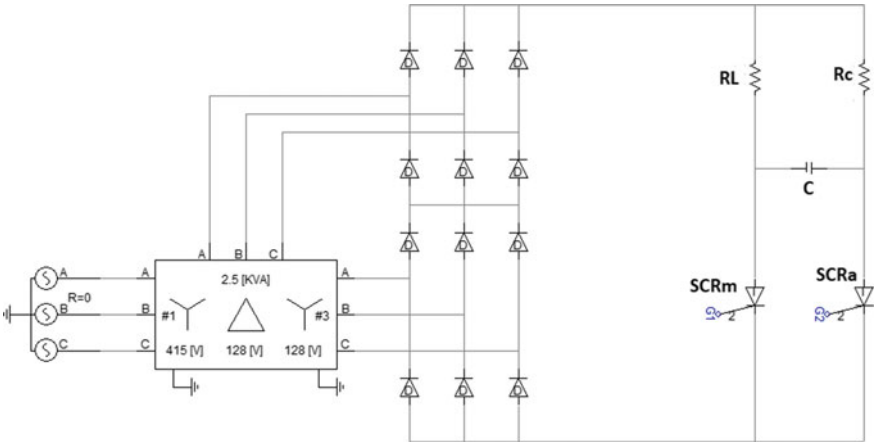

Fig. 2 Circuit diagram for complimentary commutation

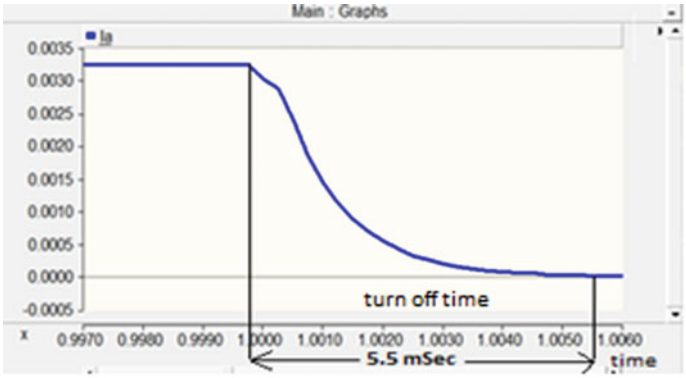

Fig. 3 Breaker turn off time for complimentary commutation

The turn off time by using complimentary commutation is more than that of the current commutation. So, the current commutation topology is used. In complimentary commutation, both the SCRs carry the load current by comparing this to current commutation; only SCRm carries the full load current while SCRa carries the current required to turn off the SCRm. So, size and cost of the SCR in current commutation are less than complimentary commutation method.

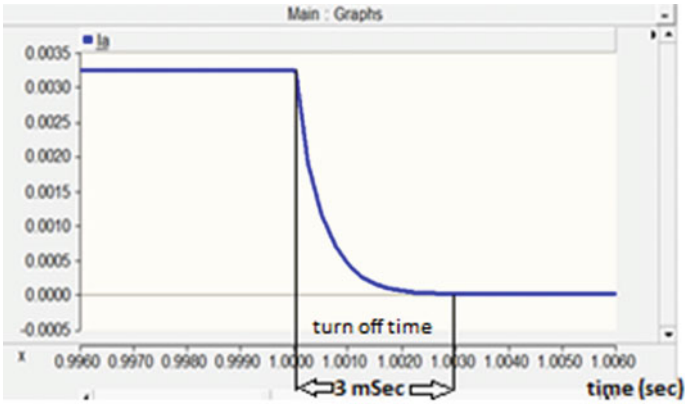

Fig. 4 Breaker turn off time for current commutation

3 Commutation Principle

3.1 Working of Current Commutation

The topology is as shown in Fig. 5. The working of this topology is as below:

Mode—1: Initially, turn on the SCRa. So, the capacitor charges with upper plate positive and lower plate negative through the path V_{dc} (+)–C+–C–-SCRa-R-Vdc (−). As the capacitor is fully charged, so the current through the SCRa is zero which turns off the SCRa. So, at the end of this mode both the SCRs are off and capacitor is fully charged with upper plate positive polarity and lower plate negative polarity.

Mode—2: Now, the SCRm is turned on. The load current flows through the SCR. The load current flows through the path Vdc (+)–SCRm-R-Vdc (−). Another current

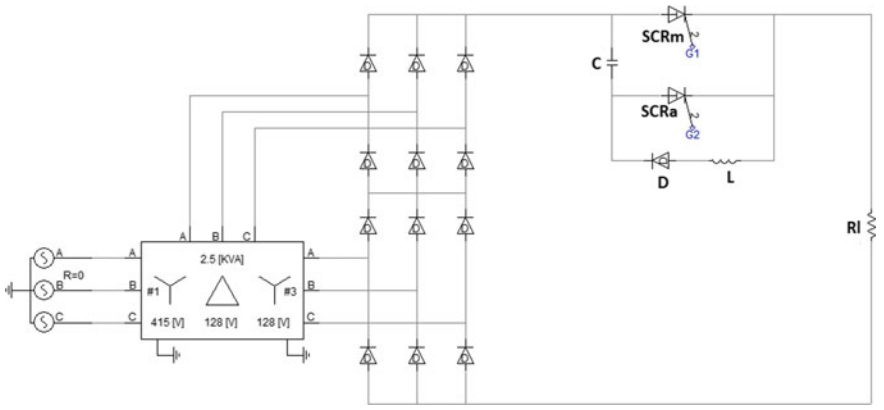

Fig. 5 Current commutation topology

flows through the path C+–SCRm-L-D-C- which discharges and reversely charges the capacitor. Inductor gives releasing time to the capacitor. Thus, the capacitor charges with upper plate negative polarity and lower plate positive polarity. So, at the end of this mode, capacitor is negatively charged, SCRa is off, and SCRm is on.

Mode—3: SCRa is turned on. Thus, the capacitor starts to discharge through the SCRm in the path of C+–SCRa-SCRm-C-. Thus, the charge across the capacitor is reversely connected to the SCRm. Thus, the SCRm is turned off forcefully when the capacitor discharges. SCRa remains on till the capacitor charges with upper plate positive polarity and lower plate charges with the negative polarity.

3.2 Equations Use for Current Commutation

Commutation capacitor $= (I_l * T_{\text{off}})/\, V_{\text{dc}}$

$I_{c(\text{peak})} = V_{\text{dc}}/(\omega_r * L)$

$\omega_r = 1/\sqrt{LC}$

So, $I_{c(\text{peak})} = V_{\text{dc}} * \sqrt{\frac{C}{L}}$

Turn off time of main SCR,

$$Tc = C * (V_{\text{dc}}/I_0)$$

Turn off time for auxiliary SCR,

$$T = \pi/(2 * \omega_o)$$

$$[\omega_o = 1/\left(\sqrt{LC}\right)]$$

where V_{dc} = supply voltage

$I_{c(\text{peak})}$ = capacitor current

ω_o = oscillating frequency

4 Simulation Results for Solid-State DC Circuit Breaker

4.1 Simulation Result

In order to give a rough idea about the proposed DC circuit breaker, simulation is carried out for 500 KVA and 33 kV.

In this system, the SCRm is on. The fault is applied in the system manually at 1 s. Thus, the SCRa is operated at the time of fault and the SCRm is turned off. The waveform of the current which becomes zero at 2.4 ms is shown in Fig. 6.

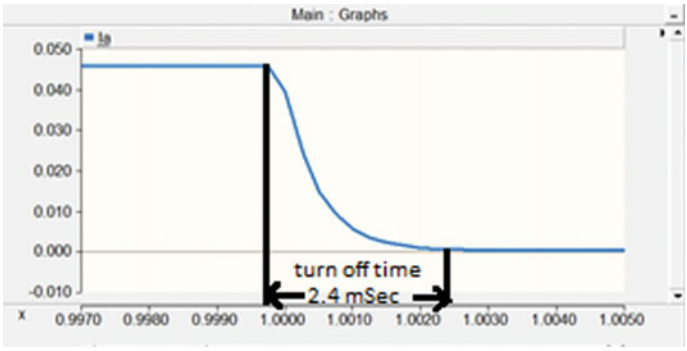

Fig. 6 Turn off time of solid-state DC circuit breaker

4.2 Practical Implementation of Breaker and Results

The experimental setup of the DC circuit breaker is shown in Fig. 7. The experimental setup specification is of 2.5 KVA and 230 V. This breaker configuration is tested on medium voltage due to the limitation of availability of source. The transformer of rating 2.5 KVA is connected to the 12-pulse rectifier. Here, diode-based uncontrolled 12-pulse rectifier is used. For 12 pulses, one bridge is connected to star and another is delta of the secondary of transformer. The rating of the SCR should be higher so that it can withstand the fault current till the load is disconnected. The device is selected based on peak inverse voltage which is double of the supply voltage. Due to the satisfactory results of current commutation than complimentary commutation of SCR, it is implemented here.

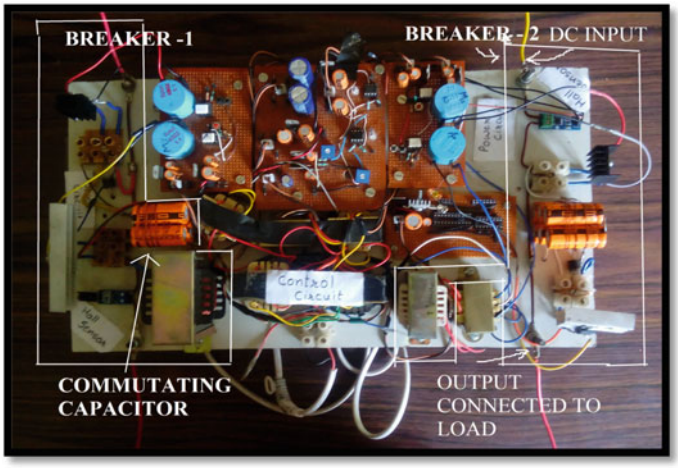

Fig. 7 Setup for DC circuit breaker

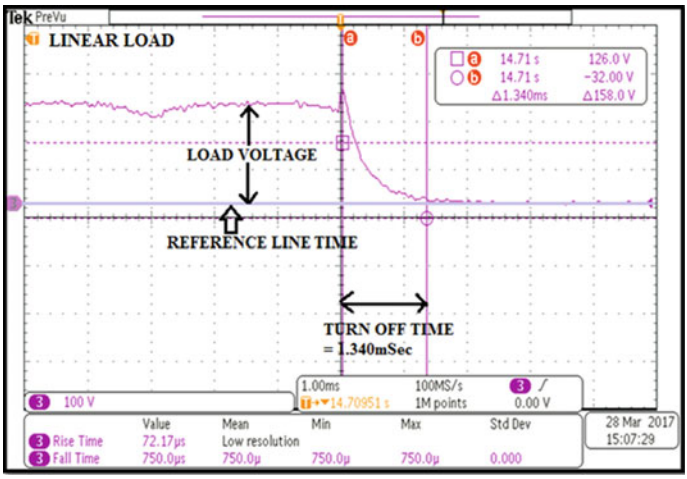

Fig. 8 Voltage across linear load at the time of fault

This breaker is tested on different types of load like linear load (rheostat), lamp load, and resistive load. For sensing the load current, Rogowski coil or the hall sensors are used.

Here, hall sensors are used to measure the load current. Whenever the current increases from its peak limit, it gives the command or the gate signal to the auxiliary SCR to make it on. As the SCRa is on, the capacitor starts to discharge via SCRm and makes SCRm off. This way the load is disconnected from the load.

Now, the breaker is applied to linear (rheostat) load. The turn off time of solid-state DC circuit breaker is 1.34 ms as shown in Fig. 8, which is very less compared to hybrid and mechanical circuit breaker used in HVDC lines. As the current increases beyond the predefined limit, the sensor gives the signal to auxiliary SCR and makes the breaker off. So, the load is isolated from the source.

Now, the breaker is connected to resistive load. The turn off time of breaker for the resistive load is 1.576 ms as shown in Fig. 9. Whenever the load current cross its predefined limit, the breaker automatically cut off the load from the supply.

Now, breaker is tested on the lamp load. The turn off time for breaker is 3 ms as shown in Fig. 10. As the number of lamp increases, the current increases. Whenever it increases beyond the predefined limit, the breaker is turn off. Graph shows the voltage and current waveforms. Here, current is measured by the clamp-on meter.

This breaker can be used in college laboratories, industries and HVDC system. For college laboratories or in low rating applications this breaker can be design and implemented easily but, for industries and HVDC system where the DC rating is high than there are some difficulties in design of breaker. The thyristor rating is limited up to certain ratings, so series–parallel connection of thyristor is needed which makes circuit more complex and needs precise control of every device.

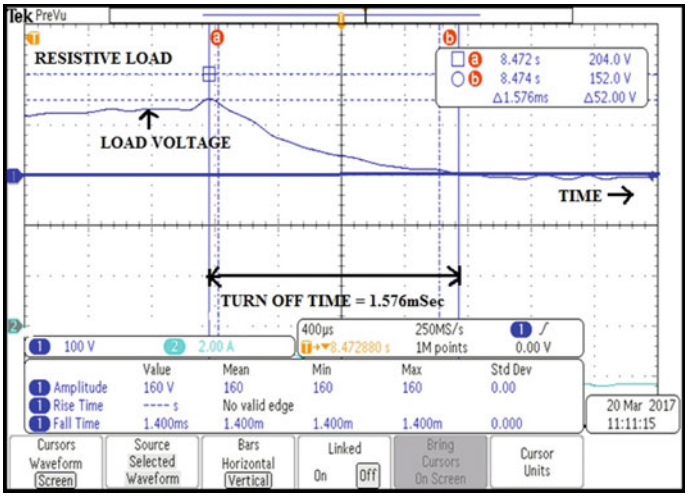

Fig. 9 Voltage across resistive load at the time of fault

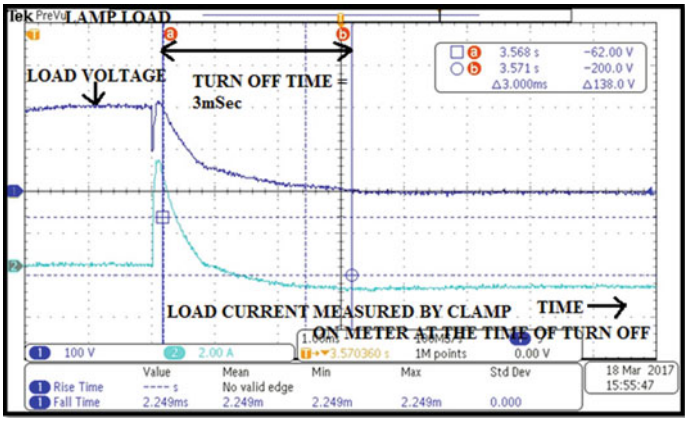

Fig. 10 Voltage across lamp load at the time of fault

5 Conclusion

This paper presents the circuit configuration of the solid-state DC circuit breaker for HVDC transmission system to clear DC line faults. In this design of circuit breaker, there is no any mechanical switch is present. So, there is no possibility of generation of arc. The operating time of breaker is very less compared to mechanical and hybrid circuit breaker. So, there is less effect of the fault current on the load. The breaker is compact in size and low cost. The design of breaker is robust. There are less devices used in this topology, so the maintenance required is less. This solid-state

DC circuit breaker can be used in different links of HVDC like monopolar, bipolar, and homopolar. It is also used in transmission, generation, and distribution system, in college laboratories where DC supply is used and in industries which uses DC as a supply such as chemical, electroplating, and arc welding industries.

References

1. Sano K (2012) A surgeless solid state DC circuit breaker for voltage source converter based HVDC systems. 978-1-4673-0803-8/12/$31.00 ©2012 IEEE
2. Deshpande MV (2001) Electrical power system design. Tata McGraw Hill Education Private Limited, New Delhi
3. Khanchandani KB, Singh MD () Modern power electronics, 2 edn. Mc Graw Hill Education
4. Meyer C, Kowal M, De Doncker RK (2005) Circuit breaker concepts for future high power DC applications. 0-7803-9208-6/05/$20.00 ©2005 IEEE
5. Henderson M, Gagnon J, Bertagnolli D, Hosie B, DeShazo GL, Silverstein B (2007) Building a plan for HVDC. 1540-7977/07/$25.00©2007 IEEE
6. Meyer JM, Rufer A (2006) A DC hybrid circuit breaker with ultra-fast contact opening and integrated gate commutated thyristors (IGCTs). IEEE Trans Power Deliv 21(2)
7. Meyer C, De Doncker RW (2004) Solid state circuit breakers and current limiters for medium voltage systems having distributed power systems. IEEE Trans Power Electr 19(5)
8. Chen Q, Tan K, Huang AQ (2012) Self-power Emitter Turn-off Thyristor (SPETO) based circuit breaker for power distribution system. 978-1-4673-0803-8/12/$31.00 ©2012 IEE
9. Meyer C (2006) Solid state circuit breaker based on active thyristor topologies. IEEE Trans Power Electr 21(2)
10. Bucher MK, Walter MM, Pfeiffer M, Franck CM (2012) Options for ground fault clearance in HVDC offshore networks
11. Bachmann B, Mauthe G, Ruoss E, Lips HP (2016) Development of a 500 kv Air Blast HVDC circuit breaker. In: 2016 IEEE 8th International Power Electronics and Motion Control Conference (IPEMC-ECCE Asia). 978-1-5090-1210-7/16/$31.00 ©2016 IEEE

A Review on Approaches Employed for Solving Directional Overcurrent Relays' Coordination Problem

Shanker D. Godwal, Kartik S. Pandya, Vipul N. Rajput and Santosh C. Vora

Abstract The directional overcurrent relay (DOCR) coordination is considered as a highly constrained, nonlinear, and non-convex optimization problem. In order to find the optimum solution of these problems, many extensive efforts have been kept by the researchers. The optimum solution of directional overcurrent relay which coordination can be obtained by choosing proper time–current characteristic of DOCR, appropriate selection of objective function, and right selection of soft computing technique. This paper gives the insight into various approaches employed for DOCRs' coordination which are as optimization method-based approach, objective function-based approach, and standard and non-standard relay characteristic-based approaches presented in the past literature. Also, this paper discusses mathematical formulation for overcurrent relay coordination.

Keywords Relay coordination · Plug setting · Time multiplier setting · Plug setting multiplier · Relay characteristics

S. D. Godwal (✉)
Department of Electrical Engineering, CSPIT, CHARUSAT, Changa, Anand, Gujarat, India
e-mail: shanker.godwal@nirmauni.ac.in

K. S. Pandya
Charotar University of Science and Technology, Changa, Anand, Gujarat 388421, India
e-mail: kartikpandya.ee@charusat.ac.in

V. N. Rajput
Dr. Jivraj Mehta Institute of Technology, Anand, India
e-mail: vipulrajput16986@gmail.com

S. C. Vora
Institute of Technology, Nirma University, Ahmedabad, India
e-mail: santoshvora@yahoo.com

A. Mehta et al. (eds.), *Advances in Electric Power and Energy Infrastructure*, Lecture Notes in Electrical Engineering 608,
https://doi.org/10.1007/978-981-15-0206-4_4

1 Introduction

For the protection of distribution system and sub-transmission networks, generally DOCRs are used. Also, in case of backup protection of transmission line, DOCRs are mostly used. It is essential to isolate faulty part from power system as soon as possible on occurrence of fault for reducing the chances of excessive power outages. Also on the failure of primary relay, after prescribed time interval backup relay must operate [1]. This is known as relay coordination. The reliability of such protective schemes depends upon proper relay coordination. Hence, right relay coordination mainly depends on the proper selection of plug setting (PS) and time setting multiplier (TMS). The optimum value of PS and TMS in case of interconnected power system is quite difficult task. And alternately optimum selection of PS and TMS can be obtained by optimization techniques. Also, the objective of the optimal coordination of overcurrent relay is to find the values of PS and TMS of all relays that minimize the sum of their operating times when they act as primary relays and all of the coordination constraints are satisfied. To achieve optimum value of TMS and PS manually is very difficult and time-consuming task [2]. In order to achieve optimum solution for said settings for primary and back up relay various approached are followed. These approaches are based on either time–current characteristic of relay, objective function-based approaches, or optimization method-based approach.

1.1 Problem Description

The relay coordination problem may be considered either as a linear or nonlinear problem. In case of linear programing problem, pickup current setting of relay is kept fixed and TMS are optimized. The possible values of PS are fixed between maximum load current to minimum fault current. However, in case of nonlinear programing problems both TMS and PS are optimized simultaneously with relay characteristic [3]. Complexity of the problem will increase due to discrete nature of PS and TMS [4]. That is why this is mixed integer nonlinear programing problem. Also in the uncertainties of load and topological changes, obtain setting of PS and TMS are not optimal over all possible scenarios. Hence, the relay coordination problems must be modifying to consider all possible scenarios. There are three possible ways to improve optimum PS and TMS which are discussed in this paper. To solve the directional overcurrent relay coordination problem, there are various approaches have been presented in the past literatures. These can be categorized mainly in three approaches. The first approach is based on modification in the existing objective function. There are many literatures available in the field of relay coordination which proposed new objective function. In [5, 6], the optimum results have been obtained bases of modification in objective functions. These studies show that optimum relay coordination solution can be obtained using this concept. The modification in objective function has been further discussed in Sect. 3. The second category is based on changing overcurrent

relay characteristics, i.e., adopting standard or non-standard relay characteristic. In [7], the research has been done for proper selection relay characteristics. Further adopting standard or non-standard characteristics of relays has shown significant improvement in results. The third category is based on the optimization techniques in which relay coordination problem has been formulated as either linear programing or nonlinear programing.

1.2 Contributions

The main contribution of this paper discusses as follows:

- Overview of various approaches for optimum relay coordination in distributions and sub-transmission system.
- The various types of relay characteristic, objective function for relay coordination problem.
- This future scope in the field of overcurrent relay coordination which will motivate the new researcher in this field.

1.3 Paper Organization

The rest of the paper is outlined as follows. In Sect. 2, for two-bus system formulation of overcurrent relay coordination problem is presented. Various constraints and objective functions have been discussed. Section 3 discusses various types of objective functions proposed in the past literature, and also this section discusses robustness and drawback of the proposed objective functions. In Sect. 4, various types of time–current characteristics are used for relay coordination, and in Sect. 5, approach based on optimization methods has been presented. Finally, in Sect. 6, the conclusions of this paper are highlighted.

2 Problem Formulation

Overcurrent relay optimization problem can be stated as that in ring main distribution system or radial system the sum of operating time of individual overcurrent relay is to be minimized when they are working as primary relay. Most of the researchers utilized objective function (OF). The main purpose of OF is to reduce the operating time of overcurrent relays when they are working as primary relay. In the upcoming section, further details are given with reference to OF.

$$\min z(\mathrm{OF}) = \sum_{i=1}^{m} t_{i,k} \tag{1}$$

where

m indicate total number of relays in system
$t_{i,k}$ operating time of the relay R_i, for fault at k.

The minimization of the said objective function can be achieved by considering at least five constraints. These constraints are required to get feasible and optimum relay setting.

2.1 Constraint Set I—Coordination Criteria

In overcurrent relay coordination scheme, fault is always sensed by primary as well as secondary relay. Also it is expected from primary relay get operate first and if primary relay is fail to operate then only secondary relay should get trip. It means if relay is working as primary relay, its operating time should be high as compared to secondary relay. The minimum operating time of secondary relay will include operating time of primary relay operating time of circuit breaker of primary zone and overshoot time of primary relay. This will maintain the selectivity of primary and secondary relays. So coordination time interval (CTI) is the sum of operating time of CB associated with primary relay and the overshoot time. If R_j is the primary relay for fault at k and R_i is backup relay for the same fault, then the coordination constraint can be stated as

$$t_{i,k} - t_{j,k} \geq \Delta t \tag{2}$$

where

$T_{i,k}$ operating time of primary relay
$t_{j,k}$ operating time of backup relay
Δt the coordination time interval (CTI).

2.2 Constraint Set II—Bounds on Relay Operating Time

Due to certain limitation of mechanical and numerical these relay will take certain minimum amount of time to get operate similarly relay should not take too much time to get operate otherwise fault current will persist in the system for longer duration and it can damage system. Keeping these constraints in coordination, problem is required [4]. These constraints can be mathematically stated as

$$t_{i,\min} \leq t_i \leq t_{i,\max} \tag{3}$$

where

$t_{i,\min}$ minimum operating time of relay at location i for the fault at any point in the zone of operation

$t_{i,\max}$ maximum operating time of the relay at location I for the fault at any point in the zone of operation.

2.3 Constraint Set III—Bounds on the TMS of Relays

TMS affects the operating time of relay. If it is required to have some intentional time delay in individual overcurrent relay, the TMS concept is utilized. Also maximum delay in relay operation can be 1 s. The bounds on TMS can be defined as

$$\text{TMS}_{i,\min} \leq \text{TMS} \leq \text{TMS}_{i,\max} \tag{4}$$

where

$\text{TMS}_{i,\min}$ minimum time delay for relay R_i

$\text{TMS}_{i,\max}$ maximum time delay for relay R.

Minimum value of TMS can be taken 0.05, and maximum can be taken 1.1 s [8].

2.4 Constraint Set IV—Bounds on the Plug Setting (PS) of Relays

This is given in terms of either ampere or percentage of relay-rated current. Plug setting is the threshold above which overcurrent relay will start to operate. In overcurrent relay, PS can vary from 50 to 200% of its rated current in 7 equal steps with 25% margin, and in case of numerical relay, it can vary from numerical relay [4].

The bounds on of relays can be stated as

$$\text{PS}_{i,\min} \leq \text{PS} \leq \text{PS}_{i,\max} \tag{5}$$

$\text{PS}_{i,\min}$ minimum value of relay R_i

$\text{PS}_{i,\max}$ maximum value of relay R_i.

PS must be chosen in such a way that it should not trip for overloading condition. If 25% overloading is considered than PS must be greater than 1.25 of maximum load current. It will avoid the false tripping of relay; i.e., relay will not operate under normal as well as over loading condition. In the same way, maximum PS should be

Table 1 Value of β and α for different characteristics of inverse overcurrent relay [10]

Slop of the time–current curve set	β	α
Normal inverse	0.14	0.02
Very inverse	13.5	1.00
Extremely inverse	80.0	2.00
Long-time inverse	120.0	1.00

less than or equal to 2/3 times of fault current. This will give surety that relay will sense minute to minute fault [8, 9].

2.5 Constraint Set V—Relay Characteristics

In overcurrent relay coordination problem, relay characteristics play significant role. In overcurrent relay coordination problems, nonlinearity is created by relay characteristic. The overcurrent relay can be characterized by various ways which are furthermore discussed in Sect. 4 in the same paper. In most of the literatures, relay characteristic is defined as

$$\text{Time of operation of relay} = \frac{\beta}{(\text{PSM})^{\alpha} - 1} \times \text{TMS} \tag{6}$$

The multiple of plug setting current is known as PSM [11]. The characteristics are plotted usually in terms of operating time versus PSM. The value of constants β and α varies for different characteristics which are given in Table 1 [12].

3 Objective Function (OF)-Based Approaches

This section deals with the approaches which are formulated based on OF. Here, various well-established objective functions are discussed which are already presented in the literature. Also, their robustness and comparisons have been discussed.

3.1 OF_1

Mostly OF used in the literature is expressed as (7). OF_1 is generally used by many researchers for achieving optimum relay coordination. This function considers only primary relay's operating time. Back relay's operating time is not incorporated in OF_1. The main drawback of this objective function is that it minimizes operating time of primary relay only, and because of this, there is possibility of larger discrimination

time between primary and backup relay.

$$\min Z_k = \alpha_1 \sum_{i=1}^{n} t_i \tag{7}$$

3.2 OF_2

Objective function OF_2 as expressed in (8) is more superior as compared to OF_1. The main feature of OF_2 is that it includes backup relay operating time along with primary relay time. This will try to reduce operating time of backup relay.

$$\min Z_k = \sum_{i=1}^{n} t_{i,k} + \sum_{i=1}^{n} t_{j,k} \tag{8}$$

where Z_k is the objective function in zone k; $t_{i,k}$ is the operating time of ith primary relay for its near end faults in zone—k; $t_{j,k}$ is the operating time of jth backup relay for its far end fault in zone—k; and N is the total number of directional overcurrent relay. Major drawback of OF_2 is that overall value of objective function will increase as compared to OF_1.

3.3 OF_3

Objective function (OF_3) is expressed based on Eq. (9). [13]

$$\min Z_k = \alpha_1 \sum_{i=1}^{n} t_i^2 + \alpha_2 \sum_{i=1}^{n} \Delta t_{pbk}^2 \tag{9}$$

$$\Delta t_{pbk} = t_{bk} - t_{pk} - \text{CTI} \tag{10}$$

where Δt_{pbk} is defined by discrimination time between kth P/B relay pairs, the total numbers of P/B relay pair is defined by n, and k represents each P/B relay pairs. The value of k may vary from 1 to n. The operating time of primary and backup relay time is denoted as t_{pk} and t_{bk}, respectively.

Positive weight factors which control the I and II terms of OF_3 are indicated by α_1 and α_2.

Main advantage of OF_3 is CTI in objective function which will minimize the value of Z_k. Major problem which is associated with OF_3 is discussed for a part of power system shown in the figure, where *Rb* and *Rp* are the backup and primary relay. Also, two cases are discussed in order to understand problem associated with OF_3. Two

cases have been taken; also, the value of α_1 and α_2 is taken 1, and CTI can be taken 0.2 s.

Case 1: $\Delta t_{pb} = -0.15, t_p = 0.15, t_b = 0.20, \mathrm{OF}_2 = 0.045$
Case 2: $\Delta t_{pb} = 0.20, t_p = 0.15, t_b = 0.55, \mathrm{OF}_2 = 0.0625.$

It can be observed from the above two cases 1 and 2. If Δt_{pb} value is taken negative as case 1, OF_3 value is more optimum as compared to case 2 and algorithm will select case 1 OF_3 value even though case 2 is more feasible because the value Δt_{pb} is positive in case 2. Due to negative value of Δt_{pb}, case 1 will present relay miscoordination. But as per relay coordination philosophy, case 2 must be chosen.

3.4 OF_4

In [14], one more objective function has been discussed to overcome the problem associated with OF_3. It is stated as (11)

$$\min Z = \alpha_1 \sum_{i=1}^{m} t_i^2 + \alpha_2 \sum_{k=1}^{n} \left(\Delta t_{pbk} - \beta_2 \left(\Delta t_{pbk} - \left|\Delta t_{pbk}\right|\right)\right)^2 \tag{11}$$

where α_1 and α_2 are the weight factor which will control terms I and II. β_2 is used to consider miscoordination constant. The OF_4 overcomes problem associated with OF_3. Observing OF_4, it can be concluded that for positive value of Δt_{pbk}, II term of OF_4 becomes $(\Delta t_{pbk})^2$ and similarly negative value of Δt_{pbk}; it is $(\Delta t_{pbk}(2\beta_2 - 1))^2$. In order to understand robustness again, two cases have been taken. From the both cases for positive value of β_2, miscoordination has been solved which was associated with OF_3, but the drawback of OF_4 can be seen from both cases. As per relay coordination philosophy, algorithm will take case 1 due to its optimum value as compared to case 2.

But it can be observed that primary and backup relay operating time will be higher as compared to case 2 in case 1.

$$\alpha_1 = 1, \quad \alpha_2 = 2, \quad \beta_2 = 100, \quad \mathrm{CTI} = 0.2.$$

Case 1: $\Delta t_{pb} = 0.5, t_p = 0.4, t_b = 1.1, \mathrm{OF}_4 = 0.66$
Case 2: $\Delta t_{pb} = 0.6, t_p = 0.2, t_b = 1.0, \mathrm{OF}_4 = 0.76.$

3.5 OF_5

Objective function 5 is the more simple form of OF_4 which is proposed [15]. It is expressed as

$$\mathrm{OF}_5 = \alpha_1 \sum_{i=1}^{m} t_i^2 + \beta_3 \sum_{k=1}^{n} \left(\Delta t_{pbk} - \left|\Delta t_{pbk}\right|\right)^2 \tag{12}$$

In OF_5, β_3 is the constant which will control the second term; also, it can be considered equal to $\alpha_2\beta_2^2$ of OF_4, because second term of OF_4 is neglected. It can be observed from OF_5, that positive value of Δt_{pbk}, OF_5 is same as OF_1. So OF_5 also suffers the same problems which OF_1. With the help of the following two cases, it can be understood:

$$\alpha_1 = 1, \quad \beta_3 = 2, \quad \mathrm{CTI} = 0.2.$$

Case 1: $\Delta t_{pb} = 1.0$, $t_p = 0.2$, $t_b = 1.4$, $\mathrm{OF}_5 = 0.04$
Case 2: $\Delta t_{pb} = 0.6$, $t_p = 0.2$, $t_b = 1.0$, $\mathrm{OF}_5 = 0.04$.

It can be seen from the both cases, OF_5 has same values. Again as per relay coordination philosophy, optimum value should be selected, but results show that in both cases, OF_5 is insensitive toward Δt_{pb} even though case 2 is much feasible.

3.6 OF_6

Even though miscoordination problem has been solved in OF_4 and OF_5, still larger value operating time of backup and higher discrimination operating time has been still persisting in case of OF_4 and OF_5. In order to overcome problem associated with OF_4 and OF_5, the authors in [16, 17] presented a new OF_6. OF_6 is expressed as (13) and this has an additional new term.

$$\begin{aligned}\mathrm{OF}_6 =& \alpha_1 \sum_{i=1}^{m} t_i^2 + \alpha_2 \sum_{k=1}^{n} \Bigg(\left|\Delta t_{pbk} - \left|\Delta t_{pbk}\right|\right| . \frac{t_{pk}^2}{t_{bk}^2} \\ &+ \left(\Delta t_{pbk} + \left|\Delta t_{pbk}\right|\right) . t_{bk}^2 \Bigg)\end{aligned} \tag{13}$$

It can be seen from [9] that if the value of Δt_{pbk} is greater than zero, the II term of OF_6 will become $(2\Delta t_{pbk} \cdot t_{bk}^2)$, and if the value of Δt_{pbk} is less than zero, II term of OF_6 will be $(2\Delta t_{pbk} \cdot t_{pk}^2)$. Also, it can be seen that for higher and positive value of Δt_{pbk} shows high value of operating time of backup relay t_{bk}. Also for higher value of Δt_{pbk}, OF_6 will try to optimize the operating time of t_{bk}.

Similarly, the negative value of Δt_{pbk} gives larger value of operating time of primary relay (t_{pk}), and OF_6 tries to minimize the operating time of t_{pk}. Thus, OF_6 minimizes the operating time of *P*/*B* relays according to Δt_{pbk}. In the OF_6, the negative effect of larger operating time of backup relays and larger discrimination time has been resolved. Even though OF_6 overcome the larger operating time of backup relay and discrimination of primary and backup relay, still there is one problem persisting in OF_6 which can be understood with the following two cases.

$$\alpha_1 = 1, \quad \alpha_2 = 10, \quad \text{CTI} = 0.2.$$

Case 1: $\Delta t_{pb} = -0.15, t_p = 0.15, t_b = 0.2, \text{OF}_6 = 0.09$
Case 2: $\Delta t_{pb} = 0.20, t_p = 0.15, t_b = 0.55, \text{OF}_6 = 1.2325.$

In case of negative value of Δt_{pbk}, miscoordination problem will arise, so for case one, the value of OF_6 is much better than case 2 and algorithm will select the case 1 even though it will create miscoordination. Also, case 2 will not be selected by algorithm because it does not have optimum value selected because in case 2 OF_6 have larger value.

3.7 OF$_7$

From the previous observation, it is concluded that each OF has either miscoordination problem or larger operating time of relay. To overcome these problems, paper [18] has proposed new objective function expressed as (14). OF_7 not only optimized the operating time of relay coordination, but also avoided the miscoordination situations.

$$\text{OF}_7 = \alpha_1 \sum_{i=1}^{m} t_i^2 + \alpha_2 \sum_{k=1}^{n} \left(|t_{pbk} - |t_{pbk}|| \cdot \frac{t_{pk}^2}{t_{bk}^2} + \left(\Delta_{pbk} + |\Delta t_{pbk}|\right) \cdot t_{bk}^2 \right) \tag{14}$$

From OF_7, it can be observed that for negative value of Δt_{pbk}, OF_7 will be ($2\Delta t_{pbk}$ $\cdot\, t_{pk}$ $2/t_{bk}$ 2). Also for positive value of Δt_{pbk}, OF_7 will work as OF_5. So in this way, OF_7 not only minimizes the operating function. It is also noted primary relay has larger operating time in case of negative value of Δt_{pbk} as compared to backup relay. In this way, OF_7 can overcome the problem associated with OF5 and discoordination problem can be avoided.

4 Overcurrent Relay Characteristics

In this section, the brief introduction of standard relay characteristics has been discussed which are published by the IEC and the IEEE. Also, non-standard relay characteristic has been discussed which are presented by various researches in the field of power system protection. The main aim of this section is to provide overall idea of standard and non-standard relay characteristics. This section gives a brief summary of the recent research in overcurrent relay characteristics. Also, this section discussed significant role of the said relay characteristics in optimum overcurrent relay coordination. This section is divided into two parts: First part deals with standard

characteristics and second part discusses non-standard characteristics of overcurrent relay.

4.1 Standard Characteristic

The standard characteristics are mostly used in industry and researcher for the coordination of overcurrent relay in distribution system as well as in sub-transmission system. There are two types of relay characteristics are available in which are based on international standard. These are known as the IEC standard characteristics and the IEEE standard characteristics. The main aim of studies in these relays is to ensure that power system should be properly protected with the help of proper representation of relay characteristics. The operating characteristics of relay mainly based on the data are obtained from laboratory experiment or relay manufacturing company. These obtained data then proceed for analytical analysis for proper relay coordination either in form of graph or mathematical equations [19].

The IEC standard characteristic
Many researchers and manufacturers of inverse overcurrent relay utilized IEC standard characteristics for optimum relay coordination. This characteristic can be expressed as (15). In this equation, the A and B are the constants which will decide the relay characteristics. For various characteristics of inverse overcurrent, the value of A and B can be taken from Table 2.

$$t = \frac{A}{\left(\frac{I_f}{I^P}\right)^B - 1}.\text{TMS} \tag{15}$$

where

A and B	the constants
t	operating time of relay
I_p	fault current in line
I_f	fault current in relay
TMS	time multiplier setting.

The IEEE Standard Characteristic
This is another widely accepted relay characteristic which is utilized by many researchers. This characteristic is expressed as (16)

Table 2 Coefficients indicated in the IEC 60255-3 standard

	Extremely inverse	Very inverse	Normal inverse
A	80	13.5	0.14
B	2	1	0.02

Table 3 Coefficients indicated in the IEEE C37.112 1996 standard

	Extremely inverse	Very inverse	Moderately inverse
A	28.2	19.61	0.0515
B	2	2	0.02
C	0.1217	0.491	0.1140

$$t = \left[\frac{A}{\left(\frac{I_f}{I^P}\right)^B - 1} + C \right] .\text{TMS} \tag{16}$$

In this characteristic, only one more constant C has been added. As it is well known, there is nonlinear relationship between the input current and the flux in the electromagnetic's relay core. When the input current value is greater to its threshold value, there may be fixed tripping time due to inductance saturation of core. For this reason, the equation of the IEEE standard characteristics contains a C parameter in order to reflect the fixed tripping time. There are three different IEEE characteristics which are similar to IEC characteristics (Table 3).

4.2 Non-standard Characteristics

This section deals with non-standard characteristics N-Sc for achieving optimum relay coordination in power system. These characteristics are divided into four parts: (i) approaches that include electrical magnitudes, (ii) approaches that use different coefficients apart from the SCs, (iii) mathematical approaches, and (iv) other approaches. In this paper, only the approaches based on electrical magnitude have been included.

Non-standard characteristics including electrical magnitudes
Previously, the relay used to take signal based on current magnitude to detect fault also intensity of fault was decided based on current magnitude. However, in the present scenario, fault can be detected by sensing voltage of the system. As directional over current relay required both voltage and current for sensing the transmission line faults. The requirement of directional overcurrent relay. The line voltage and current can be measured via potential and current transformer. So some past literatures show that better characteristics of directional overcurrent relay which can be realized based on not only current as shown in Eq. (1) but also along with voltage magnitude.

Non-standard characteristic: N-Sc can be classified by the following ways: (i) current-based characteristics, (ii) voltage-based characteristics, and (iii) admittance-based characteristics.

Current-based non-standard characteristics:
This type of characteristics is expressed by (18). This characteristic is the mostly

same as IEC or IEEE characteristics. The difference between Sc and current-based N-Sc is constant A. In case of IEC or IEEE characteristics, A is pure constant, but in case of current-based N-Sc, constant A is the function of fault current which is defined as (17) In particular problem based on fault current, the value of A is decided [20].

$$A(I_f) = A \cdot \mathrm{e}^{\frac{-I_f}{C}} \tag{17}$$

$$t = \frac{A(I_f)}{\left(\frac{I_f}{I_p}\right)^B - 1}.\mathrm{TMS} \tag{18}$$

where

I_f line fault current
I_p relay fault current.

The voltage-based characteristics This type of characteristics is expressed as (19). The main purpose to use this characteristic is that the voltage value seen by relay is more reliable coordination under high penetration of distributed generation (DG). Fault current contributed by DG, Since the DG contributes to the fault current, the bus voltages in the system are indirectly affected by the varying fault current [21].

$$t = \left(\frac{1}{\left(\mathrm{e}^{1-v_f}\right)}\right)^k \frac{A}{\left(\frac{I_f}{I_p}\right)^B - 1}.\mathrm{TMS} \tag{19}$$

where V_f is the voltage at fault point.

The admittance-based characteristics
The admittance-based characteristic can be expressed as (20); in this characteristic, admittance had been taken as fault sensing variable. This characteristic is similar to standard characteristic but instead of current fault point, admittance has been utilized; also, this characteristic does not include time multiplier setting in relay [22]

$$t = \frac{A}{Y_r^B - 1} + C \tag{20}$$

5 Approaches Based on Soft Computing Techniques

Optimization method is mostly used for achieving optimum values of plug setting and time setting multipliers for relay coordination [23]. In the past few decades, to solve optimization problem many optimization methods are widely used. Relay

coordination problem firstly kept in the frame of optimization problem in the year of 1988, and this problem was solved by linear programing (LP) [24]. Due to simplicity of LP method, it becomes popular among researchers and gained good recognition [25]. In this section, the approaches based on optimization methods for relay coordination have been discussed which are presented by researcher in the past. The optimization method can be bifurcated in three parts. These are deterministic methods, evolutionary methods, and hybrid methods [26].

5.1 Conventional Methods

Initially for relay coordination Trial and error approach was used to find optimum solutions but due to it slow convergence rates an used. To overcome this problem, breakpoint method was utilized [27]. Topological methods are used to breakpoint for finding optimum solution. This method was consisting of functional and graph theory. Further if the distribution system has one or more than one source, directional overcurrent relays are required, then curve fitting techniques, graph theoretical technique and optimization technique lay major role to find optimum value of PS and TMS. To determine the finest function to represent, data curve fitting techniques were used. Also, mathematically relay characteristics can be modeled using curve fitting techniques. Also, the relay coordination using graph theory has been reported.

5.2 Evolutionary Methods

The main advantage of optimization techniques it can overcome the drawback of conventional methods. The benefit of evolutionary method is it does not require the set of breakpoint. This feature makes it more popular among researchers. In optimization method, nonlinear programing was used to solve relay ordination problem; by some researchers, it was observed that it is complex and time-consuming [28]. Many researchers have used mixed integer nonlinear programing, and this programing was solved by general algebraic modeling system software. The major drawback of this programing was its complexity. To avoid the complexity of this programing, researchers showed their interest in linear programing techniques which are simplex, dual simplex, and two-phase simplex method. But the main drawback of these programing was that it was based on initial guess and many time solutions trapped in local minima [29]. In this programing method, plug setting and pickup current are to be assumed as known quantity, and operating time of each relay is considered as linear function of time setting multiplier. In [30] to find the optimum solution for proper relay coordination, Big M method has been proposed but again the plug setting assumed to be known. Simplex dual and two-phase simplex methods to solve relay coordination problem have been presented in [30].

5.3 Artificial Intelligence and Nature Inspired Algorithm

In the present scenario, the researchers have turned their interest toward artificial intelligence (AI) and nature inspired algorithms (NIA)-based optimization methods for optimum solutions. These types of methods are suitable for non-directional and directional overcurrent relay problems. Here in this section, some of the recent programing methods have been presented which are used by nowadays researchers for optimum solution. These are as fuzzy logic, expert system rules. Genetic algorithm has been implemented in [31, 32], particle swarm optimization, artificial bee colony, honey bee algorithm, etc., which has been presented in the past literatures [33–35].

6 Conclusion

A comprehensive review has been worked out for optimum overcurrent relay coordination. In this review paper, different types of objective functions which are used for overcurrent relay coordination problem have been discussed. The formulation of OC overcurrent relay coordination problem and various types of relay characteristic have been discussed which are proposed in the past Also, brief bifurcation of various types of optimization techniques for coordination problem has been discussed. It is hoped by authors that this review paper will help for future generation researcher in their research in the field of relay coordination using optimization techniques.

References

1. Birla D, Maheshwari RP, Gupta H (2006) A new nonlinear directional overcurrent relay coordination technique, and banes and boons of near-end faults based approach. IEEE Trans Power Deliv 21(3):1176–1182
2. Rajput VN, Pandya KS (2017) A novel approach for optimum coordination of directional overcurrent relays including far-end faults in inter connected power systems. Int J Eng Technol (IJET) 8(6)
3. Amraee T (2012) Coordination of directional overcurrent relays using seeker algorithm. IEEE Trans Power Deliv 27(3)
4. Birla D, Maheshwari RP, Gupta H (2007) An approach to tackle the threat of sympathy trips in directional overcurrent relay coordination. IEEE Trans Power Deliv 22(2):851–858
5. Bedekar PP, Bhide SR (2011) Optimum coordination of directional overcurrent relays using the hybrid GA-NLP approach. IEEE Trans Power Deliv 26(1):109–119
6. Rajput VN, Pandya KS (2017) Coordination of directional overcurrent relays in the interconnected power systems using effective tuning of harmony search algorithm. Sustain Comput Inform Syst 15:1–15
7. Kiliçkiran HC, Sengör I, Akdemir H, KekzoŠlu B, Erdinç O, Paterakis NG (2018) Power system protection with digital overcurrent relays: a review of nonstandard characteristics. Electr Power Syst Res 164:89–102
8. Oza B, Nair N, Mehta RP, Makwana VH (2013) Power system protection and switchgear. McGraw Hill education (India) Private Limited New Delhi

9. Srivastava A, Tripathi JM, Mohanty SR et al (2016) Optimal over-current relay coordination with distributed generation using hybrid particle swarm optimization–gravitational search algorithm. Electr Power Compon Syst 44(5):506–517
10. Ravindranath B, Chander M (1977) Power system protection and switchgear. New Age International Press, New Delhi, pp 57–58
11. NPTEL homepage, https://nptel.ac.in/courses/108101039/19. Last access 2019/06/12
12. Electrical notes homepage, https://electricalnotes.wordpress.com/2013/10/11/calculate-idmt-over-current-relay-setting-5051/. Last access 2019/06/12
13. So CW, Li KK, Lai KT et al (1997) Application of genetic algorithm for overcurrent relay coordination. In: Developments in power system protection, Sixth international (Conference No. 434)
14. Razavi F, Abyaneh HA, Al-Dabbagh M et al (2008) A new comprehensive genetic algorithm method for optimal overcurrent relays coordination. Electr Power Syst Res 78(4)
15. Mohammadi R, Abyaneh H, Razavi F et al (2010) Optimal relays coordination efficient method in interconnected power systems. J Electr Eng 61(2):75–83
16. Adelnia F, Moravej Z, Farzinfar M (2015) A new formulation for coordination of directional overcurrent relays in interconnected networks. Int Trans Electr Energy Syst 25(1):120–137
17. Moravej Z, Adelnia F, Abbasi F (2015) Optimal coordination of directional overcurrent relays using NSGA-II. Electr Power Syst Res 119:228–236
18. Rajput VN, Adelnia F, Pandya KS (2018) Optimal coordination of directional overcurrent relays using improved mathematical formulation. IET Gener Transm Distrib 12(9):2086–2094
19. IEEE, standard inverse-time characteristics equations for overcurrent relays, std. c37.112-1996 (1996)
20. Soriya OA, Enriquez AC, Guajardo IT (2014) Overcurrent relay with unconventional curves and its application in industrial power systems. Electr Power Syst Res 110:113–121
21. Saleh KA, Zeineldin HA, Al-Hinai A, El-Madany E-F (2015) Optimal of directional overcurrent relays a new time-current-voltage characteristic. IEEE Trans Power Deliv 30(2):537–544
22. IEC (1989) Electrical relay-part 3: single input energizing quantity measuring relays with dependent or independent time, 60255-3
23. Dewadasa M, Ghœh A, Kadwich G (2009) An inverse time admittance relay for fault detection in distribution network containing DGs. TENCON 1–6
24. Urdaneta AJ, Nadira R, Perez Jimenez L (1988) Optimal coordination of directional overcurrent relays in interconnected power systems. IEEE Trans Power Deliv 3(3):903–911
25. Shih MY, Salazar CAC, Enríquez AC (2015) Adaptive directional overcurrent relay coordination using ant colony optimization. IET Gener Transm Distrib 9(14):2040–2049
26. Singh M, Panigrahi BK, Abhyankar AR (2011) Optimal overcurrent relay coordination in distribution system. In: Proceedings—2011 international conference on energy, automation and signal, ICEAS—2011, pp 822–827
27. Birla D, Maheshwari RP, Gupta HO (2005) Time-overcurrent relay coordination: a review. Int J Emerg Electr Power Syst 2
28. Zocholl SE, Akamine JK, Hughes AE, Sachdev MS, Scharf L, Smith HS (1989) Computer representation of overcurrent relay characteristics. IEEE Trans Power Deliv 4:1659–1667
29. Smooolleck H (1979) A simple method for obtaining feasible computational models for time characteristics for industrial power system protective. Electr Power Syst Res 2:129–134
30. Jenkins L, Khincha H, Dash P (1992) An application of functional dependencies to the topological analysis of protection schemes. IEEE Trans Power Deliv 7:77–83
31. Mohammadi R, Abyaneh HA, Rudsari HM, Fathi SH, Rastegar H (2011) Overcurrent relays coordination considering the priority of constraints. IEEE Trans Power Deliv 26:1927–11938
32. Urdaneta AJ, Nadira R, Perez L (1998) Optimal coordination of directional overcurrent relay in interconnected power systems. IEEE Trans Power Deliv 3:903–911
33. Walke SB, Jangle NN (2017) Review: methods for relay coordination. In: Proceedings of the IEEE 2017 international conference on computing methodologies and communication (ICCMC)

34. Othman AM, Abdelaziz AY (2016) Enhanced backtracking search algorithm for optimal coordination of directional over-current relays including distributed generation. Electr Power Compon Syst 44(3):278–290
35. Kalage AA, Ghawghawe ND (2016) Optimum coordination of directional overcurrent relays using modified adaptive teaching learning based optimization algorithm. Intell Ind Syst 2(1):55–71

Reduction of Short-Circuit Level of EHV Substation

Jay Jogi, Chetan Sheth, Vinod Gupta and Krunal Darji

Abstract With the expansion of network, there is inclusion of new power stations and transmission lines in the network as a consequence of which the short-circuit levels at some of the substation increase apart from its design limit. This short-circuit current causes offensive electrodynamic force, thermal and mechanical stress and devastation to equipments. Hence, the contraction and regulation of this short-circuit current are crucial. To diminish this short-circuit current, one of the pragmatic solutions is to update the equipments so that the predicted fault current is inmost equipment capacity. This generally suggests the entire reconstruction of substation. However, this solution is very expensive. All the switchgear equipments are rehabilitated and certified ahead of upgrading the existing substations, which is quite problematic process. There are few techniques accessible for reduction of short-circuit level, namely application of high-impedance transformer, disconnection of some lines from the critical substation, bus bar splitting technique, current limiting reactor, etc. This paper discusses simulation of case study with current limiting reactor (CLR) technique and bus bar splitting technique in the substation and identifies the optimum solutions to control and reduce of short-circuit levels of EHV Substation.

Keywords Fault level · Short-circuit current · Uprating · Current limiting reactor · Power system planning · Reliability · Bus splitting

J. Jogi (✉) · C. Sheth
G. H. Patel College of Engineering & Technology, Vallabh Vidyanagar 388120, India
e-mail: jayjogi98@gmail.com

C. Sheth
e-mail: chetansheth@gcet.ac.in

V. Gupta · K. Darji
Electrical Research & Development Association, Vadodara 390010, India
e-mail: vinod.gupta@erda.org

K. Darji
e-mail: krunal.darji@erda.org

A. Mehta et al. (eds.), *Advances in Electric Power and Energy Infrastructure*, Lecture Notes in Electrical Engineering 608,
https://doi.org/10.1007/978-981-15-0206-4_5

1 Introduction

A fault in power system is an unwanted condition that implies the deficiency of equipments, namely transformer, generator, bus bar, etc. The topography of the power system network keeps changing as the economy of a nation grows and its power consumption increases [1]. The effect of growth of energy generation and addition of transmission line in networks causes problems of fault current in the power system. Furthermore, manipulation of computers and power electronics sensitive equipment has enforced the utilities to deliver higher and good quality power. As the power inception and power interaction increase, the fault current also increases consistently in the power system. Older but still operating switchgear equipment becomes undervalue through the system growth [2].

As soon as fault takes place, the interrupting device must proficient to suspend such fault current. The significant fault types to be considered are as follows:

(1) TPG fault,
(2) Phase-to-phase fault,
(3) SLG fault.

The inferior and very unusual case is TPG fault, and its harshness and substantial damages are very high and are used for selecting the rating of interrupting devices.

The undesired consequence of increased short-circuit fault level recaps as follows:

(1) Equipments are barren to repugnant electrodynamic forces;
(2) Equipments are barren to repugnant thermal and mechanical stresses;
(3) Faster circuit breakers are required to inhibit equipment damage;
(4) The breaking capability of previously installed circuit breakers is limited to 40 kA;
(5) Increased short-circuit level causes security issue to the workforce.

Owing to above-mentioned drawback, the fault level attenuation has picked up a notable significance in modern years among utilities.

It is very expensive to upgrade, replace and reconfigure the equipment like switchgear, transformer, cabling and bus bar to high fault level [1, 2]. And to this problem, there is one menace, i.e. economic cost.

There are numerous techniques accessible for limiting the short-circuit current and have been introduced in Sect. 2. The numerous techniques are as follows:

A. Application of high-impedance transformer [3];
B. Current limiting reactor [1–6];
C. Fault current limiter [2, 3, 7–11];
D. IS limiter [3, 12];
E. Bus bar splitting technique in the substation [3, 4];
F. Fuse;
G. Power system reconfiguration [1, 3];
H. Disconnection of some transmission lines from the critical substation;
I. HVDC links [3];

J. Application of neutral reactor.

The overhead techniques are briefly explored in Sect. 2. The persistent short-circuit estimation is accomplished to investigate beneficial outcome.

2 Short-Circuit Fault Current Limitation Techniques

In this section, the formerly instigate short-circuit depletion techniques are elucidated in brief.

A. Application of High-Impedance Transformer

There is a considerable reduction in fault current level using high-impedance transformers. This technique might change system nobility and may result in lower stability margin, so this requires careful attention [3].

B. Current Limiting Reactor (CLR)

CLR is a prominent technique to inhibit the fault current, and it is more economical. CLR renders superior impedance to the system through series associated reactance. During fault condition, this superior impedance of CLR is used to protect the switchgear equipment. The short-circuit level confers to the system demand, and stresses on the switchgear equipments are decreased by CLR. Nevertheless, CLR employs a comparatively large space in the substation, due to safety considerations [1–6].

C. Fault Current Limiter (FCL)

In FCL, a short-circuit current is bounded by volcanic charge. This volcanic charge opens a conductor and redirects the current to a alike connected fuse which suppresses the short-circuit current. In normal operation condition, fault current limiter offers low impedance and its impedance should increase immediately during fault condition so that current would get limited. When FCL is bared to high current, it has property of shifting from a super-conducting state to the normal state. In virtue of this diagnostic, they are pragmatic for limiting the fault current. The discrete types of SFCLs are as follows: resistive, inductive and transformer type. The FCL supreme is to be ideal, but it is still too much expensive [2, 3, 7–11].

D. IS Limiter

The upgraded form of fuse is IS limiter. In normal condition, the current passed through a passage parallel to fuse. At the time of short circuit, the collateral passage is opened using electrodynamic force. Thus, the fault current is replaced to fuse, and the problem of limiting the ceremonial current of fuse is clear up. The interrupting capacity of IS limiter is up to 5 kA. And it is normally used to 40 kV [3, 12].

E. Bus Bar Splitting Technique in the Substations

To deplete the fault current, the bus is split into sections. However, this technique is more effectual than CLR technique. The bus bar splitting technique is identical to CLR technique with infinite reactance. There was an unsought issue on stability, so this requires careful attention [3, 4].

F. Fuse

One of the fastest short-circuit interrupting devices is fuse. The construction of fuse is simple and cost-effective. It is constricted underneath 40 kV and 200 A. The speciality of fuse is that after every interruption, it can be replaced. However, the drawback of fuse is that it is not applicable where the uninterrupted auto-reclosing is prerequisite.

G. Power System Reconfiguration

Power system reconfiguration technique is more realistic to some extent. The power system reconfiguration is case dependent, and there is no definite rule. It mainly depends on vision and intimacy of the engineer with the system. Using this technique, fault level is depleted and stability of the system may improve [1, 3].

H. Disconnection of Some Transmission Lines from the Critical Substation

To diminish short-circuit level at bus bar, some transmission lines are isolated. Eventually, these isolated transmission lines are revamped to other the substation where the short-circuit level is low. From the systems behaviour standpoint, this technique is not acceptable. The main disadvantages of this technique are that there is unpleasant effect on the stability of system.

I. HVDC

The short-circuit current is diminished by substituting the lines with HVDC links. This will control the fault current levels. This method is not economically upheld in the present concept [3].

J. Application of Neutral Reactor

To limit the SLG fault level, reactor is placed at the neutral of transformers. As the superiority of faults incorporates ground, this method might be treated as an impressive passage.

From the above discussed techniques, bus bar splitting conceivably the uttermost pragmatic method. After all the security of system is not plagued, the system operators may accept it.

3 Case Study

In this paper, the short-circuit study is negotiated at 220 kV side of 400 kV substation. The network is modelled in MiPower software. The short-circuit level at one of the 200 kV sides of 400 kV substation increases beyond its design limit which is shown in Fig. 1. The details of associated line and associated transformer with 220 kV side of 400 kV substation are as shown in Fig. 2.

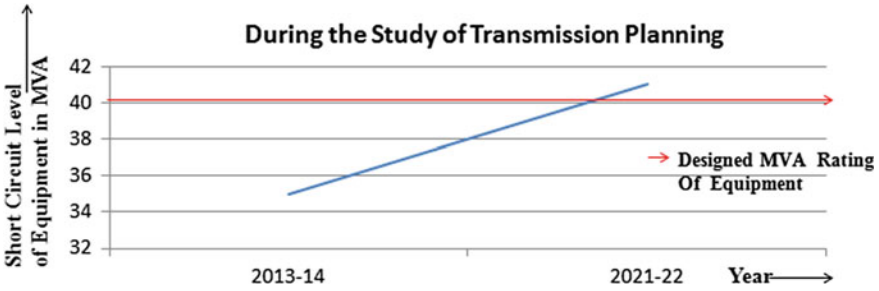

Fig. 1 Short-circuit level at 220 kV side increases beyond its designed limit

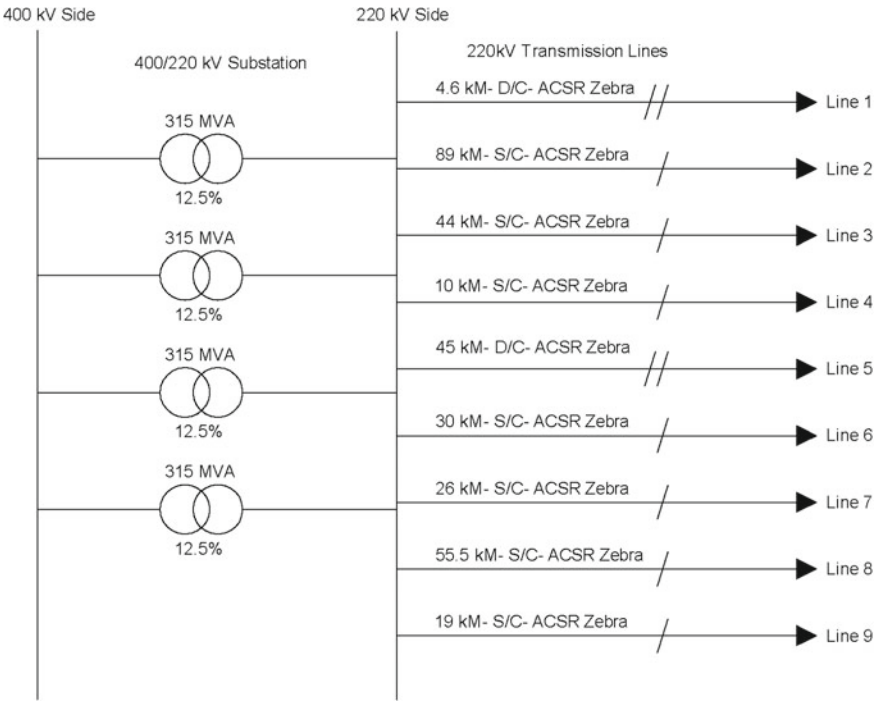

Fig. 2 Details of substation

Table 1 Short-circuit results of 220 kV side of 400 kV substation

Substation name	TPG fault		SLG fault	
	Fault MVA	Fault current kA	Fault MVA	Fault current kA
220 kV side of 400 kV substation	14,306.140	37.544	14,578.733	38.259

4 Analysis Study

4.1 Short-Circuit Study

The simulation of short-circuit study is carried out at 220 kV side of 400 kV substation in MiPower software. The simulation results are as per Table 1.

The fault level results show that single line to ground (SLG) fault of 220 kV side of 400 kV substation reaches up to 38.259 kA and within 2–3 years with increase of network, and it may reach beyond 40 kA. The switchgear equipment available at substation is of 40 kA. Thus, it is imperative to either mitigate the short-circuit level with various techniques or upgrade all the switchgear system. In this paper, we have analysed the two techniques for mitigation of short-circuit level of 220 kV side of 400 kV substation.

The short-circuit current is mainly limited by impedance of the system. The equation of short-circuit kVA is given below:

$$\text{Short-Circuit kVA of Three-Phase Circuit} = \frac{\text{Base kVA} * 100}{\%X} \tag{1}$$

From the above equation, it is clear that, as the impedance X increases, the short-circuit kVA automatically reduces.

4.2 Mitigation Techniques for Reduction of Short-Circuit Level

There are various methods available for mitigation of short-circuit current as discussed in Chapter "Symmetrical Fault—Swing Discrimination Using RMS Index-Based Superimposed Current Signals" of this paper. In this paper, current limiting reactor (CLR) technique and bus bar splitting technique are applied to mitigate the short-circuit fault current.

I. **Current Limiting Reactor (CLR) Technique**

The current limiting reactor is placed in series with the transformers and line which are majorly contributing to fault level. The CLR is placed at eight different locations as shown in Fig. 3.

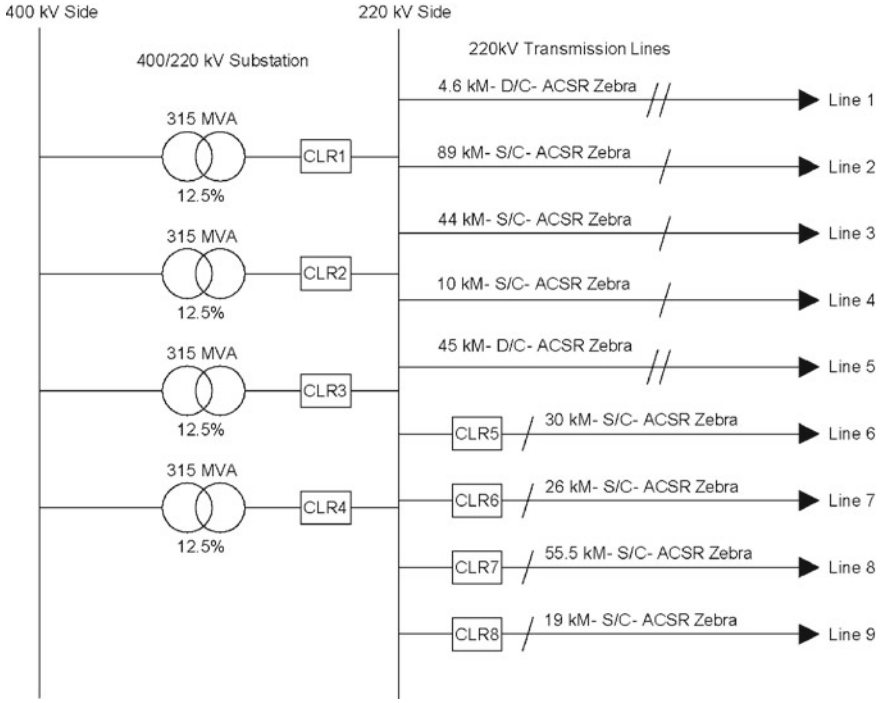

Fig. 3 CLR placed at different location

The rating of the reactor is decided by underneath equation:

$$\text{Reactor MVA} = \sqrt{3} * \text{Rated Current} * \text{Voltage} \tag{2}$$

$$X = \frac{256 * 100}{3 * \text{Rated Current} * \text{Rated Current}} \tag{3}$$

$$\text{Reactor } X \text{ in pu} = \frac{X * \text{Reactor MVA}}{\text{Rated Voltage} * \text{Rated Voltage}} \tag{4}$$

The results of short-circuit level after placing CLR are as shown in Table 2.

Table 2 Short-circuit results with CLR technique

Substation name	TPG fault		SLG fault	
	Fault MVA	Fault current kA	Fault MVA	Fault current kA
220 kV side of 400 kV substation	13,325.69	34.971	13,247.69	34.566

The above results show that fault levels of 220 kV side of 400 kV substation reduce up to 34.56 A.

II. **Bus Bar Splitting Technique**

The short-circuit level at 220 kV side of 400 kV substation is mainly contributed from 4 × 315 MVA transformers. Based on the study, the following methods have been proposed for the mitigation of short-circuit level.

The 220 kV side of 400 kV substation shall be split into two sections with following lines on each side:

Bus A:

- 220 kV side of 3 × 315 MVA Transformer
- 220 kV D/C Line 1

Bus B:

- 220 kV side of 1 × 315 MVA Transformer
- 220 kV S/C Line 2
- 220 kV S/C Line 3
- 220 kV S/C Line 4
- 220 kV D/C Line 5
- 220 kV S/C Line 6
- 220 kV S/C Line 7
- 220 kV S/C Line 8
- 220 kV S/C Line 9

Series Reactor: Reactor of **12 Ω** is placed between Bus A and Bus B (Fig. 4).

Similarly, the reactor rating is also determined based on Eqs. (2), (3) and (4).

Due to above arrangement, the short-circuit levels of both the buses are as per Table 3.

Looking to the results of Tables 2 and 3, the short-circuit level of 220 kV side of 400 kV substation is reduced and both the method can be used for reduction of short-circuit level.

The comparison of short-circuit level in kA previously and using both the techniques is shown in Fig. 5.

5 Techno-Economic Analysis

The techno-economic analysis recommends which method is preferable instead of replacing the switchgear equipment (Table 4).

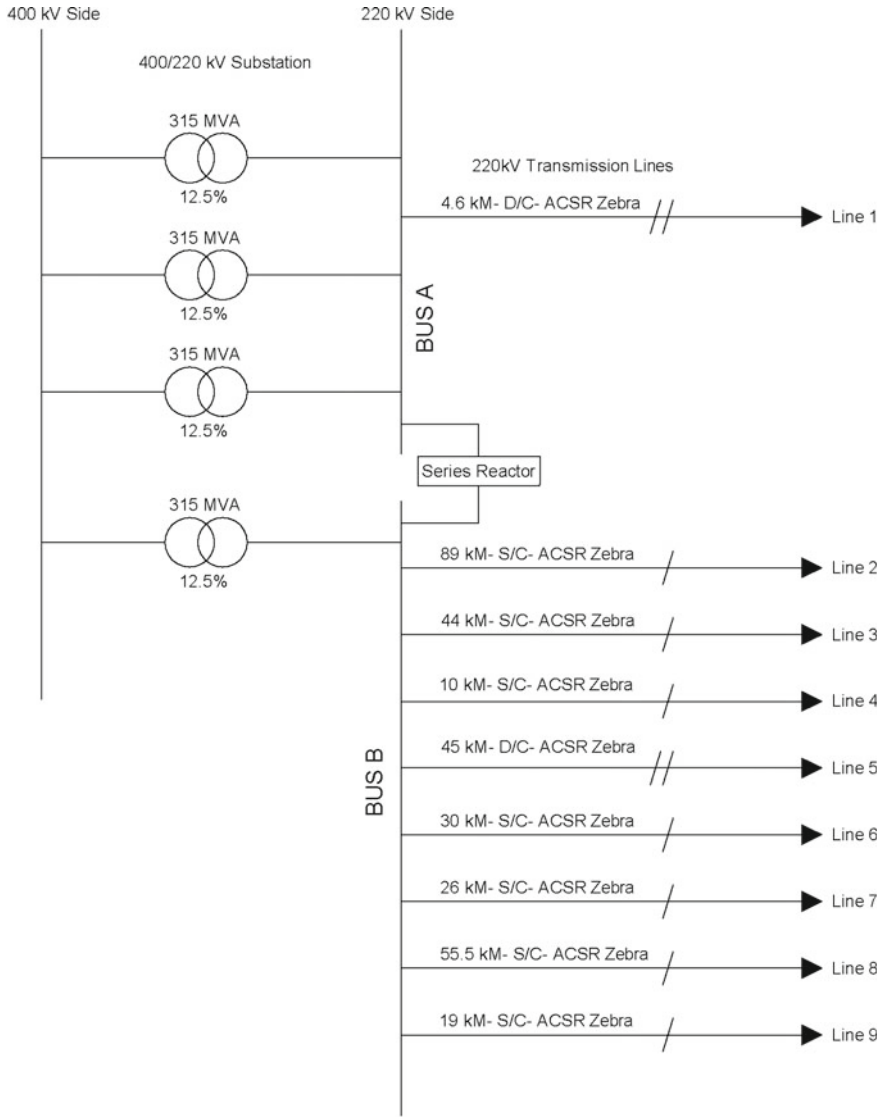

Fig. 4 Bus bar splitting technique with series reactor

Table 3 Short-circuit results with bus splitting techniques

Bus name	TPG fault		SLG fault	
	Fault MVA	Fault current kA	Fault MVA	Fault current kA
Bus A	12,015.144	31.531	12,458.549	32.695
Bus B	13,421.580	35.223	13,282.256	34.857

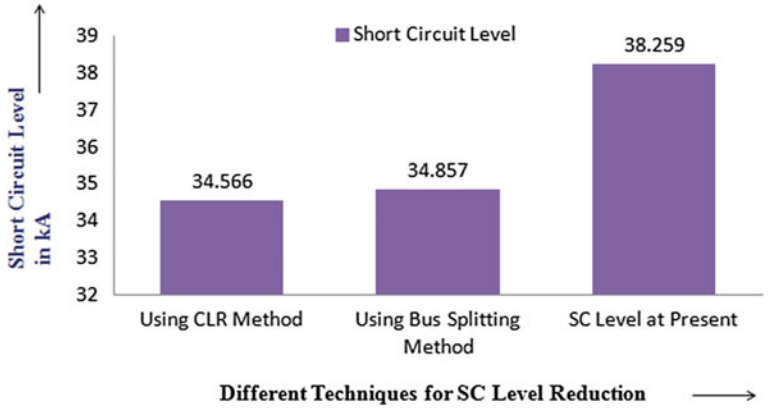

Fig. 5 Short-circuit level comparison

Table 4 Techno-economic analysis

Technique	Item	Approximate cost in Rs.
CLR technique	Eight numbers of 125 MVA reactor are placed at different location.	60
Bus splitting technique	Only one number of 125 MVA series reactor is placed.	8
Replacement of the switchgear equipment	With higher rapturing capacity of 63 kA	30

6 Conclusion

In this paper, various mitigation techniques are studied for reduction of short-circuit level below the design limit of substation. Two methods, current limiting reactor (CLR) technique and bus splitting technique are applied for the reduction of short-circuit level below the design limit of 40 kA. With both the methods, short-circuit level is reduced and hence both can be applied for the reduction of short-circuit level. In CLR technique, eight numbers of current limiting reactors are required, while in bus splitting technique only one series reactor is required. Looking to the space constraint in substation and techno-economic analysis, the bus splitting technique is found to be the most suitable for application of reduction of short-circuit level.

References

1. Gilany M, Al-Hasawi W (2009) Reducing the short circuit levels in Kuwait transmission network. (A case study). World Acad Sci, Eng Technol Int J Electr Comput Eng 3(5)
2. Tongsrichantra S, Suwanasri T, Suwanasri C (2009) System study and fault level reduction techniques for a small scale power plant in Thailand. GMSARN Int J 3
3. Seyedi H, Tabei (2012) Appropriate placement of fault current limiting reactors in different HV substation arrangements. Sci Res
4. Amon JF, Fernandez PC, Rose EH, D'Ajuz A, Castanheira A (2005) Brazilian successful experience in the usage of current limiting reactors for short-circuit limitation. In: International conference on power systems transients (IPST'05), Montreal, pp 215–220
5. Tremouille G, Parisot A, Imagawa H (2012) Short circuit Uprating, methodology throughout the diversity of required skills. CIGRE
6. Machado C Jr, Fukuoka N, Rose EA, Violin A, Martinez MLB, Saraiva CAM (2001) Switching a series reactor—a concept develop to limit the level of short circuit currents. In: IEEE Porto Power Tech Conference
7. Farrokhifar M, Esmaeilzadeh R, Heydari M, Milani AR (2013) A study on practical methods to decrease short circuit level in transmission grids. In: IECON 2013—39th annual conference of the IEEE industrial electronics society, Vienna, pp 1962–1967
8. Razzaghi R, Niayesh K (2011) Current limiting reactor allocation in distribution networks in presence of distributed generation. In: 10th international conference on environment and electrical engineering, Rome, pp 1–4
9. Tekletsadik K, Lubicki P, Nickerson S, Ludlum J, Murphy P (2014) Fault current limiter selection considerations for utility engineers. CIGRE US National Committee
10. Lee BW, Sim J, Park KB, Oh IS (2008) Practical application issues of superconducting fault current limiters for electric power systems. IEEE Trans Appl Supercond 18(2)
11. Hongesombut K, Mitani Y, Tsuji K (2003) Optimal location assignment and design of superconducting fault current limiters applied to loop power systems. IEEE Trans Appl Supercond 13(2)
12. Hartung KH (2002) IS-limiter, the solution for high short-circuit current applications. ABB Calor Emag

Recourse-based Stochastic Market Clearing Algorithm

Leena Heistrene, Poonam Mishra and Makarand Lokhande

Abstract Solutions obtained from the deterministic market-clearing problem may be feasible only for those conditions when point forecasts of random variables such as load and renewable sources of energy are within a tight range of accuracy. Unfortunately, point forecasts of renewable sources of energy have a higher error percentage. Under such circumstances, dynamism associated with renewable sources such as wind must be formulated as stochastic formulations which would encompass feasible solutions for a broader spectrum of forecast possibilities. This paper describes stochastic formulation for market clearing using recourse method. This method gives twofold solutions—the first being day-ahead market schedules obtained as here-and-now variables while the second being reserves applicable for different scenarios of wind forecast obtained as wait-and-see variables. This recourse-based stochastic formulation is validated for modified 24-node IEEE reliability test system.

Keywords Stochastic market clearing · Recourse method · Renewable energy · Here-and-now variables · Wait-and-see variables

Notations

Indices

t	Time period
i	Individual conventional power plant
j	Individual wind farm
sc	Individual scenario

L. Heistrene (✉) · P. Mishra
Pandit Deendayal Petroleum University, Gandhinagar 382007, India
e-mail: leena.santos@sot.pdpu.ac.in

M. Lokhande
Visvesvaraya National Institute of Technology, Nagpur 440010, India

A. Mehta et al. (eds.), *Advances in Electric Power and Energy Infrastructure*, Lecture Notes in Electrical Engineering 608,
https://doi.org/10.1007/978-981-15-0206-4_6

k	Individual load
r	Individual transmission line
n	Individual node/bus
ω	Individual scenario
Nt	Total time period
Ng	Total number of conventional power plants
$N\omega$	Total scenarios considered
Nj	Total wind farms
Nl	Total loads in the system
Nr	Total number of transmission lines in the system
Ng_n	Total number of generators on bus n
Nw_n	Total number of wind generators on bus n
Nr_n	Total number of transmission lines on bus n
Nl_n	Total number of load on bus n

Here-and-now and wait-and-see variables

C_{it}^{su}, $C_{it\omega}^{\text{su}}$	Start-up cost of conventional generator i at time t
P_{it}^{g}, $P_{it\omega}^{g}$	Power generated by conventional generator i at time t
R_{it}^{U}	Up reserve of conventional generator i at time t
R_{it}^{D}	Down reserve of conventional generator i at time t
R_{it}^{NS}	Non-spinning reserve of conventional generator i at time t
$rG_{it\omega}$	Additional power to be generated by conventional generator i at time t under scenario ω
P_{jt}^{wind}, $P_{jt\omega}^{\text{wind}}$	Power generated by wind farm j at time t
$S_{t\omega}^{\text{wind}}$	Curtailment due to scenario ω in time t
U_{it}, $U_{it\omega}$	Unit commitment status binary variable
$f_{\omega}(n, r)$	Transmission line flow between bus n and bus r
$rG_{it\omega}^{U}$	Up reserve for generator i at time t under scenario ω
$rG_{it\omega}^{D}$	Down reserve for generator i at time t under scenario ω

Constants

λ_{it}	Offer cost of conventional generator i at time t
λ_{it}^{su}	Cost for starting the conventional generator i at time t
λ_{it}^{RU}	Cost for up reserve of conventional generator i at time t
λ_{it}^{RD}	Cost for down reserve of conventional generator i at time t
$\lambda_{it}^{\text{RNS}}$	Cost for non-spinning reserve of conventional generator i at t
π_{ω}	Probability of scenario ω
L_{kt}	Demand of load k at time t

$P^{g}_{\min,i}$ Minimum generation limit of generator i
$P^{g}_{\max,i}$ Maximum generation limit of generator i
R^{system} System reserve

1 Introduction

Grid integration of renewable sources of energy has been increasing tremendously over the last two decades. Many of these renewable sources of energy are highly dynamic in nature. As the level of dynamism and intermittency of these sources grow, the accuracy of point forecast reduces. For example, wind is a highly dynamic source of energy as compared to solar energy. Hence, while solar energy can be forecasted within an accuracy of ±90–93% range, wind energy can be forecasted with accuracy of 80–85% range. Thus, dynamic renewable sources of energy are prone to forecasting inaccuracies.

Day-ahead market (DAM) is cleared based on load and generation forecasts. Load forecasts have an accuracy range of 97–98%. Conventional generation is controllable but susceptible to random outages. In spite of this, conventional generation can be scheduled with a high probability of realization. Hence, point forecasts can be used to determine generation and load schedule deterministically in DAM. On the other hand, dynamic renewable sources, such as wind power, can be predicted with range of 15–18% error unlike the 2–3% error of load and conventional generation forecasts. Hence, dynamic renewable sources must be predicted as probabilistic forecasts. For this reason, there is a growing need of treating market-clearing problems (MCP) as stochastic optimization problem in place of deterministic one. A deterministic MCP approach may lead to infeasible solutions in real time when the actual wind realization of point forecasts occurs. On the other hand, in a stochastic approach, multiple scenarios of the forecast are considered along with their probability of occurrence. This solution would ensure that the optimal solution obtained is feasible in real time when actual realization of wind occurs; such a solution covers a wide range of possible forecast scenarios. Hence, researchers are focusing on stochastic formulations that can cater to the uncertainties in forecast [1, 2]. This paper has implemented the recourse method to tackle the randomness involved in wind power.

The flow of this paper is as follows: Introductory Sect. 1 is followed by literature survey in Sect. 2 and mathematical formulation of stochastic market-clearing problem (SMCP) in Sect. 3. Section 4 discusses the results after implementing the SMCP on modified 24-node IEEE reliability test system followed by the conclusion in Sect. 5.

2 Literature Survey

Market clearing and the traditional unit commitment problem are treated deterministically in all electricity markets even today. But, intense research is going on in converting these deterministic expressions into stochastic ones owing to the randomness displayed by some of its decision variables such as renewable sources of energy. Stochastic programming can be broadly classified as interval-based methods and scenario-based methods. Interval-based methods are used more often due to the fact that they put relatively lesser computational burden. But, these methods are very sensitive to uncertainty intervals [3]. On the other hand, scenario-based methods have an edge over interval-based methods when it comes to giving more stable solutions, but these methods are computationally rigorous. Based on the above-mentioned stochastic methods, researchers have contributed in the area of stochastic unit commitment/market clearing in terms of joint market-clearing approaches [4], addition of new constraints, such as reliability constraints [5], inclusion of marginal pricing in market formulation [6] and hybridization of robust and stochastic approaches [7]. Researchers have also considered different factors of uncertainties in the MCP. In [8], loss of load and generation was considered as random variables. Different offers and bid orders have also been considered as seen in [9] which increases the computational complexity of the problem. Exchange and flow-based model have also been researched in [10] although it is a deterministic model.

This paper focuses on the recourse method of stochastic optimization wherein different scenarios of wind forecasting are considered. Scenarios wherein actual wind may be more or less than mean forecast are considered in the optimal problem.

3 Proposed Recourse-based Mathematical Formulation for SMCP

Random variables can be represented by a set of intervals or scenarios with a probability attached to each scenario/interval. Such a representation is far more useful than a point forecast. Probabilistic forecasts such as scenario representation can be used in discrete stochastic formulations. Recourse-based stochastic programming uses probabilistic forecasts in their mathematical formulation as shown below in (1).

$$\begin{aligned} \min \quad & (c^T)x + \sum \Pr(\omega) q(\omega)^T y(\omega) \\ \text{subject to } & Ax \leq b; \\ & T(\omega)x + W(\omega)y(\omega) \leq h(\omega) \\ & x \in X \quad y(\omega) \in Y \end{aligned} \tag{1}$$

The same can be implemented in the stochastic market-clearing formulation wherein the $(c^T)x$ shall be represented by the day-ahead market-related quantities such as scheduled generation from conventional to renewable energy sources,

reserve market-related quantities such as up, down and non-spinning reserves and commitment status-related quantities such as start-up costs involved in the time horizon under consideration. These are referred to as the here-and-now variables. Similarly, $q(\omega)^T y(\omega)$ represents the quantities that take values after the realization of the forecasted quantity in real time. These are termed as wait-and-see variables.

In this paper, the wait-and-see second stage variables represent optimal solutions after realization of individual scenarios in real time. In symbolic terms, it can be said that here-and-now variable vector x represents C^{su}_{it}, P^{g}_{it}, P^{wind}_{jt}, R^{U}_{it}, R^{D}_{it}, R^{NS}_{it}, U_{it} while vector y represents $C^{\text{su}}_{it\omega}$, $rG_{it\omega}$, $rG^{U}_{it\omega}$, $rG^{D}_{it\omega}$, $U_{it\omega}$ and $P^{g}_{it\omega}$ of time period t.

Objective function of the subproblem at the initialization stage is shown in Eq. (2).

$$(c^T)x = \sum_{t=1}^{Nt}\left[\sum_{i=1}^{Ng} C^{\text{su}}_{it} + \lambda_{it}P^{g}_{it} + \lambda^{\text{RU}}_{i}R^{U}_{it} + \lambda^{\text{RD}}_{it}R^{D}_{it} + \lambda^{\text{RNS}}_{it}R^{\text{NS}}_{it} + \sum_{\omega=1}^{N\omega}\pi_{\omega}(C^{\text{su}}_{it\omega} + \lambda_{it}rG_{it\omega})\right] \tag{2}$$

Similarly, constraints that feature in matrix A include load balance constraints, generation and reserve limit constraints and transmission flow constraints, and they are listed below from Eqs. (3) to (8). Most of the variables involved in this mathematical formulation are of continuous type except the commitment variables which are binary type. Both here-and-now and wait-and-see variables appear in these equations.

Load balance constraints at system level and node level:

$$\sum_{i=1}^{Ng} P^{g}_{it} + \sum_{j=1}^{Nj} P^{\text{wind}}_{jt} = \sum_{k=1}^{Nl} L_{kt}; \quad \& \sum_{i=1}^{Ng} P^{g}_{it\omega} + P^{\text{wind}}_{t\omega} - S^{\text{wind}}_{t\omega} - f_{\omega}(n,r) = 0 \tag{3}$$

Generation and ramping limits constraints:

$$P^{g}_{\min,i}U_{it} \le P^{g}_{it} \le P^{g}_{\max,i}U_{it}; \ \& \ P^{g}_{\min,i}U_{it\omega} \le P^{g}_{it\omega} \le P^{g}_{\max,i}U_{it\omega}; \tag{4}$$

$$\begin{aligned} 0 \le R^{U}_{it} \le (P^{g}_{\max,i} - P^{g}_{\min,i})U_{it}; \ \& \ 0 \le R^{D}_{it} \le (P^{g}_{\max,i} - P^{g}_{\min,i})U_{it}; \\ \& \ 0 \le R^{\text{NS}}_{it} \le (P^{g}_{\max,i} - P^{g}_{\min,i})U_{it}; \end{aligned} \tag{5}$$

Reserve constraint as per security policy considered:

$$R^{U}_{it} - R^{D}_{it} + R^{\text{NS}}_{it} \ge R^{\text{system}} \quad \& \ P^{g}_{\min,i} \le P^{g}_{i} + rG_{it\omega} \le P^{g}_{\max,i} \tag{6}$$

Non-anticipatory constraints:

$$P^{g}_{it\omega} = P^{g}_{i} + rG_{it\omega} \ \& \ rG_{it\omega} = rG^{U}_{it\omega} - rG^{D}_{it\omega} \quad \& \ C^{A}_{it\omega} = C^{\text{su}}_{it\omega} - C^{\text{su}}_{it} \tag{7}$$

Start-up constraints:

$$C_{it}^{\mathrm{su}} \geq \lambda_{it}^{\mathrm{su}}(U_{it} - U_{i,t-1}) \quad \& \; C_{it\omega}^{\mathrm{su}} \geq \lambda_{it}^{\mathrm{su}}(U_{it\omega} - U_{i,t-1,\omega}) \tag{8}$$

Similarly, upper and lower bounds of each of the variables mentioned above are included.

4 Results and Discussions

The stochastic market-clearing formulation has been validated using 24-node IEEE reliability test system. It has been modified to include wind sources at buses 13, 15, 16 and 20. In order to avoid overriding the power flow dynamics, the buses to which wind sources have been attached are done so by reducing the size of the conventional generators attached to them in the original system. For simplicity purpose, only three scenario forecasts have been considered for analysis. In this system, there are 12 generators, 4 wind farms and 34 transmission lines. Time period under consideration for the analysis is 2 h. Mixed integer linear programming from MATLAB® toolbox is used for solving the optimization problem. Changes made in the modified system are as shown in Fig. 1.

Table 1 compares the change in size of the optimization problem when deterministic and stochastic approaches are adopted. It can be easily observed that the size of the problem increases drastically in spite of keeping the scenarios and time period as very nominal values. For example, in a deterministic approach, since point forecast of wind is used for equality constraints, there are 25 equality constraints which include one overall system load balance constraint and 24 energy flow constraints at each bus. On the other hand, in a stochastic approach, each of the flow constraint would be pertaining to each scenario. And hence, the flow constraints would be dependent on number of scenarios as well. Secondly, additional equality constraints called non-anticipatory constraints would have to be introduced for maintaining the physical meaning and mathematical relevance of the terms. Increase in number of decision variables and the number of equality and inequality constraints is a major drawback of considering stochastic models in place of deterministic ones. But, deterministic approach does not consider the possibility of wind power being different from that which is committed in the day-ahead market. This could result into situations wherein the scheduled generation in real time is either uneconomic or sometimes even infeasible due to system congestion and other constraints.

For simplicity purpose, only three scenario forecasts have been considered for deriving the observation tables. The wind forecast probabilities have been changed with varying proportions and the overall function cost derived in each case. Results are shown in Table 2. Two things are to be noted from this table. Firstly, the costs obtained are higher than the deterministic cost, and secondly the stochastic costs increase as the forecast quality deteriorates. The rise in cost is the cost paid for obtaining solutions that are feasible for all scenarios. As the scenarios increase, they

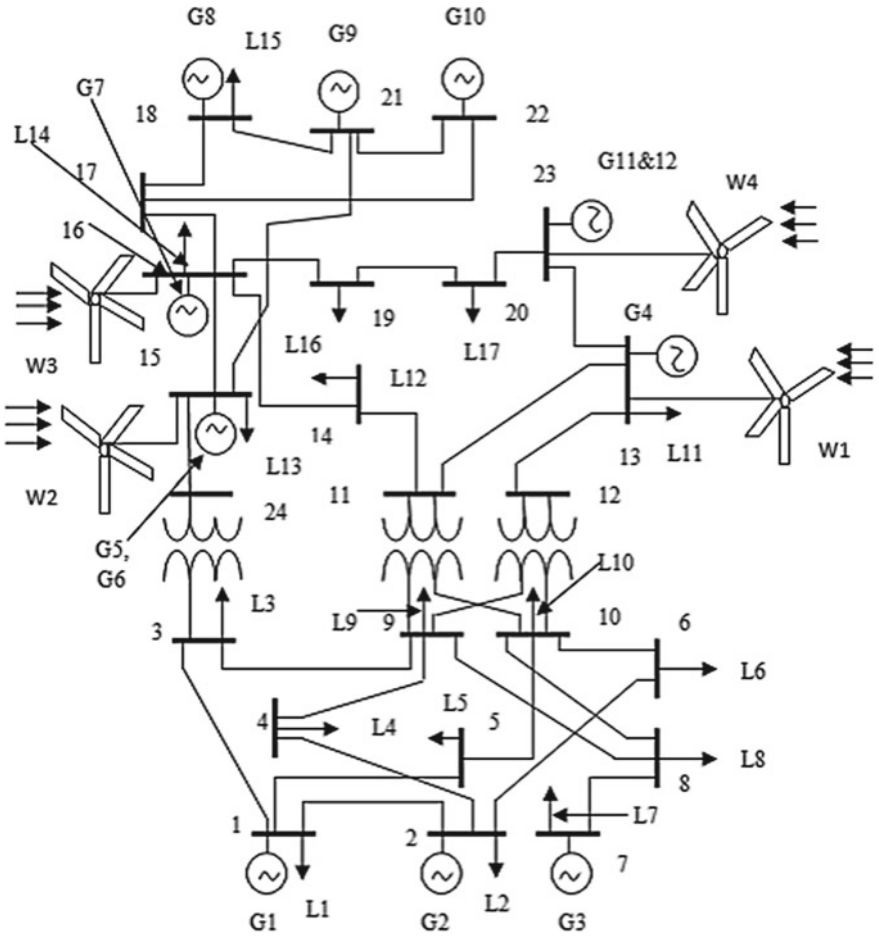

Fig. 1 Modified IEEE reliability test system

Table 1 Size of optimization problem

Sr. no.	Problem feature	Deterministic approach	Stochastic approach
1.	Number of variables	272	1172
2.	Number of equality constraints	25	566
3.	Number of inequality constraints	148	578

Table 2 Change in function cost as accuracy changes

Sr. no.	Mean forecast	High forecast	Low forecast	Stochastic cost	Rise (%)
1.	0.90	0.05	0.05	18218	0.5
2.	0.85	0.10	0.05	18265	0.7
3.	0.80	0.10	0.10	18313	1.0
4.	0.75	0.15	0.10	18360	1.3
5.	0.70	0.15	0.15	18407	1.9

tend to grow closer to the actual realization. Hence, it can be deduced that since the recourse approach, as implemented in the paper, provides feasible solutions for the scenarios considered by means of their second stage/wait-and-see compensation variables, its solution, and even though costlier than deterministic solutions still they are much better.

Considering the forecast with a per scenario probability of 0.8 for average forecast and 0.1 for high and low forecast, respectively, the solution approach is shown in Tables 3 and 4. Here, the load demand considered is 2200 MW for the first hour and

Table 3 Generation and reserve schedule using recourse approach for the day-ahead market

Generator	1st hour offer (MW)	2nd hour offer (MW)	1st hour reserve (MW)	2nd hour reserve (MW)
Gen 1.	0	121.4	0	0
Gen 2.	46.6	121.6	0	0
Gen 3.	0	0	0	0
Gen 4.	0	0	0	0
Gen 5.	0	12	0	0
Gen 6.	24	30	0	0
Gen 7.	24.4	55	30	300
Gen 8.	400	400	300	90
Gen 9.	400	400	0	0
Gen 10.	300	300	0	0
Gen 11.	0	155	0	0
Gen 12.	0	0	0	0
Total	1195	1595	330	390

Table 4 Wind generation observed

Time (hour)	Wind power gen at node 13 (MW)	Wind power gen at node 15 (MW)	Wind power gen at node 16 (MW)	Wind power gen at node 20 (MW)
1.	400	155	100	350
2.	400	155	100	350

2600 MW for the second hour. No down reserve is required in this case, and hence, not shown. These tables demonstrate the practical application of the optimal results obtained from the feasible solution set.

5 Conclusion

Implementation of recourse method, as demonstrated in this paper, has a practical approach to handling random variables such as renewable energy as opposed to deterministic approach which are cheaper but prone to infeasible in real-time operation. Additional cost borne by the stochastic approach is traded off by its solution which is feasible in all scenarios considered. Hence, it can be concluded that recourse methods are more applicable in cases wherein the forecasts are less accurate and prone to bigger error intervals.

References

1. Conejo A, Carrion M, Morales J (1999) Decision making under uncertainty in electricity markets, 2nd edn. Elsevier, London
2. Gazafroudi A (2017) A novel stochastic reserve cost allocation approach of electricity market agents in the restructured power systems, Electr Power Syst Res pp 223–236
3. Wu L, Shahidehpour M, Li Z (2012) Comparison of scenario-based and interval optimization approaches to stochastic SCUC. IEEE Trans Power Syst 27(2):913–921
4. Morales-Espana G, Ramos A, Garcia-Gonzalez J (2014) An MIP formulation for joint market clearing of energy and reserves based ramp-scheduling, IEEE Trans Power Syst 29(1)
5. Xiong P, Jirutitijaroen P (2013) A stochastic optimization formulation of unit commitment with reliability constraints, IEEE Trans Smart Grid 4(4)
6. Ye H, Ge Y, Shahidehpour M, Li Z (2017) Uncertainty marginal price, transmission reserve, and day-ahead market clearing with robust unit commitment, IEEE Trans Power Syst 32(3)
7. Ye H, Li Z (2016) Robust security-constrained unit commitment and dispatch with recourse cost requirement, IEEE Trans Power Syst 31(5)
8. Vlachos A, Biskas P (2016) An integrated intuitive exchange- and flow-based market clearing model, IEEE Trans Power syst 31(5)
9. Chatzigiannis D, Biskas P, Dourbois G (2017) European-type electricity market clearing model incorporating PUN orders, IEEE Trans Power Syst 32(1)
10. Abbaspourtorbati F, Conejo A, Wang J, Cherkaoui R (2017) Three- or two-stage stochastic market clearing algorithm, IEEE Trans Power Syst 32(4)

Generator Ranking Based on Singular Value Decomposition for Voltage Stability Assessment

Shreya D. Bhanushali and Bhavik N. Suthar

Abstract Static voltage stability analysis is an essential requirement for highly stressed power system particularly when operated in restructured environment. In this paper, generator ranking has been done for voltage stability assessment. Singular value decomposition method is used for generator ranking from stability point of view. The reduced Jacobian matrix is required in SVD method. Therefore, the reduced Jacobian matrix is obtained using NR load flow method. The generator has been ranked using minimum singular value of reduced Jacobian matrix. After ranking, the generator optimization has been done to maximize the value of the SVD so that the system can become more stable. Exhaustive search method has been used for optimization. The voltage magnitude and transformer tap changer have been used as control variable for optimization. Because of the optimization, the active power losses have been reduced and the stability of the power system has been improved. The ranking obtained can be used to provide reactive power support during the highly stressed power system operating condition.

Keywords Voltage stability · Generator ranking · Reactive power

1 Introduction

Nowadays, the demand of power in power system is increased gradually which leads the power system to operate close to their operating limit conditions; when the power system is not able to meet the demand for reactive power, the voltage instability occurs. Therefore, it is necessary to determine the steady-state voltage stability of the power system for operation and planning of the system. Voltage stability is the ability of the system to maintain the voltage of all buses within their limit [1]. During the analysis of voltage stability in power system, we consider two aspects which are mechanism and proximity [2]. The Mechanism gives information

S. D. Bhanushali (✉) · B. N. Suthar
Department of Electrical Engineering, Government Engineering College, Gujarat Technological University, Bhuj, India
e-mail: bhanushalishreya1996@gmail.com

A. Mehta et al. (eds.), *Advances in Electric Power and Energy Infrastructure*, Lecture Notes in Electrical Engineering 608,
https://doi.org/10.1007/978-981-15-0206-4_7

about which are the key factors that contributes more to make the system unstable. By using this information, we modify the system to make system reliable and stable. Voltage security is measured by proximity. We always examine a large number of contingency scenarios and a wide range of system conditions during the analysis of voltage stability.

Normally, the power system is divided into three parts: generation, transmission and distribution. Substantially, synchronous generator has used for generation, maintaining the reliability, stability of the power system and also provide active and reactive power to the load. Synchronous generator plays a most important role in the system. In power system, all generators do not have equal importance in a power system; therefore "to know which generator plays an important role in operation in power system," we give rank to the generator. It is called generator ranking. Division of importance and less importance generator based on participation coefficient given in [3]; by using this, we know the important generator in power system operation. The importance of the generator is depending upon many factors like size, cost, location, reactive and active power output. By knowing the importance of the generator in system, we redispatch the generation of generator and make our system more convenient and stable.

There are three methods reported in [4] to rank the generators and rank the generator using modal analysis described in [5]. This paper describes singular value decomposition method for generator ranking and knows the importance of generator in system. After ranking the generator, we do optimization of the system and the objective of optimization is minimization of the cost, minimization of the losses, increase in the voltage stability, etc. There are many methods for optimization like genetic algorithm, fuzzy set theory, economical load dispatch, gradient method, simulated annealing, exhaustive search method.

Here, we use exhaustive research method for optimization. This is a very simple method compared to another optimization method. Here, we use a value of the SVD as an objective function in optimization. Reason for doing an optimization is to enhancing the value of SVD of the system and reduced losses of the system to make the system more stable.

2 Generator Ranking

In this paper for generator ranking, we removed generator sequentially except slack bus generator. While removing the generator, the power balanced between load and generator has been maintained by increasing the generation of remaining generation pro rata. By this, we can know the effect of outage generator on the system. Here we use singular value decomposition method for generator ranking. The reduced jacobian describe in [2] and for jacobain require Newton Raphson method describe in [6] has been used.

2.1 Reduced Jacobian Matrix

Matrix form of power voltage equation in NR load flow is given as below.

$$\begin{bmatrix} \Delta P \\ \Delta Q \end{bmatrix} = \begin{bmatrix} J_{P\theta} & J_{PV} \\ J_{Q\theta} & J_{QV} \end{bmatrix} \begin{bmatrix} \Delta\theta \\ \Delta V \end{bmatrix} \tag{1}$$

ΔQ = incremental change in bus reactive power injection.
$\Delta\theta$ = incremental change in bus voltage angle.
ΔP = incremental change in bus real power.
ΔQ = incremental change in bus reactive power injection.
ΔV = incremental change in bus voltage magnitude.

Jacobian matrix is $J = \begin{bmatrix} J_{P\theta} & J_{PV} \\ J_{Q\theta} & J_{QV} \end{bmatrix}$
By substituting $\Delta P = 0$ in Eq. (1)

$$\begin{bmatrix} 0 \\ \Delta Q \end{bmatrix} = \begin{bmatrix} J_{P\theta} & J_{PV} \\ J_{Q\theta} & J_{QV} \end{bmatrix} \begin{bmatrix} \Delta\theta \\ \Delta V \end{bmatrix}$$

i.e.,

$$\Delta\theta = -J_{PV} J_{P\theta}^{-1} \Delta V$$

$$\Delta Q = J_{QV}\Delta V + J_{Q\theta}\Delta\theta \tag{2}$$

$$\Delta Q = (J_{QV} - J_{Q\theta} J_{P\theta}^{-1} J_{PV})\Delta V \tag{3}$$

$$J_{\mathrm{R}} = (J_{QV} - J_{Q\theta} J_{P\theta}^{-1} J_{PV}) \tag{4}$$

where

J_{R} = reduced Jacobian matrix.

Using Eq. (4), we get reduced Jacobian matrix J_{R} which represents the linearized relationship between the incremental changes in bus voltage ΔV and bus reactive power injection. J_{R} is called the reduced Jacobian matrix of the system. Matrix J_{R} is giving a direct relation between the reactive power and the bus voltage magnitude.

2.2 Singular Value Decomposition (SVD)

The SVD equation is given in [4]. The real squared matrix J_R has an SVD as

$$J_R = \mathrm{VSU}^T = \sum_{j=1}^{n} v_j \sigma_j u_j^T \tag{5}$$

where

V and U are orthogonal matrixes, and dimension is $n \times n$.
v_j is left and u_j is right singular vector.
S is diagonal matrix.

In matrix S, diagonal element is usually greater than or equal to zero. In SVD method, generators were removed individually from the system except slack bus generator from the system and removable generator generation is balanced using pro rata corresponding to reduced Jacobian matrix along with SVD factorizations which were calculated following removal of each generator. For each case, the smallest singular value is recorded. Now, arrange the value of SVD of each generator in ascending order. The generator which comes at the top of the list is most important generator in the system.

2.3 Flowchart of Generator Ranking

Flowchart of generator ranking is as above. Here, first we read the system data and then removed generator of the system except slack bus generator from the system there for the removable generator bus works like a load bus and removable generator generation is distributed to another generator using pro rata. Then, run the NR load flow to count the value of SVD of removable generator. Take a small value of SVD. Similarly, remove generator individually and calculate the value of SVD. Then, arrange the value of SVD in ascending order and rank the generator (Fig. 1).

3 Optimization of SVD Using Appropriate Control Variable

For optimization of SVD, we use an exhaustive search method. Compared to another search method, it is the simplest method. Mathematically by calculating the function value, the optimal function is bracketed. Normally, start the searching from the lower bound on the variable and three consecutive function values are compared at time based on the assumption of unimodality of the function. After, the searching has

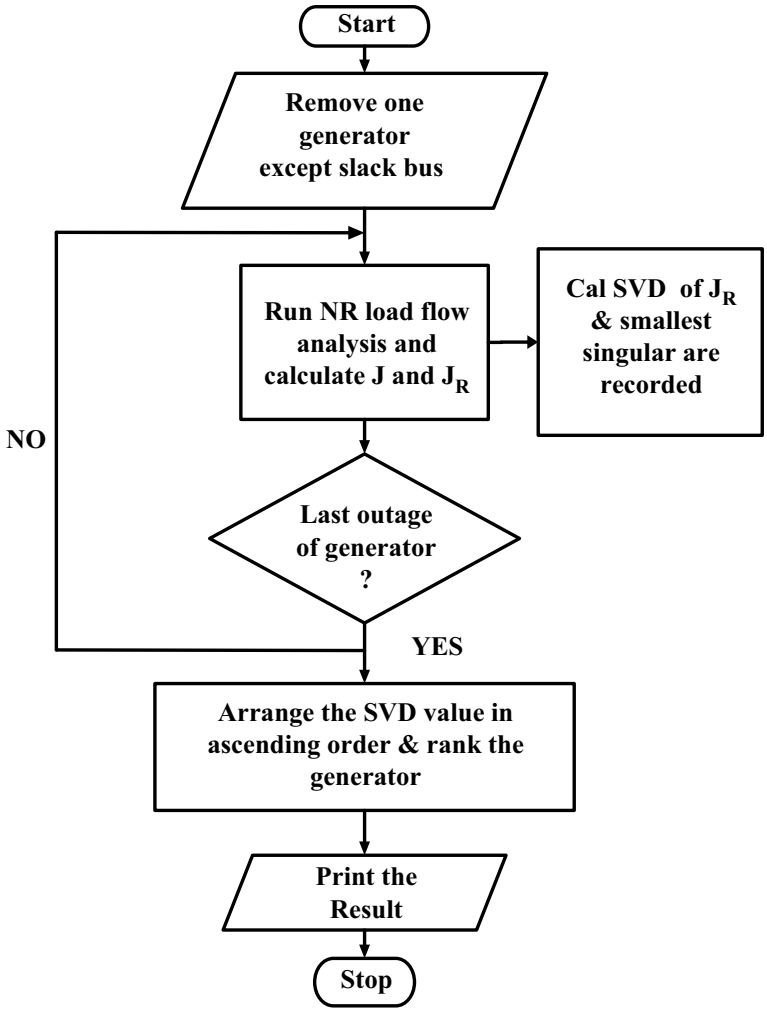

Fig. 1 Flowchart of GR

stopped or continued by replacing one of three points with new point based on outcomes of comparison.

In this case, our optimization function is value of SVD, and we consider a transformer tap change magnitude and voltage of generator bus as control variable. The effect of transformer tap changer on voltage stability is given in [7]. After ranking the generator, we do small change in generator bus voltage in generator ranking order and magnitude of transformer tap changer for individual operating condition in such a way that the value of SVD of outage generator is enhancing and losses of that system are decreasing.

4 Test System

39 Bus, 10 Machine new England test system show in Fig. 2 we use to examine the SVD ranking method. The 39 bus new England bus data and figure mention in [8]. This test system consists of 10 generators, 29 load buses and 46 transmission lines. Singular value decomposition method is successfully applied in this New England. We have used a power flow program.

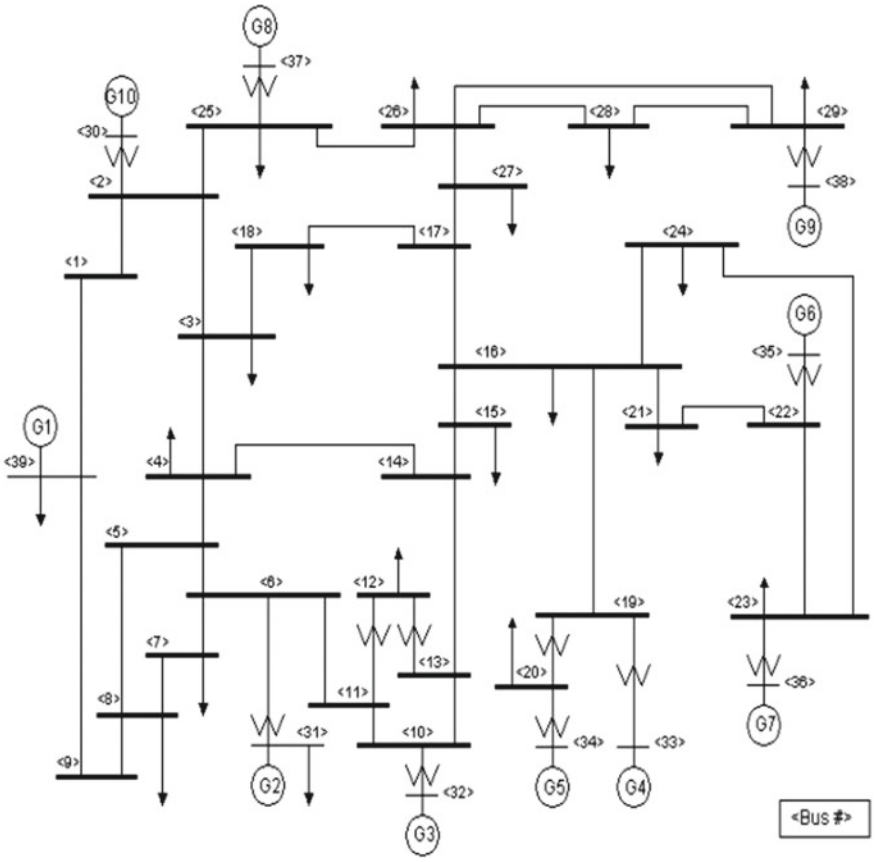

Fig. 2 New England power system

5 Result and Discussion

5.1 Result of Generator Ranking

Table 1 shows result of generator ranking. We remove the 1000 MW generator from the system, distribute this 1000 MW on generator number 10 and change the generation from 250 MW to 1250 MW. We choose this one generator to transfer the 1000 MW generation. Because when we shift the 1000 MW generation on generator number 10, the loss of the system is low compared to another generator changeable generation; therefore, we shift outage generator 1000 MW to generator number 10. Shifting the removable generator generation on other generator is different for different generator outage. See in Table 1 during the outage of 830 MW we shift the generation 830 MW on generator number 1, 10 and 8. During the outage of 1000 MW generator and distribution of its generation using pro rata, the value of the SVD is 4.2863 and power loss is 77.163 MW. In this way, we remove generator individually and find the value of SVD and power loss for individual operating condition. Result is described in Table 1. So, in all this process the value of SVD without 1000 MW generator is small compared to all generators. Therefore, 1000 MW generator is inserted at top of the list and it is most important generator in 39-bus system to maintain the stability. In the table, we go downward and the value of SVD is increasing. The highest value of SVD is 9.1088 whose generator ranks 9 and generation is 508 MW which importance is less in the system compared to another generator.

5.2 Change the Control Variable of 39-Bus System for Optimization

System without generator number 1, P_G: 1000 MW, Rank: 1
System without generator number 9, P_G: 830 MW, Rank: 2
System without generator number 3, P_G: 650 MW, Rank: 3
System without generator number 6, P_G: 650 MW, Rank: 4
System without generator number 10, P_G: 250 MW, Rank: 5
System without generator number 4, P_G: 632 MW, Rank: 6
System without generator number 8, P_G: 540 MW, Rank: 7
System without generator number 7, P_G: 560 MW, Rank: 8
System without generator number 5, P_G: 508 MW, Rank: 9.

Table 1 Result of generator ranking

Series no.	System w/o gen. no.	No. of PV bus at which gen. is connected	P_G of outa. gen. (MW)	Remaining generator			Reduced Jacobian SVD of outage gen.	Gen. ranking	P loss (MW)
				No.	Given P_G (MW)	Change in P_G (MW)			
1	1	39	1000	10	250	1250	4.2863	1	77.163
2	9	38	830	1	1000	1207.5	4.4161	2	50.367
				10	250	665			
				8	540	747.5			
3	3	32	650	1	1000	1350	5.8163	3	43.199
				10	250	300			
4	6	35	650	1	1000	1325	8.1190	4	41.443
				10	250	412.5			
				7	560	722.5			
5	10	30	250	1	1000	1250	8.5575	5	42.870
6	4	33	632	1	1000	1442.4	8.7520	6	39.747
				10	250	281.6			
				5	508	666			
7	8	37	540	1	1000	1270	8.8780	7	39.731
				10	250	520			
8	7	36	560	1	1000	1392	8.9931	8	38.828
				10	250	278			
				6	650	790			
9	5	34	508	1	1000	1304.8	9.1088	9	41.619
				10	250	402.4			
				4	632	682.81			

5.3 Result of Optimization

In Table 1, we obtain the result of generator ranking of 39-bus system generation. After ranking the generator, we do optimization of the system by exhaustive search method to increase the value of SVD and reduce the P loss of the system. For optimization, we change the value of voltage magnitude and tap changer transformer; see in Tables 2, 3, 4, 5, 6, 7, 8, 9, 10, 11, 12, 13, 14, 15, 16, 17, 18 and 19. For optimization after outage of the most importance generator 1000MW, we increase the value of voltage magnitude of all generator buses except slack bus generator in ranking order. See in Table 2 the magnitude of rank 2 generator increase 1.0265 to 1.0165, 3rd rank generator is 0.9831 to 0.985 similarly we change the voltage magnitude of generator bus voltage by 0.1, 0.001 and increase and decrease by 0.1 of some tap changer transformer value. 39-bus system has 12 tap changers in which during 1000 MW outage condition 6 tap changer values are changed to optimize the result and the remaining 6 are not more effective to enhance the stability of system. In Table 20, the value of SVD is increasing from 4.2863 to 4.3388 and the P loss

Table 2 Change the voltage

Change in voltage of remaining generator				
Remaining generator			Given V (p.u)	Change in V (p.u)
No.	Rank	Generation		
9	2	830	1.0265	1.0165
3	3	650	0.9831	0.985
6	4	650	1.0493	1.0499
10	5	850	1.0475	1.0482
4	6	632	0.9972	0.9975
8	7	940	1.0278	1.0285
7	8	560	1.06	1.06
5	9	508	1.0123	1.0223

Table 3 Change the transformer tap

Change in transformer tap		
Tap between two transmission lines	Given value of transformer tap	Changed value of transformer tap
T(6–31)	1.07	1.08
T(10–32)	1.07	1.075
T(19–33)	1.07	1.08
T(23–36)	1	0.99
T(25–37)	1.025	1.026
T(20–34)	1.009	1

Table 4 Change the voltage

Change in voltage of remaining generator				
Remaining generator			Given V (p.u)	Change in V (p.u)
No.	Rank	Generation		
1	1	1207.5	1.03	1.04
3	3	650	0.9831	0.9931
6	4	650	1.0493	1.0593
10	5	665	1.0475	1.0495
4	6	632	0.9972	0.9999
8	7	747.5	1.0278	1.0378
7	8	560	1.06	1.06
5	9	508	1.0123	1.0123

Table 5 Change the transformer tap

Change in transformer tap		
Tap between two transmission lines	Given value of transformer tap	Changed value of transformer tap
T(6–31)	1.07	1.08
T(10–32)	1.07	1.08
T(19–33)	1.07	1.08
T(22–35)	1.025	1.026
T(23–36)	1	1.01
T(25–37)	1.025	1.026

Table 6 Change the voltage

Change in voltage of remaining generator				
Remaining generator			Given V (p.u)	Change in V(p.u)
No.	Rank	Generation		
1	1	1350	1.03	1.035
9	2	830	1.0265	1.0295
6	4	650	1.0493	1.0499
10	5	300	1.0475	1.0395
4	6	632	0.9972	1
8	7	540	1.0278	1.0378
7	8	560	1.06	1.06
5	9	508	1.0123	1.0223

Table 7 Change the transformer tap

Change in transformer tap		
Tap between two transmission lines	Given value of transformer tap	Changed value of transformer tap
T(6–31)	1.07	1.075
T(19–33)	1.07	1.08
T(20–34)	1.07	1.08
T(23–26)	1.009	1
T(22–35)	1.025	1.026
T(25–37)	1.025	1.026
T(29–38)	1.025	1.026

Table 8 Change the voltage

Change in voltage of remaining generator				
Remaining generator			Given V (p.u)	Change in V(p.u)
No.	Rank	Generation		
1	1	1325	1.03	1.04
9	2	830	1.0265	1.0365
3	3	650	0.9831	0.9891
10	5	412.5	1.0475	1.0375
4	6	632	0.9972	1.0072
8	7	540	1.0278	1.0378
7	8	722.5	1.06	1.06
5	9	508	1.0123	1.0223

Table 9 Change the transformer tap

Change in transformer tap		
Tap between two transmission lines	Given value of transformer tap	Changed value of transformer tap
T(6–31)	1.07	1.08
T(10–32)	1.07	1.075
T(19–33)	1.07	1.08
T(25–37)	1.025	1.026
T(29–38)	1.025	1.026
T(23–36)	1	1.005

Table 10 Change the voltage

Change in voltage of remaining generator				
Remaining generator			Given V (p.u)	Change in V (p.u)
No.	Rank	Generation		
1	1	1250	1.03	1.035
9	2	830	1.0265	1.0295
3	3	650	0.9831	0.9931
6	4	650	1.0493	1.0499
4	6	632	0.9972	0.998
8	7	540	1.0278	1.0378
7	8	560	1.06	1.06
5	9	508	1.0123	1.0223

Table 11 Change the transformer tap

Change in transformer tap		
Tap between two transmission lines	Given value of transformer tap	Changed value of transformer tap
T(6–31)	1.07	1.08
T(10–32)	1.07	1.08
T(19–33)	1.07	1.08
T(20–34)	1.009	1
T(22–35)	1.025	1.026
T(29–38)	1.025	1.026

Table 12 Change the voltage

Change in voltage of remaining generator				
Remaining generator			Given V (p.u)	Change in V (p.u)
No.	Rank	Generation		
1	1	1442.4	1.03	1.035
9	2	830	1.0265	1.0275
3	3	650	0.9831	0.9931
6	4	650	1.0493	1.0593
10	5	281.6	1.0475	1.0375
8	7	540	1.0278	1.0378
7	8	560	1.06	1.06
5	9	666	1.0123	1.0223

Table 13 Change the transformer tap

Change in transformer tap		
Tap between two transmission lines	Given value of transformer tap	Changed value of transformer tap
T(6–31)	1.07	1.075
T(10–32)	1.07	1.075
T(19–33)	1.07	1.08
T(20–34)	1.009	1
T(22–35)	1.025	1.026
T(23–36)	1	1.01
T(29–38)	1.025	1.026

Table 14 Change the voltage

Change in voltage of remaining generator				
Remaining generator			Given V (p.u)	Change in V (p.u)
No.	Rank	Generation		
1	1	1270	1.03	1.035
9	2	830	1.0265	1.0299
3	3	650	0.9831	0.9931
6	4	650	1.0493	1.0499
10	5	520	1.0475	1.0465
4	6	632	0.9972	0.9982
7	8	560	1.06	1.06
5	9	508	1.0123	1.0223

Table 15 Change the transformer tap

Change in transformer tap		
Tap between two transmission lines	Given value of transformer tap	Changed value of transformer tap
T(6–31)	1.07	1.08
T(19–33)	1.07	1.08
T(22–35)	1.025	1.026
T(29–38)	1.025	1.026
T(19–20)	1.06	1.05

is decreasing from 77.163 MW to 76.761 MW of outage generator 1000 MW. This way we do optimize the result of all outage generator and obtain the result; see in Table 20.

Table 16 Change the voltage

Change in voltage of remaining generator				
Remaining generator			Given V (p.u)	Change in V (p.u)
No.	Rank	Generation		
1	1	1392	1.03	1.035
9	2	830	1.0265	1.0295
3	3	650	0.9831	0.9931
6	4	790	1.0493	1.0499
10	5	278	1.0475	1.0335
4	6	632	0.9972	1.0072
8	7	540	1.0278	1.0338
5	9	508	1.0123	1.0123

Table 17 Change the transformer tap

Change in transformer tap		
Tap between two transmission lines	Given value of transformer tap	Changed value of transformer tap
T(6–31)	1.07	1.08
T(19–33)	1.07	1.08
T(20–34)	1.009	1
T(22–35)	1.025	1.026
T(25–37)	1.025	1.026

Table 18 Change the voltage

Change in voltage of remaining generator				
Remaining generator			Given V (p.u)	Change in V (p.u)
No.	Rank	Generation		
1	1	1304.8	1.03	1.04
9	2	830	1.0265	1.0285
3	3	650	0.9831	0.9931
6	4	650	1.0493	1.0499
10	5	402.4	1.0475	1.0375
4	6	682.8	0.9972	1
8	7	540	1.0278	1.0378
7	8	560	1.06	1.06

Table 19 Change the transformer tap

Change in transformer tap		
Tap between two transmission lines	Given value of transformer tap	Changed value of transformer tap
T(6–31)	1.07	1.08
T(10–32)	1.07	1.075
T(19–33)	1.07	1.08
T(22–35)	1.025	1.026
T(23–36)	1	1.01
T(25–37)	1.025	1.026
T(29–38)	1.025	1.026

Table 20 Comparison of result after and before optimization

Series no.	System w/o gen. no.	Gen. rank	No. of PV bus at which gen. is connected	P_G of Outa. gen. (MW)	Before optimization value of		After optimization value of	
					SVD	P loss (MW)	SVD	P loss (MW)
1	1	1	39	1000	4.2863	77.163	4.3388	76.761
2	9	2	38	830	4.4161	50.367	4.4959	49.147
3	3	3	32	650	5.8163	43.199	5.8321	42.683
4	6	4	35	650	8.1190	41.443	8.1585	40.575
5	10	5	30	250	8.5575	42.870	8.5946	42.215
6	4	6	33	632	8.7520	39.747	8.8092	39
7	8	7	37	540	8.8780	39.731	8.9131	39.269
8	7	8	36	560	8.9931	38.828	9.0217	38.238
9	5	9	34	508	9.1088	41.619	9.1387	40.871

6 Conclusion

In this paper, using SVD we compute the smaller singular value of a reduced Jacobian matrix and get an important generator of the system. By using this method, we can know which generator is important for system stability point of view. After optimization, the value of SVD has been improved and active power loss of the system has been reduced. The method has been implemented on New England 39-bus system, it is observed that the generator can be ranked in view of voltage stability, and according to the ranking reactive power support can be provided for voltage stability enhancement. The optimization to maximize the SVD can help in improving the stability by changing the voltage magnitude and transformer tap settings.

References

1. Taylor CW (1994) Power system voltage stability. McGraw-Hill, New York
2. Kundur P, Gao B, Morison GK (1992) Voltage stability evaluation using modal analysis. IEEE Trans Power Syst 7(4):1529–1542
3. Raoufi H, Kalantar M (2008) Reactive power rescheduling with generator ranking for voltage stability improvement. IEEE, Iran
4. Alhasawi FB, Milanovic JV (2010) Generator ranking index. IEEE, Brazilian, 1–6 Aug 2010
5. Huang Z, Bao L, Xu W (2003) Generator ranking using modal analysis. IEEE Proc Gen Transm Distrib 150(6):716–719
6. Saadat H (1999) Power system analysis. McGraw-Hill, New York
7. Swe PL, Swe W, Lin KM (2011) Effect of tap changing transformer and shunt capacitor on voltage stability enhancement of transmission networks. Int J Electr Comput Eng 5(3)
8. New England 39 bus system data. https://www.reserchgate.net

Optimal Power Flow in Power Networks with TCSC Using Particle Swarm Optimization Technique

Patil Monal, Leena Heistrene and Vivek Pandya

Abstract Optimal power flow (OPF) plays an important role in power system operation and control. The OPF mainly aims to optimize the certain objective function such as minimizing the generation fuel cost, while at the same time satisfying load balance constraints and bound constraints. Particle swarm optimization (PSO) technique is an artificial intelligence-based technique. PSO technique is used to optimize the parameters like bus voltages, angles, real power generation fuel cost and the reactance values of TCSC. In this paper, the TCSC is incorporated using reactance model at fixed locations and power flow studies are carried out using Newton–Raphson method. The proposed approach is examined on modified IEEE 14-bus test system with and without TCSC device. The results are compared to the performance of the overall power network in the presence and absence of TCSC, and it is representing an analysis in order to show effectiveness of presented work.

Keywords Optimal power flow · Optimization technique · Artificial intelligence · Particle swarm optimization

1 Introduction

Industrialization, and thereby economic structure, of any country heavily relies on electricity. In the current scenario, power transmission lines are seen to be erratically loaded and some lines are heavily stressed with overloading while others are extremely underloaded. Hence, it becomes necessary to continuously monitor the power flows and all transmission line parameters. Power flow analysis gives information about the bus bar values of voltage magnitude and phase angle and real and reactive power in the lines. In this paper in the application of load flow analysis is exploited it to optimal power flow (OPF) [1].

P. Monal (✉) · L. Heistrene · V. Pandya
Electrical Engineering Departments, Pandit Deendayal Petroleum University, Raisan, Gandhinagar, Gujrat, India
e-mail: patilmonal123@gmail.com

A. Mehta et al. (eds.), *Advances in Electric Power and Energy Infrastructure*, Lecture Notes in Electrical Engineering 608,
https://doi.org/10.1007/978-981-15-0206-4_8

The operation of power industry is strongly influenced by the competitive nature of its market. The main ideology of OPF has gained approaching its application to power system solution [2]. Power flow plays a vital role while studying the performance of a system. OPF optimizes the power flow in the power network subject to certain equality and inequality constraints considering the prime objective in question. The OPF problem can solve nonlinear and multimodel optimization problems. Accordingly, conventional and modern optimization techniques, such as artificial intelligence (AI)-based techniques can be used. Conventional approach includes linear programming, quadratic programming and Newton-based search methods [3].

In recent years, several artificial intelligence techniques have been proposed for optimizing power system problems. Some of the techniques include genetic algorithm, differential evolution, artificial bee colony and ant colony optimization [4–7]. In this paper, particle swarm optimization (PSO) technique is used. It is evolutionary-based heuristic optimization technique. This technique was developed in 1995 by Dr. Eberhart and Dr. Kennedy. PSO is solving complex power system-based optimization problems. It is depending on social behavior for swarm intelligence by the flock of bird and school of fish [8]. Here, each particle changes its position by flying around in a multidimensional search space and gives optimum best value based on a certain set of algorithmic rules.

The current scenario indicates that the demand for the power transfer is increasing day by day. The power system becomes increasingly more difficult to operate and insecure with unscheduled power flows, thus handling the losses. FACTS device is effectively improving voltage profile, reducing line loading, improving power factor, reducing line loss, maximizing benefits of device. Flexible AC transmission system (FACTS) enhances the power flow capabilities, improves power quality and minimizes losses. In this paper, a series FACTS device, thyristor controlled series capacitor (TCSC), is implemented.

The overall flow of this paper is as follows. Section 2 focuses on the mathematical modeling of the FACTS device. Section 3 discusses the OPF problem formulation, while Sect. 4 discusses the implementation of OPF using PSO. Results and discussion are described in Sect. 5.

2 Static TCSC Modeling

Thyristor controlled series capacitor (TCSC) is one of the most effective series FACTS devices. TCSC can change line impedance smooth and flexible control with much faster response. The series FACTS device is implemented on transmission line based on power injection model. Transmission line is represented by its lumped π equivalent parameters connected between the two buses. During the steady-state condition, the TCSC can be implemented on Newton–Raphson method using static reactance, X_c.

The real and reactive power injections due to TCSC at buses m and n are given by the following equation [9].

$$P_m^F = V_m^2 \Delta G_{\text{mn}} - V_m V_n[\Delta G_{\text{mn}} \cos(\delta_m - \delta_n) + \Delta B_{\text{mn}} \cos(\delta_m - \delta_n)] \quad (1)$$

$$Q_m^F = -V_m^2 \Delta B_{\text{mn}} - V_m V_n[\Delta G_{\text{mn}} \cos(\delta_m - \delta_n) + \Delta B_{\text{mn}} \cos(\delta_m - \delta_n)] \quad (2)$$

$$P_n^F = V_n^2 \Delta G_{\text{mn}} - V_m V_n[\Delta G_{\text{mn}} \cos(\delta_m - \delta_n) + \Delta B_{\text{mn}} \cos(\delta_m - \delta_n)] \quad (3)$$

$$Q_n^F = -V_n^2 \Delta B_{\text{mn}} - V_m V_n[\Delta G_{\text{mn}} \cos(\delta_m - \delta_n) + \Delta B_{\text{mn}} \cos(\delta_m - \delta_n)] \quad (4)$$

$$\Delta G_{\text{mn}} = \frac{X_c r_{\text{mn}} (X_c - 2X_{\text{mn}})}{(r_{\text{mn}}\, 2 + X_{\text{mn}}\, 2)[r_{\text{mn}}\, 2 + (X_{\text{mn}} - X_c)]} \quad (5)$$

$$\Delta B_{\text{mn}} = \frac{X_c((r_{\text{mn}}\, 2 + X_{\text{mn}}\, 2 - 2\, X_c X_{\text{mn}})}{(r_{\text{mn}}\, 2 + X_{\text{mn}}\, 2)[r_{\text{mn}}\, 2 + (X_{\text{mn}} - X_c)]} \quad (6)$$

3 Optimal Power Flow Problem Formulation

Optimal power flow (OPF) is one of the most vital tools in power system, which is representing the optimization problem. The main objective of the OPF problem could be minimizing of generation cost and power losses or maximization of line efficiency. This objective is to be fulfilled subject to physical constraints of the system. Some of the constraints show the bounds of the decision variables such as active and reactive power generation limit and the generator bus voltage magnitude.

In this paper, the OPF problem is the formulation as a nonlinear optimization problem with different bound constraints and load balance constraints.

3.1 Objective Function

The main objective of optimal power flow is the reduction of the fuel cost generation of electricity within the permissible range of certain set of system constraints.

$$\text{Minimize}(F_T) = \sum_{m=1}^{Ng} F_m(P_{\text{Gm}}) \quad (7)$$

$$F_m(P_{\text{Gm}}) = a_m(P_{\text{Gm}}^2) + b_m(P_{\text{Gm}}) + c_m\ (\$/h) \quad (8)$$

Where, $F_m\ (P_{\text{Gm}})$ is the generation cost of the mth generator
P_{Gm} is the real power output generated at mth generator in MW
a_m, b_m and c_m are the cost coefficients of mth generator
Ng is the total number of generators.

3.2 Load Balance Constraints

The load balance constraint described in this subsection is an equality constraint. Under the steady-state operation, the power balance that exists in the power system network is calculated using power flow equation.

$$P_m(\theta, V) - P_{\mathrm{Gm}} - P_{\mathrm{Dm}} = 0 (m = 1 \ldots N) \tag{9}$$

$$Q_m(\theta, V) - Q_{\mathrm{Gm}} - Q_{\mathrm{Dm}} = 0 (m = 1 \ldots N) \tag{10}$$

In power balance equation in TCSC equation implemented in line between bus m and bus n, the power balance equation in node m and n are given by,

$$P_m(\theta, V) - P_{\mathrm{Gm}} - P_{\mathrm{Dm}} + P_m^F = 0 \tag{11}$$

$$Q_m(\theta, V) - Q_{\mathrm{Gm}} - Q_{\mathrm{Dm}} + Q_m^F = 0 \tag{12}$$

$$P_n(\theta, V) - P_{\mathrm{Gn}} - P_{\mathrm{Dn}} + P_n^F = 0 \tag{13}$$

$$Q_n(\theta, V) - Q_{\mathrm{Gn}} - Q_{\mathrm{Dn}} + Q_n^F = 0 \tag{14}$$

Here, P_{Gm} and Q_{Gm} are the real and reactive power generations at bus m, while P_{Dm} and Q_{Dm} are the real and reactive power loads at bus m. P_m and Q_m are the net real and reactive powers injected at bus m.

3.3 Bound Constraints

Bound constraints, also referred to as limiting constraints, are inequality constraints that represent the system operation and security limits. Some of the limit constraints include generation limits and voltage limits

$$P_{\mathrm{Gm}}^{\min} \leq P_{\mathrm{Gm}} \leq P_{\mathrm{Gm}}^{\max} \tag{15}$$

where $P_{\mathrm{Gm}}^{\min}$ and $P_{\mathrm{Gm}}^{\max}$ are minimum and maximum real power generation limits of generating unit at bus m.

$$Q_{\mathrm{Gm}}^{\min} \leq Q_{\mathrm{Gm}} \leq Q_{\mathrm{Gm}}^{\max} \tag{16}$$

where $Q_{\mathrm{Gm}}^{\min}$ and $Q_{\mathrm{Gm}}^{\max}$ are minimum and maximum reactive power generation limits of generating unit at bus m.

$$V_m^{\min} \leq V_m \leq V_m^{\max} \tag{17}$$

where $V_m^{\min}$ and $V_m^{\max}$ are minimum and maximum voltage limits at bus m.

$$X_C^{\min} \leq X_C \leq X_C^{\max} \tag{18}$$

where $X_C^{\min}$ and $X_C^{\max}$ are the minimum and maximum limits of TCSC reactance.

4 OPF Using Particle Swarm Optimization Technique

Particle swarm optimization (PSO) is an evolutionary-based heuristic optimization technique. Its techniques depend on swarm intelligence based on the behavior of a flock of birds or a school of fish. Its technique basically depends on particle position and particle velocity. Each decision variable of an optimization problem is referred to as a particle [10]. The best value among the different fitness functions and their respective decision vectors in each iteration is calculated, and the best among them are presented as the global best solution.

Some of the parameters that are predetermined before the application of PSO algorithm include the number of variables, lower and upper bounds, number of iterations, population size, inertia factor and the social and cognitive coefficients. In each iteration, particle position and particle velocity are changed. PSO finds the particle personal best value and particle global best value based on which the position and velocity are updated in every iteration. Objective function is reevaluated with the updated value in each iteration. PSO keeps searching for the best solution till it gets a feasible solution that has minimum value for the objective function.

The particle position and particle velocity of vector N-dimensional search space are expressed in Eqs. (19) and (20).

$$X_m = (x_{m1}, \ldots, x_{\mathrm{mn}}) \tag{19}$$

$$V_m = (v_{m1}, \ldots, v_{\mathrm{mn}}) \tag{20}$$

where X_m is particle position of mth in a search space. V_m is particle velocity of mth in a search space. X_{mn} is particle position of mth in a search space with n particles. V_{mn} is the particle velocity of mth in a search space with n particles.

The particle global best and particle local best obtain in below equation.

$$P\mathrm{best}_m = \left(x_{m1}^{\mathrm{best}}, \ldots, x_{\mathrm{mn}}^{\mathrm{best}}\right) \tag{21}$$

This Eq. (21) in shows $P\mathrm{best}_m$ is the particle personal best value. $x_{\mathrm{mn}}^{\mathrm{best}}$ is the particle personal best mth in a search space value. The position of a particle among other

particle in the population is expressed in Eq. (22). $G\text{best}_m$ is the particle global best value.

$$G\text{best}_m = (x_{m1}^{\text{best}}, \ldots, x_{\text{mn}}^{\text{best}}) \tag{22}$$

In general, X_m^{n+1} is the position of every particle updated at every $(n + 1)$th iteration using the Eq. (23). X_m^n is the particle position mth individual at n iteration.

$$X_m^{n+1} = X_m^n + V_m^{n+1} \tag{23}$$

The V_m^{n+1} is velocity term updated using the equation given in (24). In this equation local best, global best, acceleration coefficient and inertia weight factor parameters are used to evaluate the velocity term for updating of the upcoming particle position [11].

$$V_m^{n+1} = W\, V_m^n + c_1\, \text{rand}_1 \times \left(P\text{best}_m^n - X_m^n\right) + \text{c}_2\, \text{rand}_2 \times \left(G\text{best}_m^n - X_m^n\right) \tag{24}$$

N	Number of iteration
V_m^n	Particle velocity of iteration n
X_m^n	Particle position of iteration n
c_1 and c_2	Acceleration coefficients
w	Inertia weight factor
rand_1 and rand_2	Random number value [0,1].

Inertia weight factor parameter is denoted by w. Inertia weight factor parameter as a function of n iteration is given below.

$$w = w_{\max} - \frac{(w_{\max} - w_{\min})}{\text{max.iter}}\text{iter} \tag{25}$$

where $w_{\max}$ is initial value of inertia weight. $w_{\min}$ is final value of inertia weight max iter is maximum number of iteration and iter is current total iteration in weight factor.

Maximum velocity is expressed following equation.

$$V^{\max} = \frac{(x^{\max} - x^{\min})}{N} \tag{26}$$

where $X^{\max}$ is the maximum particle position. $X^{\min}$ is the minimum particle position. $V^{\max}$ is the maximum velocity. N is the number of intervals.

5 Result and Discussion

The proposed PSO algorithm successfully applies and solves optimal power flow problem incorporating TCSC device on a modified 14-bus system. It was implemented in MATLAB software. The simulation studied is carried out on 7.1 running on Pentium IV, 2.66 GHz and 512 MB RAM system in MATLAB.

The PSO control parameters used for the simulation are summarized: Population size is 25, the number of iteration number is 100, cognitive and social coefficients are 2, and inertia weight coefficient is 0.3–0.95.

5.1 Modified IEEE 14-Bus Power System Network

The modified IEEE 14-bus test system comprises 14 buses. Synchronous machines on 1, 2, 3, 6 and 8 are treated as generator, thereby making them PV bus while the rest are PQ bus. The system has 14 buses with 20 transmission lines and 3 tap-changing transformers. In this paper, twelve control variables have been considered. These variables comprise four generation dispatch variables, five voltage variables associated with the PV buses and three tap-changing transformers. Voltage between 0.95 and 1.06 as far as possible age limit for load bus is 0.95–1.06.

Two case studies have been discussed herewith, wherein case (a) represents power system operation without FACTS device installation while case (b) represents system with TCSC device installed on the line connected between buses 4 and 9.

The series capacitive reactance (X_c) of TCSC is set at 9.375 of transmission line; thus, inductive reactance is 1.625. Table 1 shows the details of the optimal setting of control variables. The installation of TCSC in the network gives the best performance of the system compared to that without FACTS device in terms of reduction in cost of generation and power loss. It also shows that PSO algorithm is able to enhance the system performance while maintaining all control variables and active power output within their limit and in this result.

According to the result, Fig. 1 shows the cost of generation without TCSC. In this result, optimum generation fuel cost is 8105.5 ($/h). Figure 2 shows the result generation fuel cost with TCSC. In this result, optimum generation fuel cost is 8096.9 ($/h). Figures 3 and 4 show active power flow and power loss results for both cases (a) and (b), i.e., with and without TCSC. The optimal solution obtained with TCSC and without TCSC gives generation costs such that shows the annual saving 8.7 ($/h) is observed.

Table 1 Optimal setting of control variables 14-bus system

Control variable	Minimum limits (pu)	Maximum limits (pu)	Without FACTS	With FACTS (TCSC)
P_{G1}	0	3.324	1.789	1.796
P_{G2}	0	1.40	0.377	0.372
P_{G3}	0	1	0.282	0.214
P_{G6}	0	1	0	0
P_{G8}	0	1	0.111	0.220
V_{G1}	0.94	1.06	1.049	1.048
V_{G2}	0.94	1.06	1.027	1.0272
V_{G3}	0.94	1.06	0.985	0.994
V_{G6}	0.94	1.06	0.989	0.990
V_{G8}	0.94	1.06	0.993	1.036
$T_{4–7}$	0.90	1.1	1.0546	1.030
$T_{4–9}$	0.90	1.1	0.941	1.001
$T_{5–6}$	0.90	1.1	0.987	1.014
Best cost ($/h)			8105.5	8096.9
Power loss (pu)			0.0913	0.0904

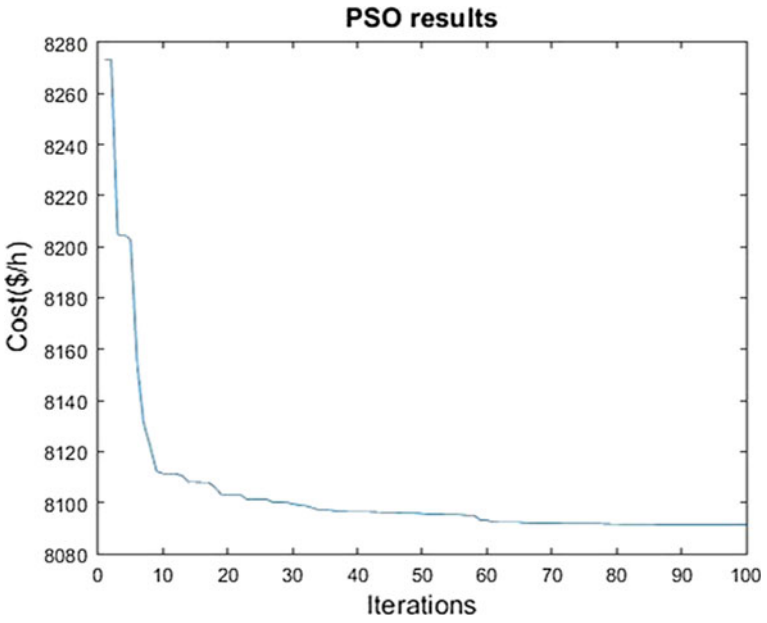

Fig. 1 14-bus system without TCSC cost convergence criterion

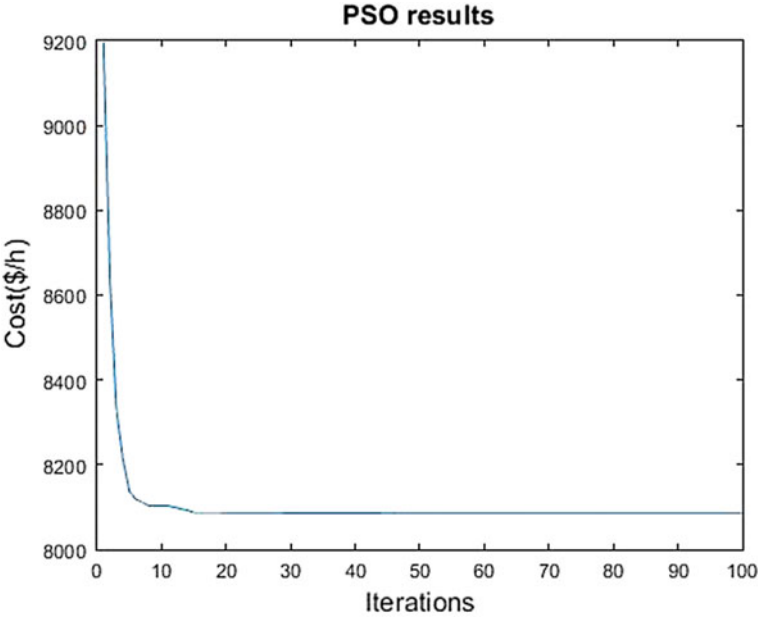

Fig. 2 14-bus system with TCSC cost convergence criterion

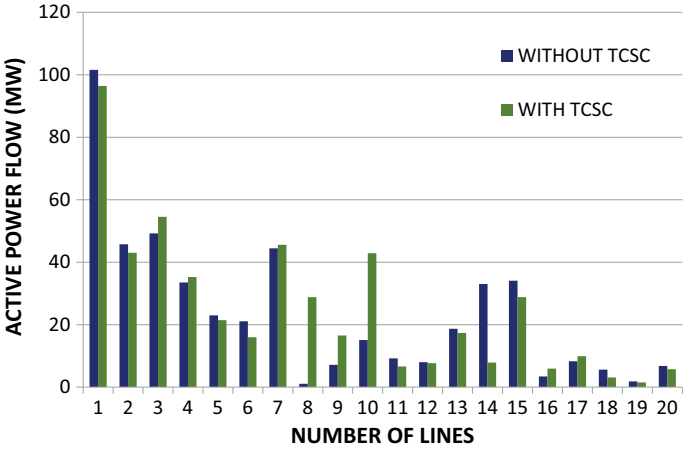

Fig. 3 Active power flow for 14-bus system with and without TCSC

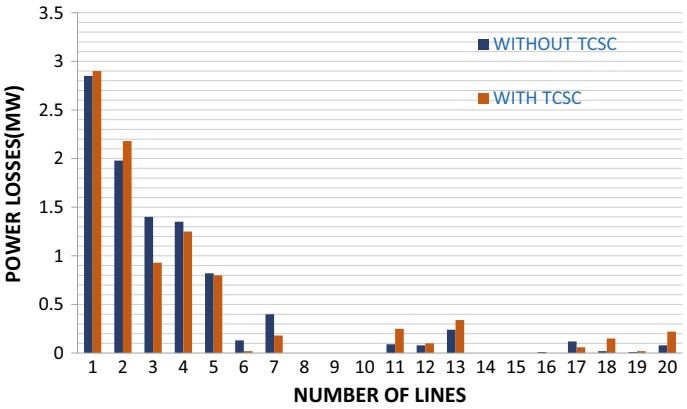

Fig. 4 Power loss for 14-bus system with and without TCSC

6 Conclusion

In this paper, particle swarm optimization-based approach is implemented on the OPF problem under two different scenarios in a power system without TCSC and with TCSC. The proposed approach has been executed on a modified IEEE 14-bus system, and results have been compared. From the results, it is observed that voltage profile has been improved, line losses are also reduced and active power flow is increasing. Optimal generation fuel cost of a 14-bus system has been compared with TCSC and without TCSC, and it is observed that cost is reduced in amount after generator fuel cost minimization. The 14-bus system result approach has been tested and examined with objective function to demonstrate its effectiveness and robustness. The result using the proposed approach was compared to those reported in the literature.

References

1. Christie R, Wollenberg B, Wangensteen I (2000) Transmission management in the deregulated environment. Proc IEEE 88(2):170–195
2. Wood AJ, Wollenberg BF (2005) Power Generation, Operationn and Control, 2nd edn. Wiley, Singapore
3. Pandya KS, Joshi SK (1991) Survey of optimal power flow methods. J Theor Appl Inf Technol
4. Man K, Tang K, Kwong S (1996) Genetic algorithms: concepts and applications [in engineering design]. IEEE Trans Ind Electron 43(5):519–534
5. Nayak MR, Krishnanand KR, Rout PK (2011) Modified differential evolution optimization algorithm for multi-constraint optimal power flow. In: International conference on energy, automation, and signal (ICEAS) Dec 2011, pp 1–7
6. Zhang G (2000) Neural networks for classification: a survey. IEEE Trans Syst Man Cybern Part C: Appl Rev 30(4):451–462

7. Sumpavakup C, Srikun I, Chusanapiputt S (2010) A solution to the optimal power flow using artificial bee colony algorithm. In: Proceeding international conference power system technology, pp 1–5
8. Kumar R, Anand S, Sydulu M (2011) A new multi agent based PSO approaches for optimal power flows with security constraints using different cost functions. In: IEEE international conference on intelligent agent & multi-agent systems, pp 67–72
9. Mithulananthan N, Acharya N (2007) A proposal for investment recovery of FACTS devices in deregulated electricity markets. Electr Power Syst Res 77:695–703
10. Smita P, Vaidya BN (2012) Particle swarm optimization based optimal power flow for reactive loss minimization. In: IEEE conference on electrical, electronics and computer science, pp 4673–1515
11. Karthik M, Reddy A (2014) Particle swarm optimization to solve economic dispatch considering generator constraints. Int J Eng Sci, pp 94–100
12. Verma KS, Singh SN, Gupta HO (2001) Location of unified power flow controller for congestion management. Electr Power Syst Res 58:89–96

Power Loss Minimization and Voltage Improvement with Small Size Distributed Generations in Radial Distribution System Using TOPSIS

Nivedita Naik and Shelly Vadhera

Abstract The distribution system suffers highest power losses, and hence, the voltage profile and stability conditions are highly affected in this part of power system. The aim of this study is to improve the power quality of the power system by minimizing power loss and improving voltage profile using small size distributed generation (DG) system. Due to limitation on land resources and intermittency, the output of renewable-based power plants is low. Hence in this paper, the effect of small size DG units is studied. Technique for order of preference by similarity to ideal solution (TOPSIS), a multi-criteria decision-making (MCDM) algorithm, is used to find the best location based on the size of DG used. The DG units of 250, 500 and 750 KW are used at these locations to check their effect on convergence of voltage profile and minimization in power losses. Only active power injecting DGs have been used in this paper. The results highlight that the small-sized DG systems installed at different locations give better results in terms of power loss and voltage profile than the large-sized DG placed at single locations and in some cases multiple locations as well. IEEE 33-bus radial distribution system has been used to test the method.

Keywords Distributed generation · TOPSIS · Radial distribution system · Power loss · Voltage improvement

1 Introduction

With due pressure on power system to avail electricity continuously, the efficiency of the power system has to be improved. The losses in the transmission and distribution

N. Naik (✉)
School of Renewable Energy and Efficiency, National Institute of Technology, Kurukshetra, Haryana, India
e-mail: niveditanaik92@gmail.com

S. Vadhera
Department of Electrical Engineering, National Institute of Technology, Kurukshetra, Haryana, India
e-mail: shelly_vadhera@nitkkr.ac.in

A. Mehta et al. (eds.), *Advances in Electric Power and Energy Infrastructure*, Lecture Notes in Electrical Engineering 608,
https://doi.org/10.1007/978-981-15-0206-4_9

system are monitored and research on minimizing these losses and improving the voltage profile have been going through all along. One of the methods is by using distributed generation (DG) systems. Distributed generation refers to the small generation units installed at the consumer end or in systems with lower voltage levels like distribution systems due to low power output and low voltage constraints. Supporting the active and reactive power demands near load center can significantly reduce total power in-flow from the source station. This further reduces the heavy current flow in the system which is responsible for contributing the total system losses. The voltage in the system is affected by the reactive power load and losses in the system. Hence, the voltage at the buses is interlinked with the system losses. Also, when the overall DG penetration levels are excessively high, voltage rise issues may be caused due to the reverse power flows [1, 2]. The DGs have a crucial effect on electric losses because of their closeness to the load centers by injection power to the system and compensating the losses [3]. In [1], DG and its effects have been explained in detail.

DG system can be renewable based (solar photovoltaic, small hydro, small wind farms) or non-renewable based (micro-turbine, fuel cells, combined heat and power units (CHP), etc.). Renewable-based generation utilities are preferred these days because of increasing awareness and concern regarding environmental degradation, the ease of electricity generation and vast non-depleting environment-friendly resource availability. Besides, the small DG systems based on renewable resource such as solar energy are more cost-effective than any conventional counterpart for same small unit generation. The demerit with solar-based plant is that the output depends on the surface area where sun's energy is absorbed, i.e., large land area requirement and the non-availability of sunlight round the clock. This results in low efficiency of the power production. Hence for large power production, large land area is required. In this paper, a comparative study has been made between small units of DG installed and comparatively larger units of DG installed as proposed by other methods. Optimal allocation and sizing have been proposed by many methods each of which has its share of own merits and demerits. Some of the analytical methods [4], statistical method [5, 6] and artificial intelligence [7, 8]-based approaches have been used for comparison of results in this study.

2 Objective

To lower the power losses while improving the voltage profile by locating DGs at optimal locations is the main objective of this paper. The decision for DG installation at a particular location is made on the basis of power quality parameters as DG penetration leads to a significant change in node voltages and power flows in the system. The performance parameters or criteria considered for selecting the best location for DG with selected size are

a. Total active power loss
b. Total reactive power loss

c. Voltage deviation.

Power losses
Active power losses are the actual power losses in the conductors which decrease the useful power to be consumed. Reactive power is useful for system stability and power flow in AC circuits. Hence, if reactive power is not enough in the system, it may affect the active power flow as well. The effect of DG placement at each location on power losses is positive, i.e., on locating a DG of a certain size at a bus, the power losses are certainly reduced at different levels. Out of all locations, there are few locations where if DG of a particular size is placed, the power losses are reduced to a maximum extent. The power losses are calculated using load flow analysis.

Node voltage deviation
Injecting power from a DG source reduces system losses and has a positive effect on the voltage profile as well. The node voltages are improved, and hence, the voltage deviation from nominal or rated voltage, i.e., 1 p.u., is reduced. Similar to power losses, DG installed at certain locations gives minimum deviation from ideal conditions. For calculation of node voltage deviation index (VDI), we use the following formula [5]

$$\text{VDI} = \sum_{i=1}^{n} (1 - V_i)^2 \tag{1}$$

where V_i = node voltage.

The objective while integrating DG into the system is to attain minimum total power losses and minimum voltage deviation to achieve maximum benefit from DG integration.

Objective = minimum (total active power loss, total reactive power loss, voltage deviation).

The objective should be attained while adhering to the constraints mentioned below.

2.1 Bus Voltage Limit Constraint

The voltage at each bus must be within permissible range.

$$V_{\min} \leq V_i \leq V_{\max} \text{ i.e. } 0.95 \text{ p.u} \leq V_i \leq 1.05 \text{ p.u} \tag{2}$$

2.2 DG Size Constraint

The DG power injected is considered to be of unity power factor. Hence, there is a limitation on real power injected only. The total real power injected by DG units must not exceed total real power demand in the system.

$$\sum_{i=1}^{N_{\mathrm{DG}}} P_{\mathrm{DG}_i} \leq \sum_{i=1}^{N} P_{\mathrm{load}_i} \tag{3}$$

3 Topsis

MCDM has been used in many fields to design a system to choose the best alternative out of all alternatives available. One of the various methods of MCDM, the technique for order of preference by similarity to ideal solution (TOPSIS), has been used in this paper. It was proposed by Hwang and Yoon in 1981 and further improved in 1987 by Yoon. TOPSIS has been satisfactorily used in many cases to solve multi-criteria or multi-objective problems. [9, 10] discusses more about this method and its application. The ideal solution selection is based on the shortest distance from the ideal solution and farthest from the worst solution. The standard TOPSIS strategy endeavors to pick choices that at the same time have the least distance from the positive-ideal solution and farthest distance from the negative-ideal solution. The steps involved in selecting the best solution using TOPSIS are as under:

1. **Construction of decision table**: A table consisting of performance parameter or criteria values for each alternative is constructed.
2. **Construction of normalized decision matrix**: In this step, all the values in each column are normalized to make a fair comparison between each performance parameter using the following relation.

$$r_{ij} = \frac{f_{ij}}{\sqrt{\sum_{i=1}^{n} \left(f_{ij}\right)^2}} \text{ For } i = 1, 2, 3 \ldots n \text{ and } j = 1, 2, 3 \ldots m \tag{4}$$

   where

   r_{ij} = normalized decision matrix element
   f_{ij} = each element of the decision matrix
   i = number of rows, j = number of columns

3. **Weighted normalized decision matrix**: Each column is multiplied with a respective weight as per preference where the sum of all weights must be equal to 1.

$$V_{ij} = w_j \times r_{ij} \tag{5}$$

where $\sum_{j=1}^{m} w_j = 1$.

4. **Determination of positive-ideal value and negative-ideal value**: Positive-ideal value and negative-ideal value for each column are noted individually and used for calculation of Euclidean distance from ideal values. The positive-ideal value can be maximum or minimum value according to the best value of performance criteria.

$$\text{Positive ideal solution} = [V_{i1}, V_{i2} \ldots V_{in}] \tag{6}$$

$$\text{Negative ideal solution} = \left[V_{j1}, V_{j2} \ldots V_{jn}\right] \tag{7}$$

5. **Calculation of Euclidean distances**: Euclidean distance from positive-ideal value and negative-ideal value for each alternative is calculated using the following equation.

$$d_{j+} = \sqrt{\sum_{i=1}^{n} \left(v_{ij} - v_{i+}\right)^2} \tag{8}$$

$$d_{j-} = \sqrt{\sum_{i=1}^{n} \left(v_{ij} - v_{i-}\right)^2} \tag{9}$$

6. **Calculation of performance index**: Performance index (PI) is calculated for each alternative. The alternative with highest value of PI is the highest ranked and lowest value of PI gives lowest ranked alternative.

$$\text{PI} = \frac{d_{j-}}{d_{j+} + d_{j-}} \text{ where } 0 < \text{PI} < 1 \tag{10}$$

4 Methodology

Using TOPSIS, a trade-off between the performance parameters, i.e., total active power loss, reactive power loss and voltage deviation, is achieved. Table 1 shows table format where TOPSIS is applied and output is obtained in the form of performance index. The first three columns are the inputs which are formed into a table format as shown below, and TOPSIS steps are applied to these three columns. For the calculation of active power loss, reactive power loss and voltage deviation, load flow analysis is performed. The last column that is performance index (PI) is the output, the maximum value of which determines the most desirable bus for DG integration.

For multi-DG placement, the location of the second DG will be based on the effect of first DG installment on performance parameter developed. PI value for

Table 1 Table format showing performance parameters against all buses as alternatives

Alternatives	Performance Parameter as input			Output
	Total active power loss (KW)	Total reactive power loss (KVAr)	Voltage deviation (p.u.)	Performance index (PI)
Bus 1	–	–	–	–
Bus 2				
…	–	–	–	–
Bus (n − 1)				
Bus n	–	–	–	–

each alternative will be re-calculated, and the node with maximum PI value will be selected for second DG installation.

Algorithm for analysis of impact of DG on radial network follows the steps below:

Step 1 Input the line data and load data for power flow analysis.

Step 2 Execute the base case (without DG) power flow analysis on test network and note down measured active power loss, reactive power loss and voltage profile.

Step 3 DG of assumed size (250 KW) is placed at each location to obtain total active power loss, total reactive power loss and voltage profile due to DG placed at that location.

Step 4 VDI is calculated using Eq. 1 and a table is formed consisting of total active power loss, total reactive power loss and VDI due to DG installation at each location.

Step 5 TOPSIS is applied on these three performance parameters calculated in step 3 and 4. The steps followed in TOPSIS are as follows:

Step 5.a. The table formed in step 4 is normalized vertically using Eq. (4).
Step 5.b. Weights are assigned to each criterion, and each element is multiplied with respective weight.
Step 5.c. Euclidean distances are calculated using determined positive-ideal solution and negative-ideal solution.
Step 5.d. Performance index list is generated which gives best location for DG installation. The performance index with highest value is the ideal condition for the purpose.

Step 6 For multiple DG placements, after one DG is installed, step 3 to step 5 is repeated.

Step 7 When DG installations for desired number of times are complete, the process is started afresh keeping unit DG size as 500 KW and then 750 KW, and all the steps above are repeated.

5 Result

IEEE 33-bus radial distribution system is considered for the implementation of this methodology. The total active and reactive load connected to nodes in the system is 3715 KW and 2300 KVAr. The rated voltage of the source station is 12.66 kV. Load flow studies are conducted without any DG source in the system, and total active power loss and reactive power loss are observed to be 201.9 KW and 134.6 KVAr, respectively. All the cases are worked out using MATLAB. Three constant size DG units of rated capacity 250, 500 and 750 KW are used in this study for implementation. The power factor is assumed to be unity.

From the power flow analysis of case without DG, power losses have been recorded, and voltage deviation is calculated using Eq. (1) from the voltage profile obtained. A program is then written using MATLAB which uses loop function and calculates the total power losses and voltage deviation index by placing each DG unit of considered size (first case-250 KW, second case-500 KW, third case-750KW) in each bus from bus no. 2 to bus no. 33 in the 33 bus radial distribution system. The result is tabulated in the format as shown in Table 1, and algorithm of TOPSIS is applied to this table using MATLAB. The output of this algorithm is a performance index list which gives values between 0 and 1 to each node or bus. The weights given to all performance parameter is equal, i.e., 0.33.

Tables 2, 3 and 4 summary the process and show the effect of DG installations using 250, 500 and 750 KW of unit DG. It can be seen that when DG unit of 250 and

Table 2 Effect of DG allocation of unit size 250 KW on 33 bus system

Number of units	Location (bus number)	Each DG size (KW)	Total size (KW)	Active power loss (KW)	Reactive power loss (KVAR)	VDI (p.u.)
1	18	250	250	171.62	113.56	0.09
2	18, 15	250	500	150.14	99.171	0.07
3	18, 15, 33	250	750	126.76	83.371	0.056
4	18, 15, 33, 13	250	1000	114.18	75.095	0.04

Table 3 Effect of DG allocation of unit size 500 KW on 33 bus system

Number of units	Location (bus number)	Each DG size (KW)	Total size (KW)	Active power loss (KW)	Reactive power loss (KVAR)	VDI (p.u.)
1	17	500	500	151.41	100.7	0.07
2	17, 33	500	1000	111.13	74.257	0.04
3	17, 33, 13	500	1500	96.126	64.59	0.02
4	17, 33, 13, 30	500	2000	83.686	57.178	0.01

Table 4 Effect of DG allocation of unit size 750 KW on 33 bus system

Number of units	Location (bus number)	Each DG (KW)	Total size size (KW)	Active power loss (KW)	Reactive power loss (KVAR)	VDI (p.u.)
1	16	750	750	137.83	91.698	0.054299
2	16, 32	750	1500	92.083	61.951	0.022808
3	16, 32, 9	750	2250	84.386	58.022	0.007393
4	16, 32, 9, 28	750	3000	90.125	63.347	0.001331

500 KW is used, the objectives are attained in all four times a new DG is installed while in case of unit DG of 750 KW, power losses and voltage deviation can be seen minimizing till third time of DG installed and values increase in fourth time. Results are desirable when lower values of the performance parameters are attained. Hence for DG unit of 750 KW, a total of three DG units used can give best result and four DG units for case of unit DG of 250 and 500 KW. However, the best and similar result is obtained when four units of 500 KW DG are integrated into the system or three units of 750 KW DG used. At this step, active power losses and reactive power losses decrease by 58% and 57%, respectively. Observing the size, four units of 500 KW make a total of 2000 KW, while three units of 750 KW make 2250 KW. Hence, though less number of DG is used in case of 750 KW, the total DG penetration is increased by 250 KW. It depends upon requirement and resources available to choose the best option.

Figures 1, 2 and 3 show the variation in voltage profile as improvements after DG installations. For case of 500 KW, all the voltages come under permissible limit after third DG installation, while for case of 750 KW, it is achieved after second DG installation. Some locations still have voltages less than 0.95 p.u. even after four DG units of 250 KW are installed.

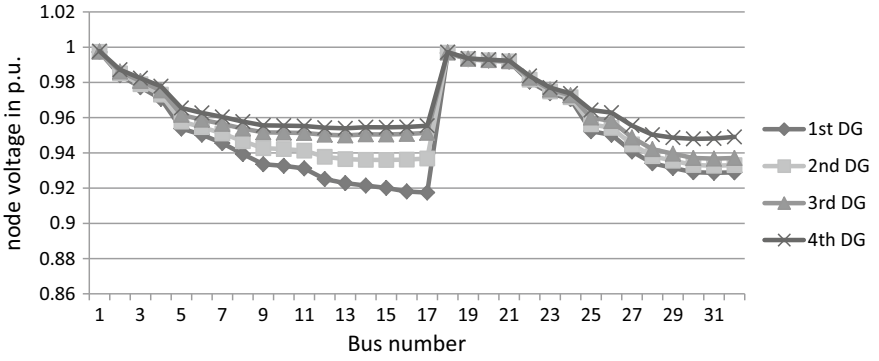

Fig. 1 Voltage profile variation using 250 KW at each installation

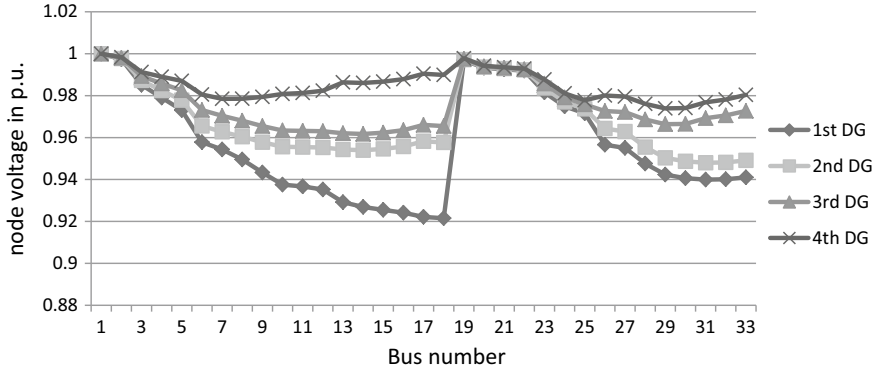

Fig. 2 Voltage profile variation using 500 KW after each DG installation

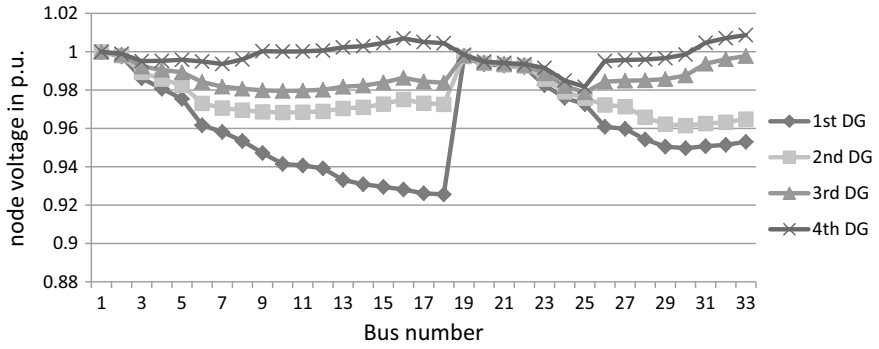

Fig. 3 Voltage profile variation using 750 KW at each installation

Table 5 Comparison with single installment methods

Methods	Location	Unit size (KW)	Total size (KW)	Active power loss (KW)	Saving (KW)	Penetration ($=S_{DG}/S_{LOAD}$) (%)
[11]	18	1000	1000	142.34	59.56	22.88
[12]	6	2380	2380	132.64	69.26	54.47
[4]	6	2490	2490	111.24	90.66	56.99
TOPSIS	**18, 15, 33, 13**	**250**	**1000**	**114.18**	**87.72**	**22.88**
TOPSIS	**17, 33**	**500**	**1000**	**111.13**	**90.77**	**22.88**
TOPSIS	**17, 33, 13, 30**	**500**	**2000**	**83.68**	**118.68**	**45.77**
TOPSIS	**16, 32**	**750**	**1500**	**92.08**	**109.82**	**34.33**

Table 6 Comparison with three DG installation methods

Methods	Location	Unit size (KW)	Total size (KW)	Active power loss (KW)	Saving (KW)	Penetration ($=S_{DG}/S_{LOAD}$) (%)
GA/PSO [7]	32, 16, 11	1200, 863, 925	2988	103.4	98.5	68.38546
QOTLBO [8]	13, 26, 30	1083.4, 1187.6, 1199.2	3470.2	103.4	98.5	79.42142
MOTA [5]	30, 7, 14	1340, 980, 960	3280	96.3	105.6	75.06837
TOPSIS	**18, 15, 33**	**250**	**750**	**126.76**	**75.14**	**17.16**
TOPSIS	**17, 33, 13**	**500**	**1500**	**96.12**	**105.77**	**34.33005**
TOPSIS	**16, 32, 9**	**750**	**2250**	**84.38**	**117.52**	**51.49507**

The cases have been compared with single DG installation methods in Table 5. Methods, involving three DG unit installation, proposed in previous works, have also been compared with respective three DG installation of 250 KW, 500 KW and 750 KW as attained in this method. The comparisons are shown in Tables 5 and 6. In Table 5, the total DG size used by [11] is same as when used by proposed MCDM TOPSIS installing two units of 500 KW DG or four units of 250 KW DG, but the power loss measured in previous method is much higher. Likewise, the active power loss and saving obtained in [4] is same as using two units of 750 KW DG, but in latter, total size or capacity of DG used is less than 50% of total DG capacity used in [4].

The comparison has been done on basis of total penetration level, active power loss and power savings. It can be observed that better results have been obtained by integrating low penetration of DG at multiple locations using MCDM TOPSIS technique.

6 Conclusion

This paper proposes MCDM TOPSIS approach for the allotment of DGs in radial distribution system to limit power loss and improve voltage profile. TOPSIS has satisfactorily been used in all other sectors and has proven good for purpose of DG installations in the radial distribution systems in this study. The advantage of using this method is in its easy application and less number of parameter population. DGs of low and fixed capacities have been used and compared to analyze whether desirable results, as attained by using high capacity DG units, are possible or not. This paper concludes that with proper allotment, small size DG and hence with low

overall penetration, better results can be attained. Low penetration of DG can result in less land use; ease with low-efficiency systems hence can aid the renewable energy system integration into the system.

References

1. Pepermans G et al (2005) Distributed generation: definition, benefits and issues. Energy Policy 33(6):787–798
2. El-Samahy L, El-Saadany E (2005) The effect of DG on power quality in a deregulated environment. In: IEEE Power Eng Soc Gen Meet, IEEE
3. Lalitha MP et al (2010) Application of fuzzy and PSO for DG placement for minimum loss in radial distribution system. ARPN J Eng Appl Sci 5(4):32–37
4. Acharya N, Mahat P, Mithulananthan N (2006) An analytical approach for DG allocation in primary distribution network. Int J Electr Power Energy Syst 28(10):669–678
5. Meena NK et al (2017) Multi-objective Taguchi approach for optimal DG integration in distribution systems. IET Gen Transm Distrib 11(9):2418–2428
6. Meena NK et al (2015) A Taguchi-based approach for optimal placement of distributed generations for power loss minimization in distribution system. In: 2015 IEEE Power Energy Soc Gen Meet, IEEE
7. Moradi MH, Abedini M (2012) A combination of genetic algorithm and particle swarm optimization for optimal DG location and sizing in distribution systems. Int J Electr Power Energy Syst 34(1):66–74
8. Sultana S, Roy PK (2014) Multi-objective quasi-oppositional teaching learning based optimization for optimal location of distributed generator in radial distribution systems. Int J Electr Power Energy Syst 63:534–545
9. Tzeng GH, JJ Huang (2011) Multiple attribute decision making: methods and applications. Chapman and Hall/CRC
10. Behzadian M et al (2012) A state-of the-art survey of TOPSIS applications. Expert Syst Appl 39(17):13051–13069
11. Naik SG, Khatod D, Sharma M (2013) Optimal allocation of combined DG and capacitor for real power loss minimization in distribution networks. Int J Electr Power Energy Syst 53:967–973
12. Shukla T et al (2010) Optimal sizing of distributed generation placed on radial distribution systems. Electr Power Compon Syst 38(3):260–274

Applied Computational Intelligence in Power Electronic Inverter to Mitigate Harmonics

Margi Shah and Kartik S. Pandya

Abstract This paper implies the application of artificial intelligence technique on cascade five-level H-bridge inverter with equal DC sources for objective of harmonic reduction. The multilevel modulation technique adopted is selective harmonic elimination. The approach is the development of optimal switching angles using particle swarm optimization technique with precise software and hardware validation. Harmonic analysis has been done at both optimized and unoptimized angles to corroborate the significance of AI method. The total harmonic distortion at optimized and unoptimized angles has corroborated that AI algorithms hold requisite dominance in one of the challenging issues of harmonic reduction.

Keywords Cascade multilevel inverter · Particle swarm optimization · Selective harmonic elimination

M. Shah · K. S. Pandya (✉)
CHARUSAT University, Anand, GJ 388421, India
e-mail: kartikpandya.ee@charusat.ac.in

M. Shah
e-mail: margishah1234@gmail.com

A. Mehta et al. (eds.), *Advances in Electric Power and Energy Infrastructure*, Lecture Notes in Electrical Engineering 608,
https://doi.org/10.1007/978-981-15-0206-4_10

Graphical Abstract

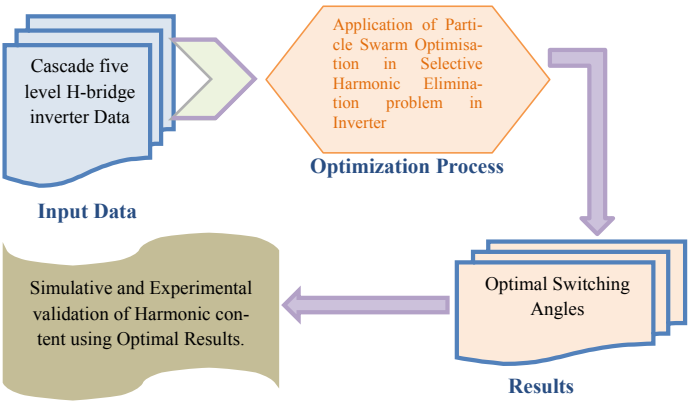

1 Introduction

The current era is remolding itself. With enormous challenges, the fusion of renewable technology into the grid has eventually become marvelous reality. Utilization of electricity from renewable energy sources directly for power injection into grid is arduous task. Hence, the system consequently necessitates power electronic converters as an interface between renewable energy sources and the grid/load. For high voltage and current applications, multilevel inverters have been enormously used [1]. Out of different structures of multilevel inverters, cascade H-bridge inverter is more suitable converter for PV applications since each PV panel can act as separate DC source for each cascade H-bridge module [2]. With the help of steps of voltages obtained from various DC sources, it can generate desired output voltage waveform. Using m number of cascade connection of series full-bridge inverters, it can synthesize $(2m + 1)$ number of levels. Due to such power electronic interface, harmonics are injected into the grid which will downgrade power quality of grid and cause an increase in total harmonic distortion content. Hence, it is essential to mitigate harmonics in the output of inverter conforming to predefined standards [3].

For controlling the voltage at the output end and eliminating the undesired harmonic content present in multilevel inverters, use of a filter circuit or by employing pulse width modulation (PWM) techniques can be implemented. Use of filter has the disadvantage of large size and cost, whereas use of PWM techniques reduces the filter requirement to a minimum or to zero depending on the type of application. There is formulation of control strategies for reduction of harmonic content owing to power quality issues. The modulation methods used in multilevel inverters can be classified according to the switching frequency. Several techniques for the implementation of PWM for multilevel inverters have been developed. The well-known high switching

frequency methods are classic carrier-based sinusoidal PWM (SPWM) and space vector PWM [4, 5]. The popular methods for low switching frequency methods are space vector modulation (SVM) method and selective harmonic elimination method. However, PWM techniques cannot completely eliminate the low-order harmonics. Therefore, the low-order harmonics cause losses and high filter requirements.

In selective harmonic elimination, to achieve adjustable amplitude of the fundamental component and minimize harmonic distortion, up to $n - 1$ harmonic contents can be removed from the voltage waveform with n number of levels in cascade multilevel inverter. In general, the most significant low-frequency harmonics are eliminated by properly selecting angles among different level inverters, and high-frequency harmonic components can be removed by using additional filter circuits [6, 7, 8]. The major difficulty for selective harmonic elimination method is to solve the transcendental equations for calculating switching angles. The selective harmonic elimination method can eliminate the number of harmonics not more than the number of the switching angles in the transcendental equations.

In the literature, various approaches have been articulated to solve the transcendental equations for the calculation of switching angles. It includes Newton–Raphson method with its specific demerit of less possibility to solve massive harmonic elimination problem if its initial guess is improper. Hence, judgment of initial guess is critical for convergence of solution [6, 7, 8, 9]. Also, another approach deals to remold transcendental into set of polynomial equations which also has its constraints due to incapability of software tools, and it is useful for specific number of switching angles for equal and unequal DC voltage sources only [10, 11, 12]. In 2005, genetic algorithm has also been applied to solve these transcendental equations to solve selective harmonic elimination problem, but it can only be applied to equal DC sources. To overcome this limitation, in 2008 H. Taghizadeh and M. Tarafdar Hagh presented particle swarm optimization technique to face the problem for equal DC sources [13].

In this paper, PSO is developed to deal with selective harmonic elimination problem with equal DC sources for cascade multilevel inverters. Harmonic analysis has been done at both optimized and unoptimized angles to corroborate the significance of artificial intelligence method.

Software and hardware validation has been done for cascade five-level inverter to prove the requisite dominance of PSO algorithm.

2 Power Topology of Cascade Multilevel Inverter

A single-phase H-bridge cascaded multilevel inverter topology consisting of separated DC sources is used to generate a $2s + 1$ staircase output voltage waveform (see Fig. 1a). Also, staircase voltage waveform generated by cascade multilevel inverter is shown (see Fig. 1b).

Cascaded H-bridge cell inverters use the least number of power electronic devices when compared to any other topology. However, they require isolated power sources

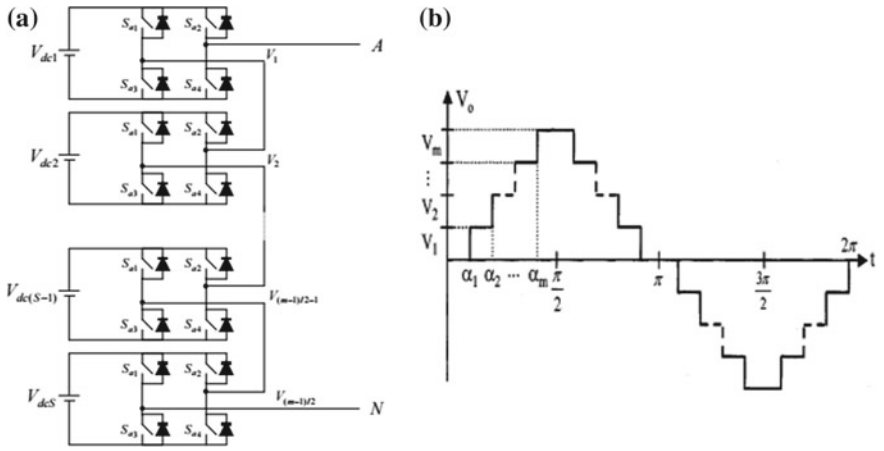

Fig. 1 **a** Single-phase cascade inverter topology. **b** Output phase voltage waveform

in each cell which in turn requires a large isolating transformer [14]. With s number of SDCs, cascade multilevel inverter can synthesize $2s + 1$ number of output phase voltage levels.

2.1 Harmonic Elimination Problem

By applying Fourier series analysis, the amplitude of any odd harmonic can be expressed by the equation, whereas the amplitude of even harmonic is zero [14].

$$V(\omega t) = \sum_{n=1,3,5\ldots}^{\infty} \frac{4V_{\mathrm{dc}}}{n\pi} * (k_1 \cos(n\theta_1) + k_2 \cos(n\theta_2) + \ldots + k_s \cos(n\theta_s))\sin(\mathrm{n}\omega t) \quad (1)$$

where $k_i V_{\mathrm{dc}}$ is the ith dc voltage, V_{dc} is the nominal dc voltage, and the switching angles must satisfy following condition. [14].

$$\theta_1 \leq \theta_2 \leq \theta_3 \leq \ldots \leq \theta_s \leq \frac{\pi}{2} \quad (2)$$

To minimize harmonic distortion and to achieve adjustable amplitude of the fundamental component, up to s-1 harmonic contents can be removed from the voltage waveform. In three-phase systems, the triple harmonics are automatically eliminated from line to line voltage. By properly selecting switching angles, it is possible to

eliminate lower-order harmonics, whereas higher-order harmonics can be removed with the help of filter circuits [14].

3 Mathematical Formulation

The objective function in this paper is to eliminate fifth-order harmonic content for cascade five-level inverter.

$$h_n = \frac{[(k_1 * \cos(5 * \theta_1)) + (k_2 * \cos(5 * \theta_2))]^2}{s * V_{\text{dc}}} + \frac{[(k_1 * \cos(\theta_1)) + (k_2 * \cos(\theta_2)) - (100 * M * \pi)]^2}{4 * V_{\text{dc}}} \tag{3}$$

where h_n is the harmonic content needed to be minimized, M is the modulation index.θ_1 and θ_2 are the solutions of harmonic minimization problem. PSO is developed to solve this SHE problem.

3.1 Particle Swarm Optimization

Optimization technique can be broadly categorized into classical methods and computational intelligence methods. Artificial intelligence techniques try to simulate human behavior. They offer an efficient optimization problem than the conventional techniques. These methods use past memory and improvise its performance. Particle swarm optimization, cuckoo search technique, genetic algorithm, seeker algorithm, harmony search algorithm, and differential evolution algorithm are some of the listed methods in the literature. Particle swarm optimization (PSO) is the most widely applied artificial intelligence technique. It is based on the behavior of flock of birds.

Particle swarm optimization (PSO) is one of the computational intelligence methods introduced by Kennedy and Eberhart in 1995. This method is motivated by the behavior of birds. In evening, they fly in particular 'V' shape to get the food source. There is one group leader. When it changes the direction, it is followed up by all birds. The individuals in this population are called particles. The direction and speed of all particles are controlled by direction and speed of one group leader called as global best particle. Each particle is associated with two variables, namely position and velocity. Each particle in the population refines its search through its present velocity, previous experience, and experience of neighboring particles. The best position of the particle found so far is called personal best, and best position in entire swarm is called global best [15, 16].

Velocity of ith particle is given by,

$$V_i^{k+1} = \omega V_i^k + c_1 r_1 \left(\text{Pbest}_i - x_i^k\right) + c_2 r_2 (\text{gbest}_i - x_i^k) \tag{4}$$

V_i^{k+1} = velocity of ith particle at $k+1$th iteration
ω = inertia weight
V_i^k = velocity of ith particle at kth iteration
c_1, c_2 = cogitative and social parameters, respectively
r_1, r_2 = random values uniformly distributed between [0, 1]
P best$_i$ = personal best position of ith particle (personal memory)
x_i^k = position of ith particle at kth iteration
gbest$_i$ = global best position of ith particle

To modify the position of the particle,

$$x_i^{k+1} = x_i^k + v_i^{k+1} \tag{5}$$

x_i^{k+1} = position of ith particle at $k+1$th iteration.
x_i^k = position of ith particle at kth iteration

In this paper, the criteria to reach optimality, i.e., convergence of algorithm, are maximum number of iterations which are predefined in the algorithm. The schematic flow for formulating the inverter harmonic elimination problem is as follows (see Fig. 2).

The landscape of the problem and the contour plot for $M = 1$ is shown (see Fig. 3).

For $M = 1$ and maximum iterations = 3000, the solution for optimality in switching angles reaches with minimum objective function value using PSO (see Fig. 4). At different modulation index ranging from under-modulation to over-modulation, the relationship is drawn between switching angles and modulation index. The switching angles tend to reduce at the over-modulation ranges (see Fig. 5).

The relation between objective function and modulation index is depicted which shows that at over modulation ranges, the magnitude tends to become higher and higher. The cost function has lower magnitude at lower modulation ranges (see Fig. 6).

Calculations of switching angles by proposed method are accomplished in MATLAB R2016a, Intel core i3-3220 CPU with 4.00 GB RAM.

4 Simulative Validation

A simulation is carried out on PSIM platform for five-level cascade H-bridge inverter at optimized and unoptimized angles. The nominal dc voltage is considered to be 50 V. MOSFETs are taken as switches in the inverter. The output focuses on the five-level cascade waveform with dominancy of fifth-order harmonic magnitudes at

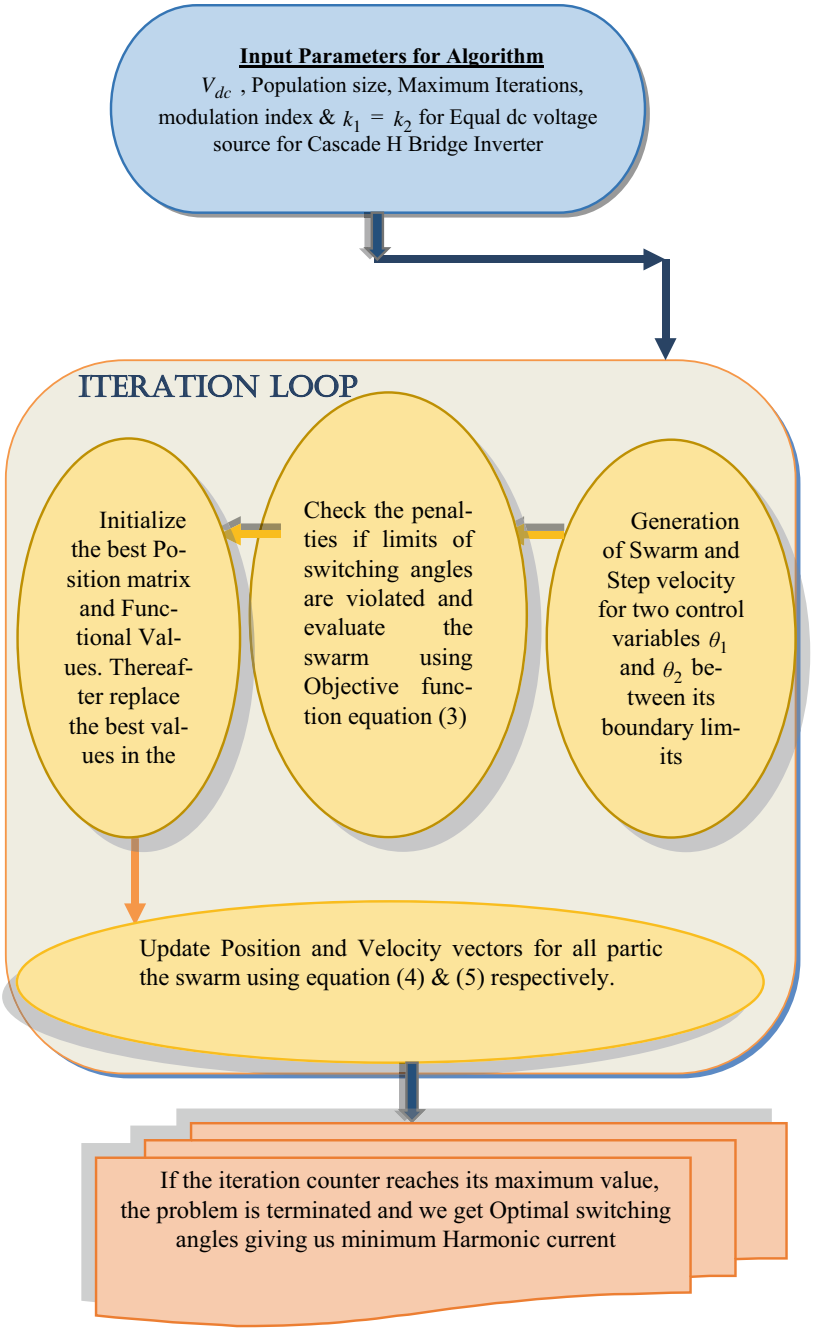

Fig. 2 Schematic flow of formulating harmonic elimination problem

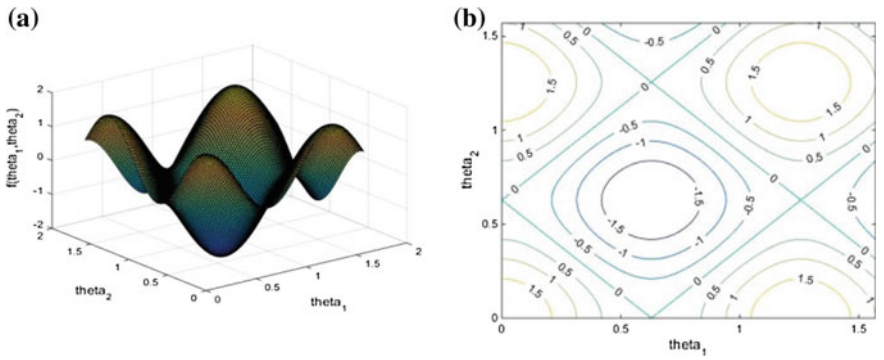

Fig. 3 Landscape and contour plot for five-level inverter with equal DC. Source where $M = 1$, $k_1 = 1$, and $k_2 = 1$. **a** Landscape of the problem **b** corresponding contour plot

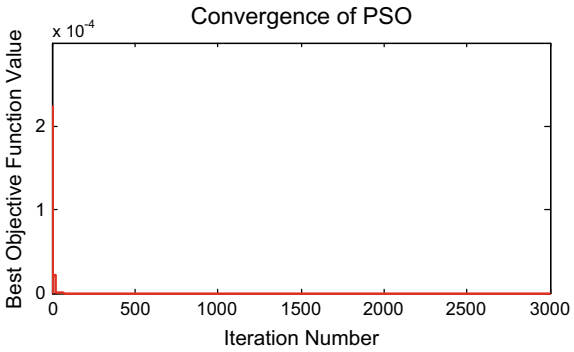

Fig. 4 Convergence of PSO

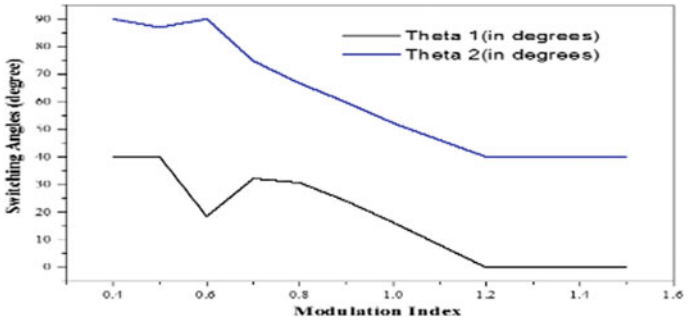

Fig. 5 Switching angles versus M

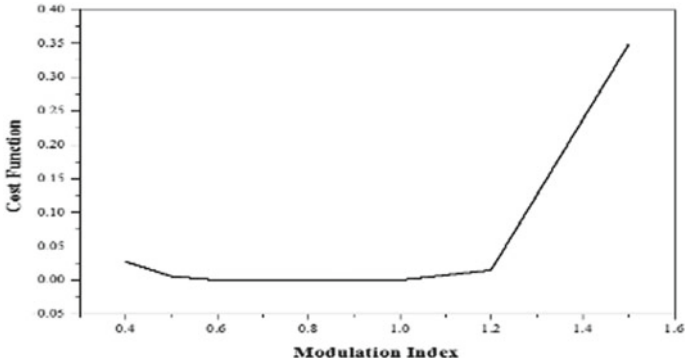

Fig. 6 Objective cost function versus M

both optimized and unoptimized angles. The total harmonic distortion is calculated using equation.

$$\text{THD} = \sqrt{\sum_{n=5,7,11..}^{19} \frac{V_n^2}{V_1}} \tag{6}$$

The output voltage waveform and FFT interpretation at unoptimized angles are shown. The fifth-order harmonic voltage is found to be 3.3 V (see Fig. 7). The total harmonic distortion in cascade five-level H-bridge inverter at unoptimized angles is presented which is obtained around 31.92% (see Fig. 8).

The output voltage waveform and FFT interpretation at optimized angles found using PSO are shown. The fifth-order harmonic voltage is found to be 0.18 V (see Fig. 9). The total harmonic distortion in cascade five-level H-bridge inverter at optimized angles is presented which is obtained around 18.21% (see Fig. 10).

As it is cascade five-level multi-inverter, the number of harmonic that can be eliminated is one. ('$s-1$' harmonic can be eliminated with 's' H-bridges.) As fifth order

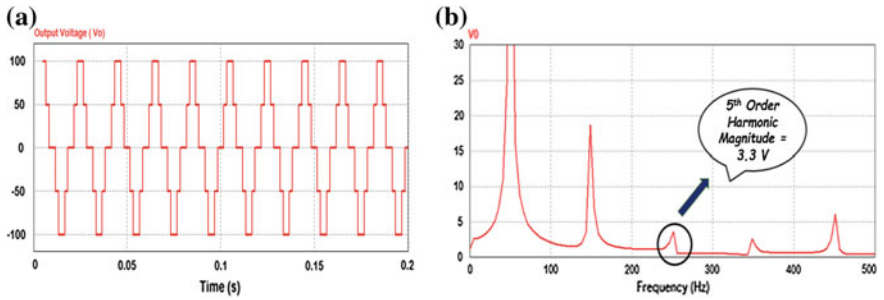

Fig. 7 Five-level output voltage waveform of cascade H-bridge inverter with equal voltage. Sources and its FFT analysis at unoptimized angles. **a** Output voltage waveform **b** FFT analysis

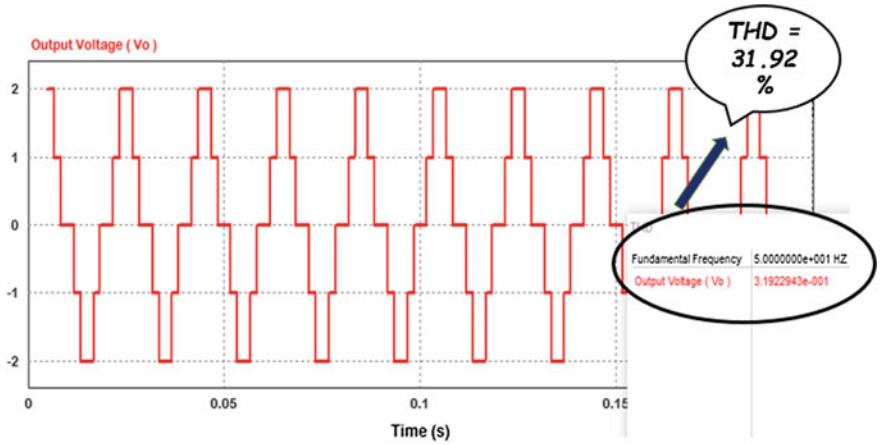

Fig. 8 THD interpretation at unoptimized angles

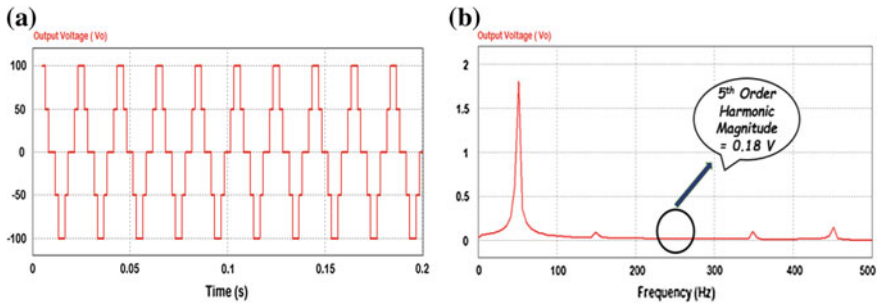

Fig. 9 Five-level output voltage waveform of cascade H-bridge inverter with equal voltage. Sources and its FFT analysis at optimized angles. **a** Output voltage waveform **b** FFT analysis

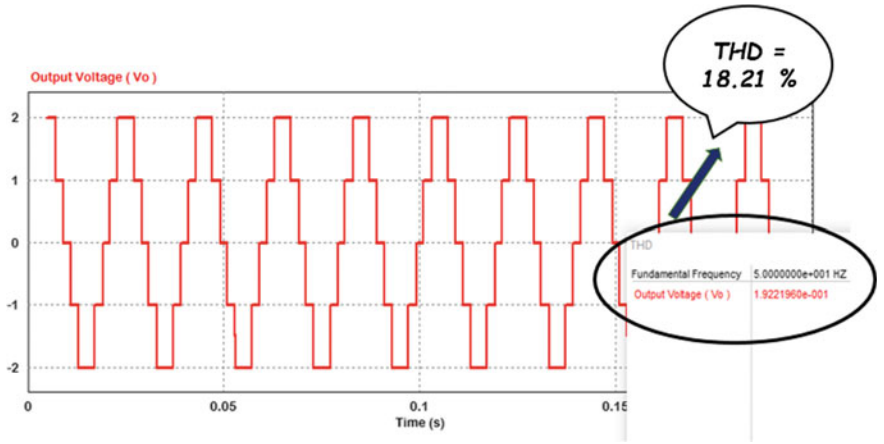

Fig. 10 THD interpretation at optimized angles

faces lower leakage reactance, current amplitude is more. Hence, particle swarm optimization algorithm focuses on reducing the magnitude of fifth-order harmonic generating two optimal switching angles. These optimal switching angles are implemented in the simulation to influence the harmonic content. With its implementation, clear effect is depicted in magnitude of harmonic as well as total harmonic distortion.

5 Experimental Validation

In order to validate the simulations, experimental results are presented for a single-phase five-level cascaded H-bridge inverter. The inverter uses 4-A 600-V MOSFETs as switching devices, and nominal DC-link voltage for each H-bridge is considered to be 50 V. Cascade H-bridge uses 1 KΩ as load resistor. The driver circuit uses 230/12 V step-down transformer, resistors of 470 kΩ, 100 Ω, 1 kΩ combination, 470 uF capacitor, 50 V, 1A diode, and TLP250 as driver IC. The gate control signals are generated by Arduino Uno. PW3198 Hioki power quality analyzer is used for harmonic analysis of the inverter output waveform. The implemented prototype is depicted (see Fig. 11).

The output voltage waveform for five-level cascade H-bridge inverter for optimized and unoptimized angles is as shown in Fig. 12. Harmonic analysis using power analyzer clearly depicts that the fifth-order harmonic value for unoptimized case is found to be 3 V with 31.35% THD whereas for optimized case is found to be 0.18 V with 18.51% THD (see Fig. 13).

Hence, the experimental results have corroborated the simulation results and proved the requisite significance of AI method.

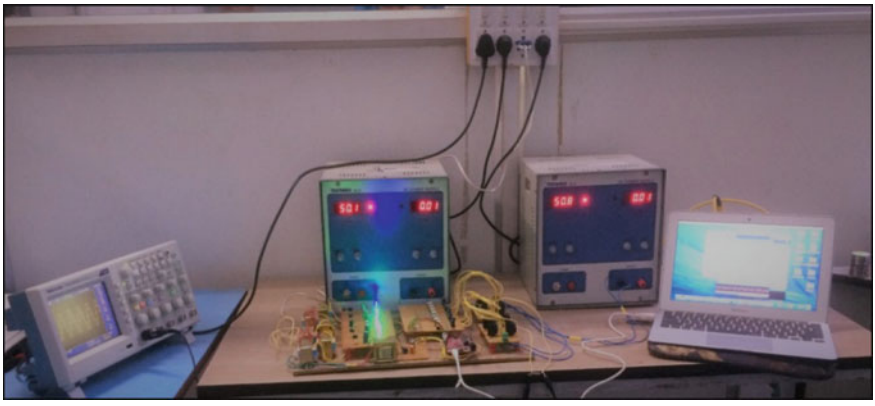

Fig. 11 Implemented five-level cascade H-bridge prototype

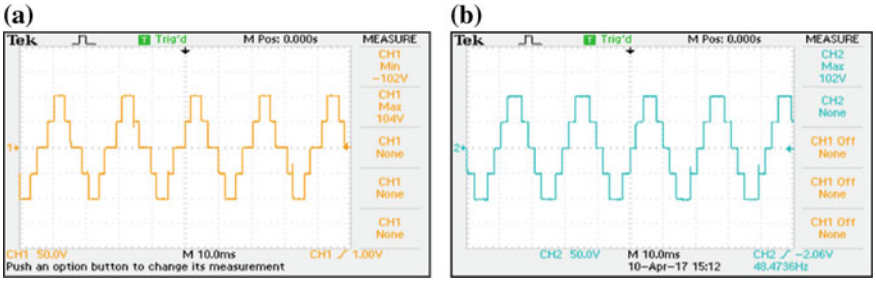

Fig. 12 Five-level output voltage waveform of cascade H-bridge inverter **a** unoptimized case **b** optimized case

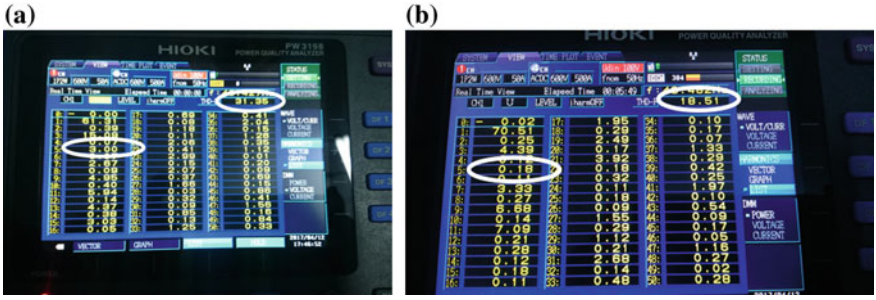

Fig. 13 Harmonic content using power analyzer **a** unoptimized case **b** optimized case

6 Conclusion

To solve SHE problem for five-level cascade H-bridge inverter with equal DC sources, PSO has been proposed. After the application of PSO, it is clearly depicted that there is great reduction in fifth-order harmonic content and total harmonic distortion from 31 to 18%. Hence, it is verified that AI algorithms hold requisite dominance in one of the challenging issues of harmonic reduction. The bandwidth of harmonic reduction can be enhanced with use of higher number of levels in cascade inverter. With greater number of harmonic component reduction, filter requirement gets reduced. It behaves partially as a STATCOM, and hence, further grid integration can be done. Eventually, the enrichment of power quality with DG penetration is the need of today.

References

1. PV Krishna, AKumar Singh, R Gupta (2015) Grid connected solar PV fed cascaded multilevel inverter implementation using XSG platform. In: IECON 2015—41st annual conference of the IEEE Industrial Electronics Society
2. Holmes DG, Lipo TA (2003) Pulse width modulation for power converters. IEEE Press, Piscataway, NJ
3. Artificial Intelligence and Evolutionary Algorithms in Engineering Systems (2015) Springer Nature America, Inc
4. Kouro S, Rebolledo J, Rodriguez J (2007) Reduced switching-frequency modulation algorithm for high-power multilevel inverters. IEEE Trans Ind Electron 54(5):2894–2901
5. HS Patel, RG Hoft (1973) Generalized harmonic elimination and voltage control in thyristor inverters: part I—harmonic elimination. IEEE Trans Ind Appl IA-9(3): 310–317
6. HS Patel, RG Hoft (1974) Generalized harmonic elimination and voltage control in thyristor inverters: part II—voltage control technique. IEEE Trans Ind Appl. IA-10(5): 666–673
7. Fei W, Du X, Wu B (2010) A generalized half-wave symmetry SHE-PWM formulation for multilevel voltage inverters. IEEE Trans Ind Electron 57(9):3030–3038
8. Enjeti PN, Ziogas PD, Lindsay JF (1990) Programmed PWM techniques to eliminate harmonics: a critical evaluation. IEEE Trans Ind Appl 26(2):302–316
9. Chiasson JN, Tolbert LM, McKenzie KJ, Du Z (2003) Real-time computer control of a multilevel converter using the mathematical theory of resultant. Math Comput Simul 63(3–5):197–208
10. Chiasson JN, Tolbert LM, McKenzie KJ, Du Z (2005) The use of power sums to solve the harmonic elimination equations for multilevel converters. EPE J 15(1):19–27
11. LM Tolbert, JN Chiasson, K McKenzie, Z Du (2003) Elimination of harmonics in a multilevel converter with non equal DC sources. In: Proceedings of IEEE application power electronic conference. Miami, FL, 9–13 Feb 2003, pp 589–595
12. H Taghizadeh, M Tarafdar Hagh (2008) Harmonic elimination of multilevel inverters using particle swarm optimization. In: Proceedings of IEEE international symposium industrial electronics, pp 393–396
13. H Taghizadeh, M Tarafdar Hagh (2010) Harmonic elimination of cascade multilevel inverters with nonequal DC sources using particle swarm optimization. In: Proceedings of IEEE international symposium industrial electronics, pp 3678–3682
14. T Jeevabharathi, V Padmathilagam (2012) Harmonic elimination of cascaded multilevel inverters using particle swarm optimization. In: International Conference on Computing, Electronics and Electrical Technologies ICCEET
15. H Taghizadeh (2008) Harmonic elimination of multilevel inverters using particle swarm optimization. In: 2008 IEEE International Symposium on Industrial Electronics
16. V Renu, NL Surasmi (2014) Optimal control of selective harmonic elimination in a grid connected single-phase PV inverter. In: 2014 International conference on advances in green energy (ICAGE)

Design and Analysis of DC Power Supply for Solid-State Power Amplifier

Rohit Agarwal, Rajesh Kumar, Gajendra Suthar and Hrushikesh Dalicha

Abstract DC power supply required for 12 kW solid-state RF power amplifier (SSPA) is designed and analyzed. Rating (30–65 V, 320 A) and topology of power supply are derived to satisfy load requirement. The selected topology is twelve-pulse rectifier followed by interphase transformer and synchronous buck converter to get desired output voltage. Modular design is selected to minimize copper losses, to reduce the voltage drop and to optimize the resources available. Simulation is done using PSIM software to analyze the performance in entire operating range and validation of the design. Prototype model is developed with same voltage range (30–65 V) but lower current rating (10 A). Testing is done at different voltage and current levels to analyze steady state and dynamic performance. The simulation and experimental results are in good agreement.

Keywords Synchronous buck converter · Power supply · RF power amplifier · Interphase transformer

1 Introduction

ITER-India is developing solid-state RF power amplifier (SSPA). It is using laterally diffused metal-oxide semiconductor (LDMOS) transistors. SSPA is the first stage in ion cyclotron resonance frequency (ICRF) amplifier chain. RF power is required for varieties of application in ITER plasma such as ion cyclotron (IC) heating and plasma current drive. SSPA has maximum RF output power of 12 kW for 35–65 MHz frequency range. It can drive the amplifier to achieve 1.5 MW RF output power [1].

R. Agarwal (✉) · G. Suthar · H. Dalicha
ITER-India, Institute for Plasma Research, Gandhinagar, Gujarat, India
e-mail: rohit.agarwal@iter-india.org

R. Agarwal · R. Kumar
HBNI, Mumbai, Maharashtra, India

R. Kumar
Institute for Plasma Research, Gandhinagar, Gujarat, India

A. Mehta et al. (eds.), *Advances in Electric Power and Energy Infrastructure*, Lecture Notes in Electrical Engineering 608,
https://doi.org/10.1007/978-981-15-0206-4_11

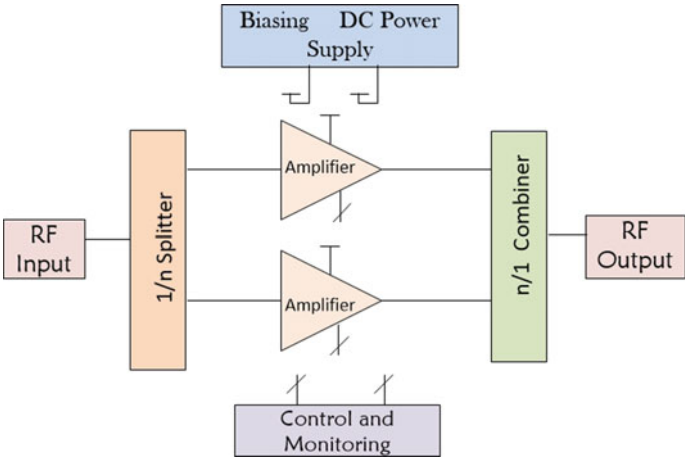

Fig. 1 SSPA block diagram

The power requirement of SSPA varies from few watts to maximum of 12 kW depending on ICRF requirement. A regulated DC power supply with low voltage ripple, good line regulation, good load regulation and good dynamic response is required to bias drain of LDMOS transistors, the building block of SSPA [2].

The biasing voltage can take any value from 30 to 65 V, depending on operating scenarios, but selected voltage should remain same during a specific operation. The load current can vary from 0 to 320 A depending on RF power output.

The functional block diagram of SSPA is shown in Fig. 1. It has RF input, splitter, amplifier, biasing DC power supply, control, monitoring and finally combiner to get RF output.

This paper provides detailed idea about prototype model of DC power supply for 30–65 V and 10 A rating. Section 2 provides detailed functional specifications of full scale and prototype DC power supply. Section 3 provides detailed idea about design of prototype DC power supply including AC–DC converter, DC–DC converter and control circuit. Section 4 provides detailed simulation results and corresponding discussion. Section 5 provides detailed experimental results of prototype DC power supply, and finally, Sect. 6 concludes this paper.

2 Requirement of Power Supply

Functional specifications of biasing DC power supply for full load operation of SSPA are shown in Table 1.

Table 1 Functional specifications of DC power supply

Functional specification	Ratings
Rated input	415 V, 50 Hz, 3 phase AC
Nominal output voltage	30–65 V DC
Rated output current (full scale)	0–320 A
Rated output current (developed prototype)	0–10 A
Output voltage ripple (p–p)	<1%
Line and load regulation	<1%

3 Design of Power Supply

The power supply is low voltage and high current type. Modular design is suitable to reduce ohmic losses associated with current. The power supply can be divided in three major stages. First stage is AC to DC converter to provide a stable DC bus. This acts as a constant input voltage for DC to DC converter. Second stage is buck chopper to step down the input voltage to get desired DC voltage. Third stage is feedback control to achieve regulated voltage [3]. The overall block diagram of power supply is shown in Fig. 2.

The simulation is done in PSIM software [4]. Simulation model and results of main building blocks of power supply will be discussed in following sections.

3.1 AC to DC Converter

PSIM model of the converter is shown in Fig. 3. Input of converter is 415 V 3-Phase 50 Hz. AC is converted in DC using parallel rectifier modules followed by interphase transformer (IPT). The DC bus capacitor is selected to limit voltage ripple less than 1% ripple. Soft start circuit is used to protect transformer and DC bus capacitor.

Twelve- **Pulse Rectifier**. Delta–Delta (TDD1) and Delta–Star (TDY1) transformers as shown in Fig. 3 are required to get 30° phase shifted AC voltage. It is rectified

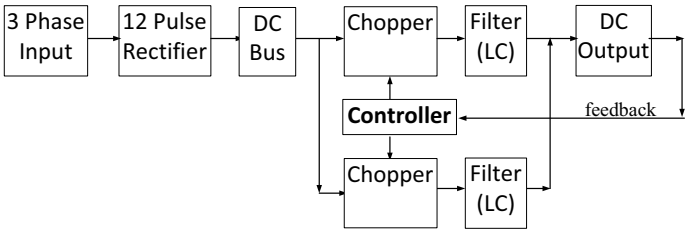

Fig. 2 Block diagram of power supply

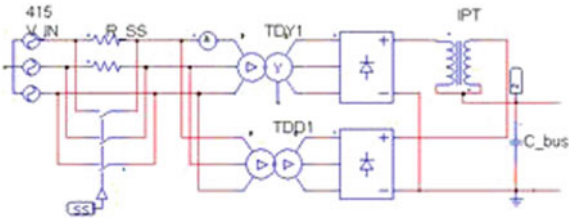

Fig. 3 PSIM model of AC to DC converter

using full bridge uncontrolled rectifier to get twelve-pulse rectified output. Rectifier modules are connected in parallel through IPT.

Interphase Transformer. The two rectifier modules have voltage difference at any instant since the two six-pulse outputs have 30 degree phase difference. IPT absorbs this voltage difference and ensures twelve-pulse output without any circulating current [5]. The IPT structure is shown in Fig. 4a. Here i1 is the output DC current of the rectifier-1(r1) and i2 is the output DC current of rectifier-2 (r2). i1 and i2 flow through the IPT having inductance L. IPT provides inductance of 2L for the differential mode current only and averages the voltages of the parallel nodes [5]. The simulation result shows twelve-pulse output (pink) in Fig. 4b.

The simulation results for continuous mode operation with 2.5 mH inductance are shown in Fig. 5a and b. IPT current and load voltage for discontinuous mode with 0.25 mH inductance are shown in Fig. 6a and b, respectively. Discontinuous

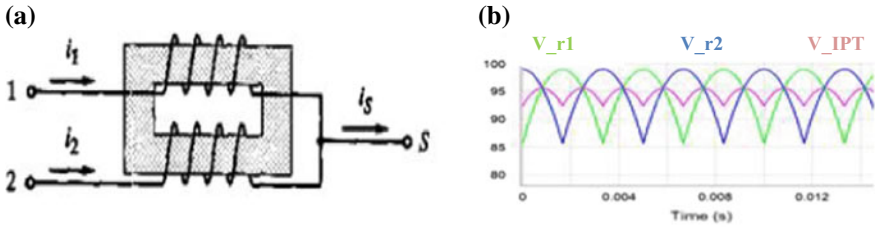

Fig. 4 **a** IPT structure, **b** twelve-pulse rectified output (pink)

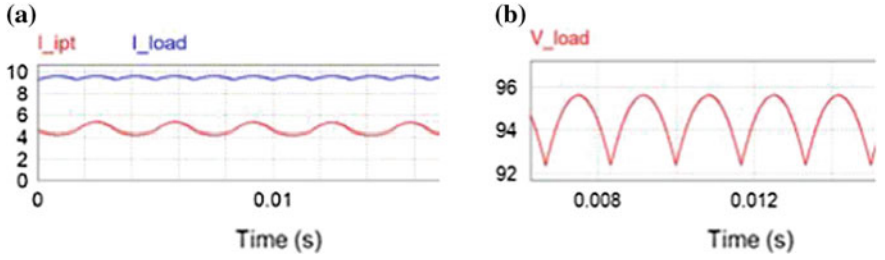

Fig. 5 Continuous mode **a** IPT current, **b** load voltage

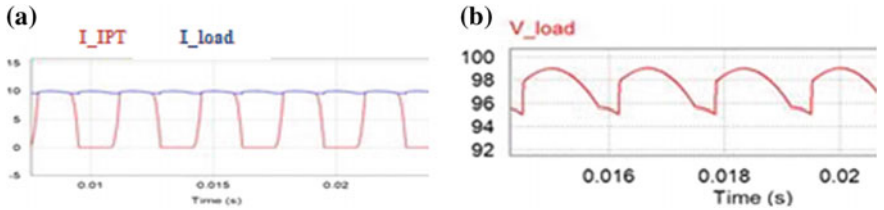

Fig. 6 Discontinuous mode **a** IPT current, **b** load voltage

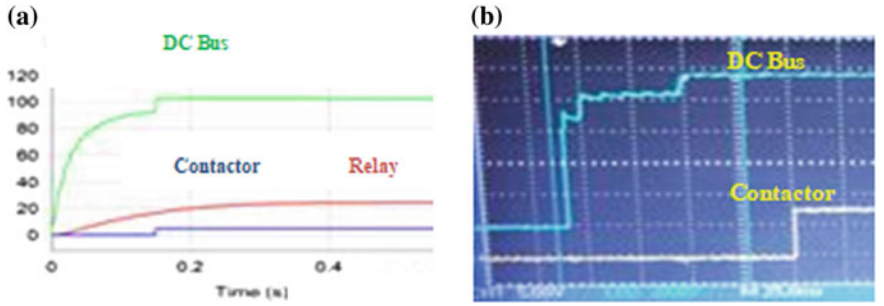

Fig. 7 Soft starting **a** simulation result, **b** experimental result

current mode (DCM) will increase the output voltage and peak current through IPT and affect its performance.

Soft Starting Circuit. To ensure gradual charging of DC bus capacitors, a soft start procedure is adopted. The soft start circuit introduces temporary resistance *R* at the input in series with the mains as shown in Fig. 3. Once the DC bus is charged to desired level, the resistance is removed by short circuiting the resistors using a contactor.

RC voltage divider is used across DC bus capacitor. When voltage across relay coil reaches pickup level, it will operate the contactor and input resistance will bypass. A 24 V relay is selected and its pickup voltage is found experimentally to be 16.5 V. The simulation and experimental results are shown in Fig. 7a and b, respectively.

3.2 DC–DC Converter

The DC bus voltage is stepped down to get required output voltage. It is done by using buck converter followed by output LC filters. There is a voltage divider at load end for feedback to control circuit. Converter modules are paralleled to increase load current capacity. The PSIM simulation model of DC–DC converter is shown in Fig. 8.

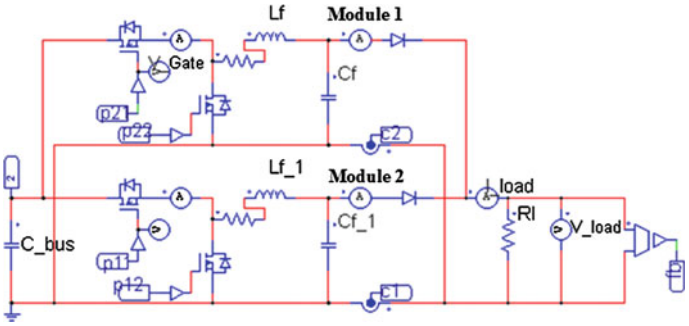

Fig. 8 Parallel synchronous buck converter modules

Buck converter. Buck converter is a step-down converter, where DC input is reduced to get lower DC output. It is done by chopping the input using a fast switch. MOSFET is selected as switch for our application.

To improve the overall efficiency of system, synchronous buck converter scheme is selected [6]. Here, freewheeling diode is replaced with MOSFET. The power loss due to voltage drop across MOSFET is lower than in freewheeling diode of the nonsynchronous converter.

Output Filter Inductor. The iron core inductors usually have ±10% tolerance. This variation will cause unequal current sharing among parallel modules shown in Fig. 8. To avoid it, multilayer air core inductors are used, where the wire length can easily be trimmed to exactly match inductance and resistance values, ensuring equal current sharing.

The Wheeler's formula [7] is used for developing 750 μH, 0.45 O inductor.

3.3 Control Circuit

Control part is required to regulate the output voltage and compensate the effect of load or line variation. The available choices are fixed frequency PWM control and variable frequency hysteresis control. Here, the possibility of using hysteresis feedback control [8] is explored.

Hysteresis Feedback Control. The load current is variable over a wide range, depending on RF power requirement. During light loading condition, the PWM control needs large inductance to operate in continuous conduction mode. The hysteresis control has advantage during such condition as it can operate in both continuous and discontinuous conduction modes. It results in smaller size, lighter weight and higher efficiency inductor. The simulation model of hysteresis feedback control circuit is shown in Fig. 9a. It uses a fast comparator to compare the output voltage with reference voltage.

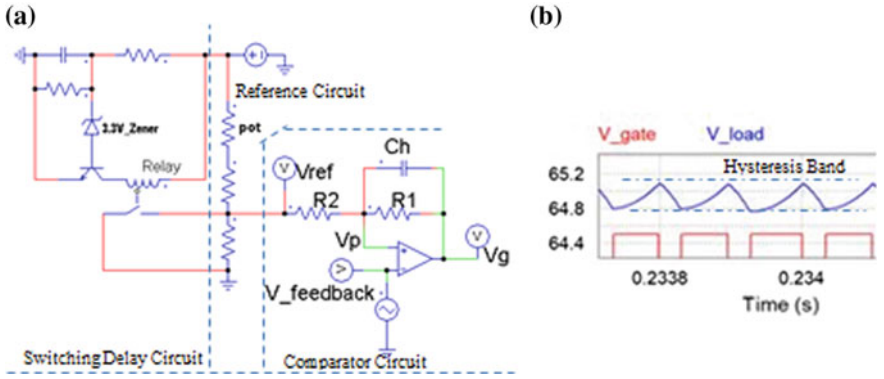

Fig. 9 Hysteresis feedback control **a** simulation model, **b** voltage band and gate pulses

Reference voltage is set using a potentiometer. Control keeps the output voltage within a desired band by switching as soon as boundary of band is encountered. The band (same as voltage ripple) and gate pulse are shown in Fig. 9b. Switching delay circuit is required to allow the DC bus to charge fully before operation starts.

4 Simulation Results

Simulation results for steady state and dynamic output of prototype power supply (specifications as per Table 1) are discussed here. The output voltage during startup is shown in Fig. 10a. It has overshoot peak of 80 V that is less than DC bus voltage. The hysteresis loop controls the gate pulse (shown in Fig. 11a) to get set voltage. Output load voltage is getting settled in approx. 3 ms. Load voltage (65 V) and load current (10 A) are shown in Fig. 10b.

Simulation model for dynamic load switching using MOSFET as a switch is shown in Fig. 11a. Fixed resistance R1 is 70 O, to get 0.9 A at 65 V. R2 is 7 O and it is switched in parallel to get 6.4 O effective resistance. The load current became

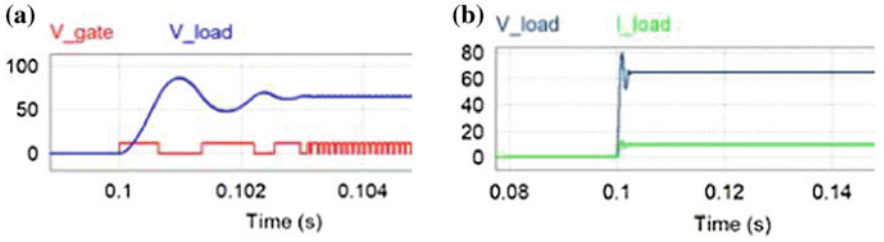

Fig. 10 Load voltage with **a** gate pulse, **b** load current

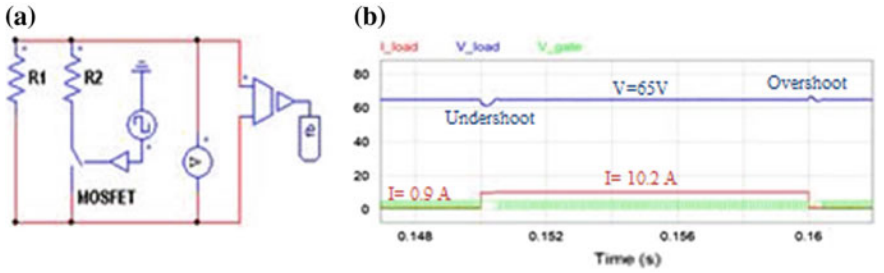

Fig. 11 Dynamic analysis **a** simulation model, **b** load voltage and current

10.2 A for 10 ms. The dynamic response during 10% to 100% load switching is shown in Fig. 11b. The undershoot (4 V) during addition of load and overshoot (3 V) during loss of load is observed.

To calculate output voltage ripple at full load (65 V/10 A), the peak to peak difference is calculated to be 0.3 V as shown in Fig. 9b. The ripple in percentage of output voltage is calculated to be 0.46%.

5 Developed Prototype

A 30–65 V/10 A prototype model as shown in Fig. 12 is developed for design, analysis and simulation validation. It has two parallel modules. The main design parameters of the prototype power supply are given in Table 1.

Delta–Star (DY) and Delta–Delta (DD) transformers are used to get twelve-pulse rectified output. Each buck converter module has its own DC bus capacitor to reduce

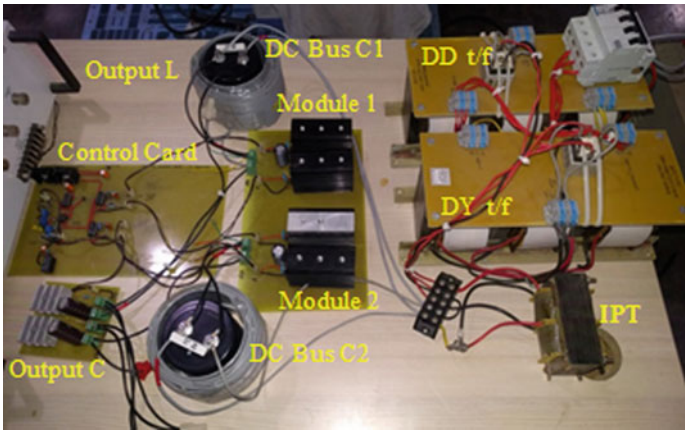

Fig. 12 Developed prototype

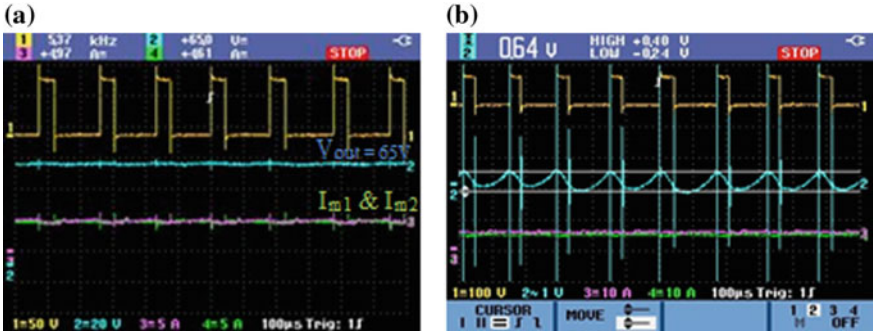

Fig. 13 Regulated output voltage and current **a** DC coupling mode, **b** AC coupling mode

the inductance due to connecting cable. It results in significant improvement in switching transient voltage. Air core inductors help in balanced operation of parallel modules.

The 65 V DC output is shown in Fig. 13a and b for DC coupling and AC coupling, respectively. Voltage across the switch is shown with yellow. It shows 90 V DC bus across the switch in blocking mode and zero voltage during conduction mode. Duty ratio is found to be 72%. Transient voltage is under 20%. Peak to peak voltage ripple in percentage of output voltage is found to be 0.98%. It can be seen that current sharing is equal for both modules.

The experimental results of prototype are summarized in Table 2. Here, % ripple is found within acceptable limits.

Capacitive snubbers are used to suppress voltage transients during switching. The power loss depends on switching frequency, capacitance value and DC bus voltage. The allowed working temperature limit is 70° degrees, and maximum temperature at steady state is found to be less than this.

Power analyzer is used to find power factor and to calculate efficiency during full load (65 V/10 A) operation of prototype. The active power, reactive power and power factor are shown in Fig. 14.

The input power is found to be 710 W, and system efficiency is calculated to be 91.55% for 650 W output power. Power factor obtained is 0.93.

Table 2 Summary of the experimental results of prototype

V out	Duty ratio (%)	Frequency (kHz)	Ripple (p–p) (V)	Ripple (%)
30.40	33.78	17.2	0.30	0.99
45.00	50.00	20.0	0.28	0.62
65.00	72.22	6.48	0.64	0.98

Fig. 14 Readings of power analyzer

6 Conclusion

Validation of simulation model with experimental results has been done as discussed in previous sections. Regulated output voltage is obtained as shown in Fig. 13a. Parallel modules worked with equal current sharing between them. Output voltage ripple is under 1% as shown in Fig. 13b. Power factor meets standard requirements as shown in Fig. 14.

The limitation of this control scheme is that the optimum performance is attained at 50% duty cycle which requires a higher DC bus voltage. Now, a full scale 30–65 V/320 A power supply will be developed based on above discussed topology.

Acknowledgements This paper is written in partial fulfillment of requirements for M.Sc. (Engineering) from Homi Bhabha National Institute (HBNI), Mumbai, Maharashtra, India.

References

1. Mukherjee Aparajita et al (2015) Status of R&D activity for ITER ICRF power source system. Fusion Eng Des 96–97:542–546
2. M Patel et al (2016) Development of wideband solid state power amplifier for ICH & CD RF source. In: 29th symposium on fusion technology (SOFT 2016), FIP/P8-16
3. Tarter RE (1993) Solid-state power conversion handbook. Wiley, New York
4. PSIM user's guide (2016) Version 10.0, Powersim Inc.
5. Sadri M et al (2010) Current sharing improvement in parallel batteries using interphase transformer. Int Rev Electr Eng (IREE) 5:530–535
6. MS Jamil Asghar (2009) Power electronics, PHI, India
7. http://www.circuits.dk/calculator_multi_layer_aircore.htm
8. Timothyl Skvarenina, Power Electronics Handbook, Industrial Electronics Series, CRC Press

Novel Current Source Multi-level Inverter for Efficient Electrical Arc Welding

Pankaj S. Sharma and Mulav P. Rathod

Abstract By improving the performance of multi-level current source inverter by the proposed modified topology to solve the various problems related to welding with better efficiency. Due to the proposed topology, good quality of current can feed into the utility of arc welding.

Keywords Current source inverter (CSI) · Multi-level current source inverter (MLCSI) · Arc welding · Transformer · Inductor · IGBTs

1 Introduction

By improving the performance of multi-level current source inverter by the proposed modified topology to solve the various problems related to welding with better efficiency. Due to the proposed topology, good quality of current can feed into the utility of arc welding. The arc welding power has the advantages of high efficiency, energy-saving, compact and low cost. It is a tendency of development of arc welding. The arc welding power supply is a new type of welding and used widely for industrial applications. The reliability of arc welding power supply is very important. In terms of effects on reliability of switching power supply, this paper details the design methods about that in place of voltage source multi-level inverter, the current source multi-level inverter is used for the efficient welding arc and then gives the calculation methods about the selection of components for protection circuit. The protection circuit described in this paper is suitable for arc welding power supply with output load voltage 100 V, output current 160 A, frequency 20 kHz and rated power 6 kW.

P. S. Sharma (✉) · M. P. Rathod
Sardar Vallabhbhai Patel Institute of Technology, Vasad, Gujarat, India
e-mail: Pankajsharma2225@gmail.com

M. P. Rathod
e-mail: mulavrathod.elect@svitvasad.ac.in

A. Mehta et al. (eds.), *Advances in Electric Power and Energy Infrastructure*, Lecture Notes in Electrical Engineering 608,
https://doi.org/10.1007/978-981-15-0206-4_12

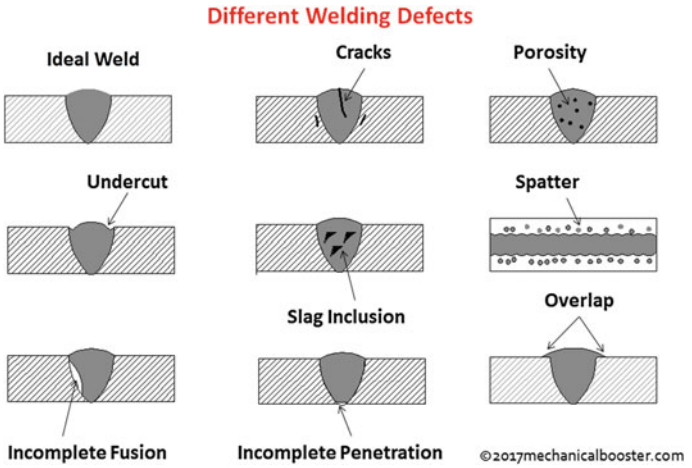

Fig. 1 Different welding defects

2 Welding

2.1 Electric Arc Welding

By definition, arc welding is the process in which the metal to be welded is brought to the proper welding temperature, at the point of contact due to which the heat liberated at the arc terminals and in the arc stream by which the metals are completely fused into each other, by forming a single layer of homogeneous mass, after it solidifies.

The heat developed is utilised to melt the part of the work piece, and the filler metal and thus forms the joint. So the welded arc joint is a union of metal parts which is made by localised heating which is not having any pressure. Therefore, this type of welding is also known as the non-pressure welding. The developed heat by the arc is also used for cutting of metals. There are many problems in welding process such as cracks, porosity, undercut, slag inclusion, spatter, incomplete fusion, incomplete penetration and overlap (Fig. 1).

2.2 Calculations

$$\text{Arc Current } I = \frac{V}{\sqrt{(R_t + R_e + R_a)^2 + (X_t + X_l)^2}} \tag{1}$$

$$= \frac{100}{\sqrt{(0.003 + 0.78 + 0.98)^2 + (0.005 + 0.70)^2}}$$

$I = 44.247\text{A}$
R_t = resistance of transformer = 0.003 Ω
R_e = resistance of electrode = 0.78 Ω
R_a= resistance of arc = 0.98 Ω
X_t = reactance of transformer = 0.005 Ω
X_l = reactance of electrode = 0.70 Ω

$$\text{Energy required for melting 100 g iron} = m[s(t_2 - t_1) + L]$$
$$= 0.1[45(450 - 125) + 272] = 1489.7\text{J}$$
$$= 1.4897\text{KJ}$$

m = mass of iron = 100 g = 0.1 kg
s = specific heat of iron = 0.450 J/g°C = 45 J/g
t_2 = melting temperature = 450 °C
t_1 = initial temperature = 125 °C
L = latent heat of fusion of iron = 272 kJ/Kg = 65 cal/g

- Calculations for Power Input

Power input

$P = \pi dlH = 3.660455W$
d =diameter of electrode = 2 mm = 0.002 m
l = length of electrode = 250–450 mm = 0.25 m
H = heat dissipated = 2331.5 ≈ 2332 W/m^2

$$H = 5.72ek\left[\left(\frac{T_1}{100}\right)^4 - \left(\frac{T_2}{100}\right)^4\right]$$

e = emissivity
= 0.9 for resistance heating element
= 1.0 for black body

k = constant radiating efficiency
= 1 for single element

T_1 = 450 °C temperature of source of heat
T_2 = 125 °C temperature of substance to be heated (Fig. 2).

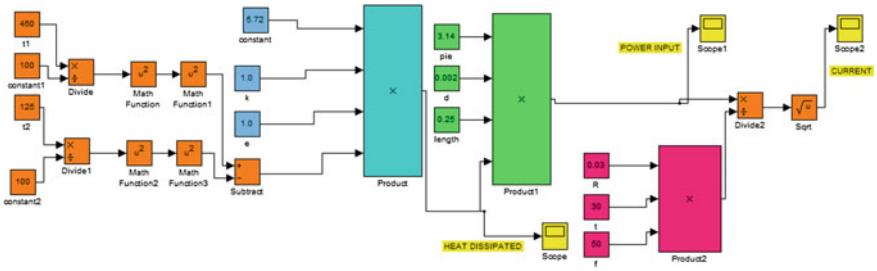

Fig. 2 Simulation of power input

3 Current Source Inverter

A. The CSI converts the input DC into AC. It is also called as current fed inverter. Input current is constant but adjustable. The amplitude of output current from CSI is independent of the load.

B. **Working**

Because there must be a continuous current flow from the source, two switches must always conduct—one from the upper and one from the lower switches. The conduction sequence is 12, 23, 34 and 41 as shown in Fig. 3. If two switches one upper and one lower conduct at the same time such that the output current is $\pm I_l$, the switch state is 1; whereas if these switches are off at the same time, the switch state is 0. The output current waveform is shown in Fig. 4. The diodes in series with the IGBTs are required to block the reverse voltages on the IGBTs.

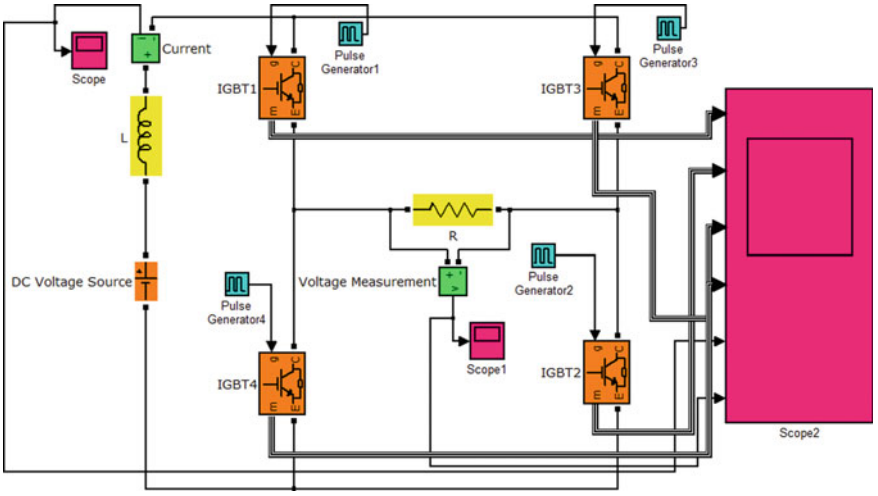

Fig. 3 Simulation of H-bridge CSI

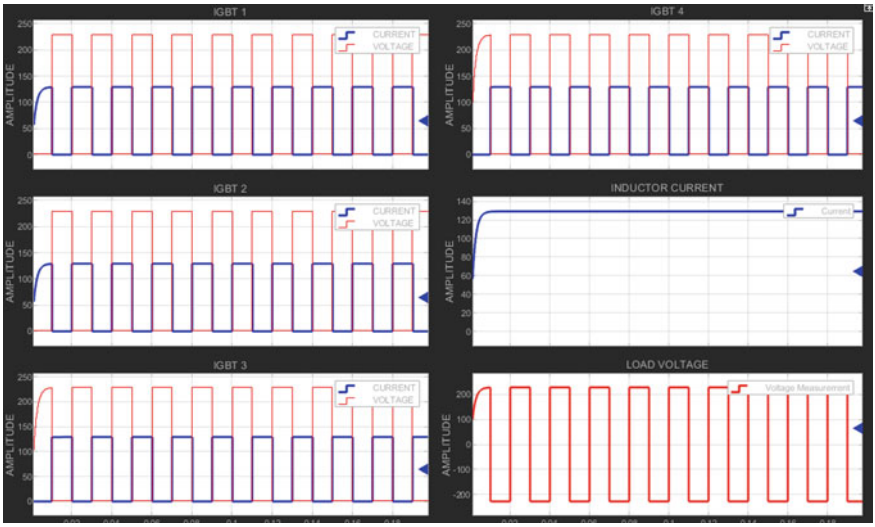

Fig. 4 Output of CSI

When two devices in different arms conduct, the source current I_l flows through the load. When two devices in the same arm conduct, the source current is bypassed from the load.

CSI with PWM technique

The purpose of the PWM technique is used to control the output voltage of the inverter and also to reduce the harmonic content which is present in the output voltage. The pulse width modulation (PWM) techniques are mainly used for voltage control. These techniques are most efficient to control the drives of the switching devices. There are different PWM techniques such as single pulse width modulation (SPWM), Multiple pulse width modulation (MPWM), phase displacement control (DPC), sinusoidal pulse width modulation (SPWM), harmonic injection modulation (HIM), space vector pulse width modulation, hysteresis (delta) pulse width modulation, selective harmonic elimination and current-controlled pulse width modulation. The hysteresis controller is one of the methods which is used for current source inverter, and all the remaining PWM techniques are used for voltage source inverter. The sinusoidal and the space vector PWM techniques are frequently used.

4 Sinusoidal Pulse Width Modulation

The sinusoidal pulse width modulation (SPWM) technique is used to produce the sinusoidal waveform by filtering an output pulse waveform with varying width.

A better sinusoidal output waveform can be obtained by using a high switching frequency and by varying the amplitude as well as frequency of a reference or the modulating voltage. In this technique generally, it is used to maintain the pulses in different widths instead of maintaining in equal widths as in multi-pulse width modulation where the distortion factor (i.e. DF) and lowest order harmonics (i.e. LOH) are more precisely reduced. In this project, we use triangular wave as carrier signal and sine wave as well as cosine wave as a reference signal and compare the two waveforms with the help of comparator for this the simulation is done and shown in Fig. 5. The output of the simulation of Fig. 5 is shown in Fig. 6 in which the first waveform shows the triangular, sinusoidal and cosine waves. From second to fifth waveforms, they show the effect on switching due to the SPWM method. The sixth and seventh waveforms show the current and load (voltage) outputs.

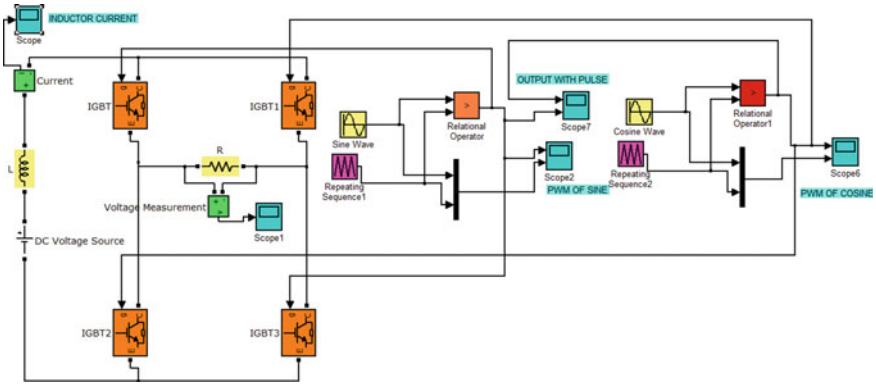

Fig. 5 CSI with PWM technique

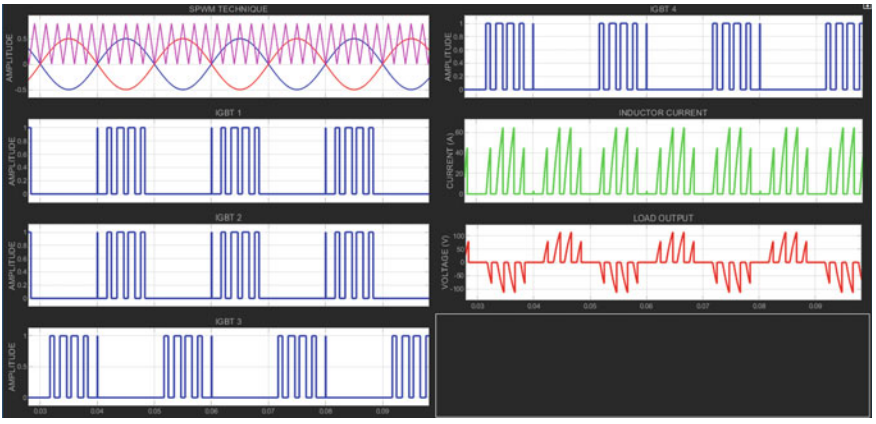

Fig. 6 Output of CSI with PWM technique

The modulation ratio can be defined as the ratio of the magnitude of the output voltage generated for SPWM to the fundamental peak value of the maximum square wave.

$$\text{ma} = \frac{V_{\text{PWM}}}{V_{\text{max-sixstep}}} = \frac{V_{\text{dc}}/2}{2V_{\text{dc}}/\pi} = \frac{\pi}{4} = 78.55\%$$

where VPWM = maximum output voltage is generated by a SPWM and

Vmax-sixstep = the fundamental peak value of a square wave.

The frequency modulation ratio is defined as the ratio of frequency of the carrier wave to the frequency of the modulating (i.e. reference) signal.

$$\text{mf} = \frac{f_c}{f_o}$$

where f_c = frequency of the carrier is signal and

f_o = the frequency of reference signal,

the value of f_o is to be chosen in order to suppress the harmonics.

C. **Transformer**

Here, Fig. 7 shows the equivalent circuit of a transformer which consists of the (Rp) primary resistance, (jxp) primary reactance, (Rs) secondary resistance, and (jxs) secondary reactance.

$$\text{lp} = \frac{2w}{\text{ip}^2} = 2 * \frac{0.0224507}{21.73^2} = 0.095091\,\text{mH}$$

$$\text{ls} = \frac{2w}{\text{is}^2} = 2 * \frac{0.0224507}{50^2} = 0.01796\,\text{mH}$$

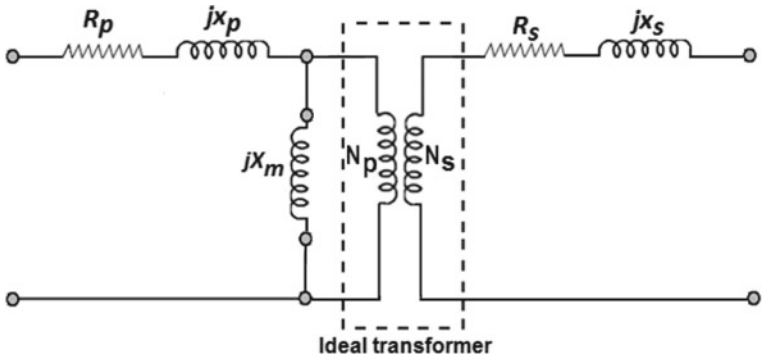

Fig. 7 Transformer circuit

Table 1 Specifications of transformer

S. No.	Parameters	Primary side	Secondary side
1	Voltage	230	100
2	Current	21.73	50
3	No. of turns	40	18
4	Self-inductance	0.095091 mH	0.01796 mH

$\frac{\text{lp}}{\text{ls}} = 5.294599 \approx \left(\frac{Np}{Ns}\right)\frac{Np}{Ns} \approx a^2 = 5.294$

lp = *self-inductance of primary side,*

ls = *self-inductance of secondary side,*

w= total magnetic energy stored (joule)

ip=21.73 A= *primary current*

is=50 A= *secondary current* (Table 1).

On the basis of these parameters, the following simulation of a transformer is carried out with the CSI as well as MLCSI.

As per Figs. 8 and 9, the required values of current and voltage for efficient welding arc are 50–60 A and 100 V, respectively (Figs. 10 and 11).

In case of MLCSI, the load output values of both the CSI are 230 V, which is without transformer. Now by using the new topology that is transformer by connecting it to the MLCI the output will be as follows:

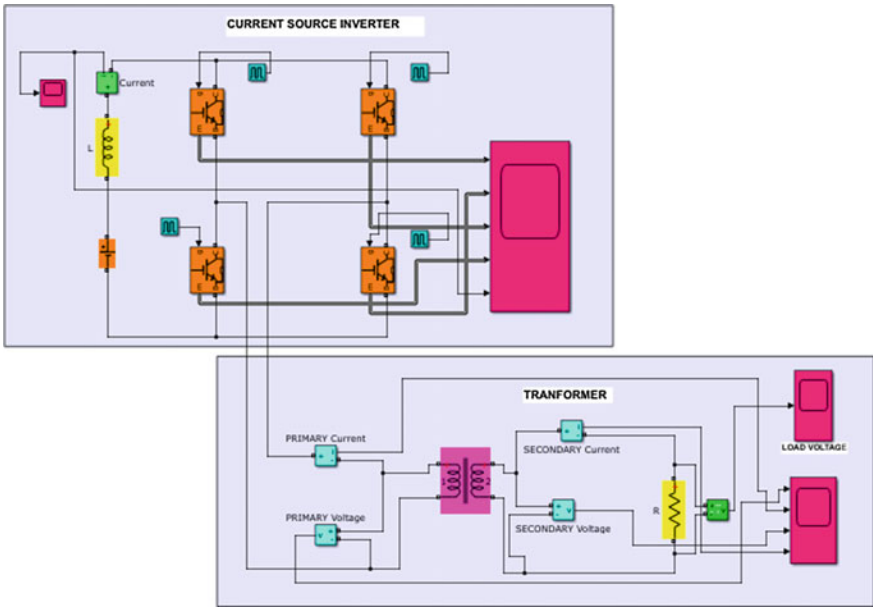

Fig: 8 CSI with transformer

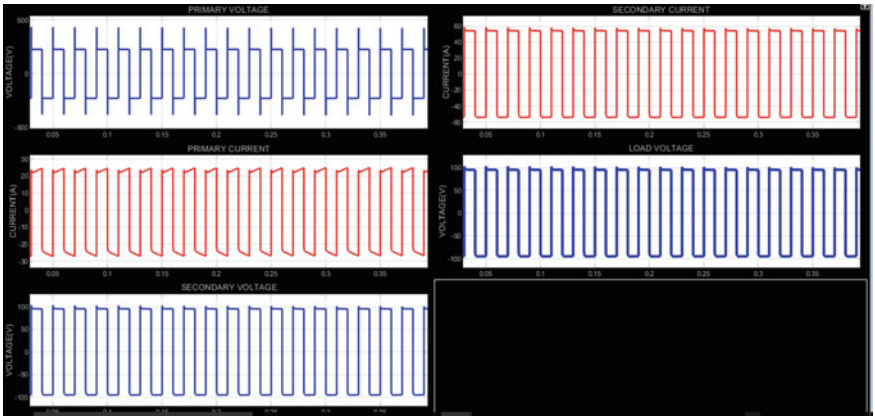

Fig: 9 Load output of CSI with transformer

Fig: 10 MLCSI with no transformer

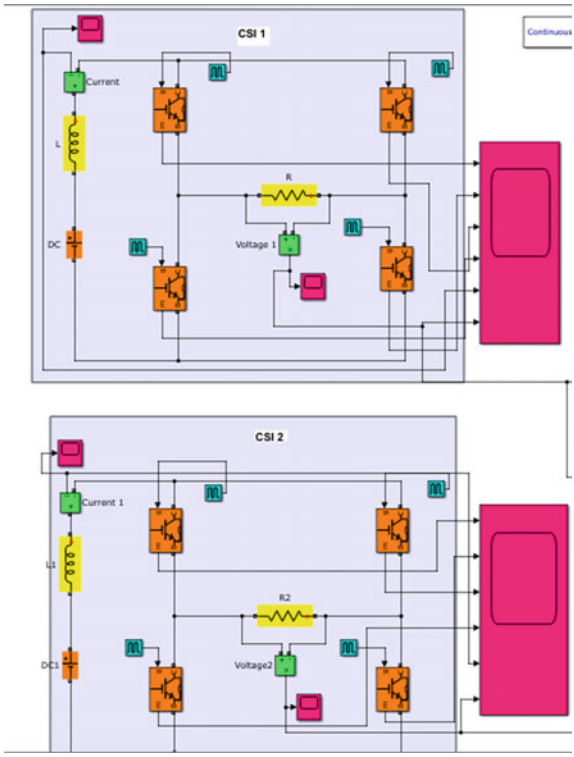

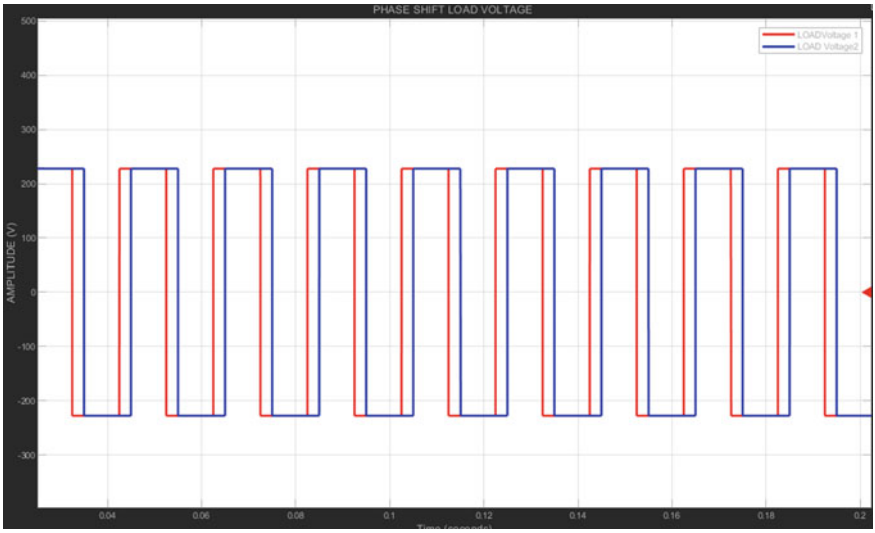

Fig: 11 Output of MLCSI

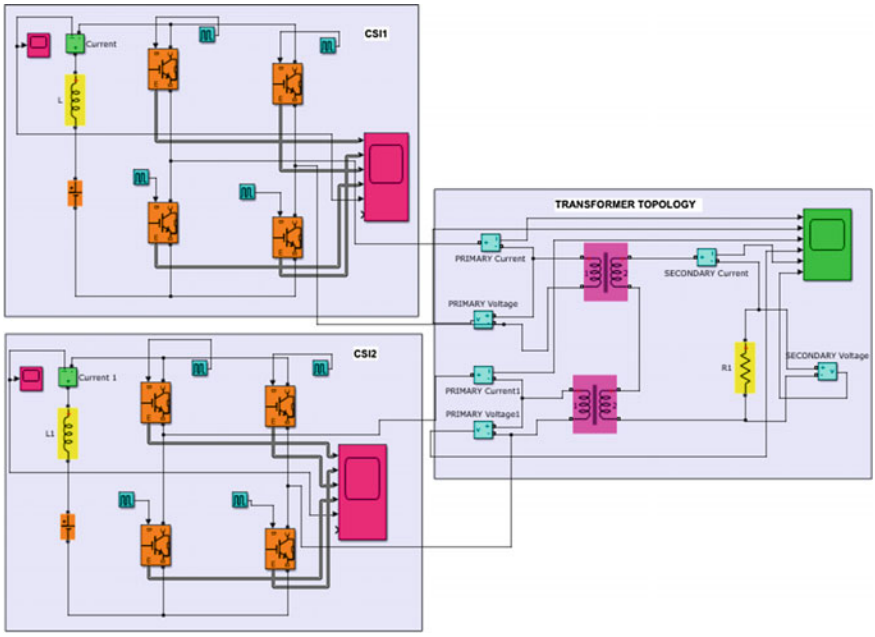

Fig: 12 MLCSI with transformer

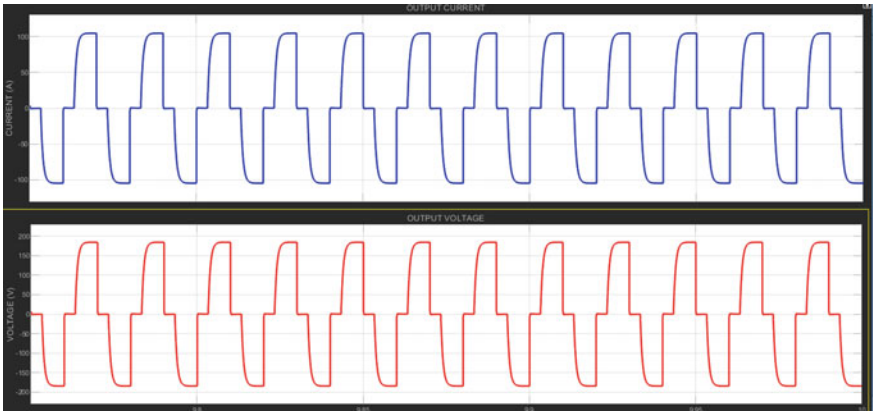

Fig: 13 Output of MLCSI with transformer

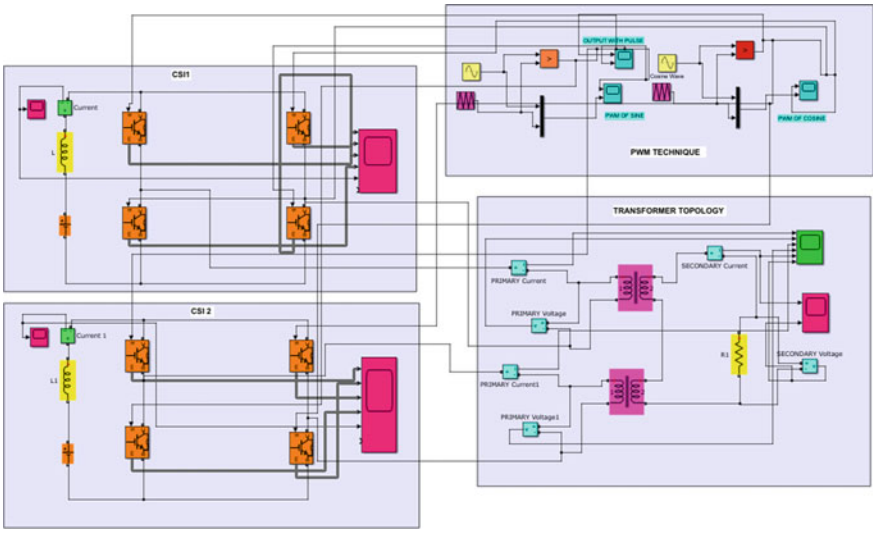

Fig:14 MLCSI using PWM technique

Figure 12 shows the simulation of MLCSI with transformer as a new topology. In this, there are two transformers used; the primary windings of first transformer are connected to the CSI-1, and the primary windings of another transformer are connected to CSI-2. Moreover, one of the secondary windings of both the transformer is series connected, whereas the remaining secondary windings are connected to the load. The load output of this is shown in Fig. 13, where the values of current and voltage are 120 A and 150 V, respectively.

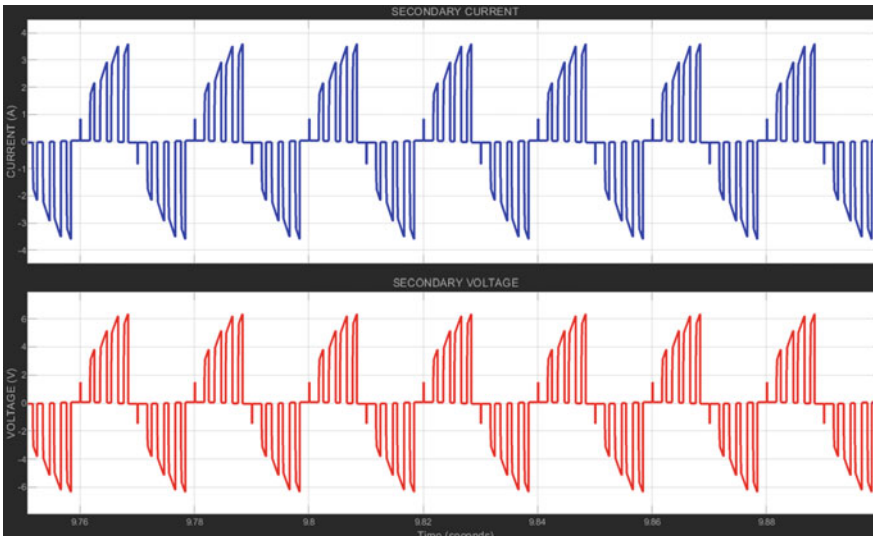

Fig:15 Output of MLCSI using PWM technique

Here, Fig. 14 shows the circuit diagram of MLCSI using PWM technique. Also, the output of MLCSI using PWM technique is shown in Fig. 15. So in this paper, we have seen many methods to get our required values for an efficient welding arc.

5 Conclusion

This paper is proposed and made for the efficient welding arc by using MLCSI, nowadays so many of the defects are arising due to the voltage instability and current. So to overcome this novel, MLCSI is used for the welding purpose. Many different topologies are shown here in the paper, and the relation between the CSI and MLCSI with the attached topologies is also explained with their outputs.

References

1. Proceeding of the IEEE international conference on automation and logistics Zhengzhou, China, August 2012
2. Paul AK (2009) Multitude of benefits for channelizing energy usage through power electronics: welding inverter—a case study. Int Conf Energy Environ: 781–789. ISSN: 2070-3740
3. Gupta JB Utilization of Electric Power & Electric Traction
4. https://www.researchgate.net/publication/265727704. An article for transformer

5. Lai JS, Peng FZ (1996) Multilevel converter the new breed of power converters. IEEE Trans Ind Appl 32(3):509–517
6. Clerk Maxwell J (1892) A treatise with the electricity and magnetism, 3rd edn, vol 2. Oxford, Clarendon
7. Jacobs IS, Bean CP (1963) Fine particles, and the thin films with exchange anisotropy. In: Rado GT, Suhl H (eds) The magnetism, vol III. Academic, New York, pp 271–350
8. Yorozu Y, Hirano M, Oka K, Tagawa Y (1982) Electron spectroscopy the studies on the magneto-optical media along with the plastic substrate interface. In: IEEE translation japan magnetics Japan, vol. 2, pp. 740–741, Aug 1987 (Digests 9th annual conference magnetics Japan, p. 301)

Design, Simulation and Development of Current Source Multilevel Inverter

Akashkumar Tarpada, Karan Chatrani and Mulav P. Rathod

Abstract As multilevel inverter delivers benefits on harmonic reduction as well as increase the output rating, current source multilevel inverter is presented in this research paper with seven numbers of switches. For the given topology, the intermediate $I/2$ current level is one of the major challenges. Simulation and experimental results are presented here to confirm the operation of five-level CSMLI. For, higher power rating superconducting magnetic material used to design and development of current sharing as well as current source inductors. This has some advantages in some circumstances like higher rating of power compare to VSI, inherent four quadrant operation of motor, direct output current controlling, etc.

Keywords Power electronics · Multilevel · Current source · Inverter

1 Introduction

The stereotypic connection of the static power electronics switches in series or parallel could never deliver the results particular application demands. However, to achieve these results a modified topology or combination of predefined H-bridge arrangement must be applied not to forget the major issue to deal with power electronics converter, i.e., reliability. Using the presented topology for CSMLI, the reliability as well as the power quality issues regarding harmonic distortion and harmonic spectrum up to 31 harmonic number is presented. The predominance of high-frequency

A. Tarpada (✉) · K. Chatrani
Electrical Engineering Department, Sardar Vallabhbhai Patel Institute of Technology, Gujarat Technological University, Ahmedabad, India
e-mail: akasht1297@gmail.com

K. Chatrani
e-mail: chatranikarann13@gmail.com

M. P. Rathod
Electrical Engineering Department, Sardar Vallabhbhai Patel Institute of Technology, Vadodara, Gujarat, India
e-mail: mulavrathod.elect@svitvasad.ac.in

A. Mehta et al. (eds.), *Advances in Electric Power and Energy Infrastructure*, Lecture Notes in Electrical Engineering 608,
https://doi.org/10.1007/978-981-15-0206-4_13

introduction for the power electronics converter is also challenged in this topology where entire design and development are done on fundamental frequency 50 Hz.

The main aim of going for this current source converter is to be able to handle high current output, reduce harmonic signature and meanwhile assure the reliability. The bucket list to protect the personnel as well as the devices is also being taken care of while designing the circuit gating configuration.

Multilevel inverter designed for mostly voltage source inverter. The reason behind it is requirement of higher power inverter [1–3]. This inverter is beneficial in terms of reduced harmonics level as well as the higher rating of output power because of the different levels of output current or voltage. The VSI is generally used for multilevel concepts [1]. The one of the most important reasons is inductors. The inductor has disadvantage in higher conducting losses as well as storage efficiency compared to capacitor [4]. By using superconducting material for inductor, this can be eliminated [5]. In this CSI, the level is being achieved by several levels of DC inductor currents, which is same as VSI using the capacitor for voltage level [3, 5]. The 7 switches topology is presented for five-level current and eight- level switches for seven-level of output current. The benefit of higher level of output is reduction in total harmonics distortion. The results of PSCAD and multisim are presented here.

In CSI, input current is constant but adjustable. The amplitude of output current from CSI is independent of the load. However, magnitude of output voltage and its waveform output from CSI is dependent upon the nature of load resistance. Generally, L filter is used before CSI to make its output ripple-free.

2 Proposed Topology

Figure 1 shows the schematic diagram of single-phase five-level current source inverter (CSI) using new topology. In this, a couple of inductors are used. The inductors are used to share equal current in each branch. The numbers of power electronic switches used are seven. The power electronic switch can be MOSFET or IGBT depending upon the range of frequency. For power MOSFET, the frequency range is greater than 100 kHz while for IGBT it is less than 20 kHz. In voltage source inverter, different voltage rated devices are combined to take advantage of their particular ratings. The principle of selecting rating device remains same but in this current is important.

For N level inverter, $[\{(N + 7)/2\} + 1]$ power switches are used while $(N - 1)/2$ current sharing inductors are used. For the particular current level, by applying proper control signal to the devices current balance is guaranteed. From this, the calculation of the current level in one current sharing inductor is calculated and is given by

$$I_1 = I_2 = I_3 = \cdots = 2I/(N - 1)$$

For example, for five-level current in current sharing inductor is $I/2$.

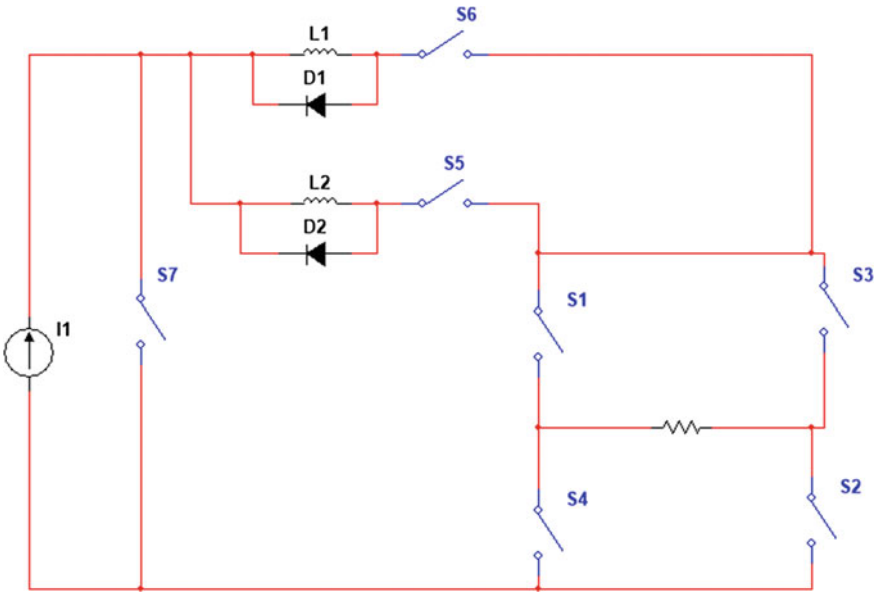

Fig. 1 Proposed topology of five-level inverter and experimental setup with seven numbers of switches

'I' is the source current and $I_1, I_2, I_3, \ldots I(N-1)$ are the current flowing through current sharing inductors.

Figure 2 is for seven-level of inverter output. To obtain the desire level output, switches must be controlled by using single pulse modulation technique. In case of VSI for five- level, totally 8 number of switches are used. Using the structure shown in Fig. 1, one is able to generate five levels in output load current.

Here, H-bridge is combined with 3 switches.

One method to make a current source is the inductance, which has high value and is connected in series with the DC source. In this manner, practical current source is possible to make. The solar panel used is also an example of current source.

Current source describes that it supplies constant current for a constant load. Ideal current source is just a concept and it is very hard to achieve. But it can be achieved near to constant current source. The internal resistance of an ideal current source is infinite. Van de graph generator is the example of the constant current source because it has very high output voltage coupled with its very high output resistance, and so it supplies constant current.

The proposed topology has several benefits like power circuit of CSI is simpler and more robust comparatively with VSI, as VSI requires numbers of capacitors for each level and freewheeling diodes as well. The different types of topology are used, so current flowing through each inductor depends on its position.

Losses are an important factor of power electronics since lower losses give higher efficiency. As different switches work on different balancing control schemes, they

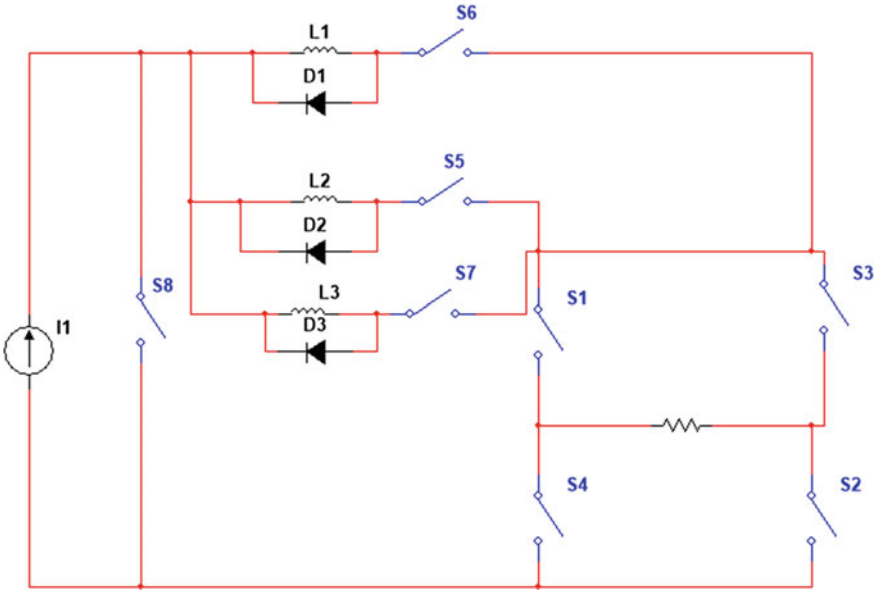

Fig. 2 Proposed topology of five-level inverter and experimental setup with seven numbers of switches

will not have same power losses or switching losses. The power losses during one second are defined by $V =$ voltage across switch during turn on, $I =$ current flowing through closed switch and $t =$ closed time of switch.

That is, $P = V*I*t$.

Power losses in CSI are less cause time of switching is in milliseconds.

If the number of levels increases in VSI, then the number of devices increases in higher rate comparing with CSI.

There is different topology in VSI even though CSI has lowest number of devices which reduce topology (Fig. 3).

The CSMLI is a three-phase topology that consists of a number of current source six-valve module, and in addition, there are also $m - 3$ positions with inductors to smooth the DC-side current and to divide its source into deferent current ratings. Only one current source is needed. As with many of the other MLI topologies, one of the advantages with the GMCSI topology is that it can eliminate the use of transformers in some high-power applications. Also the modularized conjuration is advantageous, and the topology is not as component heavy as some other topologies [5]. The above-mentioned topology is single-level three-phase topology. For five-level three-phase, the number of device required is more than 6.

One problem with the CSMLI, comparable with the voltage unbalance problem in some of the VSIs, is that there can be a current unbalance in the smoothing inductors. This problem can however be solved with the use of redundant switching states.

Generalized Multilevel Current Source Inverter (CSMLI)

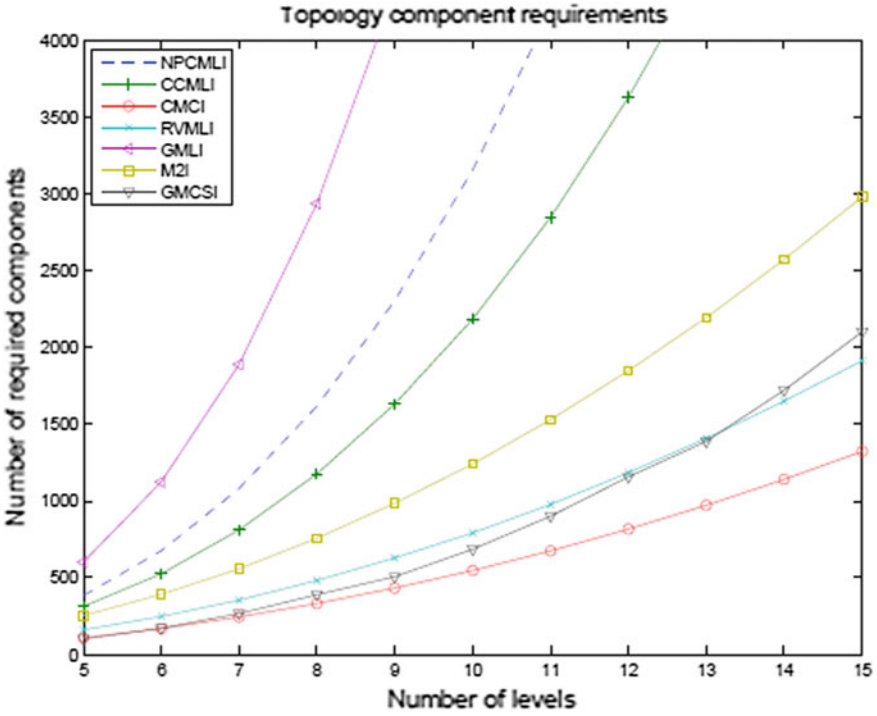

Fig. 3 Components versus graphs

+ Very few components required
+ Modularized design
+ Inductor current balancing capabilities
− Needs additional logic together with SPWM
+ Indicates benefits
− Indicates limitations or disadvantages.

3 Controlling Strategies

The possible combination of the switching is as shown in Fig. 4 for five-level and Fig. 5 for seven-level. This kind of gate pulse is generated by using microcontroller. The benefit of using microcontroller is accuracy in the switching of devices. This switching is known as the asymmetric switching. Although the symmetric switching pattern has advantage of 50% of duty cycle, it increases the ripple in the current sharing inductors. This is the disadvantage of symmetrical switching in the current source multilevel inverter (Table 1).

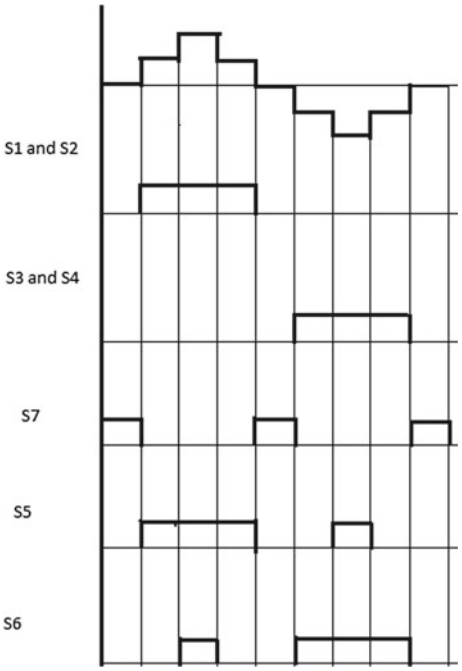

Fig. 4 Gate pulses for five-level inverter

The switching strategy should ensure two main requirements, first is generation of desired levels of output current and the second thing is current balance between current sharing inductors. These requirements are being fulfilled by different switching combinations. For five-level, two current sharing inductors are used, and for this, the control of the device in series with the inductor is shown in Fig. 4 S5 and S6. Same for seven-level is shown in Fig. 5 S5, S6 and S7.

In controlling isolation can provided by opto-coupler or driver IC's. In some cases, PWM techniques are also used. Isolation reduces the controlling circuit from power circuit. Here, different microcontrollers like STM board and digital signal processors can be used (Table 2).

Switching pattern must fulfill some specifications. To begin with, average voltage across the inductor must be zero regardless of load is connected. If not, then change in current will be there current may be unbalanced. Another point is that current sharing inductors should have minimum ripple. And current balance must be there to reduce harmonic stress on the devices.

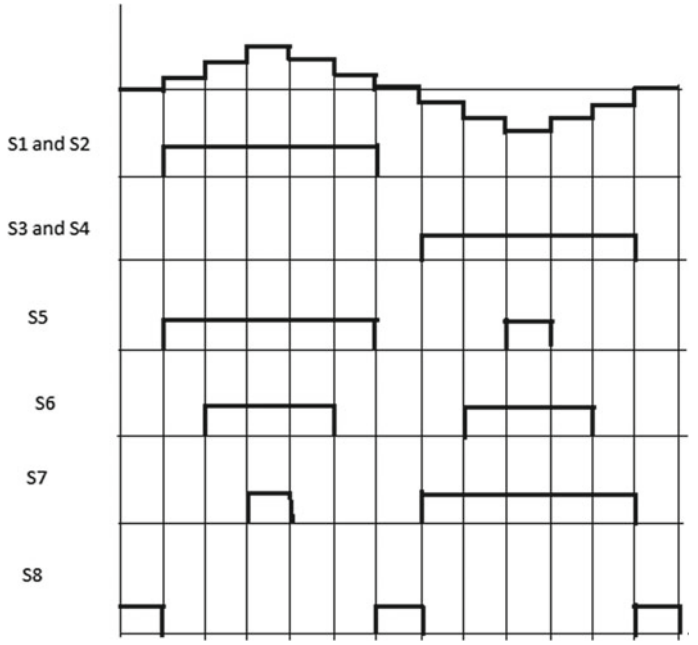

Fig. 5 Gate pulses for seven-level inverter

Table 1 Switching pattern for five-level

S. No.	S1	S2	S3	S4	S5	S6	S7
$-I$	0	0	1	1	1	1	0
$-I/2$	0	0	1	1	0	1	0
0	0	0	0	0	0	0	1
$I/2$	1	1	0	0	1	0	0
I	1	1	0	0	1	1	0

Table 2 Switching pattern for five-level

S. No	S1	S2	S3	S4	S5	S6	S7	S8
$-I$	0	0	1	1	1	1	1	0
$-2I/3$	0	0	1	1	0	1	1	0
$-I/3$	0	0	1	1	0	0	1	0
0	0	0	0	0	0	0	0	1
$I/3$	1	1	0	0	1	0	0	0
$2I/3$	1	1	0	0	1	1	0	0
I	1	1	0	0	1	1	1	0

4 Simulation Results

Here, gate pulse simulation and five-level simulation are described. For 20 A current sources, the current sharing inductor is used. The frequency of switching devices is 50 Hz. The output waveform of current is shown in Fig. 7. In this, the one level is near to the 10 A because the current sharing inductor designed for 10 A, which shares near to the 10 A in equal manner.

In Fig. 6, for switches S4 and S7 the on time is 1.25 ms and off time is 8.8 ms, and for switches S5 and S6, the on time is after some delay that is 11.25–18.75 ms. In this way, cross-conduction is avoided. The generated gate signal is for 50 Hz (Figs. 7, 8 and 9).

Here, prototype experiment is done. Supply is given through 10 V DC and 15 mH is the current source, and two 8 mH current sharing inductors are used. The given

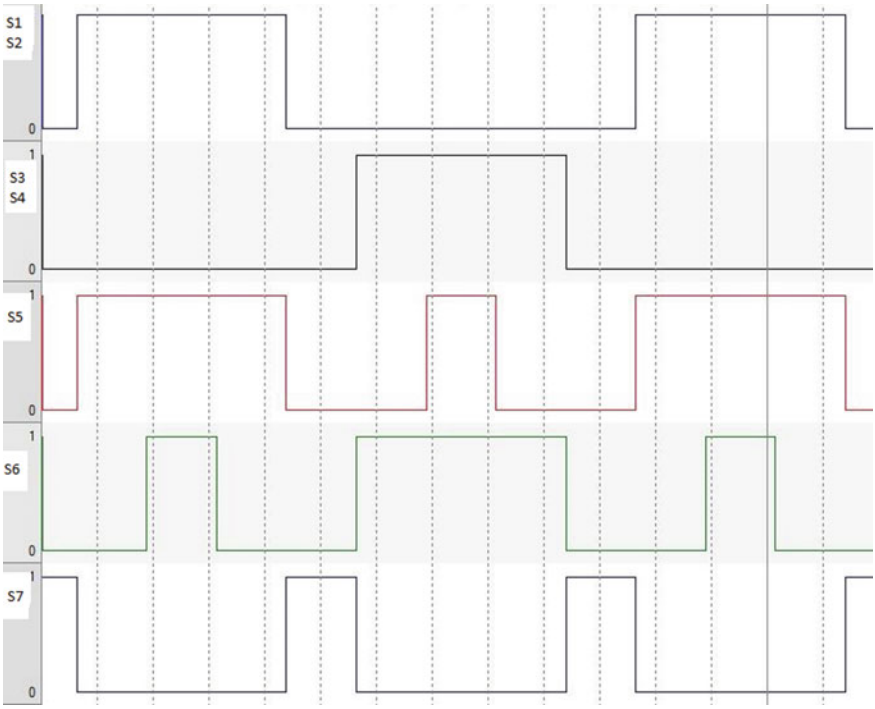

Fig. 6 Gate pulses for five- level

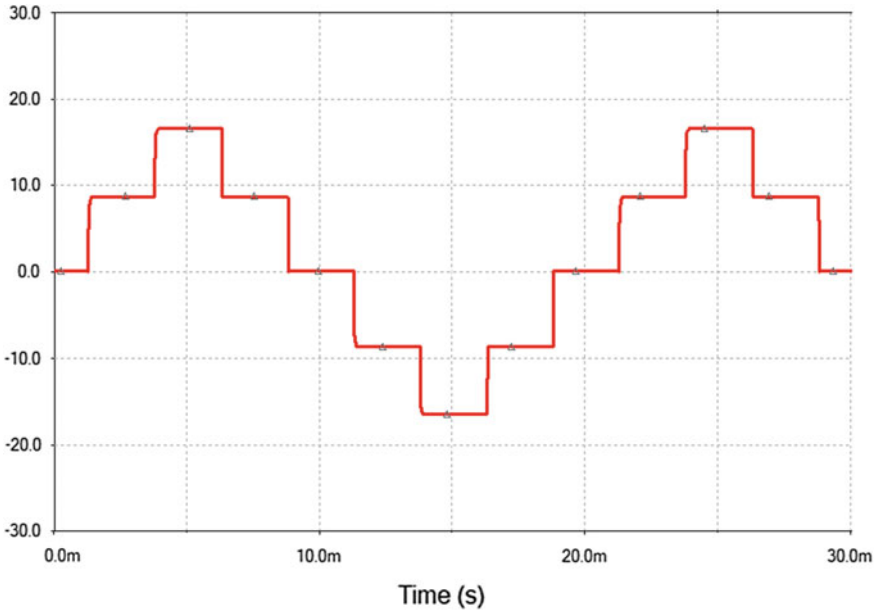

Fig. 7 Output of five-level in multisim

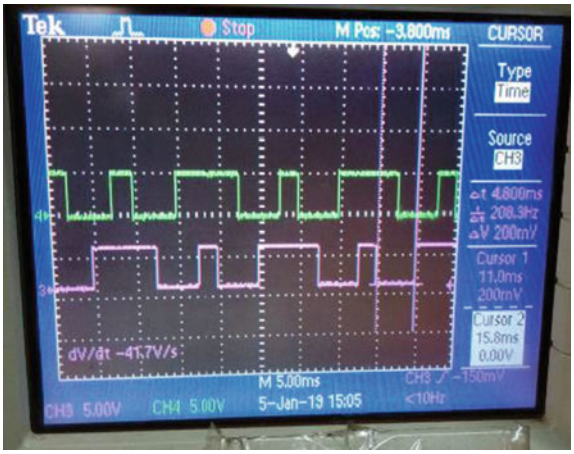

Fig. 8 Gate pulse experimental result

output is for 10 Ω, 10-W resister. The given spike is due to over current and improper design of inductors. By doing proper design of inductors, five-level can be easily achieved (Figs. 10 and 11).

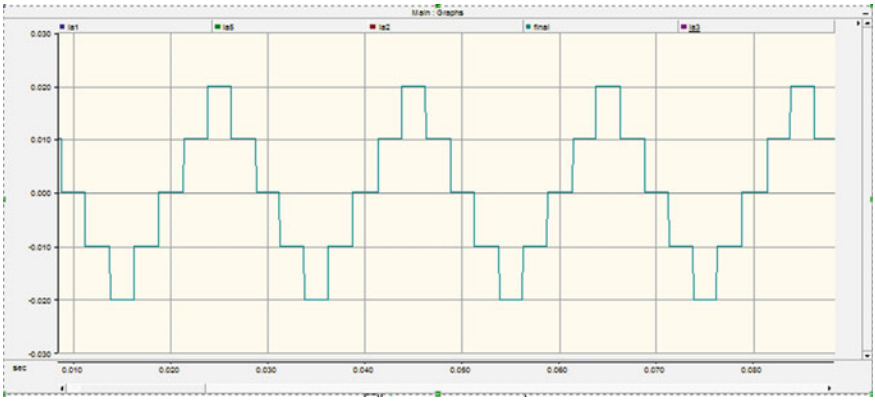

Fig. 9 Simulation result in PSCAD

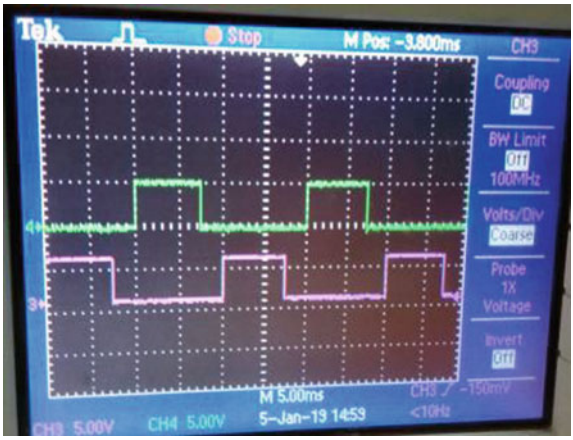

Fig. 10 Gate pulse experimental result

Fig. 11 Gate pulse experimental result

5 Conclusion

A modified proposed topology of seven switches for five-level CSI is presented in this research paper. A current source made by DC source in series with high value of inductor. Single pulse width modulation technique is used here. The single pulse is designed by AT89C51 microcontroller. Simulation as well as hardware for small prototype is presented in this paper. The current balance between two current sharing inductors is guaranteed using appropriate switching. One of the major advantages of CSI is the number of devices used for the same level of VSI is less. In CSI, there is no need of voltage balancing capacitor and freewheeling diode across switches. The main problem of cross conduction is also solved. The protection required for CSI compared to VSI is less. Applications of CSIs are speed control of ac motors, induction heating, lagging VAR compensation synchronous motor starting, etc.

References

1. Antunes FLM, Braga HAC (1999) Application of a generalized current multilevel cell to current-source inverters. IEEE Trans Ind Appl 46(1):31–38
2. Zhang ZC et al (1993) Multi-modular current-source SPWM converter for superconducting magnetic energy storage system. IEEE Trans PE 8(3):250–256
3. Xiong Y, Chen D, Deng S, Zhang Z. A single phase multilevel current source inverter
4. Hosseini SH, Kangarlu MF, Sadigh AK. A new topology for multilevel current source inverter with reduced number of switches
5. Bao J, Holmes DG, Bai Z, Zhang Z, Xu D. PWM control of a 5 level single phase current source inverter with controlled intermediate DC-link current
6. Braga HAC, Barbi I (1995) A new technique for parallel connection of commutation cells: analysis, design and experimentation. In: PESC-1995 conference, pp 81–86
7. Lai J-S, Peng FZ (1996) Multilevel converter—a new breed of power converters. IEEE Trans Ind Appl 32(3):509–517

Generalised Fault-Tolerant Structure for Multilevel Inverter

Shubham Gajbhiye, Pradyumn Chaturvedi, Sai Krishna Saketi and Pranav Mohod

Abstract Nowadays, multilevel inverter is of high importance in various applications ranging from few watts to several megawatts power levels in industries. But the failure rates of these inverters are also an area of concern. This paper proposes a generalised fault-tolerant structure of multilevel inverter. The proposed inverter delivers power to the load under faulty switch conditions. Thus, it maintains continuous power supply to the load with improved reliability. Reliability of the proposed structure is evaluated with mean time to failure (MTTF) calculations using the Markov chain method. The performance of proposed structure is validated via simulation in MATLAB/Simulink environment.

Keywords Fault-tolerant multilevel inverter · MTTF · Reliability

1 Introduction

With the recent advancements in power electronics, the power requirement and its supply to the industries have increased significantly. For this purpose, novel solution of implementing power electronics devices is considered. Thus, the power levels can be increased with increase in voltage levels and keeping the current at low values using the multilevel inverters [1]. Multilevel inverters give the advantages of better power quality, low dv/dt stress on the switches, higher voltage levels, etc. [2].

It is well known that the power electronics devices only consist of the various power semiconductor devices to operate with. The semiconductor devices with a

S. Gajbhiye · P. Chaturvedi (✉) · S. K. Saketi · P. Mohod
Department of Electrical Engineering, Visvesvaraya National Institute of Technology, Nagpur, India
e-mail: pc220774@gmail.com

S. Gajbhiye
e-mail: Shubham.gajbhiye21@gmail.com

A. Mehta et al. (eds.), *Advances in Electric Power and Energy Infrastructure*, Lecture Notes in Electrical Engineering 608,
https://doi.org/10.1007/978-981-15-0206-4_14

fact are mostly prone to faults and possess less reliability [3]. If any fault occurs at inverting stage in the system, then the whole system will go out of service and there is huge financial loss due to high initial investments. Thus, the fault-tolerant approach instead of conventional inverters will not only increases its reliability but also ensures better quality of output voltages. Although with the increase in reliability, there is slight increase in its cost but in many industrial applications continuous operation is of most importance which will serve its purpose. Now so as to improve the fault-tolerant ability, various structures are proposed in the different research works. Some consist of redundant switches, redundant modules and standby units [4].

The main topologies for conventional multilevel inverters used in industries are flying capacitor converter [5], diode-clamped converter [6] and cascaded H-bridge inverter [7]. Among these topologies, cascaded H-bridge is considered as the most reliable and gained a huge demand among researchers. In [8], topologies have been proposed to tolerate open circuit faults but it cannot tolerate fault on all the switches. Also, the utilisation of DC sources is zero during faulty conditions. Inner-leg switch faults cannot be tolerated in the topology proposed in [9]. The topology given in [10] uses relays to operate during fault in each module and makes the DC sources in series to keep the peak-to-peak voltage level.

In this paper, a technique of maintaining peak-to-peak output voltage magnitude, even after fault occurs, and a new topology using CHB is proposed which bypasses the faulty module. This is achieved by employing variable DC source. The variable DC source is a boost converter which operates depending upon module output signal. This is a complete fault-tolerant topology which can handle fault on any of the switches without deteriorating the output voltage levels and prevents the complete shutdown of the system. Reliability of the system for under different operating conditions is presented and compared with the existing system.

In Sect. 2, the proposed fault-tolerant structure of MLI and its control strategy is given. Markov reliability chain theory is discussed with reliability evaluation under different fault conditions is presented in Sect. 3. In Sect. 4, the simulation and results are presented. Finally, in Sect. 5, conclusion for the work is given.

2 Proposed Circuit and Controlling Method

2.1 Proposed Fault-Tolerant Scheme

The proposed circuit is based on cascaded H-bridge multilevel inverter. This circuit can eliminate and isolate the defected module from the whole circuit in the event of a component failure in one of the modules, so it can prevent the whole system to fail. The load can be feed by the remained modules in the proposed circuit with decreasing output voltage level and without changing the peak-to-peak value of output voltage (still symmetrical sinusoidal output). Figure 2 shows a five-level structure of the proposed cascaded MLI which by means of voltage sensors and variable DC source in each module can perform the isolation and elimination of the defected module from the whole circuit (Fig. 1).

V_1 is the voltage sensor provided in the upper module and V_2 is the voltage sensor for lower module. V_1 and V_2 can measure the output of each module for healthy as well as faulty condition. Figure 3 shows the variable DC source. Variable DC source is a boost converter which can perform boost operation on one module in case of fault in another module. It means that it will perform boost operation only if fault condition arises in specific simultaneous module.

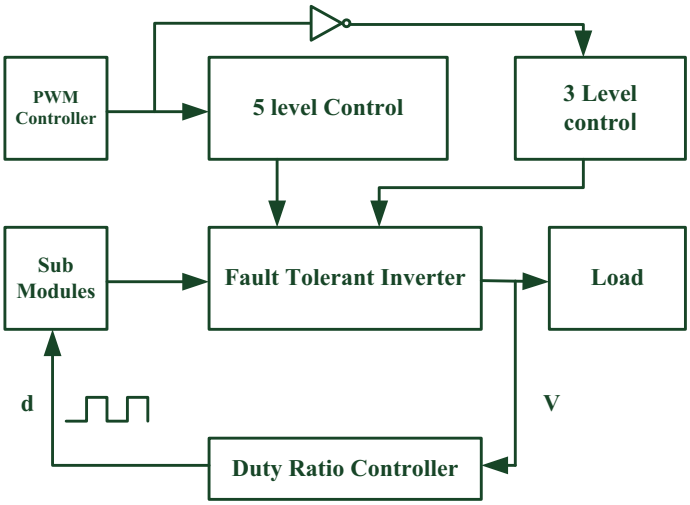

Fig. 1 Block diagram of fault-tolerant structure

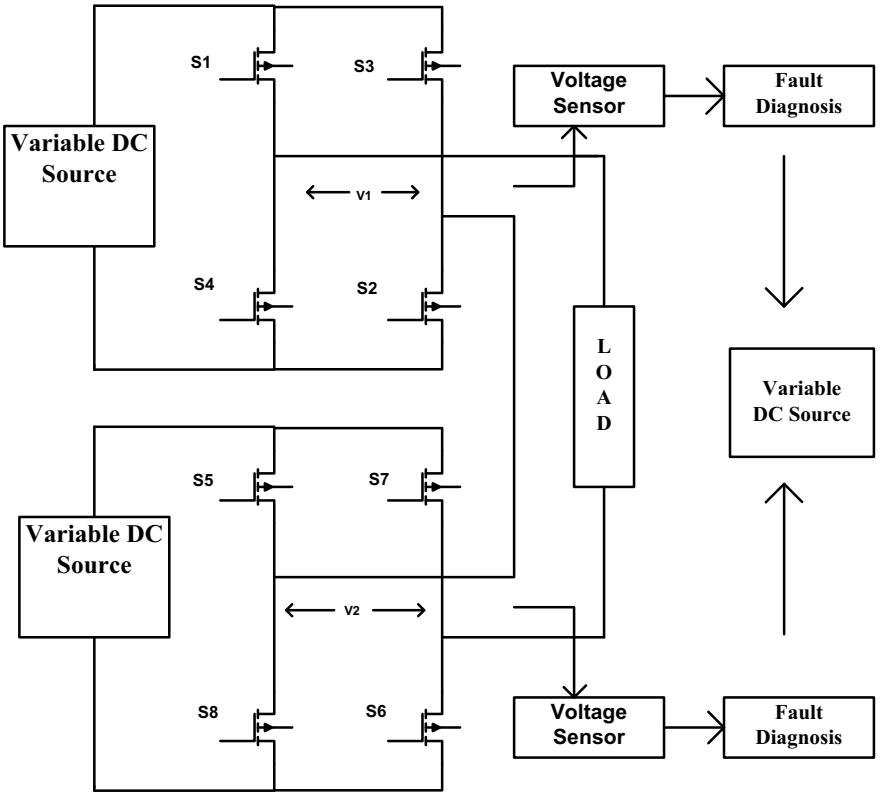

Fig. 2 Proposed five-level CMI

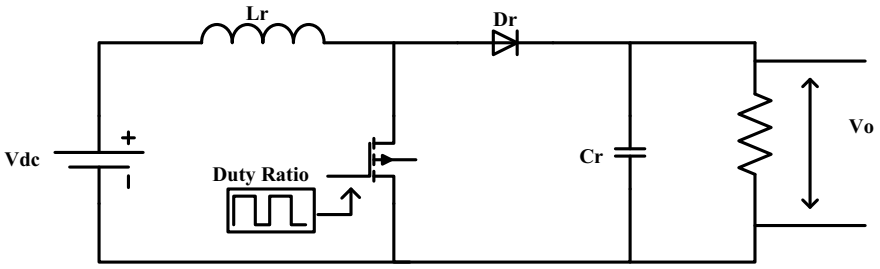

Fig. 3 Variable DC source (boost converter)

The mentioned voltage sensors are connected in a way that in an open-circuit failure occurrence of any component, they can eliminate and isolate the defected module which has the faulty component from the whole system and assure the normal operation of the inverter with one healthy module. Operation of the inverter will continue till the next failure occurs in the only remained module, which will lead

whole system to fail. For instance, suppose if one of the S1–S4 switches (related to upper module) fails, the failure will be detected by fault diagnosis system and based on voltage sensor output variable DC source will operate with increase in output voltage of boost converter. Therefore, beside isolating and eliminating upper module from the circuit, they disconnect V_1 in case of fault in upper module and V_2 in case if fault in lower module with increase in voltage in respective healthy module, so the output voltage peak would not be changed. This can be done by operating the boost converter in variable duty-ratio mode. It is obvious that by isolating upper module, modulation technique must be changed and it is not possible to use the same modulation technique for the three-level inverters with only remaining modules (Tables 1, 2 and 3).

2.2 *Fault Diagnosing Method*

Figure 4 shows the control strategy of proposed CHB. There are two voltage sensors at each module of five-level CHB. These sensors continuously check the output voltage of each module. During healthy condition, the output will be V_{dc1} for module 1 and V_{dc2} for module 2. If the output voltage of respective module not equal to V_{dc}, then the corresponding module is surely not working properly hence can be stated as faulty. Due to this, the inverter is not going to deliver the corresponding desired output. In such case, the fault diagnosis mechanism will then check the output voltage of each module and along with disconnecting the faulty module; it will change the duty ratio of boost converter associated with another module so as to maintain peak-to-peak

Table 1 Proposed CMI switching pattern in normal condition

Device	S1	S2	S3	S4	S5	S6	S7	S8
$+2V_{DC}$	1	1	0	0	1	1	0	0
$+V_{DC}$	1	1	0	0	0	1	0	1
0	1	0	1	0	0	1	0	1
$-V_{DC}$	1	0	1	0	0	0	1	1
$-2V_{DC}$	0	0	1	1	0	0	1	1

Table 2 Proposed CMI switching pattern in upper module fault

Device	S1	S2	S3	S4	S5	S6	S7	S8
$+2V_{dc}$	0	1	0	1	1	1	0	0
0	1	0	1	0	1	0	1	0
$-2V_{dc}$	0	1	0	1	0	0	1	1

Table 3 Proposed CMI switching pattern in lower module fault

Device	S1	S2	S3	S4	S5	S6	S7	S8
$+2V_{dc}$	1	1	0	0	1	0	1	0
0	1	0	1	0	1	0	1	0
$-2V_{dc}$	0	0	1	1	1	0	1	0

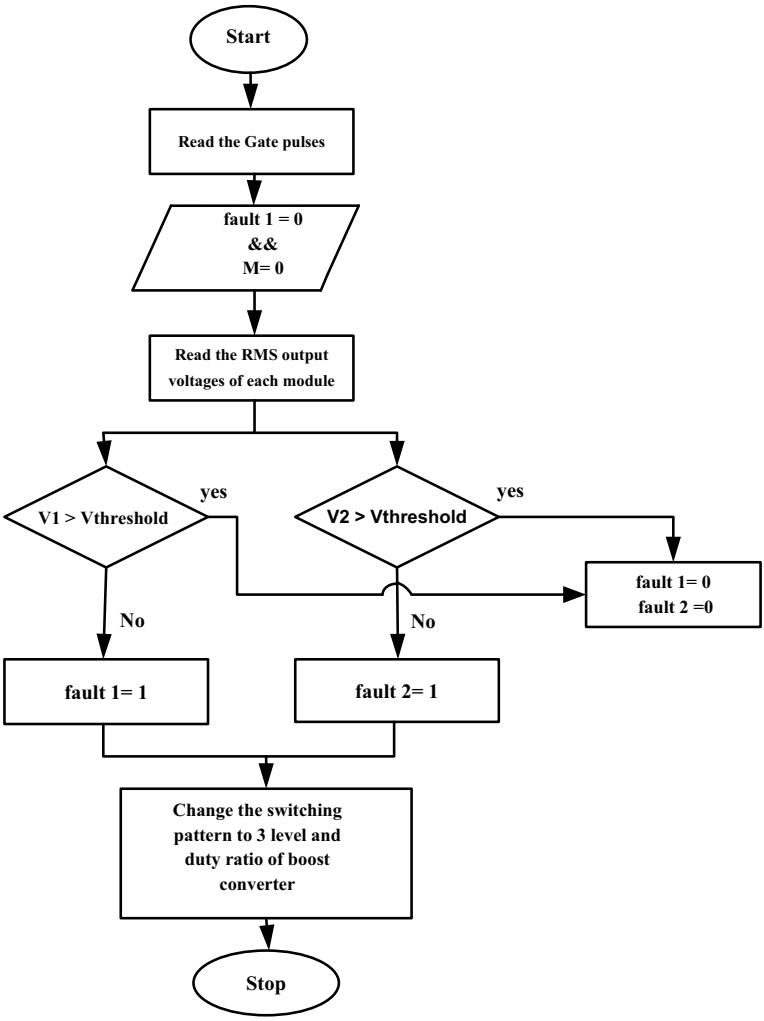

Fig. 4 Control strategy flow chart

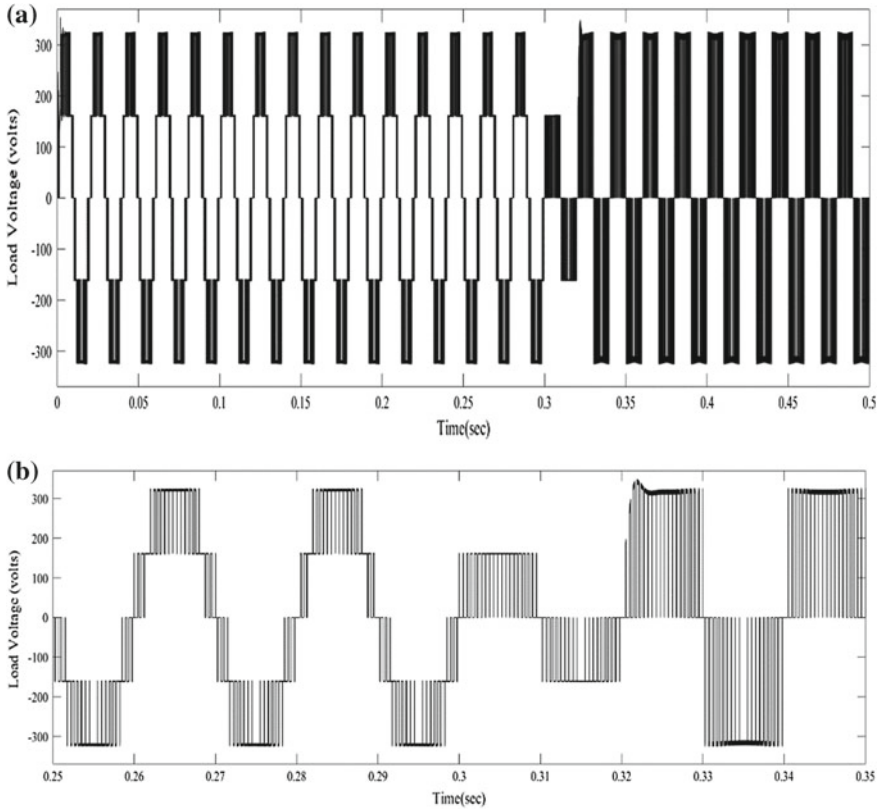

Fig. 5 **a** Output load voltage. **b** Output load voltage closed view at fault instance

voltage with reduced voltage levels. The simulation results are presented in Figs. 5a, b and 6a, b which shows the output voltage before during and after the fault. In this simulation, fault is introduced in upper module at 0.3 s. Simultaneously current through the load is also presented which is remaining constant before and after fault operation is implemented.

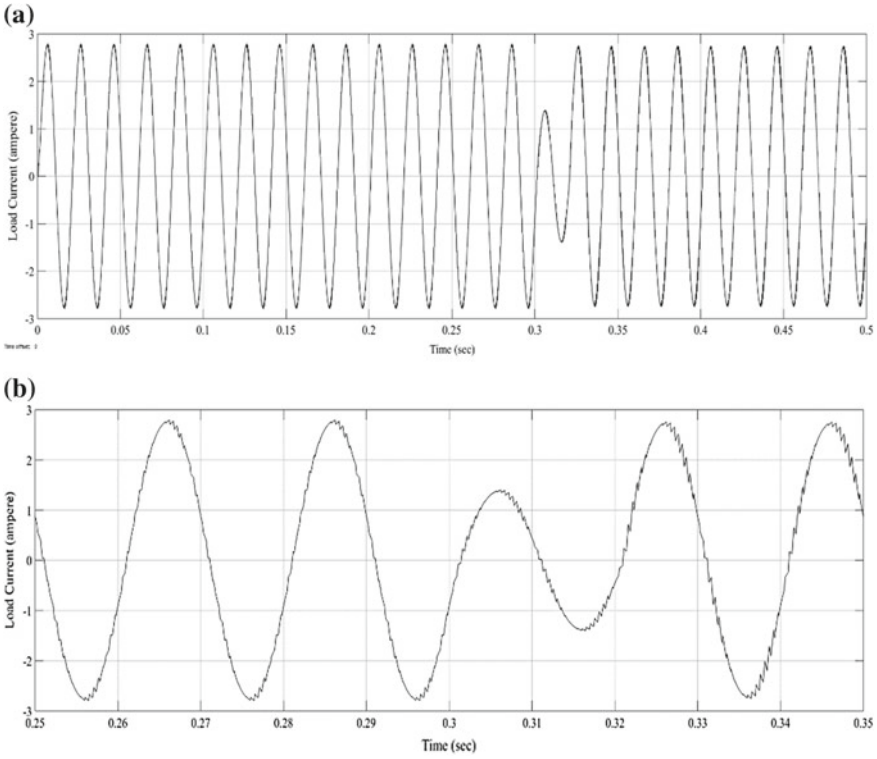

Fig. 6 **a** Output load current. **b** Output load current closed view at fault instance

3 Reliability Evaluation

The proposed fault-tolerant two-module CHB is depicted in Fig. 1. The conditional probability is used in this part to evaluate reliability of the proposed scheme. The first condition is the proper operation of semiconductor switches on the proposed CHB and the second condition is the existence of a failure in one of the semiconductor switches on the any of the modules. Markov chain of the proposed scheme is shown in Fig. 7. It is worth mentioning that improper operation of sensors with fault in switches could result in operation of the inverter in the absorbing state. Probability of each state is calculated as stated in (1)–(4)

$$\mathrm{d}/\mathrm{d}t[P_1(t)P_2(t)P_3(t)P_4(t)] = [P_1(t)P_2(t)P_3(t)P_4(t)] * \begin{bmatrix} -(\lambda_{12}+\lambda_{13}) & \lambda_{12} \\ 0 & -\lambda_{23} \end{bmatrix} \quad (1)$$

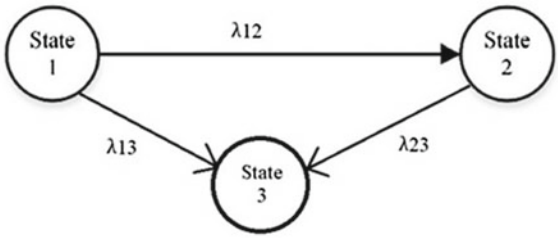

Fig. 7 Markov Chain for proposed circuit

Failure rates of each state in Markov chain

$$\lambda_{12} = 8(\lambda S + \lambda D) * P_r \tag{2}$$

$$\lambda_{13} = 8(\lambda S + \lambda D) * (1 - P_r) + 2\lambda C + 2\lambda BD \tag{3}$$

$$\lambda_{23} = 4(\lambda S + \lambda D) + \lambda C + \lambda BD \tag{4}$$

where P_r is the probability of the proper operation of the Fault mechanism. Since P_1 and P_2 are the upstate of this structure, the reliability is equal to

$$R(t) = \sum_{i=1}^{2} P_i(t) \tag{5}$$

The healthy mode is initially

$$P(0) = [1\ 0\ 0] \tag{6}$$

Probability of each state is

$$P_1(t) = \mathrm{e}^{-(\lambda_{12}+\lambda_{13})} \tag{7}$$

$$P_2(t) = \frac{\lambda_{12}}{\lambda_{23} - \lambda_{12} - \lambda_{13}}\left[\mathrm{e}^{-(\lambda_{12}+\lambda_{13})t} - \mathrm{e}^{-(\lambda_{23})t}\right] \tag{8}$$

$$R(t) = P_1(t) + P_2(t) \tag{9}$$

The failure rates of power electronic components are calculated in this part. The failure rate of each component is obtained by multiplication of different factors related to components.

$$\lambda_{\text{component}} = \lambda b \sum_{i=1}^{n} \pi i \text{ (failure/10}^6 \text{ h)} \tag{10}$$

where n is the number of factors affecting the component failure rate and the basic failure rate of component is λb which is turns related to the components quality and their performance at a given temperature. It is necessary to calculate the power loss of component in order to evaluate the influence of temperature.

4 Simulation Results

In this section, the numerical results of reliability and MTTF calculations are presented. Output power is considered to be equal to $P_{\text{Load}} = 200$ W at the lagging power factor of 0.9. The output frequency is equal to 50 Hz. The maximum output voltage value is 320 V. Thus, in the symmetric CMI, the DC sources are equal to each other and they are considered to be $V_1 = V_2 = 160$.

The calculated power losses, junction temperatures, and temperature factors in different states of operation for MOSFETS and diodes of the proposed CMI scheme, the effective factors of components in the high-frequency link are provided in the table. Where λS and λD are failure rates of switches and diodes of inverter, the failure rates of components of the inverter are given in Table 4 and are taken from [11].

Healthy operation of fault diagnosis system and variable DC source is assumed to be equal to $P_{\text{r}} = 0.9$. Failure rates are presented is Table 5. Reliability equations for the proposed fault-tolerant CHB are, respectively, shown in the following equations:

Table 4 Numerical results

Index	Value
λS	1.18
λD	0.010
λBD	0.013
λC	0.066

Table 5 Failure rates

Failure rates (failure 10^6/h)	λ_{12}	λ_{13}	λ_{23}
Value	8.646	9.756	4.882

$$R(t) = 0.361\mathrm{e}^{-18.396t} + 0.639\mathrm{e}^{-4.882t} \tag{11}$$

$$\mathrm{MTTF} = \int_0^\infty R(t) = 0.149 * 10^6\,\mathrm{H} \tag{12}$$

5 Conclusion

In this project, a novel generalised fault-tolerant structure employed in five-level H-bridge is proposed. It is a flexible topology that means it can be reconfigurable when different faults occur in any of power semiconductor switch of the two modules of five-level CHB. The voltage sensors and variable DC source, i.e. boost converter plays a significant role in reconfiguration of proposed structure from five-level to three-level with maintaining same peak values. For the diagnosis of fault in inverter, a simple methodology is also used. In this methodology, the output voltage of each module of inverter is continuously observed weather it is giving normal output or not according to switching pattern given to inverter. This methodology only requires one sensor for one module hence it is maintaining its simplicity and no complicated is employed for fault diagnosis. Generalised fault-tolerant structure is evaluated in different modes of operation and corresponding Markov chain is also modelled. Then the reliability of the generalised fault-tolerant structure is also validated using this Markov chain. The reliability of generalised fault-tolerant structure is then compared with the convention five-level H-bridge as shown in Fig. 8 and it can be easily seen with fault-tolerant structure its reliability has increased. Finally, by using MATLAB/Simulink, simulation results for various fault conditions are obtained.

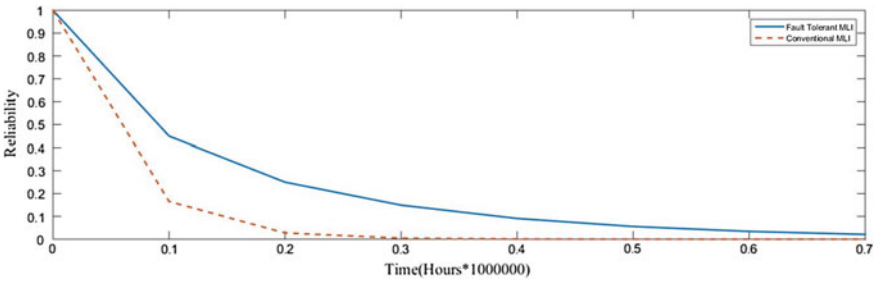

Fig. 8 Reliability comparison of convention and fault-tolerant CHB

References

1. Maddugari SK, Borghate VB, Sabyasachi S, Karasani RR (2017) Fault tolerant cascaded multi-level inverter topology for open circuit faults in switches. In: IEEE transportation electrification conference, 978-1-5386-2668-9/17
2. Semiconductor devices, general specification for, MIL-S-19500 (1994)
3. Chiodo E, Lauria D (2015) Some basic properties of the failure rate of redundant reliability systems in industrial electronics applications. IEEE Trans Ind Electron 62(8):5055–5062
4. Jalhotra M, Kumar L, Gautam SP, Gupta S (2018) Development of fault-tolerant MLI topology. IET Power Electron 8(1):1755–4535
5. Caseiro LMA, Mendes AMS, Cruz SMA (2014) Fault tolerance in back-to-back three-level neutral-point-clamped induction motor drives. In: IET international conference power electronics, machines and drives, Manchester, Apr 2014, pp 1–6
6. Richardeau F, Pham TTL (2013) Reliability calculation of multilevel inverters: theory and applications. IEEE Trans Ind Electron 60(10):4225–4233
7. Kandasamy K, Vilathgamuwa M, Tseng KJ (2015) Inter-module state-of-charge balancing and fault-tolerant operation of cascaded H-bridge converter using multi-dimensional modulation for electric vehicle application. IET Power Electron 8(10):1912–1919
8. Siddique MD, Mustafa A, Sarwar A, Mekhilef S (2018) Single phase symmetrical and asymmetrical design of multilevel inverter topology with reduced number of switches. In: 2018 IEEMA engineer infinite conference, vol 6, no 14, p 17856772
9. Liu H, Loh PC, Blaabjerg F (2013) Review of fault diagnosis and fault-tolerant control for modular multilevel converter of HVDC. In: IECON 2013—39th annual conference of the IEEE Industrial Electronics Society, vol 1, no 14, p 14016062
10. Haji-Esmaeili MM, Naseri M, Khoun-Jahan H, Abapour M (2015) Fault-tolerant structure for cascaded H-bridge multilevel inverter and reliability evaluation. IET Power Electron 8(1):1755–4535
11. Jahan HK, Panahandeh F, Abapour M, Tohidi S (2018) Reconfigurable multilevel inverter with fault-tolerant ability. IEEE Trans Power Electron 33(9)

A Comparative Study of Grid Synchronization Techniques SRF-PLL and DSRF-PLL Under Unbalanced Grid Voltage Condition

Atul Kunpara and Vithal N. Kamat

Abstract This paper presents a comparative study of two grid synchronization techniques, synchronous reference frame phase-locked loop (SRF-PLL) and double synchronous reference frame phase-locked loop (DSRF-PLL) that could be used in grid integration of distributed generation systems. As PLL is playing a vital role in the operation of grid-connected power electronic converters, it is very much important to study their behavior in grid voltage fluctuating condition. It is shown that SRF-PLL gives suitable response when the grid voltage is balanced, but during fluctuating condition of voltage its performance gets deteriorated. But DSRF-PLL is able to track grid voltage phase properly in both conditions as it is having two components separated and decoupled from each other using decoupling network. Performance comparison is verified by MATLAB simulation, and the results are presented.

Keywords Phase-locked loop · Grid synchronization · Grid-connected converter

1 Introduction

Day by day there is a rise in consumption of electricity, and this increases the demand of electrical energy continuously. Due to the constraint on fossil fuel availability and pollution created by conventional power generation plant, all countries are promoting distributed generation like wind power and solar power. To use electricity generated by this distributed power generation means, it is necessary to integrate distributed power generating unit with grid.

A. Kunpara (✉)
Gujarat Technological University, Ahmedabad, India
e-mail: atuls86@gmail.com

V. N. Kamat
Baroda Electric Meters Ltd., Anand, India

A. Mehta et al. (eds.), *Advances in Electric Power and Energy Infrastructure*, Lecture Notes in Electrical Engineering 608,
https://doi.org/10.1007/978-981-15-0206-4_15

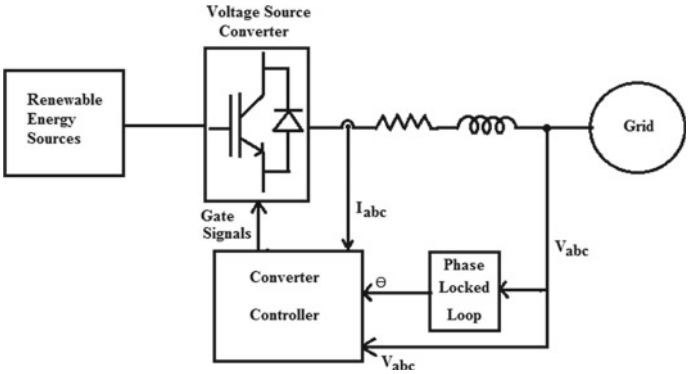

Fig. 1 Grid-connected VSC for renewable energy sources

The performance of grid-connected voltage source converter mainly depends on the effective detection of phase and frequency of grid at point of common coupling. This job of detecting phase and frequency is performed by grid synchronization techniques which have been discussed in [1]. Figure 1 shows the position of PLL in block diagram representation of grid-connected converter. Apart from the use of PLL in grid-connected converter, it is also used in many applications like AC to DC converter, FACT devices and HVDC systems [2, 3].

Though there are many methods of grid synchronization using PLL, SRF-PLL and DSRF-PLL have got more popularity because of their simplicity in implementation and better performance. In this paper, the performance of these two synchronous reference frame PLL is investigated with grid voltage amplitude fluctuations. From the comparative study presented here, we can choose proper topology for the application of grid connection of power electronic converters.

Organization of this paper is divided into different section as follows. In Sect. 2, the basic theory aspects of SRF-PLL and DSRF-PLL are discussed, and in Sect. 3 MATLAB simulation setup is presented. In Sect. 4 results and discussion of both PLL are given, and the conclusion of study is drawn in Sect. 5.

2 Grid Synchronization Methods

In the applications where there is a requirement of grid integration of power electronic converter, most important is to have information of grid voltage frequency and phase. This information is obtained with the help of phase-locked loop. In this section, SRF-PLL and DSRF-PLL will be discussed.

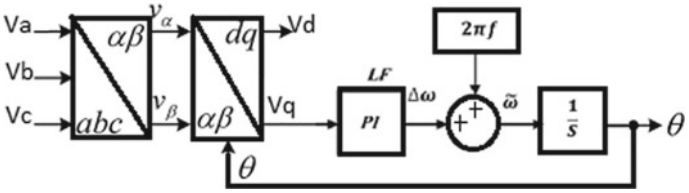

Fig. 2 Basic structure of SRF-PLL

2.1 SRF-PLL

This is the most widely used synchronous reference frame PLL, and its basic block diagram is given in Fig. 2. From figure, we can see that in this topology of PLL, the first three-phase voltage is transformed from abc reference frame to α-β reference frame and then from α-β reference frame to synchronously rotating positive d-q reference frame by using Clarke and Park transformation technique [4].

The formula used for Clarke and Park transformation to obtain V_d and V_q component from V_{abc} voltage of grid is given below:

$$\begin{bmatrix} V_\alpha \\ V_\beta \end{bmatrix} = \frac{2}{3}\begin{bmatrix} 1 & -1/2 & -1/2 \\ 0 & \sqrt{3}/2 & -\sqrt{3}/2 \end{bmatrix}\begin{bmatrix} V_a \\ V_b \\ V_c \end{bmatrix} \tag{1}$$

$$\begin{bmatrix} V_{d+} \\ V_{q+} \end{bmatrix} = \begin{bmatrix} \cos\theta & \sin\theta \\ -\sin\theta & \cos\theta \end{bmatrix}\begin{bmatrix} V_\alpha \\ V_\beta \end{bmatrix} \tag{2}$$

where θ is the phase angle of grid voltage.

With d-q reference voltage, a PI feedback controller with feed forward component of $\omega = 2\pi f$ (nominal grid frequency) is used to get synchronization with grid voltage. With proper tuning of PI controller, the grid parameters like voltage frequency and phase angle are detected. However, in SRF-PLL, only positive sequence component of grid voltage is used to detect the phase and frequency, also cross-coupling of negative sequence component is not canceled out, and its performance during unbalanced voltage condition gets deteriorated.

2.2 DSRF-PLL

In this topology of PLL, symmetrical component of unbalanced grid voltage is first obtained using Clarke and Park transformation combination in double reference frame rotating opposite to each other [5]. Then, the positive sequence component is used to apply with PLL, and thus, it is known as DSRF-PLL as it is working on two

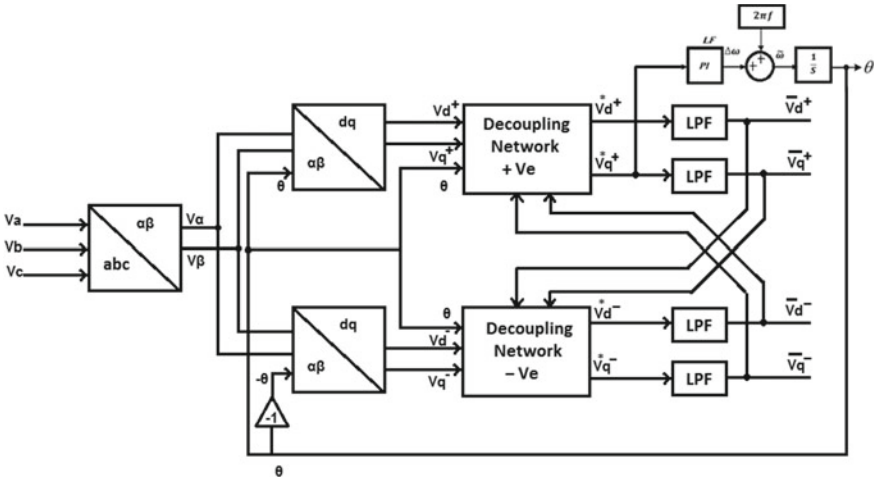

Fig. 3 Block diagram of DSRF-PLL

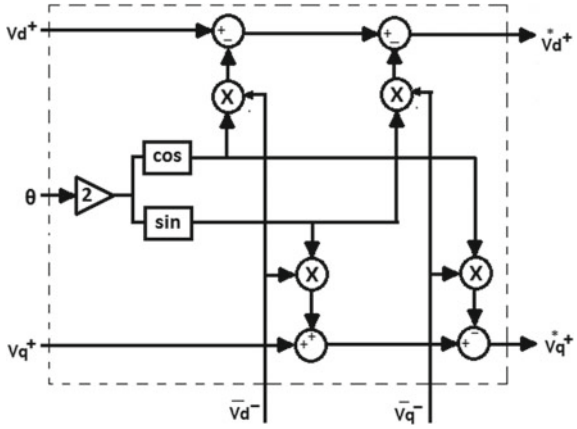

Fig. 4 Decoupling network positive (+Ve)

reference frame parameter separately. The block diagram representation of DSRF-PLL is shown in Fig. 3. It can be divided into three parts: (1) obtain positive and negative symmetrical component of grid voltage, (2) remove the coupling between two reference frames using decoupling network and (3) obtain phase and frequency.

In double synchronous reference frame, two reference frames are rotating in opposite direction to each other, and thus, voltage in each sequence will have double frequency coupling component. A decoupling network is used to remove the coupling effect of double frequency component. The detailed structure of decoupling network positive (+Ve) used in DSRF-PLL is shown in Fig. 4, and decoupling network negative (−Ve) can be drawn in a similar manner. In DSRF-PLL, improvement in

performance is coming because of this decoupling network [5] which is canceling the effect of cross-coupling of positive and negative sequence component of unbalanced voltage.

3 Simulation Model

In this section, simulation model of SRF-PLL and DSRF-PLL using MATLAB/Simulink software is presented. Figure 5 shows the Simulink model of SRF-PLL, and Fig. 6 shows the Simulink model of DSRF-PLL. In DSRF-PLL, it can be seen that decoupling network is used in combination with SRF-PLL to detect the phase of positive sequence grid voltage.

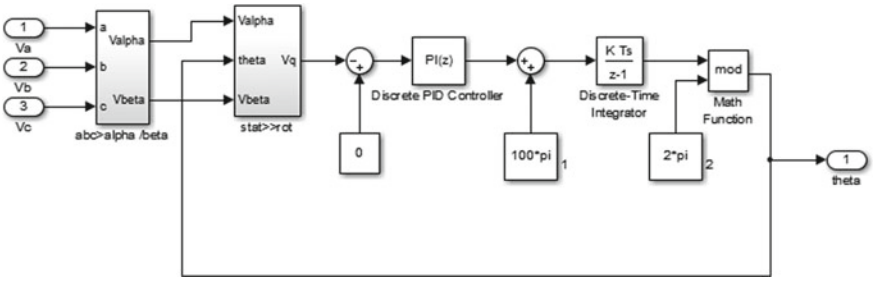

Fig. 5 Simulink model of SRF-PLL

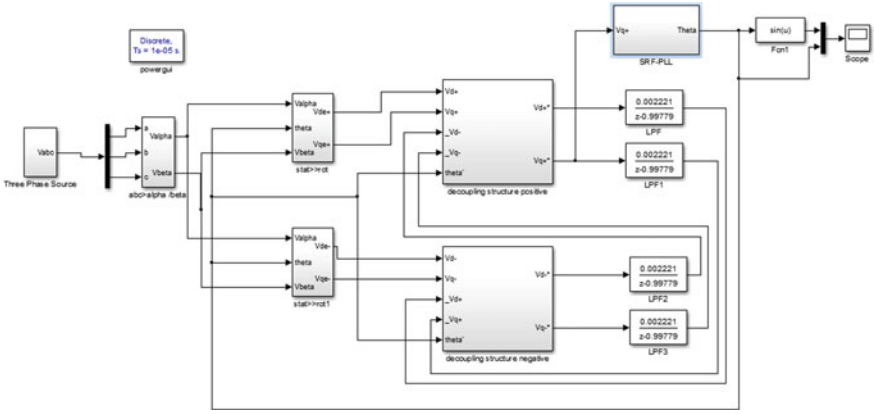

Fig. 6 Simulink model of DSRF-PLL

4 Results and Discussion

In order to compare the performance of SRF-PLL and DSRF-PLL, here simulation results are presented with non-ideal case of balanced and unbalanced grid voltage condition. The parameter of simulation is given Table 1.

Both the PLL is tested with balanced supply with phase to neutral magnitude of 325 V and 50 Hz as well as unbalanced supply voltage with 360 V, 200 V and 200 V, respectively, for A, B and C phase of supply. In all results presented here, a step change in grid voltage is applied after one second simulation time, and thus, in all results before one second time balanced condition of grid voltage and on other side unbalanced condition of grid voltage is presented. In Fig. 7, one can see that during balanced condition, both the PLL are performing good and detecting perfect phase of the positive sequence of grid voltage. But when unbalanced is applied in grid voltage after one second from simulation start time in SRF-PLL, the detected phase gets deteriorated, and it can be seen that it does not exactly coincide on supply phase. While in case of DSRF-PLL, perfect phase detection is able to obtain during unbalanced condition also, and in result it can be seen that detected phase and supply phase coincide on each other in both conditions.

In Figs. 8 and 9, phase-A voltage of grid along with detected phase and detected phase voltage is shown. From Fig. 8b, it can be seen that during unbalanced condition of grid voltage SRF-PLL is not able to detect the exact phase of grid voltage, but from Fig. 9b it is very clear that in DSRF-PLL it can detect phase properly during the unbalanced condition.

Table 1 Simulation parameter setting

Name of parameter	Selected value
Grid voltage (normal condition)	325 V
Frequency	50 Hz
Kp (SRF and DSRF)	0.7306
Ti (SRF and DSRF)	0.0507
Cut-off frequency of LF in DSRF-PLL	50 Hz

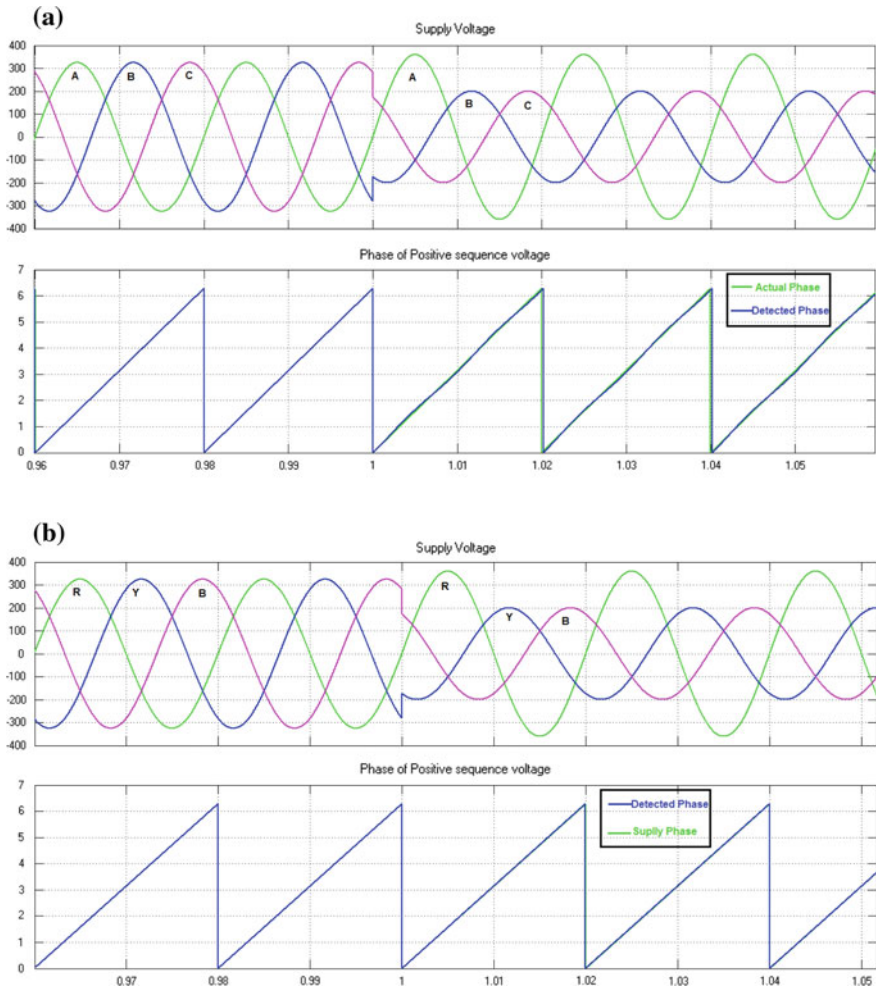

Fig. 7 **a** Three-phase grid voltage and detected phase of SRF-PLL. **b** Three-phase grid voltage and detected phase of DSRF-PLL

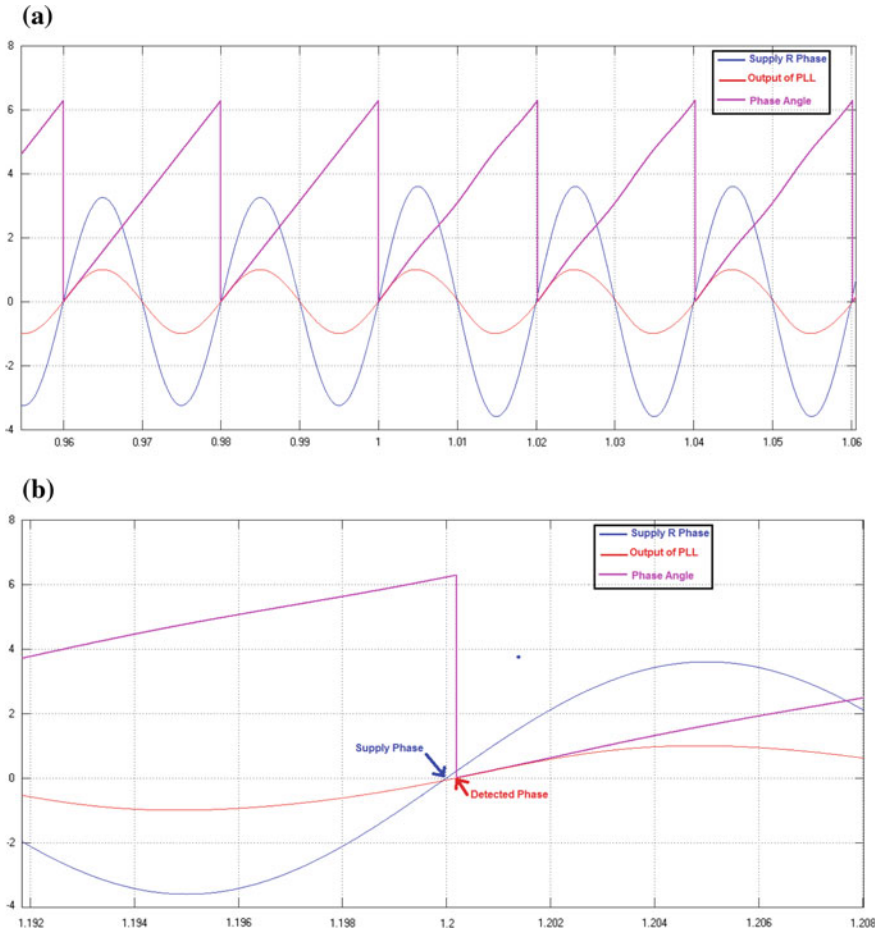

Fig. 8 **a** Phase-A voltage, detected phase and detected phase voltage of SRF-PLL. **b** Zoom view of (**a**)

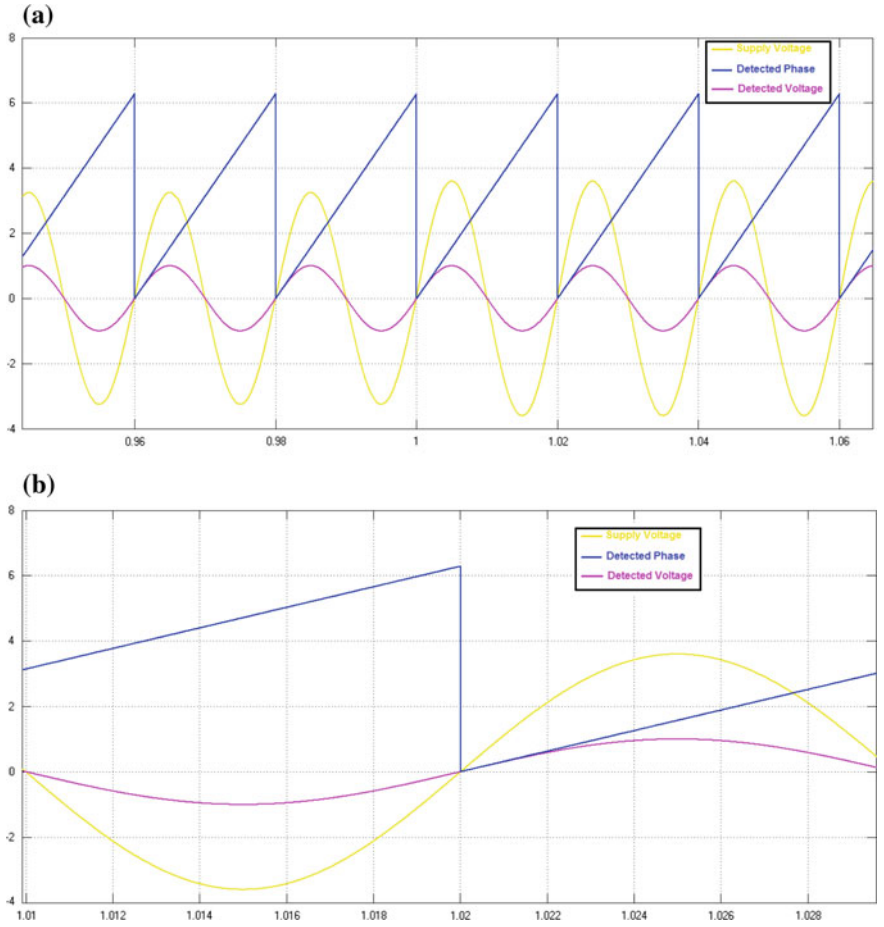

Fig. 9 **a** Phase-A voltage, detected phase and detected phase voltage of DSRF-PLL. **b** Zoom view of (**a**)

5 Conclusion

The study and results presented in this paper have shown that SRF-PLL is not able to detect grid voltage phase properly for unbalanced condition, but DSRF-PLL is capable of tracking exact grid phase during balanced and unbalanced condition of grid voltage as in this PLL the use of decoupling network removes the effect of cross-coupling component. So, in the application where the possibility of voltage unbalanced condition is there, it is suitable to use DSRF-PLL.

References

1. Timbus FBA, Liserre M, Teodorescu R (2005) Synchronization methods for three-phase distributed power generation systems. An overview and evaluation. In: Proceedings of the IEEE 36th power electronics specialists conference, pp 2474–2481
2. Yan Z, Milanovic JV (2010) Global voltage sag mitigation with FACTS-based devices. IEEE Trans Power Deliv 25:2842–2850
3. Ding G et al (2008) New technologies of voltage source converter (VSC) for HVDC transmission system based on VSC. In: Power and energy society general meeting-conversion and delivery of electrical energy in the 21st century, IEEE
4. Golestan S, Monfared M, Freijedo FD (2013) Design-oriented study of advanced synchronous reference frame phase-locked loops. IEEE Trans Power Electron 28(2)
5. Rodríguez P, Pou J, Bergas J et al (2007) Decoupled double synchronous reference frame PLL for power converters control. IEEE Trans Power Electron 22(2)

Investigation on Impact of Rooftop Solar System on LV Distribution Network

Dhaval Y. Raval and Saurabh N. Pandya

Abstract Energy is prime requirement to have prosperous and convenient life. Diversified use of electrical energy is due to its transferability and storability. Solar energy is being promoted worldwide to meet increasing electricity demand and to cope with spoiling environment. Consumer participation is key to achieve large scale power generation using compact photovoltaic (PV) systems. Grid-integrated PV system introduces power quality issues like local voltage rise, voltage unbalance, reverse power flow (RPF) and neutral to ground voltage rise (NGV). PV-integrated LV distribution network has been analyzed to recognize the seriousness of negative impact of PV generation in conventional radial distribution network. Simulation study has been carried out using MATLAB/Simulink.

Keywords Photo-voltaic · Power quality · Voltage rise · NGV · Reverse power flow

1 Introduction

Grid-connected photovoltaic (PV) system extracts power from the PV array and feeds it to the grid. First component of this PV plant is PV cell which converts solar energy into electrical energy. Efficiency of this solar cell is varying from 3 to 15%, generally depends on material, temperature, surface deposits, tilt angle, light spectrum [1]. PV cells are grouped to make PV module and PV modules are grouped to make PV array. Various PV array topologies are available like series-parallel, total cross-tied and bridge linked. Series-parallel is most favorable among them [2, 3]. DC-to-DC converter, isolated or non-isolated with various MPPT algorithms are used to linearized PV source, as PV is a non-linear source of energy [4].

D. Y. Raval (✉)
Electrical Engineering Department, Atmiya University, Rajkot, India
e-mail: dhavalraval004@gmail.com

S. N. Pandya
Electrical Engineering Department, Lukhdhirji Engineering College, Morbi, India
e-mail: saunipandya@gmail.com

A. Mehta et al. (eds.), *Advances in Electric Power and Energy Infrastructure*, Lecture Notes in Electrical Engineering 608,
https://doi.org/10.1007/978-981-15-0206-4_16

Grid-connected solar system can be categorized into two types (1) Large-scale commercial plant and (2) Small-mid-scale rooftop plant. Facility of net metering and subsidy of 10,000 INR/kW (MAX-20,000 INR) by Gujarat government and 20,700 INR/kW by Central government have been provided to promote rooftop solar generation in India [5].

Rooftop solar system required great coordination between inverter and grid. Battery used to manage surplus/shortage of power in standalone PV system can be eliminated in grid-connected PV system. PV inverter controls grid current, ensures grid synchronization and maintains DC link voltage [6]. Usually to control active and reactive power transfer, inverter current is controlled using different controllers like hysteresis controllers, PI controllers, resonant controllers and dead-beat controllers. Usually, three-level control schemes are sufficient to control active and reactive power flow from inverter which are power control-highest level, current regulation-mid level and PWM controller-lowest level [7, 8].

Grid-connected PV system causes many problems due to intermittent nature of solar and continuously varying grid condition. Large efforts are being made worldwide to define standards for grid-connected PV system. IEEE1547 [9], IEC61727 & ENC61000−3–2 deals with power quality issues like detection of islanding operation, amount of injected DC current into the grid, total harmonic distortion (THD), etc. Apart from these basic standards, PV inverters also required some advanced features like fault ride through, frequency droop control and anti-islanding to prevent undesirable condition mentioned in [10] and very serious in the case of high penetration of PV generation.

In this paper, impact of PV generation on LV distribution network has been investigated. Section 2 provides conceptual details about impact of PV system in distribution network. LV distribution network with PV generation has been simulated and analyzed in Sect. 3.

2 PV-Integrated LV Distribution Network

Figure 1 shows layout of LV distribution network. Different phases are allocated to single-phase consumers and mentioned as Load Sector–A, Load Sector–B and Load Sector–C. Detailed layout of Load Sector–A is shown. Distance of consumers from distribution transformer is shown in feet. Al 1/0 conductor is assumed which has resistance of 0.7119 Ω/km. In Load Sector–A, three consumers P1L2, P3L1 and P4L1 are having rooftop PV system. Load Sector–B and Load Sector–C assumed to have same layout, without any rooftop PV generation. This assumption is fairly valid as owing a rooftop PV system is completely based on consumers' willingness residing in particular phase.

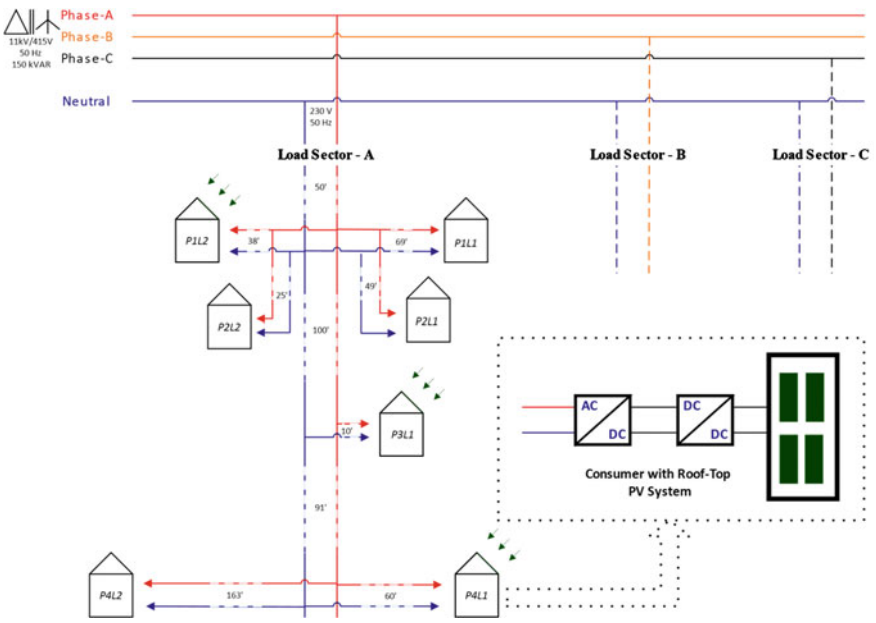

Fig. 1 LV distribution network

2.1 *Rooftop PV System*

Rooftop PV system is having PV panels as source, DC-to-DC stage to maintain PV voltage at Vmpp and DC-to-AC stage to fed extracted power into the grid as shown in Fig. 1. DC-to-DC stage can be realized by means of any DC-to-DC converter (Isolated/Non-Isolated). By acting as virtual impedance and maintaining Vmpp at the input side of PV panels, DC-to-DC stage ensures maximum power extraction. Maximum Power Point Tracking (MPPT) algorithms are used to modulate power flow in such manner that input capacitor of DC-to-DC stage remains at Vmpp voltage. DC-to-AC converter (inverter) used to convert DC voltage/current into AC voltage/current.

2.2 *Power Quality in PV-Integrated LV Network and Its Significance*

Uneven distribution of PV generation shown in Fig. 1 introduces power quality issues like local voltage rise, voltage unbalance, reverse power flow (RPF) and neutral to ground voltage (NGV). Distribution network typically designed for specific load profile based on consumption pattern. When rooftop PVs are deployed on any arbitrary phase as shown in Fig. 1, the pattern of power consumption will change and

introduces local voltage rise problem [11]. Fluctuating nature of PV generation can cause continuous voltage fluctuation and voltage unbalance in the distribution system. Literature [12–17] examines the effect of PV generation on voltage profile of distribution network. For a consumer connected to the same distribution transformer, voltage fluctuation depends on the size of PV plant, distance from distribution transformer and length of shared secondary between consumers. It is also observed that voltage variation caused by a single PV generator, with no reverse power flow through transformer, can be worse than that caused by a group of PVs causing reverse power flow [12]. From measurement and analysis carried out on different countries having high penetration of PV, it has been concluded that introduction of large PV power can cause voltage rise of 1–2% and voltage unbalance of 1–2% [13].

Voltage unbalance has a harmful effect on grid-connected appliances and protective devices. Voltage unbalance can cause extra power loss, safety deficiency, relay malfunction (due to zero and negative sequence current), inaccurate measurement, transformer/motor life cycle decrement [14]. Due to unbalanced voltage supply, motor experiences torque pulsation and produces excessive noise. Voltage imbalance introduces current imbalance which results in temperature rise of the motor. According to National Electrical Manufacturers Association (NEMA), voltage imbalance in induction motor should not exceed 5%. In rectifier, line current through switching element significantly increased with unbalanced voltage supply. Switching devices and capacitors of rectifier experience extensive stress due to this increased current. Also, larger peak of supply current worsens the supply distortion power factor (DPF) [15].

Unbalanced voltage which is caused by unbalanced allocation of PV or varying generation/consumption of consumer has a potential to worsen the classical neutral current and neutral potential problem [16]. Neutral conductors, which are usually sized the same as the phase conductors, can be overloaded if the neutral current exceeds the rated phase current. Excessive amount of neural current can overload the distribution transformer. Neutral current can create common mode noise when impedance of neutral is not negligible. Computer vendor specifications typically call for less than 0.5–3 V RMS, neutral to ground (NGV), regardless of frequency [17].

Impact of PV system in regard to local voltage rise and NGV in LV distribution network has been studied and explained in further sections.

3 Impact of PV Integration on LV Distribution Network

To understand the impact of PV integration, two scenarios have been considered.

1. PV Generation Concentrated Far from Distribution Transformer.
2. PV Generation Concentrated Near the Distribution Transformer.

In each scenario, PV Generation is assumed to be in Load Sector–A. Load Sector–B and Load Sector–C are assumed not to have any consumer with rooftop PV system.

To investigate the effect of PV generation on NGV, Load Sector–B and Load Sector–C are also having same layout and load demand as of Load Sector–A.

3.1 PV System Integrated Far from Distribution Transformer

Figure 2 shows layout of Load Sector–A in first scenario. P4L1 is having rooftop PV system of 50 kW which is at 301 ft from the distribution transformer. As the PV system is designed to inject only active power, all other loads are considered to be linear and active load. Effect of PV power injection is studied in following two cases:

1. Maximum Loading Condition (40 kW/Phase).
2. Minimum Loading Condition (12 kW/Phase).

Maximum Loading Condition (40 kW/Phase)

PV power injection in LV distribution network has been simulated in peak loading condition of 40 kW/Phase. PV penetration is varied from 10 to 85% during the time span of 0.5–3 s. PV penetration at different time is shown in Fig. 5 (Fig. 4).

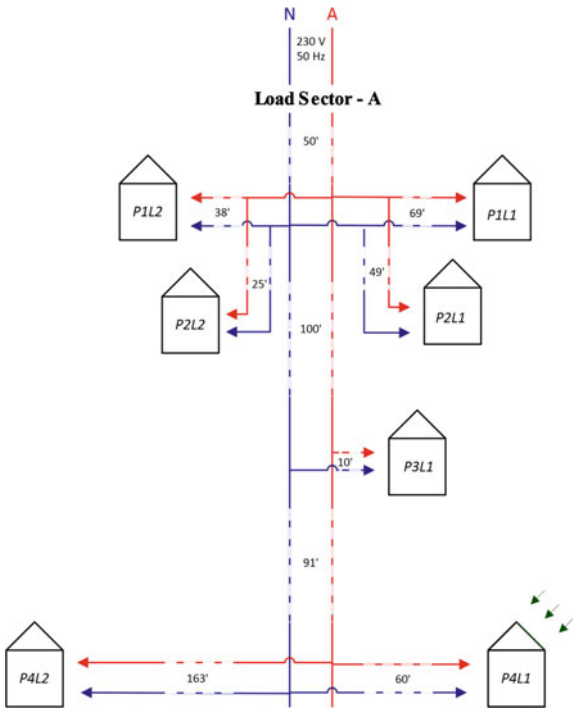

Fig. 2 LV distribution network in Scenario–1

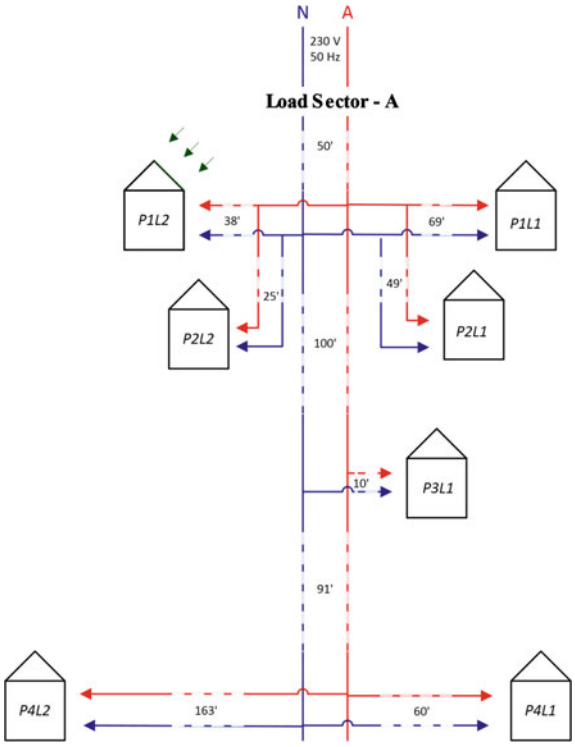

Fig. 3 LV distribution network in Scenario–2

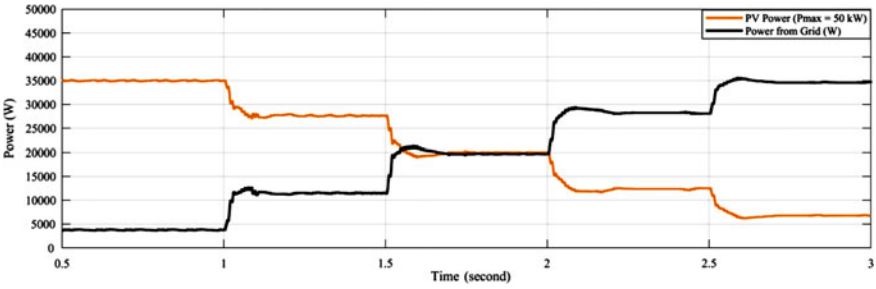

Fig. 4 Power flow in Scenario–1 (Condition–1)

Tables 1 and 2 show deviation of local voltage and NGV, respectively. Graphical representation for deviation of local voltage and NGV is shown in Figs. 6 and 7, respectively. From the above result, the following observations are made.

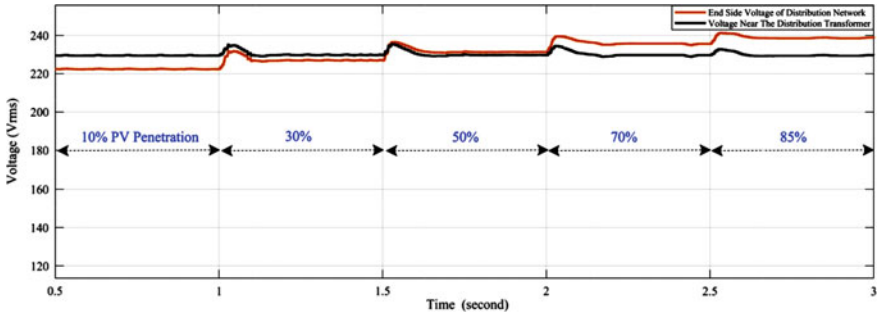

Fig. 5 LV distribution network voltage in Scenario–1 (Condition–1)

Table 1 Voltages at different load in Scenario–1 (Condition–1)

PV penetration	P1L1 119 ft	P1L2 88 ft	P2L2 99 ft	P2L2 75 ft	P3l1 160 ft	P4L1 301 ft	P4L2 404 ft
0	226.5	226.8	226.7	227	224	222	222
10	227	227.3	227.2	227.4	225.2	224.2	222.7
30	227.2	227.5	227.4	227.7	226.8	227.6	227.6
50	228	228.3	228.3	228.5	229.1	231.8	231.8
70	228.2	228.5	228.4	228.7	230.7	235.4	235.4
85	228.5	228.8	228.7	229	231.1	238.2	238.2

Table 2 NGV at different load in Scenario–1 (Condition–1)

PV penetration	P1L1 119 ft	P1L2 88 ft	P2L1 99 ft	P2L2 75 ft	P3l1 160 ft	P4L1 301 ft	P4L2 404 ft
0	1.326	1.161	1.22	1.092	2.575	3.354	3.886
10	1.236	1.072	1.13	1.003	2.155	2.597	3.298
30	1.062	0.898	0.9526	0.8292	1.353	1.27	2.172
50	0.8726	0.708	0.7656	0.6381	0.4828	1.084	0.9156
70	0.6816	0.5179	0.5759	0.4495	0.7313	2.746	0.7808
85	0.5455	0.3835	0.4407	0.3165	1.362	4.009	1.602

Observation

- During peak loading condition, PV power injection at the end of distribution feeder improves the voltage profile of distribution network.
- Power supplied from PV within the distribution network reduces burden on distribution transformer and increases its life span.
- Voltage deviation of load far from distribution transformer is greater than the load near distribution transformer.

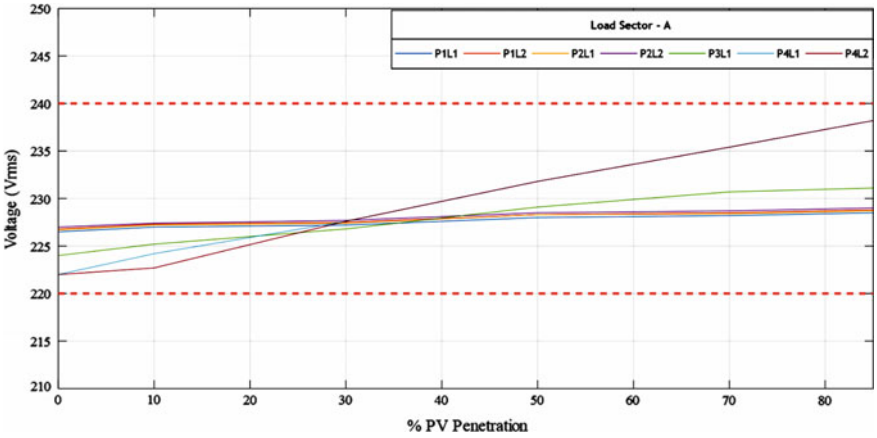

Fig. 6 Voltage at different loads in Scenario–1 (Condition–1)

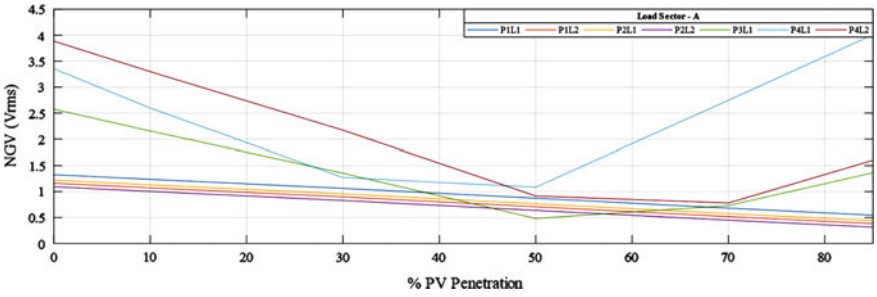

Fig. 7 NGV in Scenario–1 (Condition–1)

- Voltage profile of all the load tends to improve up to 30% of PV penetration. Above 30%, load at the end of distribution network experiences voltage rise beyond permissible level of 240 V.
- High PV penetration improves NGV near the transformer, for the loads far from the transformer NGV rise has been observed at high PV penetration.

Minimum Loading Condition (12 kW/Phase)

In this section, PV power injection in LV distribution network has been simulated in light loading condition 12 kW/Phase. PV penetration is varied from 10 to 85% during the time span of 0.5–3 s (Tables 3 and 4; Figs. 8, 9, 10 and 11).

Observation

- During light loading condition injection of power at the end of distribution feeder introduce serious voltage rise problem.
- Load at the end of distribution feeder likely to suffer from voltage rise more than permissible voltage level of 240 V.

Table 3 Voltages at different load in Scenario–1 (Condition–2)

PV penetration	P1L1 119 ft	P1L2 88 ft	P2L1 99 ft	P2L2 75 ft	P3l1 160 ft	P4L1 301 ft	P4L2 404 ft
0	230.6	230.7	230.6	230.7	229.8	229.2	229.2
10	231.2	231.3	231.2	231.3	231.1	231.5	231.5
30	231.5	231.6	231.6	231.7	232.9	235.1	235.1
50	231.1	231.2	231.1	231.2	233.9	238	238.1
70	230.9	231	231	231	235.3	241.4	241.4
85	230.6	230.7	230.7	230.7	236.1	243.7	243.7

Table 4 NGV at different load in Scenario–1 (Condition–2)

PV penetration	P1L1 119 ft	P1L2 88 ft	P2L1 99 ft	P2L2 75 ft	P3l1 160 ft	P4L1 301 ft	P4L2 404 ft
0	0.4063	0.3561	0.3739	0.335	0.7943	1.036	1.201
10	0.3209	0.2702	0.2875	0.25	0.4813	0.6802	0.7385
30	0.1467	0.1061	0.1196	0.09198	0.6669	1.654	0.8517
50	0.1106	0.1466	0.1328	0.164	1.561	3.368	2.086
70	0.28666	0.33377	0.31688	0.3537	2.516	5.164	3.417
85	0.4263	0.4745	0.4574	0.4949	3.206	6.46	4.379

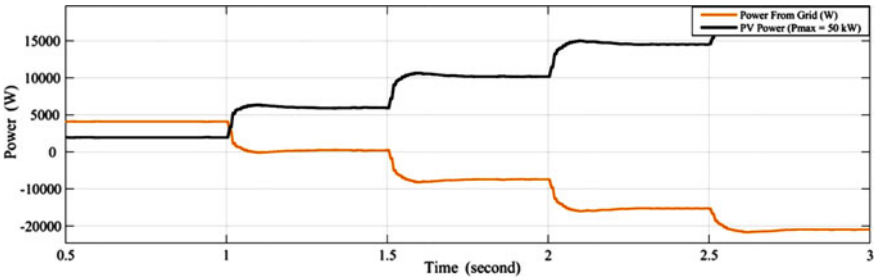

Fig. 8 Power flow Scenario–1 (Condition–2)

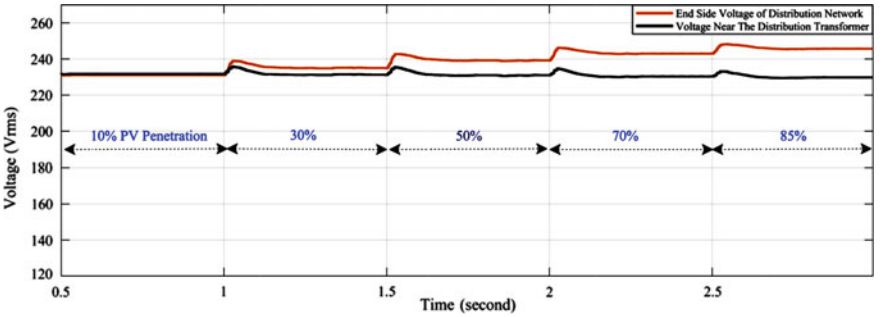

Fig. 9 LV distribution network voltage in Scenario–1 (Condition–2)

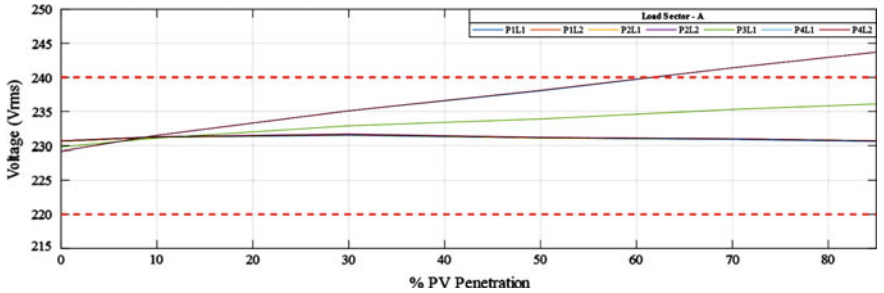

Fig. 10 Voltage at different loads in Scenario–1 (Condition–2)

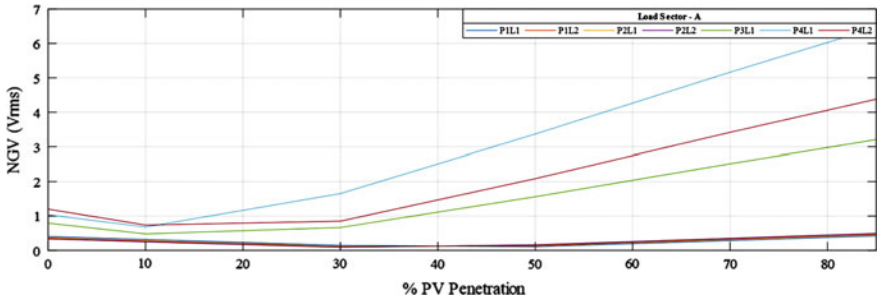

Fig. 11 NGV in Scenario–1 (Condition–2)

- For $P_{pv} < P_{\text{load}}$, PV system reduces burden on the distribution transformer.
- For $P_{pv} > P_{\text{load}}$, excess of power feedback to the grid through distribution transformer.
- This will introduce unbalanced current in transmission line having Positive, Negative and Zero sequence components.
- During light load condition, high PV penetration causes voltage rise beyond the allowable limit at the end node of distribution network.

3.2 PV System Integrated Near the Distribution Transformer

Figure 3 shows layout of Load Sector–A in second scenario. P1L2 is having rooftop PV system of 50 kW which is at 88 ft from the distribution transformer. Effects of PV system observed more savior during low demand in Scenario–1; hence, only minimum loading has been considered for Scenario–2. Figure 12 shows voltage deviation of sending end and receiving end nodes in different PV penetration. PV penetration is increased from 10 to 85% as considered in previous sections. Voltage deviation is significantly reduced due to less distance from the distribution transformer. NGV

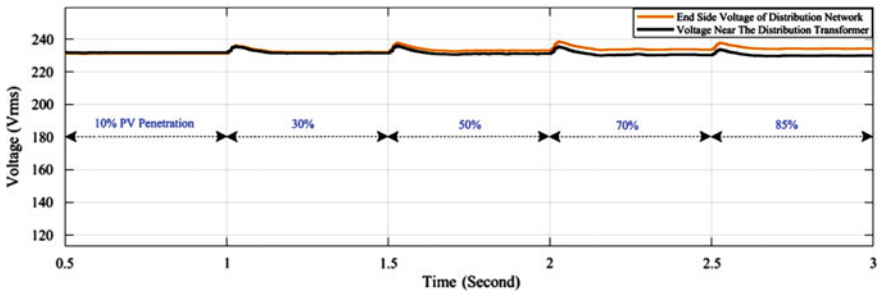

Fig. 12 LV distribution network voltage with different PV penetration in Scenario–2

also improved when PV generation is concentrated near the distribution transformer and not shown due to limitation of space. Result clearly shows that if the PV generation is concentrated near the transformer, same amount of power can be injected without violating voltage limit.

4 Conclusion

Active power injection from PV system in distribution network changes voltage profile at significant level. Certain amount of PV penetration is beneficial for distribution network as it reduces power loss and burden on distribution transformer. Injection of PV power at far end of distribution network can increase the voltage beyond tolerable limit. This voltage rise limits the PV hosting capacity of any distribution network. Distance of PV system from the distribution transformer is crucial factor. More amount of power can be injected without violating voltage limit, if PV system is near the distribution transformer. Reverse power flow can occur in highly PV-penetrated distribution network during low power demand.

References

1. Mohamed MM (2015) Enhancing photoelectric conversion efficiency of solar panel by water cooling. J Fundam Ren Energy Appl 5.4:1–5
2. El-Dein MZS, Kazerani M, Salama MMA (2013) An optimal total cross tied interconnection for reducing mismatch losses in photovoltaic arrays. IEEE Trans Sustain Energy 4.1:99–107
3. Nguyen D, Lehman B (2008) An adaptive solar photovoltaic array using model-based reconfiguration algorithm. IEEE Trans Ind Electron 55(7):2644–2654
4. Raval DY, Munjani PJ, Mansoori NR (2016) Reference based maximum power point tracking algorithm for photo-voltaic power generation. In: 2016 International Conference on Electrical Power and Energy Systems (ICEPES). IEEE
5. Roof-top solar project G. R. No. SLR-11/2015/401/B

6. Xi Z, Deng M, Li K (2013) Research on control strategy of photovoltaic grid-connected inverter. In: 2013 5th International Conference on Intelligent Human-Machine Systems and Cybernetics (IHMSC), vol 2. IEEE
7. Kabiri R, Holmes DG, McGrath BP (2016) Control of active and reactive power ripple to mitigate unbalanced grid voltages. IEEE Trans Ind Appl 52.2:1660–1668
8. Raval DY, Munjani PJ, Mansoori NR (2017) Design, simulation and performance analysis of grid connected photo-voltaic system with decoupled current control. In: 2017 Nirma University International Conference on Engineering (NUiCONE). IEEE
9. Langella R, Testa A (2014) IEEE recommended practice and requirements for harmonic control in electric power systems. IEEE Std (Revision of IEEE Std 519-1992) 519:1–29, 11 June 2014
10. Adithya SN (2016) Large-scale implementation of grid-connected rooftop solar photovoltaic system in India—potential, challenges, outlook, and technical impact. In: 2016 International Symposium on Electrical Engineering (ISEE). IEEE
11. Wong PKC, Kalam A, Barr R (2017) Modelling and analysis of practical options to improve the hosting capacity of low voltage networks for embedded photo-voltaic generation. IET Ren Power Gener 11.5:625–632
12. Parchure A et al (2017) Investigating PV generation induced voltage volatility for customers sharing a distribution service transformer. IEEE Trans Ind Appl 53.1:71–79
13. Katiraei F, Mauch K, Dignard-Bailey L (2007) Integration of photovoltaic power systems in high-penetration clusters for distribution networks and mini-grids. Int J Distrib Energy Resour 3(3):207–223
14. Chen TSAI-HSIANG, Yang CH, Hsieh TY (2009) Case studies of the impact of voltage imbalance on power distribution systems and equipment. In: Proceedings of the WSEAS international conference on Mathematics and Computers in Science and Engineering. No. 8. World Scientific and Engineering Academy and Society
15. Bennett B (2017) Unbalanced voltage supply the damaging effects on three phase induction motors and rectifiers. ABB Pow Cond Electr Prod Div, 1–5
16. Balda JC et al (1997) Measurements of neutral currents and voltages on a distribution feeder. IEEE Trans Power Delivery 12(4):1799–1804
17. Gruzs Thomas M (1990) A survey of neutral currents in three-phase computer power systems. IEEE Trans Ind Appl 26(4):719–725

Review of the Impact of Vehicle-to-Grid Schemes on Electrical Power Systems

Praghnesh Bhatt, Chao Long and Mahammadsoaib Saiyad

Abstract The vehicle-to-grid (V2G) describes plug-in electric vehicles (PEV), such as battery electric vehicles (BEV) and plug-in hybrid electric vehicles (PHEV), communicate with the power grid and sell demand response services by either returning electricity to the grid or by restricting their charging rate. Simultaneous charging of EV fleet can lead to an excessive loading, under-voltages and energy losses in distribution networks. On the other hand, the EVs in their idle mode has the ability to feed power back to grid which is useful for active power balancing, peak shaving, and stability enhancement. This paper reviews the V2G schemes to assess their impacts on the electrical power systems. The framework for coordinated operation of EVs with renewable energy sources in the various electricity markets was reviewed. The EVs' capability in energy loss minimization and provision of ancillary services such as frequency and voltage control was also investigated.

Keywords Ancillary service · Demand-side management · Electric vehicle · Optimal charging scheme · Vehicle-to-grid

1 Introduction

Electric vehicles (EVs) have been introduced into the market globally owing to the fact that EVs could significantly contribute towards the targets of the greenhouse gas emission reduction. The increasing share of EVs may have impact on power system performance, e.g. distribution network losses, peak power demand, voltage profiles, efficiency, reliability, and stability [1]. EVs are capable of delivering active and reactive power support, thus providing ancillary services for frequency regulation,

P. Bhatt (✉)
Pandit Deendayal Petroleum University, Gandhinagar, Gujarat 382007, India
e-mail: praghnesh.bhatt@sot.pdpu.ac.in

C. Long
School of Engineering, Cardiff University, Cardiff CF24 3AA, UK

M. Saiyad
C S Patel Institute of Technology, CHARUSAT, Changa Gujarat 388421, India

A. Mehta et al. (eds.), *Advances in Electric Power and Energy Infrastructure*, Lecture Notes in Electrical Engineering 608,
https://doi.org/10.1007/978-981-15-0206-4_17

voltage control and spinning reserve. Tracking of renewable energy sources such as wind and photovoltaics (PVs), load balancing and current harmonic filtering is possible with EV technologies [2]. The technology requirements, economic costs, challenges, and strategies for vehicle-to-grid (V2G) interfaces of both individual plug-in EVs (PEVs) and vehicle fleet in the power system were reviewed in [2]. In [3], the review on different power levels and infrastructures was compared based on the amount of required power, charging time, cost, component ratings, and other factors. The impact analysis of coordinated/uncoordinated charging on distribution network performance was presented in [4]. This paper aims to present the review on EVs' participation in electricity market, coordination of EVs and renewable energy sources to improve the network performance in minimizing the system losses. The comprehensive review for the role of EVs' contribution to frequency regulation is also carried out covering various types of interconnected systems, frequency controller structures, and methods adopted for frequency control.

2 Electric Vehicle Chargers and Charging Schemes

Based on the nature of the EV charging, the EV chargers are broadly classified as (1) Unidirectional and bidirectional and (2) Conductive and inductive. Based on the type of the converter, the EV chargers are categorized by basic converter, multi-level converter (with some advanced switching techniques), and advanced wireless charger.

The architecture of the review work is presented in Fig. 1. Different V2G schemes have been adopted depending on the electricity market an individual EV or EV fleet is proposed to participate in, and/or also depending on the type of renewable energy sources the EV is coordinated with, and the objectives of the scheme.

3 EVs Participation in Electricity Market

EVs have been participating in the various electricity markets, such as flexible electricity ramp, ancillary services, electricity buying bidding, and social welfare (see Fig. 1). Moreover, a significant cost saving in EV charging can be made when the EV charging methods are in response to the time-of-use (TOU) electricity prices.

A comparison between an uncontrolled EV charging and a market-based charging was addressed in [5]. The objective was to maximize social welfare where a "fairness constraint" was proposed. In [6], participation of EV in the flexible ramp market was presented to clear the market under uncertainties and variations in net load. In [7], the deterministic algorithm and fuzzy linear programming (FLP) were adopted for optimal bidding of coordinated charging for EVs. The FLP approach resulted in more aggregator's profits considering different uncertainties in ancillary service prices and deployment signals for regulation up, regulation down, and responsive reserves. In

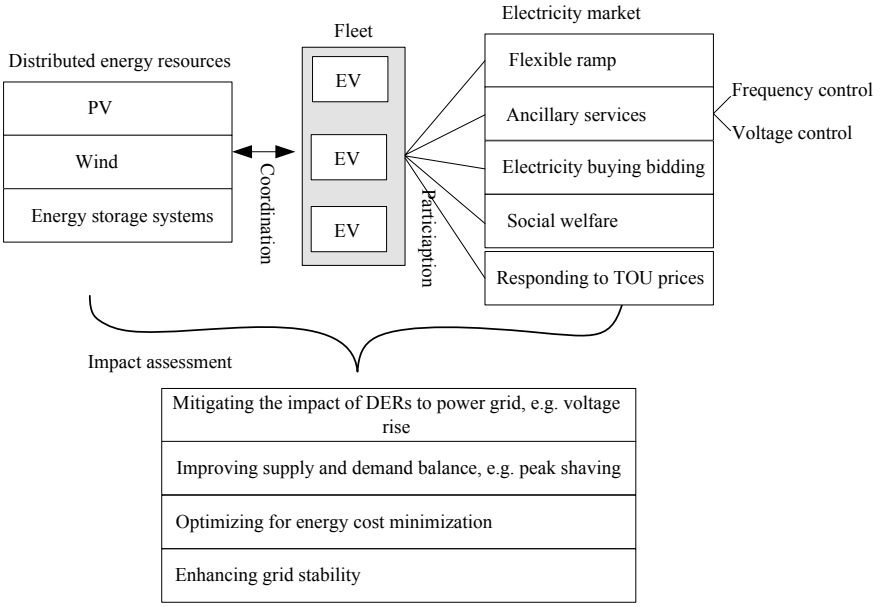

Fig. 1 Impact assessment of V2G schemes on the electrical power grid

[8], two optimization methods, namely global and divided, were used to represent forecasted information based on a statistical model when EV fleet was participating in a day-ahead market. This study was extended to a numerical analysis, and the two proposed optimization approaches were implemented to the Iberian day-ahead electricity market [9]. This work was intended to support an EV aggregation agent in optimizing their buying bids. Optimal EV bidding strategies for the day-ahead market, such as (a) spot market, (b) spot market and downward reserve sessions, and (c) spot market and reserve sessions, were compared in [10] to assess the impact of forecasted errors.

The EV charging methods in response to time-of-use (TOU) prices were reported in [11–13]. In [11], learnable partheno-genetic algorithm (LPGA) was presented, and the results were compared against tabu search (TS), genetic algorithm (GA) and ant colony optimization (ACO). In [12], a discretized optimization model was adopted, where minimizing the costs that EV users are required to pay was considered as the objective function, and the product of unit price and power drawl during that time was taken as input variables. The problem was solved with an intelligent heuristic algorithm. The reduction in cost of 51.52% and 39.67% was obtained with an optimized charging pattern for single EV and multi EV models, respectively. A decision tree model was proposed in [13] and results showed that a careful choice of TOU rates helps to reduce fuelling cost, increase the incentives and simultaneously minimize the grid impacts due to EV penetration. The problem of coordinated charging and discharging of EVs was proposed as a linear problem in [14] for a day-ahead

market. The objectives were defined as to minimize charging costs and maximize profits obtained from energy trading.

4 Coordination of EVs with Renewable Energy Sources

Coordination between EV charging and discharging and many distribute energy resources (DERs) has been carried out to mitigate the adverse system impacts resulted from the DERs, to facilitate the supply and demand balancing (e.g. peak shaving), and to bring economic benefit for the system operation.

The charging/discharging strategies for PEV batteries were devised in [10] to mitigate the adverse impact (i.e. voltage rise) due to higher power generation from solar PVs in a distribution network in New South Wales, Australia. Marra et al. and Alam et al. [15–18] have also addressed the utilization of PEV batteries for mitigating the voltage rise impact due to PV penetrations.

A method using valley searching, interruptible and variable-rate energy dispatching of EV batteries was adopted in [19] to ensure a secure energy balance with a coordinated wind-EVs model, considering uncertainties in wind power production and driving patterns of EVs. A smart charging of EVs was proposed in [20] for wind power balancing. The wind generation and EV loads were first nominated in the day-ahead market and then a smart controlling of EVs was achieved to minimize the forecasted errors. A fuzzy chance-constrained unit commitment model was proposed in [21] considering demand response (DR), EVs and wind power. EV charging station fitted with PV panels, fuel cell, and energy storage was proposed in [22] to accomplish sustainable transportable electrification.

A stochastic dynamic programming method was used to minimize cost of EV charging as well as to have reduced impact on distribution grid. The coordination of wind-PV-EVs was reported in [23] based on stochastic optimization model considering uncertainties in PV and wind power generation. Similarly, a novel control strategy was proposed in [24] to coordinate both charging-discharging of EVs and intermittent renewable energy generation using certainty equivalent adaptive control (CEAC) principle. The economics of integrating wind, EVs and mixtures of Level 1/Level 2 charger infrastructures was addressed in [25] considering wholesale electric energy market. Grouping of EVs into fleets based on daily driving patterns was carried out using fuzzy c-means (FCM) clustering, followed by optimization done by genetic algorithm (GA) in combination with a Monte Carlo simulation (MCS). Artificial bee colony (ABC) algorithm was applied in [26] to minimize overall cost of power system consists of offshore wind farm-thermal units-EVs power system connected through HVDC link.

5 EVs Role for Active Power Balancing and Frequency Regulation

The power generated by all the generating resources in the system must balance the electric load in order to operate the system with desired nominal frequency. The V2G concept is one of the most promising solutions for providing faster and efficient power balancing service through faster charging and discharging of EV batteries. A significant amount of research has been carried out on the techniques and applications of V2G for frequency regulation [27] where focuses were given to EVs on their fast adjustments of V2G power. A fleet of thousands of EVs can be used as controllable energy storage devices to participate in power system operation [28]. The economic feasibility of V2G control performing frequency regulation service was investigated in [29, 30].

Area control error (ACE) and frequency characteristic of plug-in hybrid EV (PHEV) was suggested in [31] where load frequency control (LFC) signal was calculated based on the charging power of PHEV. Participation of EVs for secondary frequency control was reported in [32]. Frequency regulation issue in Danish power grid with EV and large penetration of wind power was investigated in [33] by modelling aggregated EV-based battery storage for the use in long-term dynamic power system simulations.

Smart charging with a droop control based on system frequency deviation was used to realize a fast and synchronized response among multiple vehicles for frequency regulation in [34]. EVs and the heat pump water heater (HPWHs) as controllable loads are modelled for LFC in [35] which can be helpful to reduce the capacity of battery storage systems. The dynamic PEV model considering dynamic battery storage capable battery discharging/charging characteristics and SOCconstraints was proposed in [36] based on distributed acquisition approach. A decentralized V2G control (DVC) method was proposed in [37] for EVs for primary frequency control.

Estimation of the EV charging load based on a statistical analysis of EV type, maximum travel range, battery capacity and battery state of charge was carried out in [38] to observe the contribution of EVs in primary frequency control of Great Britain (GB) power system. The comparison of "dumb" charging, "off-peak" charging, and "smart" charging of EVs were compared to show the impact of EVs to stabilize the grid frequency in the GB system. The coordinated V2G control and conventional frequency controller for robust LFC in the smart grid with large wind farms was proposed in [39]. The battery SOC was controlled by optimized SOC deviation using the particle swarm optimization.

In [40], control strategies for EVs to participate in supplementary frequency regulation (SFR) was proposed by framing a systematic framework including an EV aggregator, with many individual EVs and EV charging stations. A detailed model of a four-area power system with AC/HVDC links with smart charging of EVs was formulated in [41]. Fuzzy control of PV systems along with V2G for frequency control was proposed in [42, 43] where grid frequency deviation signal and SOC of batteries were used to control EVs charging.

V2G technologies are able to provide frequency regulation of a power grid with various types of interconnected systems, frequency controller structures and methods adopted for frequency control. The voltage violations in distribution network due to penetration of EVs and wind turbine have been quantified in [44] with time series approach considering time-dependent behaviour of wind speed, daily electrical load and EVs charging load.

6 EVs and Demand Side Management

In demand-side management (DSM), demand response of end-consumers who responds to price signal by voluntary changes their normal pattern of energy consumption [45–47]. DSM is adopted in smart grid for peak shaving, reduction in electricity bills, adequate usage of generation resources, energy loss minimization and for flattening the load profile [46]. In smart grid, EVs can be connected to network and shifted to different nodes based on applicable charging requirement and its charging price. In [47, 48], EVs are included in DSM and its impact is analyzed on demand profile. The problems of peak shaving and valley filling have been solved in [49] by proposing game theory approach for scheduling EVs charging whereas in [50] similar approach has been implemented by considering V2G and load profile is matched to target load curve. Coordination mechanism for allocating efficient EVs charging is proposed in [51] considering renewable energy generation. The problems such as congestion is solved in [52] by changing charging patterns for EVs. The issues of loss minimization and voltage violations are solved in [53] without including electricity market issues by presenting smart load management applicable to EVs. The maximization of profile for all agents is obtained in [54] by formulating DSM based on optimization approach on hourly available load-generation data. In this work, agents in smart grid are modelled in two types (a) EVs which can be shifted among the nodes of distribution network and (b) the agents which cannot be shifted and remain connected on same load such as loads, batteries, dispatchable and non-dispatchable generators and EVs.

The loads are modelled as the sum of fixed demand and shiftable demand depending on time. Non-renewable generator is modelled by its operational cost which is the sum of fixed, variable, start-up and shut-down cost. Renewable generators such as PV and wind turbine are modelled based on scenario tree and priority. A bank of electric batteries are considered as fixed storage elements and considers following aspects: (a) charging of battery (draws energy from the grid) or discharging of battery (delivers energy to the grid), (b) considering limits of power drawn or supplied by a battery, and (c) tracking of energy contained in the battery based on its state of charge (SOC). EVs are modelled as mobile storage device with some characteristics in addition to that of fixed storage elements such as batteries. In DSM, EVs can be modelled either in uncontrolled mode or in controlled mode by aggregator. For EVs, three time periods of operations are important (a) transition period when EVs are in transit state and consume energy from its batteries itself (b) charging period when EVs takes

energy from network to charge its battery again (c) resting period when EVs neither consume energy from its own batteries nor from the network. An uncontrolled mode of operation of EVs follows a fixed pattern for all three periods. In controlled mode of operation, the decision of charging and resting will be taken by aggregator. Okeanos, a fundamental, game theoretic, Java-based, multi-agent software framework for DR simulation is proposed in [55] which can now modelled plug-in electric vehicles (PEVs). Flattening of load curve with controlled charging of PHEV at low-voltage transformer is reported in [56] by formulating DSM problem as convex optimization problem and decentralized water-filling-based algorithm is used to solve it. Scalable approach following three steps such as aggregation, optimization, and control are proposed for DSM including PHEV in [57].

7 Conclusion

This work reviews the V2G schemes to assess their impacts on the electrical power systems. The coordinated operation of EVs with renewable energy sources in the various electricity markets and the EVs' capability in providing ancillary services, in particular the frequency control, were investigated.

EVs have been participating in various electricity markets, such as flexible electricity ramp, ancillary services, electricity buying bidding, and social welfare. Moreover, a significant cost saving in EV charging is able to be made when the EV charging methods are in response to the time-of-use (TOU) electricity prices. Coordination between EV charging and discharging and the distribute energy resources (DERs) has been carried out to mitigate the adverse system impacts resulted from the DERs, to facilitate the supply and demand balancing, and to bring economic benefit for the system operation. V2G technologies are able to provide frequency regulation of a power grid with various types of interconnected systems, frequency controller structures and methods adopted for frequency control.

Acknowledgements This work was partly supported by Royal Academy of Engineering under Newton-Bhabha Fund with grant reference IAPP(I)\19 for "Industry-Academia Collaborative Project to Address System Wide Impacts of Renewable Energy Sources in Engineering Program".

References

1. Lopes JAP, Soares FJ, Almeida PMR (2011) Integration of electric vehicles in the electric power system. Proc IEEE 99(1):168–183
2. Yilmaz M, Krein PT (2013) Review of the impact of vehicle-to-grid technologies on distribution systems and utility interfaces. IEEE Trans Power Electron 28(12):5673–5689
3. Yilmaz M, Krein PT (2013) Review of battery charger topologies, charging power levels, and infrastructure for plug-in electric and hybrid vehicles. IEEE Trans Power Electron 28(5):2151–2169

4. Habib S, Kamran M, Rashid U (2015) Impact analysis of vehicle-to-grid technology and charging strategies of electric vehicles on distribution networks—a review. J Power Sources 277:205–214
5. de Hoog J, Alpcan T, Brazil M, Thomas DA, Mareels I (2016) A market mechanism for electric vehicle charging under network constraints. IEEE Trans Smart Grid 7(2):827–836
6. Zhang B, Kezunovic M (2016) Impact on power system flexibility by electric vehicle participation in ramp market. IEEE Trans Smart Grid 7(3):1285–1294
7. Ansari M, Al-Awami AT, Sortomme E, Abido MA (2015) Coordinated bidding of ancillary services for vehicle-to-grid using fuzzy optimization. IEEE Trans Smart Grid 6(1):261–270
8. Bessa RJ, Matos MA (2013) Global against divided optimization for the participation of an EV aggregator in the day-ahead electricity market. part I: theory. Electr Power Syst Res 95:309–318
9. Bessa RJ, Matos MA (2013) Global against divided optimization for the participation of an EV aggregator in the day-ahead electricity market. part II: numerical analysis. Electr Power Syst Res 95:319–329
10. Bessa RJ, Matos MA, Soares FJ, Lopes JAP (2012) Optimized bidding of a EV aggregation agent in the electricity market. IEEE Trans Smart Grid 3(1):443–452
11. Yang H, Yang S, Xu Y, Cao E, Dong Z (2015) Electric vehicle route optimization considering time-of-use electricity price by learnable partheno-genetic algorithm. IEEE Trans Smart Grid 6(2):657–666
12. Cao Y et al (2012) An optimized EV charging model considering TOU price and SOC curve. IEEE Trans Smart Grid 3(1):388–393
13. Davis BM, Bradley TH (2012) The efficacy of electric vehicle time-of-use rates in guiding plug-in hybrid electric vehicle charging behavior. IEEE Trans Smart Grid 3(4):1679–1686
14. Pantos M (2012) Exploitation of electric-drive vehicles in electricity markets. IEEE Trans Power Syst 27(2):682–694
15. Marra F et al (2013) EV charging facilities and their application in LV feeders with photovoltaics. IEEE Trans Smart Grid 4(3):1533–1540
16. Marra F et al (2013) Improvement of local voltage in feeders with photovoltaic using electric vehicles. IEEE Trans Power Syst 28(3):3515–3516
17. Alam MJE, Muttaqi KM, Sutanto D (2013) Mitigation of rooftop solar PV impacts and evening peak support by managing available capacity of distributed energy storage systems. IEEE Trans Power Syst 28(4):3874–3884
18. Alam MJE et al (2016) Effective utilization of available PEV battery capacity for mitigation of Solar PV impact and grid support with integrated V2G functionality. IEEE Trans Smart Grid 7(3):1562–1571
19. Wu T, Yang Q, Bao Z, Yan W (2013) Coordinated energy dispatching in microgrid with wind power generation and plug-in electric vehicles. IEEE Trans Smart Grid 4(3):1453–1463
20. Leterme W, Ruelens F, Claessens B, Belmans R (2014) A Flexible stochastic optimization method for wind power balancing With PHEVs. IEEE Trans Smart Grid 5(3):1238–1245
21. Zhang N et al (2015) A fuzzy chance-constrained program for unit commitment problem considering demand response, electric vehicle and wind power. Int J Electr Power Energy Syst 65:201–209
22. Liao YT, Lu CN (2015) Dispatch of EV charging station energy resources for sustainable mobility. IEEE Trans Transp Electr 1(1):86–93
23. Wang G, Zhao J, Wen F, Xue Y, Ledwich G (2015) Dispatch strategy of PHEVs to mitigate selected patterns of seasonally varying outputs from renewable generation. IEEE Trans Smart Grid 6(2):627–639
24. Nguyen HNT, Zhang C, Mahmud MA (2015) Optimal coordination of G2V and V2G to support power grids with high penetration of renewable energy. IEEE Trans Transp Electr 1(2):188–195
25. Valentine K et al (2016) Relationship between wind power, electric vehicles and charger infrastructure in a two-settlement energy market. Int J Electr Power Energy Syst 82:225–232
26. Jadhav HT, Ranjit R (2015) Stochastic optimal power flow incorporating offshore wind farm and electric vehicles. Int J Electr Power Energy Syst 69:173–187

27. Sekyung H, Soohee H, Sezaki K (2010) Development of an optimal vehicle-to-grid aggregator for frequency regulation. IEEE Trans Smart Grid 1(1):65–72
28. Guille C, Gross G (2009) A conceptual framework for the vehicle-to-grid (V2G) implementation. Energy Policy 37(11):4379–4390
29. Sortomme E, El-Sharkawi MA (2012) Optimal scheduling of vehicle to-grid energy and ancillary services. IEEE Trans Smart Grid 3(1):351–359
30. Tomic J, Kempton W (2007) Using fleets of electric-drive vehicles for grid support. J Power Sources 168(2):459–468
31. Takagi M, Yamaji K, Yamamoto H (2009) Power system stabilization by charging power management of plug-in hybrid electric vehicles with LFC signal. In: Proceedings of vehicle power and propulsion conference, Dearborn, MI, pp 822–826
32. Galus MD, Koch S, Andersson G (2011) Provision of load frequency control by PHEVs, controllable loads, a cogeneration unit. IEEE Trans Ind Electron 58(10):4568–4582
33. Pillai JR, Bak-Jensen B (2011) Integration of vehicle-to-grid in the western Danish power system. IEEE Trans Sustain Energy 2(1):12–19
34. Ota Y et al (2012) Autonomous distributed V2G (vehicle-to-grid) satisfying scheduled charging. IEEE Trans Smart Grid 3(1):559–564
35. Masuta T, Yokoyama A (2012) Supplementary load frequency control by use of a number of both electric vehicles and heat pump water heaters. IEEE Trans Smart Grid 3(3):1253–1262
36. Yang H, Chung CY, Zhao J (2013) Application of plug-in electric vehicles to frequency regulation based on distributed signal acquisition via limited communication. IEEE Trans Power Syst 28(2):1017–1026
37. Liu H, Hu Z, Song Y, Lin J (2013) Decentralized vehicle-to-grid control for primary frequency regulation considering charging demands. IEEE Trans Power Syst 28(3):3480–3489
38. Mu Y, Wu J, Ekanayake J, Jenkins N, Jia H (2013) Primary frequency response from electric vehicles in the Great Britain power system. IEEE Trans Smart Grid 4(2):1142–1150
39. Vachirasricirikul S, Ngamroo I (2014) Robust LFC in a smart grid with wind power penetration by coordinated V2G control and frequency controller. IEEE Trans Smart Grid 5(1):371–380
40. Liu H, Hu Z, Song Y, Wang J, Xie X (2015) Vehicle-to-grid control for supplementary frequency regulation considering charging demands. IEEE Trans Power Syst 30(6):3110–3119
41. Pham TN, Trinh H, Hien LV (2016) Load frequency control of power systems with electric vehicles and diverse transmission links using distributed functional observers. IEEE Trans Smart Grid 7(1):238–252
42. Datta M, Senjyu T (2013) Fuzzy control of distributed PV inverters/energy storage systems/electric vehicles for frequency regulation in a large power system. IEEE Trans Smart Grid 1(4)
43. Falahati S, Taher SA, Shahidehpour M (2016) A new smart charging method for EVs for frequency control of smart grid. Int J Electr Power Energy Syst 83:458–469
44. Long C, Farrag MEA, Zhou C, Hepburn DM (2013) Statistical quantification of voltage violations in distribution networks penetrated by small wind turbines and battery electric vehicles. IEEE Trans Power Syst 28(3):2403–2410
45. Gellings C (2009) The smart grid: enabling energy efficiency and demand response. Fairmont Press
46. Albadi M, El-Saadany E (2007) Demand response in electricity markets: an overview. In: IEEE power engineering society general meeting, p 1–5
47. Jenkins N, Long C, Wu J (2015) An overview of the smart grid in great Britain. Engineering 1(4):413–421
48. Strbac G (2008) Demand side management: benefits and challenges. Energy Policy 36:4419–4426
49. Darabi Z, Ferdowsi M (2011) Aggregated impact of plug-in hybrid electric vehicles on electricity demand profile. IEEE Trans Sustain Energy 2:501–508
50. Shao S, Pipattanasomporn M, Rahman S (2012) Grid integration of electric vehicles and demand response with customer choice. IEEE Trans Smart Grid 3:543–550

51. Sheikhi A, Bahrami S, Ranjbar A, Oraee H (2013) Strategic charging method for plugged in hybrid electric vehicles in smart grids; a game theoretic approach. Int J Electric Power Energy Syst 53:499–506
52. Wang Z, Wang S (2013) Grid power peak shaving and valley filling using vehicle-to-grid systems. IEEE Trans Power Deliv 28:1822–1829
53. Oviedo RM, Fan Z, Gormus S, Kulkarni P (2014) A residential PHEV load coordination mechanism with renewable sources in smart grids. Int J Electr Power Energy Syst 55:511–521
54. López M, Martín S, Aguado J, de la Torre S (2013) V2G strategies for congestion management in microgrids with high penetration of electric vehicles. Electr Power Syst Res 104:28–34
55. Masoum A, Deilami S, Moses P, Masoum M, Abu-Siada A (2011) Smart load management of plug-in electric vehicles in distribution and residential networks with charging stations for peak shaving and loss minimization considering voltage regulation. IET Gener Transm Distrib 5:877–888
56. López MA, de la Torre S, Martín S, Aguado JA (2015) Demand-side management in smart grid operation considering electric vehicles load shifting and vehicle-to-grid support. Int J Electr Power Energy Syst 64:689–698
57. Lausenhammer W, Engel D, Green R (2016) Utilizing capabilities of plug in electric vehicles with a new demand response optimization software framework: Okeanos. Int J Electr Power Energy Syst 75:1–7
58. Mou Y, Xing H, Lin Z, Fu M (2015) Decentralized optimal demand-side management for PHEV charging in a smart grid. IEEE Trans Smart Grid 6(2)
59. Vandael S, Claessens B, Hommelberg M, Holvoet T, Deconinck G (2013) A scalable three-step approach for demand side management of plug-in hybrid vehicles. IEEE Trans Smart Grid 4(2)

Reviewing Surface Defects for the Performance Degradation in the Solar Devices

Kruti Pancholi, Mosam Pandya and Dhyey Raval

Abstract A silicon based photovoltaic (PV) cells are underlying a surface analysis for understanding its performance degradation. Approach for the split investigation based on the surface images with electrical parameter was used for analyzing the performance factors. Solar devices which are having a power hotspot for proficient electrical vitality are over time span. The defect in the cell due to the surface deformity leads to decreased in the performance parameter and affects the overall maximum power capability. The continuation to diminish wafer thickness in the fabrication process of silicon cells causes increase in the defects patterns as seen in the numerous cases studies. Reviewing the model-based system dependent on image processing algorithm especially designed for the degradation analysis capable to recognize any miniature crack before its large penetration to avoid major damage in the system. Study is based on the board surface and with the measurable symptoms in the initial phase of the degradation process. Analysis of PV cells with ARIMA model with voltage, current and power butt-centric analysis has been investigated to understand the process of its degradation. Recognition of the break and split division technique with edge detection was used in the model for its observation. Channel for split finding and recognizing its pattern is used in the modern application as seen in the recent field of the photovoltaic.

Keywords Solar cells · Imaging · Degradation and silicon

K. Pancholi · D. Raval (✉)
Swarrnim Institute of Technology, Swarnim Startup & Innovation University, Gandhinagar, Gujarat 382420, India
e-mail: dhyey.raval.research@gmail.com

K. Pancholi
e-mail: Krutij.pancholi@gmail.com

M. Pandya
L. J. Institute of Engineering and Technology, Ahmedabad, Gujarat 382210, India
e-mail: mosam.pandya@ljinstitutes.edu.in

A. Mehta et al. (eds.), *Advances in Electric Power and Energy Infrastructure*, Lecture Notes in Electrical Engineering 608,
https://doi.org/10.1007/978-981-15-0206-4_18

1 Introduction

Renewable energy is available from the inexhaustible assets like sunlight, wind, tides, waves, and geothermal warmth [1]. Energy conversion based on the sustainable resources is popular concepts in the present scenario. There will be the rise in the renewable electricity power from 83.7 TWh in 2000 to 1178.2 TWh in 2015 [1]. According to United Nations (UN), energy statistics has been update as 1431.3 TWh in 2016 [2]. Predicting breakdown of renewable energy growth from 2017 to 2050, the gross power generation will be increased [3]. Photovoltaic (PV) will add an important part to the future renewable energy generation [1]. With the certain current headwind, the significance of renewables and PV is possible to increase in the upcoming decades [1]. In the solar cells based on the photovoltaic conversion having crack or hotspots in the location can be analyzed with different algorithms which have been investigated for the present study. Cracks reduce the electrical performance or the mechanical deformity in the silicon (Si)-based cells in the photovoltaic (PV) modules. An extensive split could be result in breakage and crush the series of cells in a PV module, causes decreases of the electrical performance of the system. Performance change arises in the cell due to the manufacturing processes or mechanical handling [1].

Present study emphasis the several approaches to examine the performance of the cell parameter based on the ARIMA model, linear regression, with classification of a few decomposition of the imaging methods. Review on the articles reports and details is shown in the tabular form for its comparison.

2 Methods and Discussion

Several approaches have been presented for the given cases as seen in the Table 1, and algorithms were investigated to find its integrity in the current review. The vesselness channel depends on the Eigen-esteem investigation of the Hessian in various Gaussian scales [1]. Coarse scale structures are ordinarily by smoothing the picture with Gaussian literation. The Hessian framework is a square network of second-request incomplete subsidiaries of the smoothed picture. It is very well determined by convolving the first picture fix straight forward with a 2-D bit Gσ (where Gaussian (G) and σ is the standard deviation), which is the second-request halfway subsidiary of Gaussian σ literation. When utilizing a Gaussian piece with a standard deviation, vessels whose widths equivalent to 2σ have the most noteworthy vesselness reaction.

Table 1 Review on the recent PV case study and its details

Sr. no.	Article title	Year	Details	Reference
1	A novel crack detection algorithm for solar panel surface images	2013	Algorithm as tensor voting is used for noise removal, Less computation time, low computation costs, Faster, more stable, and more effective. Need to set parameters	[4]
2	Quantitative local current-voltage analysis with different spatially resolved camera based techniques of silicon solar cells with cracks	2014	Physical parameters as open circuit voltage, fill-factor, and cell efficiency analyzed. 0.2% absolute efficiency loss for global current voltage, 1% absolute efficiency loss for local current voltage in the crack location. 1–2% Loss in detection rate	[5]
3	A crack analysis model for silicon based solar cells	2014	The accuracy for extraction technique applied has been validated with comparison of the results of energy approach high accuracy, high time complexity	[6]
4	Application of an image processing software tool to crack inspection of crystalline silicon solar cells	2011	Fast, accurate, high efficiency and reliable performance. The hardware equipment's such as the illuminating source, camera, lens, and frame grabber are used	[7]
5	Analysis and simulation of cracks and micro cracks in PV cells	2013	Work on 2-D frame	[8]
6	Solar cell panel crack detection using particle swarm optimization algorithm	2011	High crack detection rate, High Cost solution	[9]
7	Enhanced crack segmentation (eCS): a reference algorithm for segmenting cracks in multicrystalline silicon solar cells	2018	High accuracy, low time complexity Low precision and recall	[1]
8	Feature extraction, supervised and unsupervised machine learning classification of PV cell electroluminescence images	2018	High accuracy, standard deviation and work on small size database	[10]

The breadth of Frangi-Net: A Neural Network Approach to Vessel Segmentation 3 retinal vessels in this work run from 6 to 35 pixels. Consequently, we pick a progression of σ as 3; 6; 12 pixels as per the needs. Rather than convolving a fix with three unique bits (G3; G6; and G12), we make a three-level goals chain of command and convolve each dimension with G3 as it were. The goals chain of importance comprises of the first fix and two down tested renditions, utilizing factors 2 and 4, respectively [11].

2.1 Tensor Voting Algorithm

The tensor voting has been used in the 2-D with a view of perceptual group, and then after extended for 3-D and N-D space, as a set of points x_i ($i = 1; 2 ::: N$) in 2-D space [12]. Perspective of the study was to deduce local geometric structure x_i, to analyze x_i. Using structure tensor (T) with polarity (P) will define native information at point $x \in R^2$. Where Term T is given as 2 by 2 symmetric with nonnegative definite matrix, and p is given as 2 by 1 vector.

$$T = \lambda_1 e_1 e_1^T + \lambda_2 e_2 e_2^T = (\lambda_1 - \lambda_2)\left(e_1 e_1^T\right) + \lambda_2\left(e_1 e_1^T + e_2 e_2^T\right) \quad (1)$$

The eigenvector (e_1) with respect to the biggest eigenvalue (λ_1) represents normal space for local-manifold, eigenvector (e_2) represents tangent space. A local-manifold is $\lambda_1 - \lambda_2$, shows how clear will be the structure. The polarity vector (p) will be used for sensing the endpoint as seen in local maxima of polarity (p).

For eigenvalues are very small, the point was classify as an outlier, and as a junction for both large and nearly equal.

2.2 Particle Swarm

Swarm intelligence (SI) is an inventive circulated savvy worldview for taking care of enhancement issues that initially took its motivation from the organic test by swarming, rushing, and grouping marvels in vertebrates [13]. Subterranean insect settlement optimization, genetic calculation, and molecule swarm enhancement are different developmental calculations proposed by scientists [13]. Because of straightforwardness for PSO condition with quick convergence, PSO was observed as better. Subsequent to investigating factor for PSO condition, Yuhui Shi and Russell Eber-

hart proposed new parameter "w" as inertia inactivity weight in essential condition. It looks like a nearby hunt calculation. Expansion of this factor bases investigation and abuse in pursuit space. Right off the bat estimation of w was kept static. Later on, it was kept straight from 0.9 to 0.4. At the point when Clerc's choking technique was utilized, φ was 4 and steady multiplier was along these lines taken as 0.729. As per Clerc, expansion of narrowing component might be important to guarantee combination the molecule particle swarm optimization algorithm.

$$V[\text{id}] = K[V[\text{id}] + c1 * r(\text{id}) * (\text{pbest}[\text{id}] - x[\text{id}]) + c2 * (\text{gbest}[\text{id}] - x[\text{id}]] \tag{2}$$

where $\phi = c1 + c2, \quad \varphi > 4$ where K is particle constant.

For PSO having a constraint parameter has been considered for a example of algorithm and inertia weight van nook Bergh et al. [13] had developed guaranteed convergence particle swarm optimizer (GCPSO). GCPSO has solid nearby assembly properties rather than PSO. Calculation performs better and modest number of molecules. This marvel was characterized as stagnation by GCPSO i.e., a molecule's present location agrees to the worldwide good position molecule, at that point the molecule will possibly move far with point it past speed and w is nonzero. If it past speeds are extremely near zero, at that point every one of the particles can move once their make up for lost time for the worldwide good molecule, which can prompt premature combination of the calculation. Truth be told, this does not ensure that the algorithm has met on a local.

2.3 ARIMA Model

An ARIMA model has computable properties and better fitted for direct information designs [14]. It is expected in an ARIMA model that the future estimations of a variable are straight capacity of various past perceptions and irregular blunders. The key procedure of generating a period arrangement can be given as Eq. (3)

$$y_t = \alpha_0 + \alpha_1 y_{t-1} + \alpha_2 y_{t-2} + \cdots + \alpha_p y_{t-p} + \varepsilon_t - \beta_1 \varepsilon_{t-1} - \beta_2 \varepsilon_{t-2} - \cdots - \beta_q \varepsilon_{t-q} \quad (3)$$

where y_t and ε_t shows value and random error for the time period *t,* respectively;α_i ($i = 1, 2, 3,\ldots, p$) and β_j ($j = 0,1, 2, 3,\ldots, q$) were model parameters; also *p, q* are integers usually referred for the order of the model. The random errors, Σt, were assumed to individually and identically distribute within a mean zero and constant variance as σ^2. This converge an autoregressive (AR) method of order *p*, where $q = 0$ in the Eq. (1), and converge to moving averages (MA) of order *q*, where $p = 0$ from Eq. (1). With the help of the seminal works carried out in the past, has developed the method for calculating ARIMA model. Box and Jenkins et al. have shown simple three- step method of ARIMA model for constructing and finding the factor for estimation and understanding for the model.

(Step1) For checking time arrangement was stationary or dynamic; if time arrangement was not stationary and demonstrates pattern and heteroscedasticity, at that point the distinction with power trans-development was connected. In the time arrangement changes over into a time arrangement with difference for parameter of the ARIMA model. (Step2) Perspectives on objective of minimized and large blunders, the model parameters are analyzed appropriately for the plan in a conditional method. (Step3) For checking and approving, model doubts and mistakes Σt were practiced. In this manner, the demonstrative data helps in accomplishing the fitting ARIMA model. The previous stated three stages of the model describing process were repeated and accomplish an epitome goal for an ARIMA model. The model after the required cycles might be utilized for the determining purpose.

Above methods can be utilized for finding surface defects. Development in technology results into various level PSO, which is known as progressive rendition of PSO called as Hierarchical PSO (H-PSO) [13]. In their calculation, particles are masterminded in active chain and significant. In H-PSO, all particles are prearranged in a tree and shape the progressive with the goal that every hub of tree contains precisely one particle. The particle swarm optimization has homogeneity i.e., the swarm bunch contain a similar sort of particle. Other system called heterogeneous particle swarm contains the characteristic sort of swarm. The hybrid method for detection of PV module crack and degradation is shown in Fig. 1.

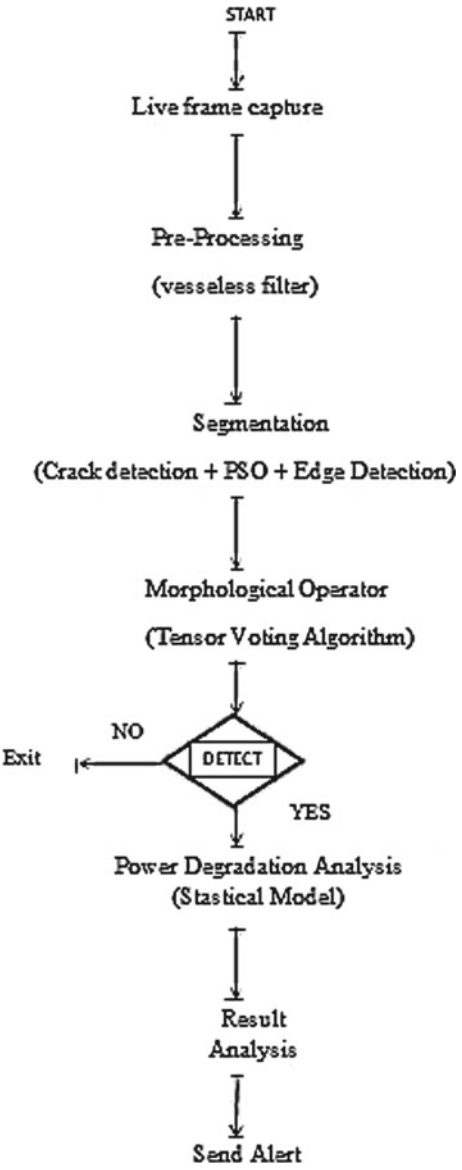

Fig. 1 Flowchart for the algorithm

3 Pseudo Code for the Model

```
Begin {
get live Frame
(left side)
(right side)
if  (noises == Frame)
             {
Remove it using filter
             }
   else
    Frame1 = Frame
*Apply segmentation on Frame1
                    if (detection + PSO) = detection edge

                                {
                    Segment Frame = Frame 1
 }
                    else
{
                    Continue…
{
                    Morphological Frame = segmented Frame
1

{
                                          If (ans==1)
                        {
                                            Detected
                         }
                Else
                                  {
                                   For Degradation Analysis
}

If (detection = = 1)
{
        Apply PV degradation model & Result Analysis
}
else
{
Exit
}
```

4 Conclusion

In this study, several reviews with different methods of the analysis of the surface defects and degradation have been presented. In a hybrid approach for the detection and analyzing degradation process by using present algorithm reduces the complexity of finding surface defects.

References

1. Stromer D, Vetter A, Oezkan HC, Probst C, Maier A (2019) Enhanced crack segmentation (eCS): a reference algorithm for segmenting cracks in multicrystalline silicon solar cells, pp 2156–3381
2. Energy Statistics Pocket Book (2019) United Nations Publications, New York, USA
3. Gielena D, Boshella F, Sayginb D, Bazilianc MD, Wagnera N, Gorinia R (2019) The role of renewable energy in the global energy transformation, pp 2211–467X
4. Feng B, Shen X, Long J, Chen H (2013) A novel crack detection algorithm for solar panel surface images, pp 650–654. 978-0-7695-5125-8/13
5. Pletzer TM,van Molken JI, RiBland S, Hallam B, Comagliotti E, John J, Breitenstein O, Knoch J (2014) Quantitative local current-voltage analysis with different spatially resolved camera based techniques of silicon solar cells with cracks, pp 3473–3478. 978-1-4799-4398-2/14
6. Al Ahmar J, Wiese S (2014) A crack analysis model for silicon based solar cells. In: 15th international conference on thermal, mechanical and multi-physics simulation and experiments in microelectronics and microsystems. 978-1-4799-4790-4/14
7. Jean J-H, Chen C-H, Lin H-L (2011) Application of an image processing software tool to crack inspection of crystalline silicon solar cells. In: Proceedings of the international conference on machine learning and cybernetics. Guilin
8. Al Ahmar J, Wiesel S (2013) Analysis and simulation of cracks and micro cracks in PV Cells. In: 14th international conference on thermal, mechanical and multi-physics simulation and experiments in microelectronics and microsystems
9. Aghamohammadi AH, Prabuwono AS, Sahran S, Mogharrebi M (2011) Solar cell panel crack detection using particle swarm optimization algorithm. In: International conference on pattern analysis and intelligent robotics. Putrajaya, Malaysia
10. Karimi AM, Fada JS, Liu JQ, Braid JL, Koyuturk M, French RH (2018) Feature extraction, supervised and unsupervised machine learning classification of PV cell electroluminescence images. 978-1-5386-8529-7/18
11. Fu W, Breininger K, Würfl T, Ravikumar N, Schaffert R, Maier A (2017) Frangi-net, a neural network approach to vessel segmentation
12. Gong D, Medioni G (2012) Probabilistic tensor voting for robust perceptual grouping. Institute for Robotics and Intelligent Systems. https://doi.org/10.1.1.310.2157
13. Urade HS, Patel R (2011) Study and analysis of particle swarm optimization: a review. In: 2nd national conference on information and communication technology (NCICT)
14. Chauhan A, Singh A (2017) An ARIMA model for the forecasting of healthcare waste generation in the Garhwal region of Uttarakhand, India. Int J Serv Oper Inf. https://doi.org/10.1504/IJSOI.2017.086587

Identification of the Source of Power Quality Degradation Using Signature Extraction from Voltage Waveforms

Parth Vaghera, Dinesh Kumar, Nishant Kothari and Sayed Niamatullah

Abstract This paper provides the understanding of features and method used for classifying the root cause of the fault event using those unique features. In particular, the paper focuses on identification of fault caused by the animal, lighting, tree, equipment and vehicle events. Different features are extracted to provide the input to neural network. For extracting features voltage and current samples collected during the fault at the monitoring, stations were analyzed. Artificial neural network with multilayer perceptron model is trained for the classification. Features were calculated using 154 real-world fault events and applied to the classifier. It estimated to be having 76.47% of classification rate.

Keywords Diagnosis (faults) · Power quality disturbance · Wavelet decomposition · Artificial neural network · Classification

1 Introduction

Power quality is the most important issue for the electric utilities. So, its study is gaining interest day by day. Power quality disturbance can be caused by various internal or external factors. Internal events can be due to equipment malfunctioning or failure [1]. Fault causing due to the contact of animals like squirrels, birds and snakes or due to contact of tree or due to vehicle accidents and natural phenomenon like lightning can be possible causes of the external events [2]. Because of several power

P. Vaghera (✉) · D. Kumar · N. Kothari · S. Niamatullah
Department of Electrical Engineering, Marwadi Education Foundation's Group of Institution, Rajkot, India
e-mail: parth.vaghera15489@marwadieducation.edu.in

D. Kumar
e-mail: dinesh.kumar@marwadieducation.edu.in

N. Kothari
e-mail: nishant.kothari@marwadieducation.edu.in

S. Niamatullah
e-mail: sayed.niamatullah11945@marwadieducation.edu.in

A. Mehta et al. (eds.), *Advances in Electric Power and Energy Infrastructure*, Lecture Notes in Electrical Engineering 608,
https://doi.org/10.1007/978-981-15-0206-4_19

quality monitoring stations, the amount of measuring data is increasing. Therefore, there should be some means to develop that may automatically analyze the abnormal conditions, characterize and then classify the possible cause or the source of the event [1].

Several works can be found in the literature for the identification of fault cause and their automatic classification. In the problem of the identification of the cause behind the fault or type of fault, two-fold solution is prepared, first is to extract features from the voltage/current waveform, and the second is employing these features to a classifier. Using signal processing tools, some features like time of the fault, fault insertion angle, number of faulted phases, time duration of fault, wavelet transform and arc voltage were extracted of the faults resulting from animal contact, tree contact and lightning. These characteristics were studied and suggested that the source of power quality disturbance can be identified if these are given to the classifier [2]. An analysis based on the three aspects, time domain, frequency domain and electric arc was done on the waveform of different fault types such as animal, tree, lightning, equipment and vehicle [3]. A multivariable analysis of variance (MANOVA) and rules extracted using CN2 induction, algorithm was used for the cause identification using the same features and obtained a good accuracy [4]. The same set of feature was employed in a support vector machine (SVM)-based classifier that amounts to produce better classification results [5]. S-transform, a time-frequency representation transform-based features like energy of signal, mean of signal, peak value of signal and standard deviation were extracted, and it was given to ANN for classification of seven types of power quality disturbances such as sag, swell, harmonic, transient, outage and voltage fluctuation [6]. It was seen to perform better in terms of accuracy and even in the noisy environment.

In this paper, we focused on the identification of the sources causing power quality disturbance. Five different types of sources in EPRI database [7], for instance, disturbance that instigated by animal contact, tree contact, vehicle accident, equipment failure and lightning are taken for this study. In earlier work, maximum three classes of sources were considered [2–4]. Some features such as crest factor, form factor, RMS values, and peak-to-peak are included with the features used in the earlier work for classification. The proposed set of features contributes significant accuracy level in classification.

The introduction of this paper was provided in Sect. 1. The description of data is given in Sect. 2, and the feature description is written in Sect. 3. The methodology for fault classification and results is shown in Sect. 4. Finally, some conclusions of this paper and future work are given in Sect. 5.

2 Power Quality Dataset

The data set used in this paper is obtained from the National Database Repository of Power System Events located in USA [7]. The data includes events due to animal contact, tree contact, vehicle accident, equipment failure and lightning-induced

faults. Fault event consists of time and day of the commencement of the fault and three-phase instantaneous voltage and current. The PQ data set consists of 154 total events in which animal contact includes 14 events, equipment consists of 55 events, lightning includes 24 events, tree fault consists of 42 events, and vehicle consists of 19 events.

3 Power Quality Features

The features extracted for the identification of the fault cause of the power quality disturbance are described in this section. Two main groups of features are taken into account: first one is time and day at which power quality waveforms are registered, and second is signatures of the waveforms. Five of them are proposed in [4].

3.1 Time and Day

As time and day cannot be referred as the electrical quantities, still it can provide better influence in detecting the power quality deterioration caused due to weather condition which cannot be avoided. It is found that certain type of power quality drop or fault happens merely because of weather or external sources that are present in specific time in a day or specific days in a year.

Since the data collected is labeled with the date and time date of fault occurrence. For instance, it is observed that most of the animal events were observed during summer and spring (days between 100 and 200 out of 365 days in Fig. 1a), few of the events caused due to animal contact were occurred in other seasons, and the lightning events were occurred in the summer (days between 150 and 250). Most of the tree events were occurred in fall due to heavy wind.

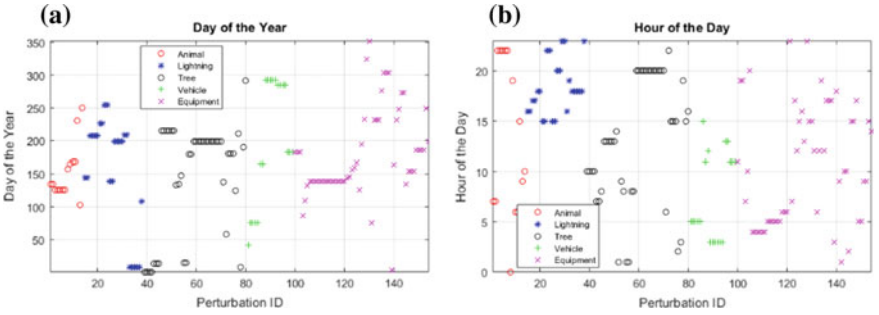

Fig. 1 Events classified according to the **a** day of the year, **b** time of the day

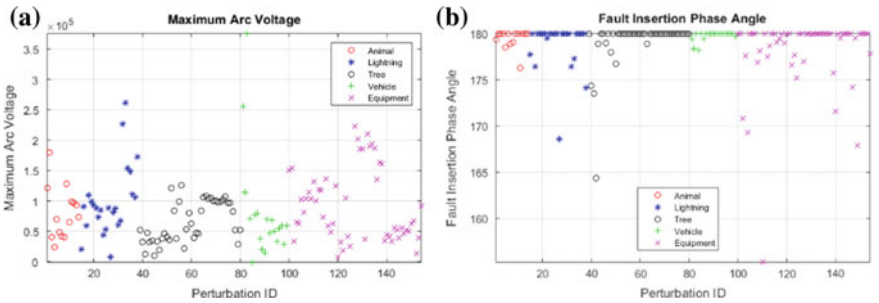

Fig. 2 Plot of **a** maximum arc voltage, **b** fault insertion phase angle

It can be seen from Fig. 2b that majority of the animal events occurred during daytime, most of the lightning events were occurred during night time, and the tree events were spread out in time.

3.2 Features from Waveform Signature

Several features can be computed from the signatures of the voltage and current waveforms. As waveform signature at the time of power quality disturbance originated by different source are different. Hence, in order to separate one power kind of the disturbance from the others, the characteristics of the waveforms are studied. In the section, the computational methods of some the characteristics are described.

(i) *Maximum arc voltage*:
This feature is based on the fact that an arc gets struck between the animal and the line when they are about to be in contact with each other, it is observed that most of the animal contact events have arc voltage greater than 40% of the pre-fault voltage, and lightning contacts have arc voltage value less than 40% of the pre-fault value. It can be obtained from the (1).

$$V_{\text{arc}} = \frac{V_f - I_f \times R - L \times \left(\frac{\mathrm{d}I_f}{\mathrm{d}t}\right)}{\text{sign}\left(I_f\right)} \tag{1}$$

where V_{arc} = peak arc voltage at the fault location, V_f = fault phase voltage, I_f = current during the fault, L = inductance of the line, R = resistance of the line $\text{sign}\left(I_f\right) = 1$, if $I_f > 0$ and -1 if $I_f \leq 0$. Figure 2a shows the plot of maximum arc voltage of each fault event.

(ii) *Fault insertion phase angle*:
This feature reveals that animal and tree contacts events are inserted around peak of the voltage wave. The value of the phase angle is between $\pm 180°$. The phase angle value roughly around $\pm 90°$ corresponds to event starting

around peak of the waveform. Most of the animal events are having phase angle between 60° and 120°. Figure 2b is the plot of fault insertion phase angle of each event.

(iii) *Fault impedance magnitude*:
It can be calculated by taking voltage of the faulted phase and neutral current, as given in (2).

$$Z_{\text{fault}} = \min\left(\left|\frac{V_k \angle \theta_k}{\text{In}_k \angle \Phi_k}\right|\right) \tag{2}$$

where Z_{fault} = fault impedance value, k is number of voltage and current cycle.
V_k = Fundamental voltage magnitude of the faulted phase in cycle 'k,' θ_k = Phase angle of the faulted phase voltage in cycle 'k,' In_k = Fundamental magnitude of the neutral current in cycle 'k,' Φ_k = Phase angle of the neutral current in cycle 'k.'
In the computation of the fault impedance, neutral current is used as it contains only fault current. Figure 3a shows the impedance at the fault point of each event.

(iv) *Crest factor*:
It can be computed by dividing peak values with the effective values. In case of waveform which is sinusoidal, the crest factor is the ratio of peak value to the RMS value, and its value is 1.414. It is calculated using (3). It is observed that in Fig. 3b that crest factor of the voltage waveform in case of equipment and vehicle instigated faults varies more than rest of the sources.

$$\text{Crest Factor} = \frac{V_{\text{peak}}}{V_{\text{rms}}} \tag{3}$$

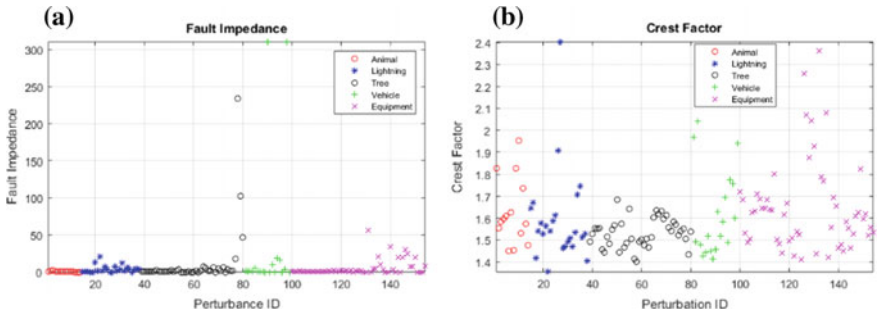

Fig. 3 Plot of values of **a** fault impedance magnitude, **b** crest factor of each event

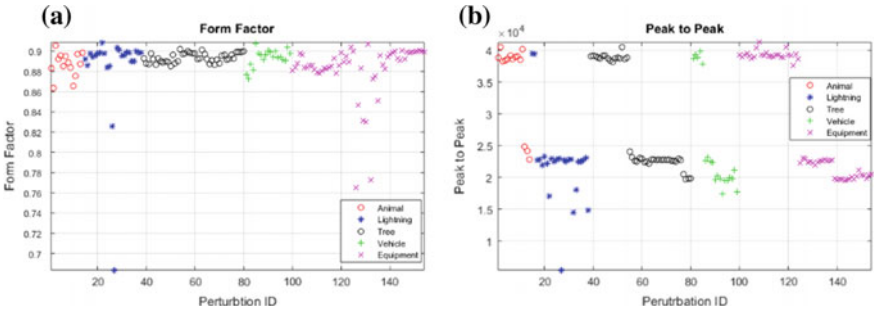

Fig. 4 Values of **a** form factor, **b** peak-to-peak of each event

(v) *From factor*:
Form factor of an alternating current waveform can be obtained by dividing the RMS value by the average value as given in (4). Figure 4a shows the plot of the form factor of each event whereby it can be noticed that form factors of the voltage waveforms in equipment failure.

$$\text{Form Factor} = \frac{I_{\text{rms}}}{I_{\text{av}}} \tag{4}$$

(vi) *Peak2peak*:
It gives the value which determines the maximum to minimum difference of the signal. It differentiates some of the events like lightning, vehicle and animal. Figure 4b is the peak-to-peak value of the fault of each event.

(vii) *RMS value*:
RMS value of a signal is its root mean square over time period. It differentiates some of the events like lightning, vehicle and animal. Figure 5 is the plot of the RMS values of faulted phase of each event.

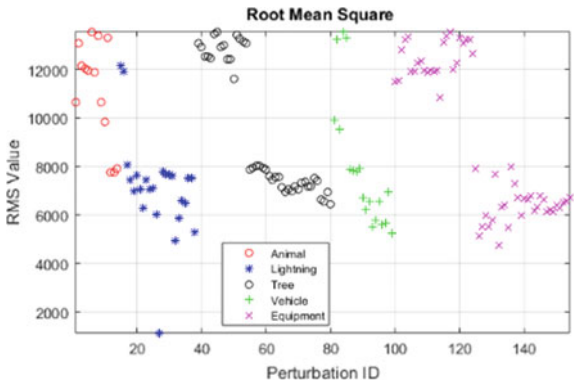

Fig. 5 Root mean square value

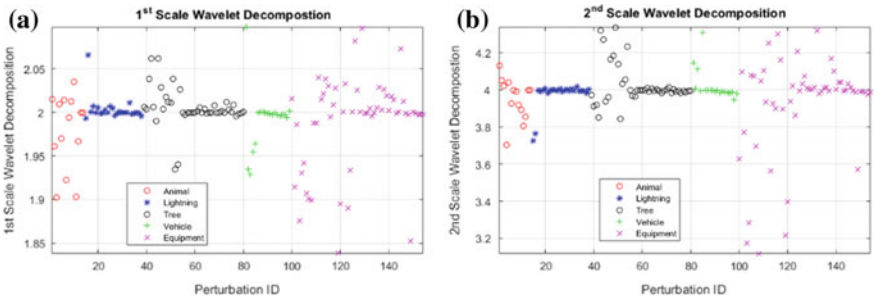

Fig. 6 Energy of wavelet decomposition of: **a** first scale, **b** second scale

(viii) *Maximum energy of* first-*scale and* second-*scale wavelet*:
Since voltage and current waveform exhibit transient and broad range of frequency at the time of faults, therefore, a decomposition of the frequency bands is performed. It is obtained applying wavelet decomposition of mother wavelet 'db6.' In this wavelet decomposition method, the signal is decomposed into approximation (low pass filtered) and detailed coefficient (high pass filtered), and then, again approximation coefficient is further decomposed. Second level of decomposition is performed for feature extraction. In order to examine changes in the first-level or the second-level frequency bands, maximum energy of the both levels is calculated. It is observed that most of the tree and animal instigated faults show higher and diverse range of energy in the first-level decomposition than in the second level. However, energy for rest of sources does not change significantly in both levels. Figure 6a,b shows the plot of energy of wavelet decomposition of first scale and second scale.

4 Fault Cause Identification Methodology

The proposed methodology uses the features extracted in the previous section for the classification using the artificial neural network for the identification of the cause.

4.1 Artificial Neural Network (ANN)

An artificial neural network-based model is constructed for classification for power quality disturbance's source. As it is known that ANN model includes input layer, hidden layers and output layer, where number of neurons and depth of hidden layers are adjusted to obtain desired output. The input layer is consisted of the above features calculated, and output layer includes the sources of faults that are to be identified. The ANN uses the multilayer perceptron (MLP) model in which the number of hidden

layers can be varied. The network used is feedforward network with the activation function used is hyperbolic tangent function. Trial and error method is used to select the required number of neurons in each hidden layer.

The method involves the data to be divided into training set and testing set for both features as inputs and target as outputs. The input matrix to the ANN model is constructed with the size 462 × 12 for total of 462 cases, and each case has 12 features. Later, out of 462, some percentage (here 80 and 75) from each source class is included into input matrix.

4.2 Results of Classification Methodology

In this section, some results of the proposed technique are shown in Tables 1 and 2. The tables show the number of layers used in ANN classifier and also the number of neurons used in each layer. In the table, we have taken 75% data from each class for training, and remaining 25% data is used for testing purpose. By using different combinations, 76.47% maximum accuracy was obtained.

The set of constructed features and MLP-based classifier are seemingly yielding significant accuracy. Previously known similar works reported classification results higher accuracy, while number of classes is less.

Table 1 Training data = 75% and testing data = 25%

No of layer	No of neurons in each layer				Test accuracy (%)
	1st	2nd	3rd	4th	
3	3	13	13		69.33
3	5	14	4		70.66
3	4	7	6		69.33
3	5	10	8		72
4	7	9	8	8	69.33

Table 2 Training data 80 and training data = 20%

No of layer	No of neurons in each layer				Test accuracy (%)
	1st	2nd	3rd	4th	
2	4	6			69.11
2	4	8			76.47
2	5	14			66.17
2	6	10			64.7
2	7	13			67.64

5 Conclusions and Future Work

In this paper, a new set of features was analyzed for fault classification. These features were extracted and statistically analyzed for fault classification. Animal contact, tree contact, lightning, equipment, vehicle events were classified using these events. These features were used for the classification using ANN, and it was found that proposed technique performs significantly compared to other previously proposed methods.

No waveform-based features were able to distinguish the cause with the high accuracy. The wavelet analysis of instantaneous current of faulted phase will be analyzed in the future. The signal will be analyzed in different scales of the wavelet, and their maximum energy will be calculated and used as the features. These features will be used as input to the classifier for the classification to get the maximum accuracy.

References

1. Bollen MH, Gu IY, Axelberg PG, Styvaktakis E (2007) Classification of underlying causes of power quality disturbances: deterministic versus statistical methods. EURASIP J Adv Signal Process 2007(1):079747
2. Kulkarni S, Lee D, Allen AJ, Santoso S, Short TA (2010) Waveform characterization of animal contact, tree contact, and lightning induced faults. In: IEEE power and energy society general meeting, IEEE, July 2010, pp 1–7
3. Qin X, Wang P, Liu Y, Guo L, Sheng G, Jiang X (2018) Research on distribution network fault recognition method based on time-frequency characteristics of fault waveforms. IEEE Access 6:7291–7300
4. Nunez VB, Kulkarni S, Santoso S, Joaquim MF (2010) Feature analysis and classification methodology for overhead distribution fault events. In: IEEE power and energy society general meeting, IEEE, July 2010, pp 1–8
5. Nunez VA, Kulkarni S, Santoso S, Melendez J (2010) SVM-based classification methodology for overhead distribution fault events. In: 14th international conference on harmonics and quality of Power (ICHQP), IEEE, 26 Sep 2010, pp 1–6
6. Kaewarsa S (2009) November Classification of power quality disturbances using S-transform based artificial neural networks. In: 2009 IEEE international conference on intelligent computing and intelligent systems (ICIS), vol 1. IEEE, pp 566–570
7. http://pqmon.epri.com/disturbance_library/see_all.asp

Study and Analysis of HTLS Conductors for Increasing the Thermal Loading of 220 kV Transmission Line

Akshit Kachhadiya, Chetan Sheth, Vinod Gupta and Krunal Darji

Abstract In the present scenario, demand of electricity is increasing drastically across the country in order to revolutionize development in industrial, agriculture and commercial section. As a consequence, the amount of power transfer capacity has to be enhanced on overhead transmission lines. However, the existing lines are gaining their utmost critical limits of ampacity and sag. This complication has become very predominant to obtain reliable, secure and economic operation of power system. In India, ACSR conductors are generally used in overhead transmission lines for transmission of power. The higher power transferability in existing lines, reduction in losses and optimization of Right of Way of electrical network are the requirement of the today's power system network. New generation high-performance conductors would help in electric power delivery system for efficient transmission of energy by way of enhancement of power flow per unit of Right of Way and reduction in losses under normal as well as under critical conditions can help in resolving the issues like growing congestion in existing corridors of transmission/distribution network and Right of Way problems. Low-resistant conductor—AL59 alloy conductors and high temperature low sag (HTLS) conductors can be used for re-conductoring of existing lines to mitigate the overloading issues. Several HTLS conductors like STACIR, ACSS, ACCC, TACSR, etc., are available in the market. Selection of HTLS conductor is also an important parameter for re-conductoring of any transmission line. This paper discusses the issues of overloading of transmission line and mitigation by re-conductoring through HTLS conductors. A case study is described by

A. Kachhadiya (✉) · C. Sheth
G. H. Patel College of Engineering & Technology, Vallabh Vidhyanagar 388120, India
e-mail: Akshitkachhadiya86@gmail.com

C. Sheth
e-mail: chetansheth@gcet.ac.in

V. Gupta · K. Darji
Electrical Research & Development Association, Vadodara 390010, India
e-mail: Vinod.gupta@erda.org

K. Darji
e-mail: krunal.darji@erda.org

A. Mehta et al. (eds.), *Advances in Electric Power and Energy Infrastructure*, Lecture Notes in Electrical Engineering 608,
https://doi.org/10.1007/978-981-15-0206-4_20

re-conductoring of several HTLS and AL59 conductors, and optimum solution is proposed for avoiding overloading of transmission line.

Keywords High temperature low sag conductors · Overhead lines · Re-conductoring · Ampacity · Thermal loading limit

1 Introduction

The demand of electric power is increasing at a rapid growth, while new transmission line facilities are being constructed at a slow rate. This leads to overloading of transmission line. The loading limit of line is thermal loading limit. Thermal loading limit of line is also an important constraint of transmission line in power system. The overloading of line causes heating of the conductor, and it can damage the conductor. Overloading of the transmission line and Right of Way issues are the major challenges for any utility [1].

In India, generally, power transmission lines are constructed using ACSR conductors. However, ACSR conductors cannot be operated at higher temperatures, and their losses are higher at higher power transmission. Thus, it becomes necessary to up-rate the transmission line or construction of new line. The construction of new transmission lines involves higher cost and time-consuming task. ROW is also a major challenge in construction of new transmission line [2]. Thus, it becomes necessary to up-rate transmission capacity. Various methods available for up-rating of overhead lines like up-gradation of transmission lines, i.e. alteration in the existing transmission line to allow it to operate at a higher voltage and up-rating of transmission lines, i.e. alteration in the existing transmission line to enable increased current flow. The various capacity enhancement methods are summarized in Fig. 1.

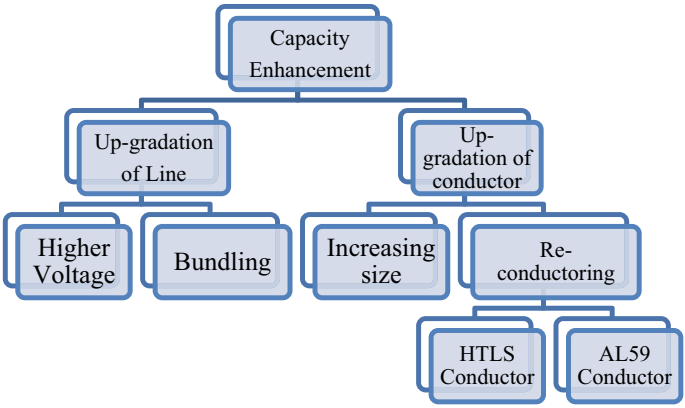

Fig. 1 Capacity enhancement methods [3]

The increase of voltage level requires the re-insulation of the line to the new voltage level which increases phase to phase distances and ground clearances. It required high cost also [3].

One of the methods to achieve the above is by re-conductoring the transmission line. This can be achieved using conductors larger than the existing ones or using conductors with the same diameter having higher temperature capacity. Increasing the thermal loading of an existing line by replacing the conductor larger than the original will increase both tension load and transverse wind loads on existing structures.

Increasing the thermal loading of an existing line by replacing the conductor having the same diameter but capable of operation at higher temperature (within existing sag clearance) may avoid the need for extensive reinforcement of suspension structures [4].

Replacing the existing ACSR conductors with high-performance conductors with the same diameter is one of the advanced solutions to increase the thermal rating of existing lines with a minimum of structural reinforcement. The most important features of HTLS conductor is that double the power can be transferred in comparison with the ACSR conductor of same size. Re-conductoring with HTLS conductors is most suitable option due to higher temperature capacity and low sag conductor [5].

2 High-Performance Conductors

2.1 Low-Resistant Conductors—Al59 Alloy Conductors

AL59 alloy conductors are manufactured from Al–Mg–Si (Aluminium–Magnesium–Silica) rods. The conductor comprises an inner core and concentrically arranged strands forming the inner and outer layers of the conductor. These are low resistance with high-conductivity alloy conductors.

2.2 HTLS (High Temperature Low Sag) Conductors

HTLS stands for “high temperature low sag” conductors. They can be operated at high temperature beyond 100 °C for longer periods of time without dropping their tensile strength and have less sag. They elongate less with temperature than normal all aluminium or steel-cored aluminium conductors [6]. The several types of HTLS conductors are given below:

(1) ACSS—Aluminium Conductor Steel Supported
(2) TACSR—Thermal Alloy Conductor Steel Reinforced
(3) STACIR—Super Thermal Aluminium Alloy Conductor INVAR Steel Reinforced
(4) ACCR—Aluminium Conductor Composite Reinforced
(5) ACCC—Aluminium Conductor Composite Core.

3 Case Study

The study of re-conductoring is performed using ACCC, ACSS, TACSR, STACIR and AL59 conductors on 220 kV double circuit transmission lines from 400 kV substation to 220 kV substation. The line is having Zebra conductor and having 4.6 km length. The line can transmit up to 213.38 MVA per circuit at ambient temperature of 45 °C and maximum operating temperature of 75 °C. For the analysis, the network is modelled using Mi-Power software.

It is observed that during peak load conditions of the line, loading of each circuit is around 87.3% of loading limit. We have performed $N - 1$ contingency analysis of one of the circuits of 220 kV D/C transmission line. During $N - 1$ condition, it is observed another line will be loaded as 164% of loading limit. Looking to the $N - 1$ contingency results, it is observed that it is necessary to up-rate the 220 kV D/C transmission lines from 400 kV substation to 220 kV substation (Fig. 2).

The ampacity of different conductor with conductor size at ambient temperature at 45 °C is listed as per Table 1.

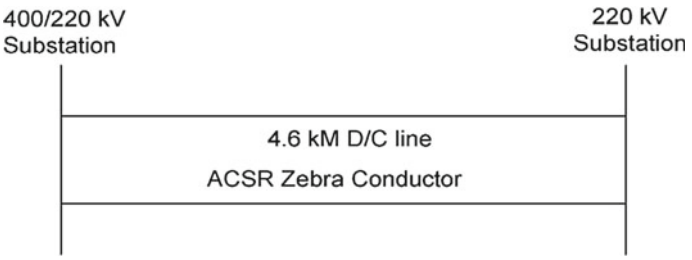

Fig. 2 220 kV D/C line from 400 kV substation to 220 kV substation

Table 1 Thermal loading limits for ACSR Zebra equivalent conductors [7]

	Conductor size					
Zebra equivalent conductor	Metal area in mm^2	Dia in mm	Min temperature (°C)	Ampacity (A)	Max temperature (°C)	Ampacity (A)
ACSR	484	28.62	75	560	85	703
AL59	383	25.41	75	516	95	743
TACSR	462.63	27.93	85	667	150	1142
STACIR	419.39	26.61	85	642	200	1296
ACSS	413.69	26.40	85	625	200	1260
ACCC	588.30	28.14	85	780	175	1472

Simulation study for re-conductoring of 220 kV D/c line is carried out with AL59 and ACCC, ACSS, TACSR and STACIR HTLS conductors is carried out considering the above parameter.

4 Simulation Results and Discussion

4.1 Simulation Results

In simulation, three cases have been studied: (1) Conductors ampacity while maintaining minimum operating temperature (2) Conductors ampacity with maximum operating temperature and (3) $N - 1$ contingency analysis of one circuit of D/c line with conductors ampacity with maximum operating temperature. The case-wise results and discussion are given below:

Case-1

(See Table 2).
Case-2
(See Table 3).
Case-3
(See Table 4).

4.2 Discussion

A case study for re-conductoring of 220 kV D/c line with several HTLS conductor and AL59 conductor is carried out with three different cases. The comparison of several HTLS conductors with ACSR Zebra equivalent in terms of % loading and % losses is shown in Figs. 3, 4, 5, 6, 7 and 8.

Table 2 Comparison of various HTLS conductors with ACSR conductors at minimum operating temperature

Parameter	ACSR	ACCC	ACSS	STACIR	TACSR	AL59
Operating temperature °C	75	85	85	85	85	75
Voltage level (kV)	220	220	220	220	220	220
AC resistance Ω/km	0.0847	0.07062	0.1070	0.10163	0.09613	0.0961
Ampacity (A)	560	780	625	642	667	516
Power flow (MW)	189.66	189.72	189.712	189.715	189.718	189.71
Loss in (MW)	0.2517	0.2381	0.3601	0.3421	0.3237	0.3236
% Line loading	87.2	62.7	78.2	76.1	73.3	94.7

Table 3 Comparison of various HTLS conductor with ACSR conductor at maximum operating temperature

Parameter	ACSR	ACCC	ACSS	STACIR	TACSR	AL59
Operating temperature °C	75	175	200	200	150	95
Voltage level (kV)	220	220	220	220	220	220
AC resistance Ω/km	0.0847	0.0902	0.1455	0.1382	0.1156	0.1023
Ampacity (A)	560	1472	1260	1296	1142	743
Power flow in (MW)	189.66	189.72	189.68	189.69	189.7	189.71
Loss in (MW)	0.2517	0.3039	0.4890	0.4645	0.3891	0.3444
% Line loading	87.2	33.3	38.7	37.7	42.8	65.7

Table 4 Comparison of various HTLS conductor with ACSR conductor at maximum operating temperature in $N - 1$ contingency analysis

Parameter	ACSR	ACCC	ACSS	STACR	TACSR	AL59
Operating temp. °C	75	175	200	200	150	95
Voltage level (kV)	220	220	220	220	220	220
AC resistance Ω/km	0.0847	0.0902	0.1455	0.1382	0.1156	0.1023
Ampacity (A)	560	1472	1260	1296	1142	743
Power flow (MW)	356.35	356.34	356.14	356.182	356.27	356.32
Loss in (MW)	1.0085	1.0725	1.7214	1.6357	1.3717	1.2149
% Line loading	164.0	62.4	72.7	70.7	80.3	123.5

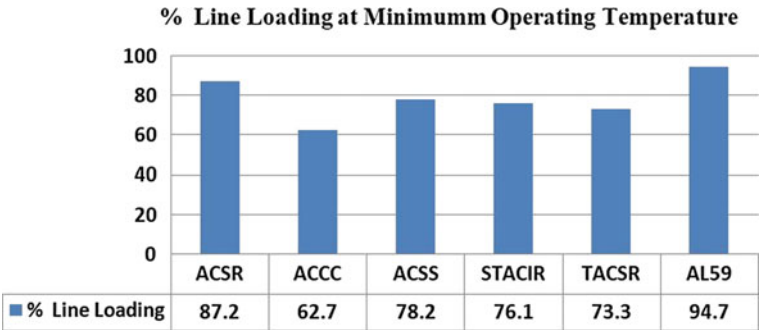

Fig. 3 Comparison of percentage of line loading in minimum operating temperature

As per the results of Table 2, it can be clearly seen that out of various HTLS conductors, at 85 °C, ACCC conductor has less % of line loading (62.7) MW and losses (0.2381) MW compared to ACSR Zebra conductor's % of line loading (87.2) MW and losses (0.2517) MW at 75 °C. According to results of Table 3, at maximum operating temperature, ACCC conductor has less losses (0.3039) MW and % of line loading (33.3) MW at 175 °C as compared to other HTLS conductors, while ACSR

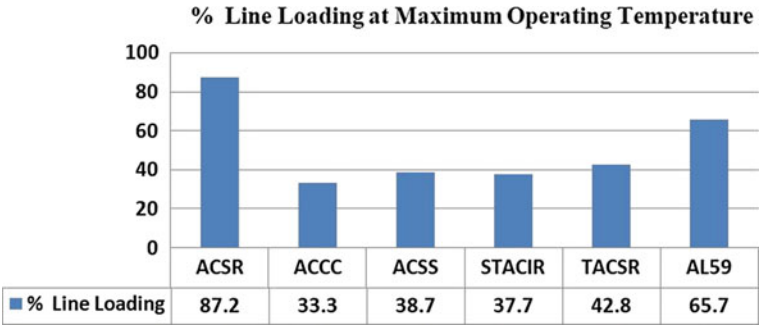

Fig. 4 Comparison of % of line loading in maximum operating temperature

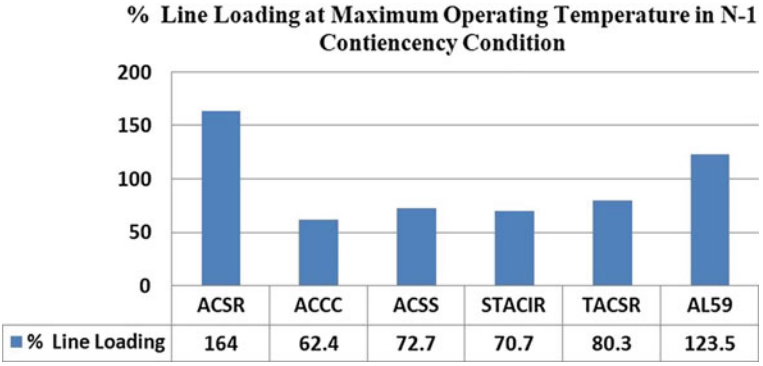

Fig. 5 Comparison of % of line loading at maximum operating temperature in $N - 1$ contingency condition

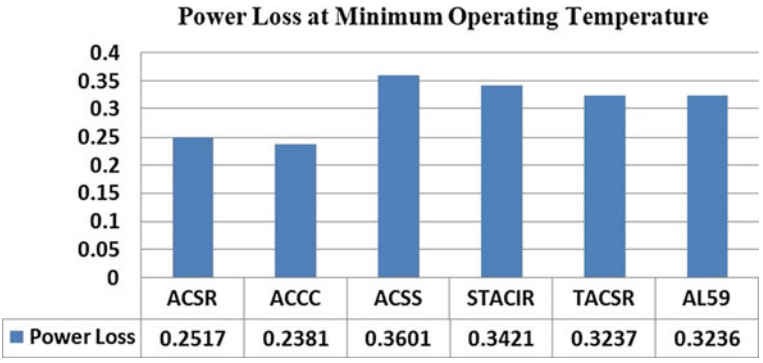

Fig. 6 Comparison of losses in minimum operating temperature

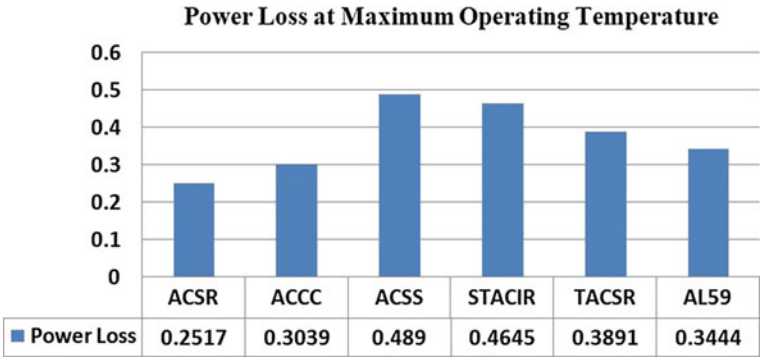

Fig. 7 Comparison of losses in maximum operating temperature

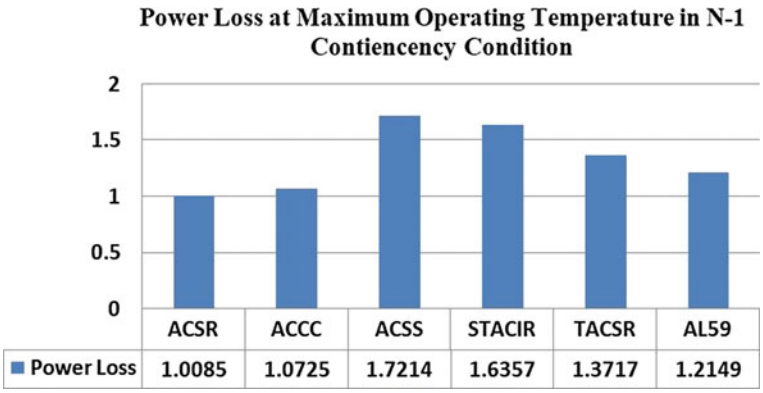

Fig. 8 Comparison of losses at maximum operating temperature in $N - 1$ contingency condition

conductor cannot be operated beyond 75 °C, so losses and % line loading remain same as per results of Table 2 at 75 °C. In case of $N - 1$ contingency analysis, the line will not be overloaded if re-conductoring of 220 kV D/c line is carried out with ACCC conductor because of % of line loading is around (62.4) MW.

5 Techno-Economic Analysis

(See Table 5).

After obtaining the best suitable conductor (ACCC) from the various conductors as per the simulation results, we can say that more power can be transferred (1156) MW from D/C line which having length of 4.7 km. Total cost for re-conductoring of 220 kV D/c line is Rs. 2.27 Cr, while the total cost of the construction of the new S/C transmission line will be 5.5 Cr (approx) Rs.

Table 5 Techno-economic analysis comparison with various HTLS conductors [8]

Conductor type	ACCC	STACIR	TACSR	ACSS
220 kV D/C transmission line from Indore 400 kV to Indore South Zone 220 kV substation—line length	4.7	4.7	4.7	4.7
Power flow with existing ACSR Zebra conductor in MW	189.66	189.66	189.66	189.66
Maximum power flow with HTLS conductor in MW	572.9	504.26	447.82	491.02
Total power transferred from D/C line in MW	1156	1000.52	895.64	982.04
Per km cost for re-conductoring of 220 kV D/C line in Rs.	4,841,390	75,377,770	2,705,570	3,361,030
Total cost for re-conductoring of 220 kV D/c line in Rs.	22,754,533	354,275,519	12,716,179	15,796,841

Note The total cost of the construction of the new S/C transmission line will be 5.5 Cr (approx) Rs.

6 Conclusion

In this paper, various methods of up-rating a transmission network with various HTLS conductor and AL59 conductor are studied. Looking to the various tabular and graphical results, it is observed that re-conductoring of existing transmission line with HTLS conductors would be the best suitable option. As per the case study results, it is concluded that for up-rating the existing 220 kV D/c transmission line from 400 kV substation to 220 kV substation, line that re-conductoring with ACCC HTLS conductor will be the best suitable option due to twice the power transfer and no overloading issues during $N - 1$ contingency analysis. The line losses of line also reduce with the use of ACCC conductor for re-conductoring of transmission line. Other HTLS conductors can also be used on requirement of the transmission line.

Use of HTLS conductors is more beneficial for the utilities in terms of economic point of view. As per the tabular results of techno-economic analysis, we can say that if we construct a new 220 kV S/C transmission line, it requires the total cost around 5.5 Cr (approx) Rupees, while if we re-conductoring this D/c line with ACCC, it takes the total cost around 2.27 Cr. Rupees. Other HTLS conductors can also be used on requirement of the transmission line.

References

1. Yan Z, Wang Y, Liang L (2017) Analysis on ampacity of overhead transmission lines being operated. J Inf Process Syst 13(5):1358–1371
2. Reddy BS, Chatterjee D (2016) Performance evaluation of high temperature high current conductors. IEEE Trans Dielectr Electr Insul 23(3):1570–1579

3. Mateescu E, Marginean D, Florea G, Gal SIA, Matea C (2011) Re-conductoring using HTLS conductors. In: Case study for a 220 kV double circuit transmission LINE in Romania. 2011 IEEE PES 12th international conference on transmission and distribution construction, operation and live-line maintenance (ESMO), Providence, RI, pp 1–7
4. Kavanagh T, Armstrong O (2010) An evaluation of high temperature low sag conductors for up-rating the 220 kV transmission network in Ireland. In: 45th international universities power engineering conference UPEC2010. Cardiff, pp 1–5
5. Kenge AV, Dusane SV, Sarkar J (2016) Statistical analysis & comparison of HTLS conductor with conventional ACSR conductor. In: 2016 international conference on electrical, electronics, and optimization techniques (ICEEOT). Chennai, pp 2955–2959
6. Energy Research and Development Division, EPRI (2008) Demonstration of advanced conductors for overhead transmission lines. Final project report 1007448, July 2008
7. Central Electricity Authority (2013) Transmission planning criteria. January 2013
8. Yasaranga HBD, Wijayapala WDAS, Hemapala KTMU (2017) Techno economic analysis of the use of high temperature low sag (HTLS) conductors in the Sri Lanka's transmission system. Engineer L(01):41–52

Energy Audit: A Case Study in a Rubberwood Processing Industry

Anith Krishnan, Saji Justus, Ajay Raj, Jestin Jaison, Nizy Susan Shaji, V. S. Unnimaya, Salini M. Venugopal and A. Sriram

Abstract This paper deals with the identification of energy savings by energy audit analysis in rubberwood industries. Energy auditing was conducted at Meenachil Rubberwood Limited, Poonjar, Kerala. Energy audit focuses mainly on the analysis of energy-consuming processes. Several energy conservative proposals and their cost-benefit analysis along with the payback period calculation are done.

Keywords Energy audit · Rubberwood industry · Energy · Energy conservation · Energy efficiency · Energy savings · Power factor · Carbon footprint · Compressor · Boiler · Diesel generator

1 Introduction

Energy audits have become an important tool in the process of energy consumption analysis and optimization. Energy audits have enabled to strike a balance between the supply and demand. It can be used as a tool to accomplish a threshold energy consumption for concrete accomplishment of demand slashing.

Energy audit is a procedure including, but not limited to, verification of the achievement of energy cost savings and energy unit savings guaranteed resulting

A. Krishnan (✉) · S. Justus · A. Raj · J. Jaison · N. S. Shaji · V. S. Unnimaya · S. M. Venugopal
College of Engineering Kidangoor, Kottayam, Kerala, India
e-mail: anithkrishnan@gmail.com

S. Justus
e-mail: sajijustus@gmail.com

A. Raj
e-mail: ajayraj10000@gmail.com

N. S. Shaji
e-mail: nizy1416@gmail.com

A. Sriram
Kerala State Productivity Council, Kochi, India

A. Mehta et al. (eds.), *Advances in Electric Power and Energy Infrastructure*, Lecture Notes in Electrical Engineering 608,
https://doi.org/10.1007/978-981-15-0206-4_21

from implementation of energy conservation measures and determination of whether an adjustment to the energy baseline is justified by conditions beyond the contractor's control. Simply put, energy audit is a procedure to establish an energy baseline to reduce the quantity of energy that is used for different purposes. Energy audit can be classified into small scale and large scale or industrial energy audits.

1.1 Energy Audit: Definition

According to the definition in the ISO 50002 standard, an **energy audit** is a systematic analysis of energy use and energy consumption within a defined energy audit scope, in order to identify, quantify and report on the opportunities for improved energy performance.

Also, According to the Energy Conservation Act [1] of 2001, Section 1, definitions (i), energy audit is defined as: *Energy audit means the verification, monitoring and analysis of use of energy including submission of technical report containing recommendations for improving energy efficiency with cost-benefit analysis and an action plan to reduce energy consumption.*

1.2 Audit Approach

The audit process can be divided into three distinct phases each of which consists of an interrelated set of procedures necessary to conduct an effective audit:

- Pre-audit phase (or planning phase)
- Audit phase (or auditing phase)
- Post-audit phase (or reporting phase).

2 Energy Consumption Analysis

2.1 Baseline Data

The basic information about the Meenachil Rubberwood Limited from the last three available bills is given below. The industry belongs to Poonjar section in Pala circle. The electricity is supplied from the 110 kV substation at Erattupetta. Details obtained from the KSEB bill are given in Table 1.

2.2 Power Sharing of Sub-switchboards

The industry has five sub-switchboards (SSBs). The power sharing each SSB is shown in Fig. 1. The major portion of electrical energy is used for boiler pumps

Table 1 Baseline data

1	Electricity provider	KSEBL		
2	Tariff	HT I (A)		
3	Substation feeder	11 kV, HT		
4	Contract demand (kVA)	**130**		
	Year	2016	2017	2018
5	Connected load (kW)	223	223	318.344
6	Maximum demand (kVA)	128	121	118
7	Average power factor	0.83	0.81	0.76
8	Average monthly energy charge (Rs.)	88123.5	61868.8	62874.6
9	Average monthly demand charge (Rs.)	38587.5	33968.18	30831.8
10	Average monthly energy consumption (kWh)	16656.7	12113.3	10300.9
11	Average monthly electricity cost (Rs.)	144910.5	109061.7	99885.4
12	Per unit cost (Rs.)	8.7	9	9.7

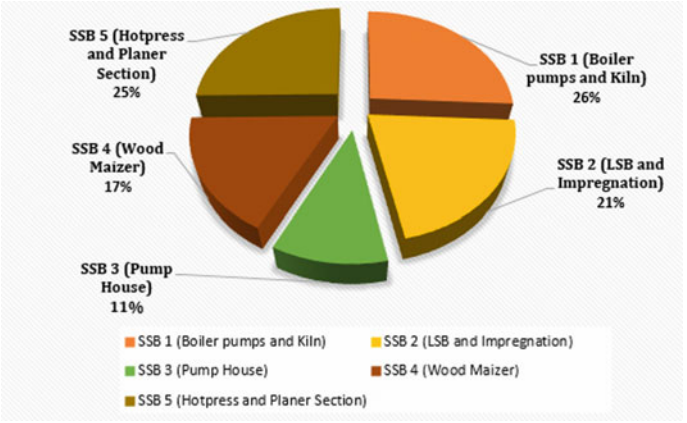

Fig. 1 Energy sharing in various SSBs

and kiln, which is 26%. Hot press and planer section use 25% of energy. LSB and impregnation unit use 21% of energy. Wood-Mizer uses 17% of energy, and pump house uses 11% of energy.

2.3 Electrical Power Demand in Various Time Zones

By analyzing the demand in various time zones, we get a picture of the load in the industry at different time zones. The comparison of demand in three time zones is shown in Fig. 2. The industry functions for 24 h a day. The demand is comparatively

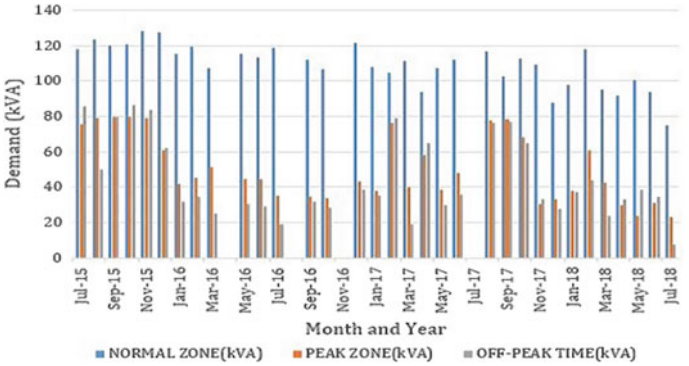

Fig. 2 Electrical power demand in three zones

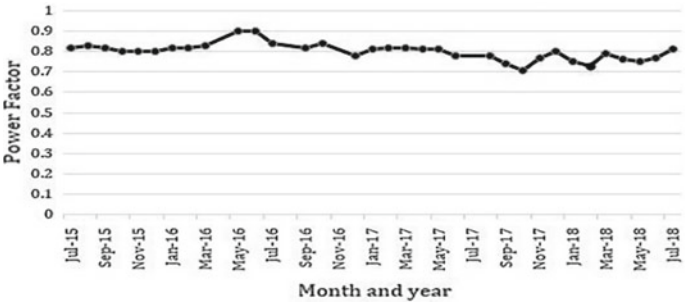

Fig. 3 Power factor curve

higher during the normal zone since majority of the production-related tasks are done during this period. Only a few processes like kiln, boiler, etc., function during other billing zones.

2.4 Running Average of Power Factor

Power factor is a measure of how effectively the electricity is used. The power factor curve based on the available electricity bills of the last three years is given in Fig. 3.

The industry is observed to have a very low power factor. The maximum power factor observed during the interval from June 2015 to July 2018 was 0.9. The average power factor of the industry from the available electricity bills of the last three years is 0.79.

For improving the power factor to 0.99, a 40kVAr APFC panel is proposed. APFC panel installation cost is Rs. 55,000, and simple payback period is 3.3 months.

If the power factor is improved to 0.99, the contract demand can be reduced from 130 to 100 kVA.

3 System Description and Analysis

3.1 Transformer

There is a 250 kVA 11 kV/415 V transformer in the industry. The secondary transformer was logged for a period of 24 h, from November 27, 2018, to November 28, 2018, using the instrument Fluke 434 Energy Analyzer.

kW rating of transformer = kVA × cosϕ = 250 × 0.76 = 190

For a 250 kVA transformer,

Total loss at 50% loading = 3.32 kW

Total loss = copper loss + core

Core loss is a constant value irrespective of the load and

Core loss, $P_c = 0.29$ kW

i.e., Cu loss at full load, P_{Cu} = total loss at full load − core loss = 3.02 kW

Fractional load at maximum efficiency,

$$x = \sqrt{\frac{P_c}{P_{\text{CuFL}}}} = 0.3$$

Percentage Efficiency of the transformer

$$\%\eta = \frac{\text{P}_{\text{out}}}{\text{P}_{\text{out}} + \text{Losses}} \times 100$$

The transformer efficiency curve is shown in Fig. 4. From the graph, the maximum efficiency is obtained at 30% loading. The installed transformer meets the load requirements.

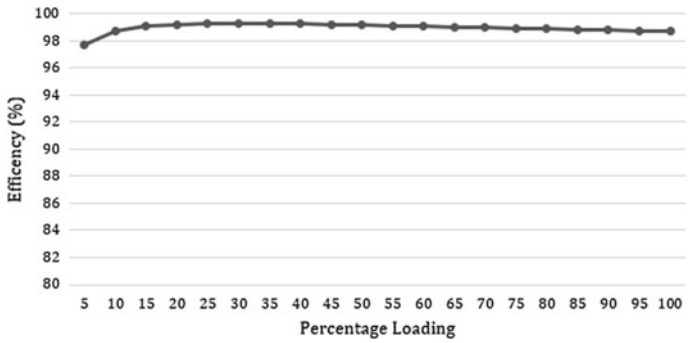

Fig. 4 Transformer efficiency curve

Table 2 Analysis of diesel generator

Average loading (kVA)	43.75
Percentage loading	*35*
Diesel consumed (l)	25
Diesel consumed (kg)	20.8
Diesel consumed (kcal)	224,640
Electricity generated (kWh)	70.007
Electricity generated (kcal)	60,206.02
Specific energy consumption ratio (kWh/l)	2.8
Efficiency (%)	*26.8*
Per unit consumption (l/kWh)	0.36
Diesel price (Rs./l)	68.24
Per unit cost	24.57

3.2 Diesel Generator

The industry has a diesel generator of 125 kVA. It is connected to the bus bar via a switch. This generator was logged using Fluke 434 Energy Analyzer for two hours, and generator percentage loading was obtained. At that respective loading, the efficiency, the specific energy generation ratio (SEGR) and per unit cost of generation were calculated. These data are given in Table 2.

The equations that were used include:

Diesel consumption (kg) = diesel consumption (l) × density of the diesel

Diesel consumption (kCal) = diesel consumption (kg) × specific energy of diesel

Electricity generated (kCal) = electricity generated (kWh) × 860

$$\text{Specific energy generation ratio} = \frac{\text{electricity generated (kWh)}}{\text{diesel consumption (l)}}$$

$$\text{Efficiency in percentage} = \frac{\text{electricity generated (kCal)}}{\text{diesel consumption (kCal)}}$$

$$\text{Per unit consumption} = \frac{\text{diesel consumed (l)}}{\text{energy generated (kWh)}}$$

Per unit cost = per unit consumption × diesel price

Other general observations made about the generator are:

- The air filters of the diesel generator were observed to be dusty.
- Unbalancing in load in a way which affects the system stability was not observed.
- The diesel generator set is not properly serviced.

3.3 Air Compressor

Air compressors account for a significant amount of electricity consumption in industries. Air compressors are used in the industry to supply process requirement, to operate pneumatic tools and equipment, and to meet instrumentation needs. Only

Table 3 Leakage test

Rating of compressor motor	20 hp
Capacity of compressor (m/min)	2.49
Cut-out pressure (kg/cm)	7.4
Cut-in pressure (kg/cm)	6.4
Load drawn (kW)	17.715
Time on load, T (min)	0.3
Time to unload, t (min)	0.6
Leakage quantity (m/min)	0.83
Leakage quantity per day (m)	398.4
Energy loss due to leakage per day (kWh)	47.239
Energy loss due to leakage per year (kWh)	**14,171.73**
Annual cost on leakage (Rs.)	**1,47,952.90**

10–30% of energy reaches the point of end-use, and balance 70–90% of energy of the power of the prime mover is converted to unusable heat energy and to a lesser extent is lost in the form of friction, misuse and noise.

Leakage Test: The compressors have leakages which reduces the efficiency of the system, and thus it has to be evaluated. A quantifiable leakage was detected in the compressor pipes and valves.

The system leakage is calculated as

$$\text{Leakage quantity}\,(\%) = \frac{\text{Load time} \times 100}{\text{Load time} + \text{Unload time}}$$

From the details obtained from leakage test which is given in Table 3, a leakage quantity of 33.33% is calculated. Air leak is detected inside the two planer machines and in the finger joining section. Also, a large leak of air is noticed in the pipeline connected to the painting section.

VFD Installation: Air compressor is logged using Fluke 434 Energy Analyzer. The logged data is shown in Fig. 5.

While analyzing the data, the compressor consumes a no-load power of 10.5 kW. So in order to decline the no-load loss, a variable frequency drive (VFD) can be proposed. The basic function of the VFD is to act as a variable frequency source in order to vary the speed of the motor as per the user settings. Variable speed depending upon the load requirement provides significant energy savings. A reduction of 20% in the operating speed of the motor from its rated speed will result in an almost 50% reduction in the input power to the motor. By installing the VFD, a cost saving of approximately Rs. 1,17,000/- can be obtained and the details are shown in Table 4.

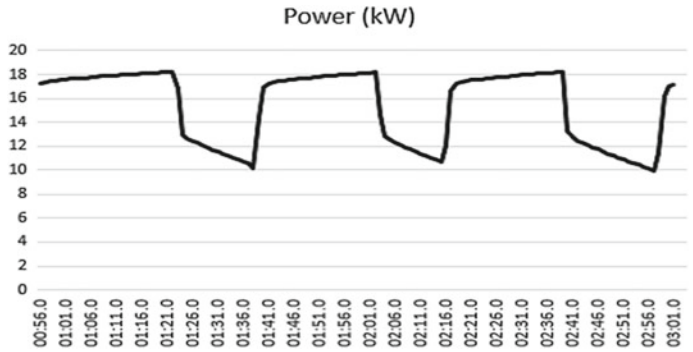

Fig. 5 Compressor logged data

Table 4 VFD calculation

On-load time (min)	1.06
No-load time (min)	0.17
Cycle time (min)	1.23
No-load power (kW)	10.05
Hours of operation in an year	5280
Energy saving per year (kWh)	11237.08235
Cost saving (Rs.)	117315.1398
Cost of VFD (Rs.)	73,395
Payback period (Years)	1.6

3.4 Boiler

The performance of a boiler, like efficiency and evaporation ratio, reduces with time due to poor combustion, poor operation and maintenance. Deterioration of fuel quality and water quality also leads to poor performance of boiler. Efficiency testing helps us to find out how far the boiler efficiency drifts away from the best efficiency. Any observed abnormal deviations could therefore be investigated to pinpoint the problem area for necessary corrective action. Hence, it is necessary to find out the current level of efficiency for performance evaluation, which is a prerequisite for energy conservation action in industry.

Performance Evaluation and Analysis: The purpose of the performance is to determine the actual performance and the efficiency of the boiler and compare it with the design values or norms. It is an indicator for tracking day-to-day and season-to-season variations in boiler efficiency and energy efficiency improvements.

Table 5 Performance analysis of boiler

Steam generated (m^3)	0.2875
Steam generated (kg)	287.5
Weight of wood used (kg)	62
Heat input (°C)	155
Heat output (°C)	115
Boiler efficiency (%)	74.19
Evaporation ratio	4.63

$$\text{Boiler efficiency (\%)} = \frac{\text{Heat Output}}{\text{Heat Input}} \times 100$$

$$\text{Evaporation Ratio} = \frac{\text{Quantity of Steam Generated}}{\text{Quantity of Fuel Consumption}}$$

The boiler efficiency can be tested using two methods, i.e., direct and indirect method. Here, indirect method could not be used due to lack of availability of measuring instruments.

So, from the performance analysis in Table 5, the efficiency of the boiler was found out to be 74% which is acceptable. Some general observations found are:

- The air intake in the boiler can be optimized.
- Waste wood is used as fuel, but it is not given any monetary value.
- Fuel consumption is not recorded.
- Steam leakages were identified.
- Boiler possesses a closed-loop system.

4 Light Audit

In the industry, there are 60 fluorescent tube lights of 40 wattage each. These 60 fluorescent tubes can be replaced by energy-efficient 20 W t8 LED tube lights which have same illuminance as the fluorescent tube lights. The daylight is not properly used by the industry. The calculations of the light audit are given in Table 6.

5 Carbon Footprint

Carbon footprint is the sum of all emissions of CO_2, which were generated by our activities in a given time frame. Usually, a carbon footprint is calculated for the time period of a year. Carbon footprints from energy consumption can be reduced

Table 6 Lighting audit

Number of fluorescent tube lights	60
Wattage of each fluorescent tube light	40
Total load (kW)	2.4
Lumens per fluorescent tube lights	2300
Average working hours of tube lights	12
Wattage of new t8 LED tube lights	20
Annual energy savings (kWh)	4320
Reduction in demand (kVA)	1
Annual demand savings (Rs.)	3600
Annual savings (Rs.) (demand + energy)	48700.8
Installation cost (Rs.)	36,000
Simple payback period (months)	8.9

Table 7 Carbon footprint

Annual energy consumption (kWh)	158682.24
Annual diesel consumption (l)	4000
Annual wood consumption (kg)	14,600
Carbon footprint (ton)	160
Annual energy savings	67269.58
Reduction in carbon emission (ton)	57.17

through the development of alternative energy products such as solar energy, which are renewable resources.

By installing the proposed energy-saving techniques, 57 tons of CO_2 emission can be reduced which is given in Table 7.

6 Conclusion

This paper is an energy audit performed at Meenachil Rubberwood Ltd, Poonjar, which is a rubberwood processing industry. The energy consumption of the industry was analyzed. Energy bill from the year 2016 to 2018 was studied to identify the management of electrical energy and identified a low power factor due to defective capacitor banks. Transformer, compressor, boiler, lighting and diesel generator were audited for identifying the mismanagement of energy. The identified energy-saving opportunities have the potential to save approximately 20% of total energy consumption and an annual cost saving of Rs. 600,000, thereby a reduction of 57 tons of CO_2 in the total carbon footprint. A similar work can be done at various rubberwood processing industries for the conservation of energy.

Acknowledgements We would like to acknowledge the support received from TEQIP-II.

References

1. Indian Electricity Act 2001
2. Bohar A, Allouhi A, Jamin A (2015) Analysis of electrical energy consumption and energy audit of interior lighting for an industrial site in Morocco
3. Wang X, Hung C, Energy audit of building: a case study of a commercial building in Shanghai
4. Energy efficiency in electrical utilities by Bureau of Energy Efficiency (BEE)
5. General aspects of energy management and audit by Bureau of Energy Efficiency (BEE)
6. Energy efficiency in thermal utilities by Bureau of Energy Efficiency (BEE)
7. Energy performance assessment for equipment and utility systems by Bureau of Energy Efficiency (BEE)

Energy Audit: A Case Study of Tyre Retreading Unit in Kerala

Anith Krishnan, Rose Mary Francis, K. R. Rahul Raj, Nikhil Thomas, V. K. Muhammed Sadique and A. Sriram

Abstract In this paper, we have discussed the analysis of the energy consumption from the energy audit conducted at transport workshop, Edappal, Kerala, India, and we have identified opportunities to reduce energy expense and carbon footprint. We found out that the most of the energy consumption is by the curing chambers in the Tyre Workshop. So we have done a targeted audit on the curing chambers. The energy audit showed that the industry consumed a monthly average electrical energy of 31394.71 kWh and has a potential to save 7751.71 kWh of energy by implementing the recommendations suggested in this paper.

Keywords Energy audit · Compressor · Energy conservation · Energy efficiency · Reactive power management · Tyre retreading unit · Power factor · Specific energy

1 Introduction

Energy audit can be defined as a scientific approach for decision-making within the space of energy management. It tries to balance the overall energy inputs with its use and serves to spot all the energy streams during a facility. It quantifies energy usage of all types of equipments according to its semantic functions. Industrial energy audit is literary to a comprehensive energy management programme. According to Energy Conservation Act 2001 [1] as follows: *Energy Audit means the verification, monitoring and analysis of the use of energy together with submission of technical*

A. Krishnan (✉) · R. M. Francis · K. R. Rahul Raj · N. Thomas · V. K. Muhammed Sadique
College of Engineering Kidangoor, Kottayam, Kerala, India
e-mail: anithkrishnan@gmail.com

R. M. Francis
e-mail: rosemondoth96@gmail.com

K. R. Rahul Raj
e-mail: rahulrj618@gmail.com

A. Sriram
Kerala State productivity council, Kochi, Kerala, India

A. Mehta et al. (eds.), *Advances in Electric Power and Energy Infrastructure*, Lecture Notes in Electrical Engineering 608,
https://doi.org/10.1007/978-981-15-0206-4_22

Table 1 Baseline data—energy consumption

Baseline data (based on last 24 months)		
1	Electricity provider	KSEBL
2	Tariff	HT I (A)
3	Sub-station incoming feeder	11 kV, HT
4	Contract demand (kVA)	120
5	Connected load (kW)	354.499
6	Maximum demand (July 2017)	153.83
7	Average monthly energy consumption	31394.71
8	Average cost of electrical energy (Rs./kWh)	7.45
9	Average monthly energy charge (Rs.)	174114.44
10	Average monthly demand charges (Rs.)	43648.75
11	Average monthly electricity cost (Rs.)	227,751
12	Average power factor	0.85
13	Average monthly diesel consumption (l)	332

report containing recommendations for rising energy efficiency with price–benefit analysis and a work plan to reduce energy consumption [2].

The paper introduces the energy consumption of a public sector industry in Kerala as a case study. By conducting a survey on the energy use, the instrumentation load within the building is gathered for the analysis. Some recommendations and energy conservation options to extend energy efficiency are proposed in the upcoming sections.

Section 2 deals with the description of the industry, main plants in the industry and the processes occurring in each of the plants and the total production capacity of the industry.

The baseline data of the industry is given in Table 1 of Sect. 3. On the subsequent sections, reactive power management and their required conservation options are described.

Sections 3.6 and 3.7 deal with the details of the targeted audit on the curing chambers that we have done at the transport workshop Edappal, Kerala, India. Along with that, the energy conservation options are explained in detail.

Section 4 deals with the compressors in the workshop. On the subsequent sections, we have dealt with the energy conservation options for the compressors.

Section 5 deals with other proposals. In Sect. 6, we concluded by comparing the present specific energy consumption and the new specific energy consumption of tyre that we have calculated after all the energy options are implemented by the industry.

2 Outline of Industry

Major Units

Main workshop, UNIT Reconditioning, Store and office, Body Building Shop, Tyre Shop, Staff training centre, Accommodation facility for staff.

The main process in the industry is the tyre retreading process. It is a 24-h plant with a capacity to produce 144 tyres per day.

3 Energy Consumption Analysis

Baseline data is derived from the electricity bill provided by the utility (KSEBL) and diesel consumption logs available at the industry.

3.1 Power Factor

The maximum demand and power factor (as per the energy bills) during the last 1 year is given in Fig. 1.

3.2 Reactive Power Management

Six capacitors were found to be damaged/faulty. It has been found that out of the total 77 kVAR, only 23.87 kVAR is available. That accounts to a performance of only

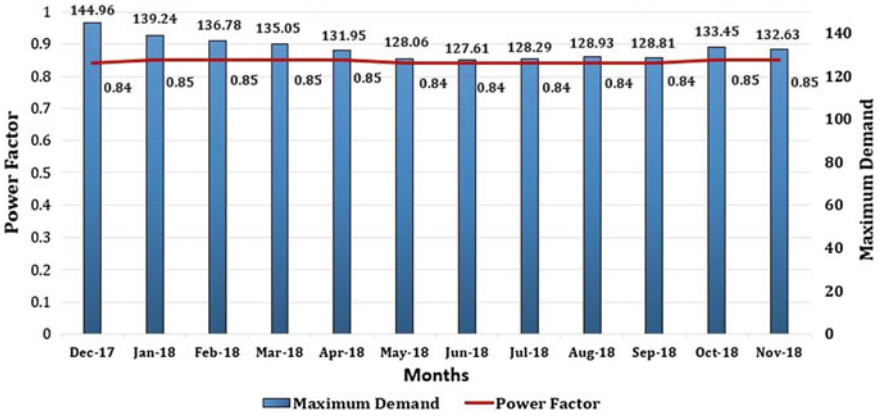

Fig. 1 Maximum demand and power factor during the last 1 year

31%, which is not satisfactory. The daily power factor profile of the industry is given in Fig. 1. This profile is based on the on-site measurements done by the team, at the sub-station. The proposal for improving the power factor is given in the following section.

3.3 *Proposal for Installing an Automatic Power Factor Controller Unit*

Based on the logged data, the kVAR required to get unity power factor is calculated as shown in Eq. (1). The actual power factor at 135.63 kW is 0.94 and is due to the major load contribution by the electric heater (resistive) in the curing chambers. An additional requirement of 50 kVAR capacitor is required to increase the power factor to unity.

The kVAR rating of capacitors to be installed in order to improve the power factor can be calculated using Eq. (1), where kW is the power drawn, $\tan \phi_1$ is the trigonometric ratio for the present power factor, and $\tan \phi_2$ is the trigonometric ratio for the desired power factor.

$$\text{kVAR rating} = \text{kW} \, (\tan \phi_1 - \tan \phi_2) \tag{1}$$

- It is proposed to install a APFC unit along with 50 kVAR capacitor bank for improving the power factor.
- The cost–benefit analysis for the APFC unit is given in Table 2.
- Further, the improvement in power factor will automatically bring down the maximum demand of the industry.

3.4 *Electrical Load Analysis*

The major SSBs of the industry were logged for a period of 15 min on 02 December 2018, and the following measurement data were obtained (Table 3).

Table 2 Cost–benefit analysis of APFC

Avg. monthly energy cost (Rs.)	Avg. power factor	New power factor	Savings per month (Rs.)	Annual savings (Rs.)	Cost of installation (Rs.)	Simple payback period (months)
178,668	0.85	0.99	16,973	203,676	65,000	3.83

Table 3 Electrical load analysis

S. no	Panel board name	Maximum measured (kW)	Maximum measured (kVA)	Power factor
1	Workshop	8.31	14.28	0.63
2	Body building section	14.7	18.78	0.79
3	Tyre shop	93.42	95.16	0.89
4	Workshop	3.54	4.23	0.57

3.5 Specific Energy Analysis

Since 70–80% of the overall energy consumption is at the tyre retreading unit, the specific energy consumption is calculated for each tyre that is retreaded.
The average specific energy consumption = 15044.8 kCal/tyre.

3.6 Curing Chamber

The industry has two curing chambers inside the tyre retreading plant. The curing chamber consists of electric resistive heating coils and a fan for circulation and even distribution of heat. The chamber has a maximum loading capacity of 12 tyres.

The set point of the temperature controller (of the curing process) is 125 °C. When the tyres are initially loaded into the chamber, the temperature inside will be far less than the set point and as such the heater coils will be turned on (see Fig. 2). The heating will continue until the inside temperature reaches 125 °C. After that the heater coils are turned off by the controller. The process explained here is the same for both the chambers present in the industry.

- It is found (measured) that the total heater load of chamber 1 is 30 kW, and the same is balanced across all the phases, which is good.

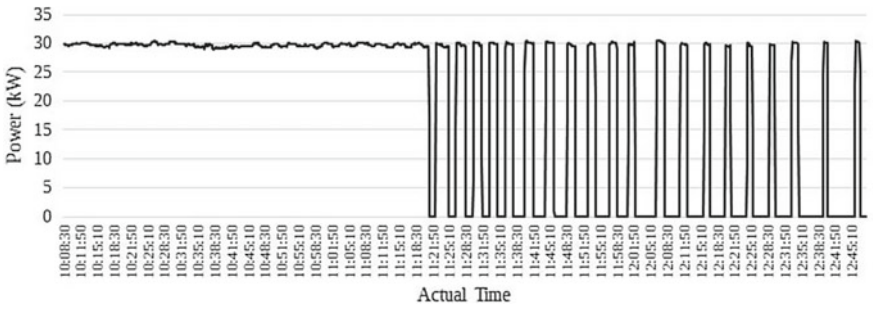

Fig. 2 Load profile of chamber 1 for one curing process

- It is found (measured) that the total heater load of chamber 2 is 39 kW, and the same is balanced across all the phases, which is good.
- Although the minimum temperature to be maintained inside the chamber is 120 °C, the controller is set at 125 °C. This is the case for both the chambers.
- There is scope for energy conservation by installing a suitable temperature controller mechanism that maintains the temperature at 121 °C. The constraint on the process is that the internal temperature should always be greater than 120 °C.

3.7 Proposal for Voltage Control of Heater Coils in Curing Chamber

Heat energy inside the curing chamber is provided by the heating coils. If the line voltage which is applied to the heater coil is reduced with a thyristor-based voltage controller, the heat generated can be controlled, since I is directly proportional to the applied voltage. Thus, the controller can be tuned to maintain the internal temperature of the chamber at 121 °C.

The existing SEC was already determined (see Table 4). Figure 3 shows the comparison between the SEC before and after the proposed voltage controller installation (Table 5).

- Thyristor-based voltage control is a soft-switching device, and as such the heater load will be gradually introduced in to the system. This will also result in demand reduction.

Table 4 Specific energy consumption (SEC) in curing chambers

Chamber	Energy consumed per process (kWh)	SEC (kWh/tyre)
1	63.25	5.27
2	70.42	5.87

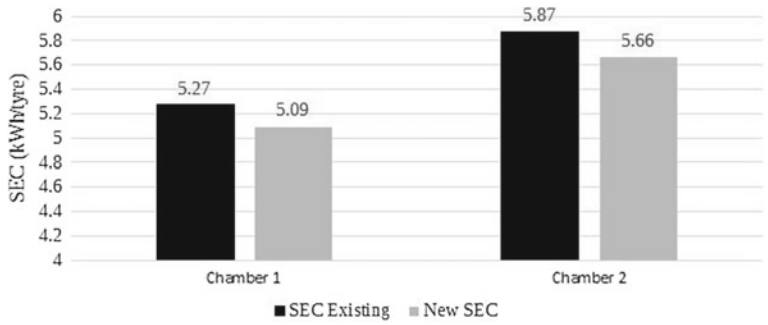

Fig. 3 Comparison of SEC before and after implementation of voltage control

Table 5 Energy savings and payback analysis of voltage controller proposal

Chamber	Energy savings per process (kWh)	Energy savings per year (kWh)	Cost savings per year (Rs.)	Cost of investment (Rs.)	Simple payback period (months)
1	2.14	3783.52	28187.22	60,000	25.54
2	2.45	4331.60	32270.42	60,000	22.31

4 Compressors

4.1 Compressor Capacity Assessment

Compressor capacity assessment is done as per reference [3] (Table 6).

The following are the inferences after conducting the test:

- The capacity shortfall of 5.5 kW and 7.5 hp compressors is more than 10% and is due for maintenance.
- At the time of taking measurements, the audit team found that the temperature inside the compressor room was 2–6 °C above the ambient temperature. For every 4 °C rise in air inlet temperature will increase power consumption by 1%. Therefore, it is good to maintain air circulation inside the compressor room.
- It is observed that air inlet filters are found not cleaned regularly, and compressor efficiency will be reduced by 2% for every 250 mm water column (WC) pressure drop across the filter.
- Keep compressor valves in good condition by removing and inspecting once every six months. Worn-out valves can reduce compressor efficiency by as much as 50%.

Table 6 Calculation of FAD test

Compressor rating	5.5 kW	7.5 hp	20 hp
Location	Workshop	Bodybuilding WS	Tyre WS
Atmospheric pressure (kg/cm^2)	1.03	1.03	1.03
Initial pressure (kg/cm^2)	1.03	1.03	1.03
Final pressure (kg/cm^2)	9.2	12	8
Receiver volume V (m^3)	0.5	0.25	0.42
Time taken to build up pressure (min)	9.76	6.58	1.75
Compressor output (m^3/min)	0.406354449	0.404653702	1.62407767
Rated capacity (m^3/min)	0.4945	0.4813	1.7273
Capacity shortfall (%)	17.83	15.92	5.98

Table 7 Calculation of leakage test

Leakage test		
	7.5 hp compressor	20 hp screw compressor 2
Capacity of compressor (m^3/min)	0.49	1.73
Cut out pressure (kg/cm^2)	9.2	8
Cut in pressure (kg/cm^2)	6	7
Load drawn (kW)	4.5	14.25
Time to load, T (min)	3.73	0.45
Time to unload, t (min)	6.5	4.6
Leakage quantity (m^3/min)	0.18	0.15
Leakage quantity per day	86.55	221.99
Specific power for compressed air generation (kWh/m^3)	0.15	0.14
Energy loss due to leakage per day (kWh)	13.15	30.48
Energy loss due to leakage per year (kWh)	3943.95	11123.47
Annual cost on leakage (Rs.)	29382.47	82869.82

Annual cost on leakage from the 7.5 hp compressor and 20 hp 2nd screw compressor is 29382.47 Rs. and 82869.82 Rs. respectively

4.2 Leakage Test

The compressors have leakages which reduce the efficiency of the system, and thus, it has to be evaluated (Table 7).

4.3 Compressed Air Leakage—A System Level Approach

The following test is an abridged version of the standard leakage test. The test is conducted on the compressor located near the curing chamber.

The load profile of the 20 hp compressor under steady-state conditions is given in Fig. 4. Steady-state condition means that the compressor is compensating only for the compressed air leakages occurring in the line as well as in the curing process (Table 8).

Compressed air leakage from curing chamber = total leakage − line leakage

- We have calculated the annual cost on leakage from the curing chamber itself to be Rs. 227379.96.

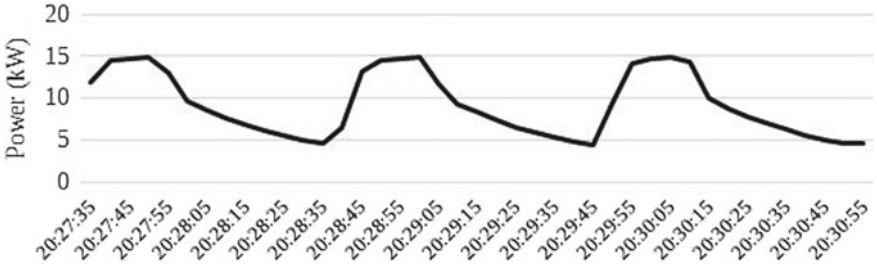

Fig. 4 Load profile of 20 hp compressor

Table 8 Compressed air leakage

	Line leakages	Total system leakages	Leakage from curing chamber
Capacity of compressor (m^3/min)	1.73	1.73	
Cut out pressure (kg/cm^2)	10	10	
Cut in pressure (kg/cm^2)	8	8	
Load drawn (kW)	15.56	15.56	
Time to load, T (min)	0.21	0.5	
Time to unload, t (min)	3.05	0.67	
Leakage quantity (m^3/min)	0.111	0.739	
Leakage quantity per day (m^3)	159.84	798.12	678.24
Specific power for compressed air generation (kWh/m^3)	0.15		0.15
Energy loss due to leakage per day (kWh)	23.976		101.736
Energy loss due to leakage per year (kWh)	8751.24		30520.8
Annual cost on leakage (Rs.)	65196.738		227379.96

4.4 Compressed Air Leakage

The details of compressed air leakage are given in the section. In a practical scenario, the compressed air system will not be leak proof. Hence, a best estimate of 90% savings is taken for the following calculations.

$$\text{Total energy savings} = 0.9 \times \text{energy savings as in section} \quad (2)$$

$$= 48905.51\,\text{kWh} \quad (3)$$

$$\text{Total savings} = 7.45 \times 48905.51 \quad (4)$$

$$= 364{,}346\,\text{Rs.} \quad (5)$$

5 Other Proposals

5.1 Proposal for Increasing Contract Demand

The contract demand (CD) on the industry is 120 kVA. The analysis of the last 2 year bills shows that the industry has been paying excess demand charges for almost all the months. The maximum and average values of the maximum demand during the last 12 months were 144.9 kVA and 131.15 kVA, respectively. The CD can be increased to a value such that the actual demand shall fall within 75–100% of the new CD. If contract demand is 160 kVA, then excess demand charge becomes zero. The increase in CD to 160 kVA from the existing 120 kVA will result in an average yearly savings of Rs. 1671.8 × 12 = Rs. 20061.60 (Fig. 5).

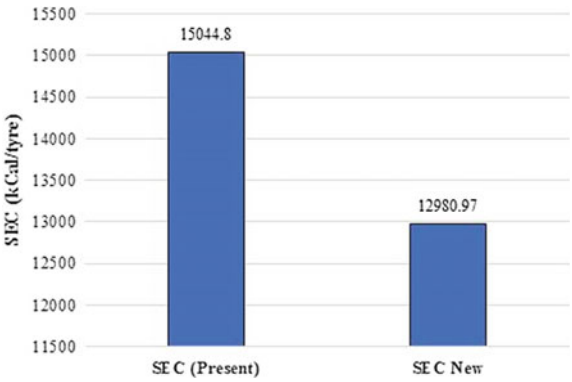

Fig. 5 Specific energy consumption of tyre

5.2 Installation of Grid-Connected Solar Inverter

The main building of the industry has enough shade-free south-facing rooftop area which makes it an apt place for mounting solar panels. A system of 25 kW_p size can be installed at the industry with an installation cost of Rs.1,375,000. The cost of 1 unit is Rs. 5.5. With these observations, the total savings per year is calculated to be Rs. 198,000. The typical lifetime of solar PV system is 25 years, and hence, the payback period is well within its lifetime [4].

6 Conclusions

For 25,008 tyres produced, a specific energy of 15044.8 kCal is used at the present condition. If all our energy conservation recommendations are implemented, then the specific energy of the tyre can be reduced to 12980.97 kCal/tyre. So there will be a 13.71% decrease of specific energy consumption from the present condition.

Acknowledgements We would also like to acknowledge the support received from TEQIP-II.

References

1. The Energy Conservation Act, 2001 No 52 of 2001, Chap. III. http://www.beeindia.in
2. Bureau of energy efficiency guide books, Book 1, Chap. 03. Energy management and audit
3. Bureau of energy efficiency guide books, Book 3, Chap. 03. Compressed air system, pp 67–91
4. http://mnre.gov.in. Concept of grid connected solar inverter

Author Index

A. Mehta et al. (eds.), *Advances in Electric Power and Energy Infrastructure*, Lecture Notes in Electrical Engineering 608,
https://doi.org/10.1007/978-981-15-0206-4